Theoretical and experimental investigation of anaesthetic effects in the brain

A thesis submitted

for the degree of

Doctor of Philosophy

in Physics

by

Leyla Noroozbabaee

THE UNIVERSITY OF
WAIKATO
Te Whare Wānanga o Waikato

October 2016

The University of Waikato

Abstract

The main motivation of this study is to develop a better understanding of anaesthetic drug effects on brain dynamics including the paradoxical enhancement of seizure activity by some anaesthetic drugs. This thesis investigates two mean-field descriptions for the effect of general anaesthetic agents on brain activity: the extended Waikato cortical model (WM) and the Hindriks and van Putten (HvP) thalamocortical model. In the standard Waikato model, the population-average neuron voltage is determined by incoming activity at both electrical (gap-junction) and chemical synapses, the latter mediated by AMPA (excitatory) and $GABA_A$ (inhibitory) receptors. Here we extend the standard WM by including NMDA (excitatory) and $GABA_B$ (inhibitory) synapses. GABAergic anaesthetics, such as propofol, boost cortical inhibition by prolonging the tail of the unitary IPSP (inhibitory postsynaptic potential) at $GABA_A$ receptors, while increasing the synaptic gain at the slower-acting $GABA_B$ receptors. Dissociative anaesthetics act on NMDA receptors to give a voltage-dependent alteration of excitatory synaptic gain. We find that increasing $GABA_B$ or NMDA effect can alter the spatiotemporal dynamics of the standard WM, tending to suppress spatial (Turing) patterns in favour of temporal (Hopf) oscillations. The extended WM predicts increased susceptibility to seizure when $GABA_B$ effect is increased, particularly if the GABAergic agent reduces gap-junction diffusion.

We tested these WM predictions with two biological experiments. We found that potentiation of $GABA_B$ receptors in slices of mouse cortical tissue tended to enhance seizure-like activity. However, our in vivo investigation of the effect of closure of gap junctions did not reveal any seizure patterns in mouse EEG signals.

In the second part of this thesis, we present a detailed analysis of the HvP thalamocortical mean-field model for propofol anaesthesia. While we were able to confirm the Hindriks and van Putten predictions of increases in delta and alpha power at low levels of anaesthetic sedation, we find that for deeper anaesthetic effect, the model jumps from the low-firing state to an extremely high-firing stable state ($\sim$250 spikes/s), and remains stuck there even at $GABA_A$ prolongations as high as 300% which would be expected to induce full comatose suppression of all firing activity. To overcome this pathological behaviour, we tested two possible modifications: first, eliminating the population-dependent anaesthetic sensitivity (efficacy) of the HvP model; second, incorporating reversal potentials and tuning the excitatory sigmoid parameters defining the mapping from voltage

to firing rate. The first modification removes the pathological state, but predicts *decreasing* alpha and delta power as drug concentration increases. The second modification predicts induction-emergence hysteresis (drug concentration is higher at induction than at emergence), but the alpha rhythm is lost, being replaced by a dominant delta-band oscillation.

Original contributions

To the best of my knowledge, this thesis contains no copy or paraphrase of work published by another person, except where duly acknowledged in the text. In Chapter 3, the mathematical formulation of the cortical model developed by Prof Moira Steyn-Ross and colleagues at Waikato University. Otherwise, other components of the research originated with me.

My major contribution in this thesis is the detailed study of the dynamical behaviour of the Hindriks and van Putten (HvP) thalamo-cortical system equations across the full physiological range of anaesthetic concentration, highlighting a deficiency of the HvP model under deepening anaesthesia. Then, I investigate some modifications to overcome the unphysiological behaviour observed in the HvP model.

Publications and presentations

1. Noroozbabaee, L., Steyn-Ross, D.A., Steyn-Ross, M., and Sleigh, J.(2015). Analysis of the Hindriks-van Putten model for propofol anaesthesia: Limitations and extensions. In New Zealand Institute of Physics Conference. Conference held at University of Waikato, Hamilton, New Zealand.
2. Noroozbabaee, L., SteynRoss, D.A., SteynRoss, M., and Sleigh, J.(2015). Hindriks Meanfield model of propofol: It's limitation and correction. In Southern California Regional Systems Biology Conference. Conference held at University of California, Irvine.
3. Noroozbabaee, L., Steyn-Ross, D.A., Steyn-Ross, M., and Sleigh, J.(2013). Investigation of inhibitory mechanisms in a mean-field anaesthesia model. In Computational Neuroscience Conference CNS. Conference held in Paris, France.
4. Noroozbabaee, L., Steyn-Ross, D.A., Steyn-Ross, M., and Sleigh, J.(2013). Modelling anaesthetic effects on the Waikato cortical model. In New Zealand Institute of Physics Conference (Winner of Best Student Award). Conference held in Nelson, New Zealand.

Papers being prepared for publication

1. Noroozbabaee, L., Steyn-Ross, D.A., Steyn-Ross M., and Sleigh J., Critique of the Hindriks and van Putten meanfield model of anaesthesia: limitations and extensions.
2. Noroozbabaee, L., Steyn-Ross, D.A., Voss, L., Steyn-Ross, M., and Sleigh, J. Theoretical and experimental investigation of $GABA_B$ enhancement and gap junction closure in the extended Waikato cortical model.
3. Noroozbabaee, L., Steyn-Ross, D.A., Steyn-Ross, M. and Sleigh, J. Theoretical investigation of NMDA enhancement and gap junction closure in the extended Waikato cortical model.

Dedication

To my husband for his endless supports

To my mother

And to the memory of my father.

Acknowledgements

I would like to thank all those people who made this thesis possible and an unforgettable experience for me.

First of all, I would like to express my sincere gratitude to my chief supervisor, Associate Professor Alistair Steyn-Ross, who offered his continuous advice and encouragement throughout the course of this thesis; I believe working under his supervision with his excellent work and his knowledge has helped me a lot through my achievements in this field.

Besides my chief supervisor, I would like to thank the rest of my thesis committee: Professor Moira Steyn-Ross for her guidance through theoretical analysis, Professor Jamie Sleigh for his encouragement, insightful comments.

I would like to also thank Dr Logan Voss for training and supervising me through my clinical experiments.

I would also like to thank funding supports from Fisher and Paykel Healthcare Study Award.

List of Figures

List of Tables

Acronyms and Abbreviations

AMPA	α-amino-3-hydroxy-5-methyl-4 isoxazole propionic acid
DE	differential equation
DDE	delay differential equation
EEG	electroencephalogram (brain activity recorded via scalp electrodes; cf. ECoG)
EPSC	excitatory postsynaptic current
EPSP	excitatory postsynaptic potential
DFT	discrete Fourier transform
GABA	γ-aminobutyric acid (an inhibitory neurotransmitter)
GHK	Goldman–Hodgkin–Katz formula for membrane voltage
IPSC	inhibitory postsynaptic current
IPSP	inhibitory postsynaptic potential
LOC	loss of consciousness
LSA	linear stability analysis
MAC	minimum anaesthetic concentration (a standard measure of anaesthetic potency)
NMDA	N-methyl-D-aspartate (a neurotransmitter associated with the slowly-decaying "late" current in the excitatory postsynapse; cf. AMPA)
ODE	ordinary differential equation
PDE	partial differential equation
PDF	probability density function
PSP	postsynaptic potential
SDE	stochastic differential equation (Langevin equation)
2-D	two dimension
aCSF	artificial cerebrospinal solution fluid
SLE	seizure-like event
TC	thalamocortical
HvP	Hindrks and van Putten
mHvP	modified Hindrks and van Putten

Contents

Chapter 1

Introduction

The main motivation of this study is to improve our understanding of patients' responses to anaesthetics and to reduce the risk of seizures. This is accomplished by studying drug effects on brain dynamics, focusing on anaesthetic drugs, as some anaesthetics induce seizures.

The brain is a complex system characterized by its structures and its dynamics. Although its structural architecture has been studied for more than a hundred years, its dynamics has been investigated for just the last few decades. In this thesis, we study the dynamical behaviour of an anaesthetised brain through two different modelling approaches: cortical and thalamo-cortical.

Having a basic knowledge of brain structure is a necessary prerequisite for investigation of brain dynamics. We start this chapter with an overview of fundamental neurophysiological concepts and definitions relevant to single neurons as the primary elements of the nervous system.

Then follows a brief summary of brain architecture, focusing on cerebral cortex and thalamus, brain rhythms and functional states. We are particularly interested in the altered rhythms of the anaesthetized brain, attempting to identify the underlying mechanisms for anaesthesia induction and recovery.

In the second part of this chapter, I review several computational mean-field approaches for an anaesthetised brain and their related formulations. I conclude with a comparison between the different models and their outcomes.

1.1 Elements of neurophysiology

Capturing the essential neurological features of spiking neurons is necessary since these comprise the basic building blocks of the nervous system. Similarly, understanding single-neuron dynamics is the first step towards the large-scale modelling of neural populations.

1.1.1 Neuron

Nerve cells known as neurons are functional units of nervous system that contain specific structures: cell body, dendrites, axon and axon terminals. The cell body is the metabolic

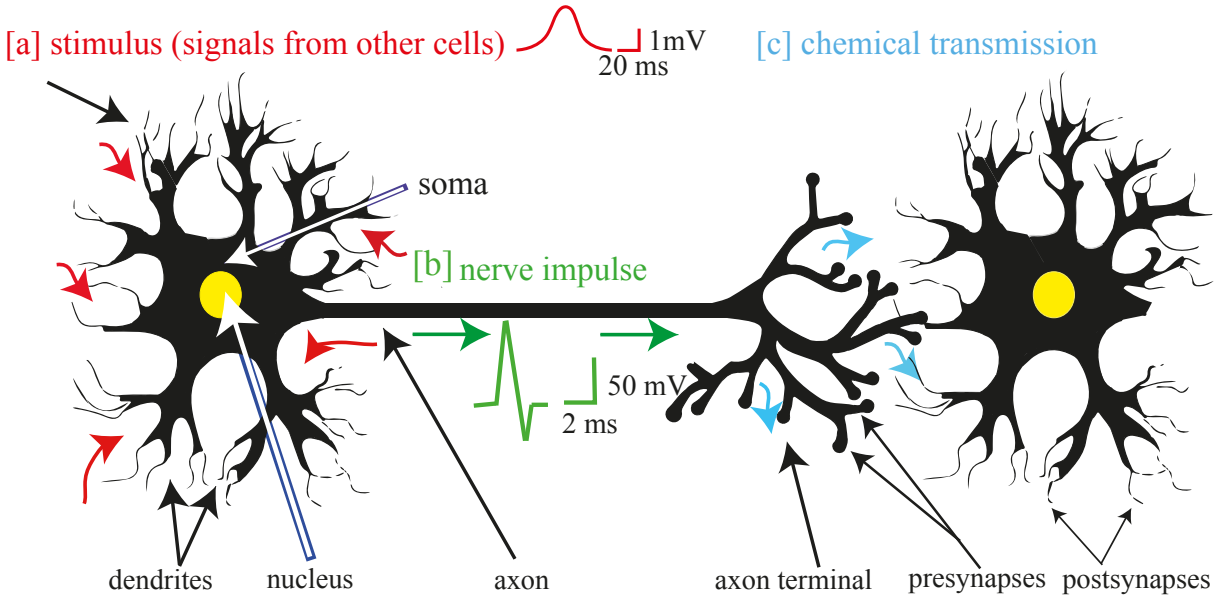

Figure 1.1. Schematic of a biological neuron. Neurotransmitters released at the axon terminal of a presynaptic neuron induce small excitatory or inhibitory voltage pulses in the dendritic branches of the receiving neuron [a]. These incoming voltage events propagate to the cell body (soma) where they are integrated. If a threshold voltage is exceeded, a large voltage spike or action potential is generated [b], which propagates down the axon towards the axon terminal, where neurotransmitters are released to stimulate the next neuron [c].

centre of the neuron responsible for cell protein synthesis. Dendrites are short cytoplasmic processes that extend from the cell body and serve as the main apparatus for receiving stimuli from other neurons. The cell body also gives rise to the axon, a long cytoplasmic process that transmits electrical impulses from the cell body to other neurons via the axon terminals. As shown in Fig. 1.1, when a nerve cell is stimulated, the electrical current from local neural populations is sampled by the postsynaptic dendrites. These currents propagate toward the cell body where they are integrated, producing changes in the internal voltage of the cell. If the voltage change is small, then the voltage can propagate along the axon for a short distance. But if the perturbed voltage exceeds the voltage threshold, then a large voltage spike (action potential) is triggered, and travels along the axon away from the soma body towards the terminal branches, causing release of neurotransmitters into the synaptic cleft.

1.1.2 Synapses

Neurons communicate with each other through synapses. Synapses can be either chemical or electrical:

- In chemical synaptic signalling, the sending cell is called the presynaptic neuron while the cell receiving the signal is the postsynaptic neuron. The presynaptic axon terminal is separated from the postsynaptic cell by a small space called the synaptic

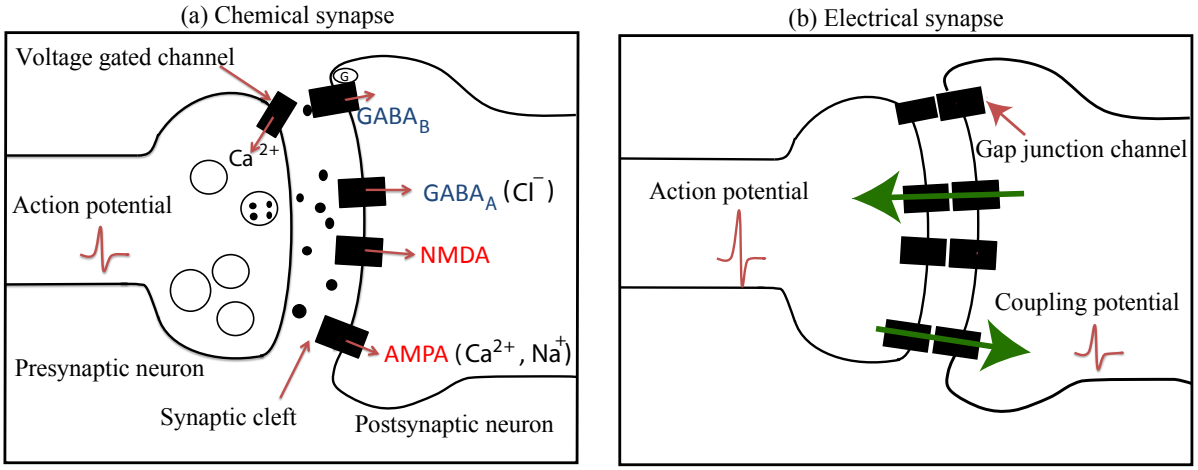

Figure 1.2. Schematic diagram of synapses. (a) Chemical synapse. In response to the arrival of an action potential, voltage-gated calcium channels are activated, causing the release of neurotransmitters from vesicles in the axon terminal of presynapses into the synaptic cleft where neurotransmitters bind to the appropriate receptors on the postsynaptic neuron. (b) Electrical synapse. Electrical transmission is mediated by clusters of intercellular channels called gap junctions that connect the cytoplasm of the two neighbouring cells, and thereby enable bidirectional passage of electrical currents carried by ions.

cleft, Fig. 1.2(a). Most presynaptic axons terminate near the dendrites of the postsynaptic cell. Signals from presynaptic neurons cause release of neurotransmitters that diffuse across the synaptic cleft to bind with receptors on the postsynaptic dendrite resulting in changes in the membrane potential [37]. Receptors are classified as either ionotropic receptors (ligand-gated) or metabotropic receptors:

1. For ionotropic (direct) receptors, the postsynaptic receptor contains both the transmitter binding site and the ion channel which can be opened by the transmitter as part of the same receptor. These receptors can be activated by neurotransmitters (ligands) like α-amino-3-hydroxy-5-methyl-4-isoxazolepropionic acid (AMPA) or deactivated by neurotransmitters like gamma-aminobutyric acid (GABA$_A$) and glycine.
2. For metabotropic (indirect) receptors, the transmitter binds to receptors like G protein-coupled receptors that are neither excitatory nor inhibitory. They are not able to open ion channels themselves, but modulate the actions of excitatory and inhibitory neurotransmitters. GABA$_B$ is a metabotropic receptor.

Direct receptors are often referred to as fast receptors, since their activation time is much shorter than the response time of indirect receptors [5].

- In electrical synapses, Fig. 1.2(b), there is a direct connection from one neuron to another through gap junctions. These gaps allow physiological components like molecules and ions, and electrical impulses to pass directly from one cell to another [65].

Ion	Inside (mM)	Outside (mM)	Nernst potential (mV)
K^+	140	5	89
Na^+	5 to 15	145	90 to 61
Cl^-	4	110	−89
Ca^{2+}	10^{-4}	2.5 to 5	136 to 145

Table 1.1. Typical ion concentrations and Nernst potentials for a resting neuron. Nernst voltage which represents the equilibrium potential is calculated using Eq. (1.8) in the standard condition for a neuron at body temperature (37°C) with $RT/F = 26.7\,\mathrm{mV}$ ($R = 8.314\,\mathrm{J\,K^{-1}\,mol^{-1}}$ is the ideal gas constant; $F = 9.648 \times 10^4\,\mathrm{C\,mol^{-1}}$ is the Faraday constant; T is the absolute temperature in K) [78].

In Chapter 3, we present the extended version of the Waikato model with four different receptor populations: AMPA, $GABA_A$, $GABA_B$ and N-methyl-D-aspartate (NMDA). For modelling their response functions, we need to be able to estimate their relative rise and decay times.

1.1.3 Membrane potential

All living cells maintain a potential difference across the cell membrane. The membrane potential of a postsynaptic cell may either increase or decrease relative to its resting potential, depending on the nature of the released neurotransmitter and the type of receptor it binds to. The membrane potential arises from two physical concepts: ionic concentration gradients and electric forces.

- Na^+, Cl^- and K^+ are the three main ionic species found inside a living cell. The concentration of K^+ ions inside the cell is about 10 times higher than that outside, while the concentrations of Na^+ and Cl^- are much higher outside than in; see Table 1.1. Due to these concentration differences, sodium and chloride ions tend to move into the cell, while potassium ions diffuse outwards.
- Electrical forces arise due to the separation of charges.

The membrane potential at which the diffusion and electrical forces are exactly balanced is known as the equilibrium potential. We discuss this concept in more detail in the following section.

1.1.4 Rest potential

When a neuron is at rest state, there is a potential difference across its membrane due to an imbalance of electrical charges between the interior and exterior of the cell. The resting potential of excitable cells lies in the range −60 to −95 mV. Two different equations can be used to calculate rest potential; the choice of equation depends on the number of ion species free to move across the membrane.

Nernst equation

If only one type of ion channel is present, then the Nernst potential sets the equilibrium or resting membrane potential. It can be calculated from the charge on the ion and its concentration gradient across the membrane using Fick's law of diffusion [22].

If the concentration of ions at point x is $C(x)$ [ions/cm^3], then the diffusive flux through the membrane, J_{diff} [ions/cm^2.s], is given by Fick's law of diffusion which in one dimension reads

$$J_{\text{diff}} = -D\frac{dC}{dx}, \tag{1.1}$$

where x is the spatial dimension and D is the diffusion constant [cm^2/s]. The other physical force which is responsible for the movement of ions is the electrical drift described by the microscopic version of Ohm's law:

$$J_{\text{drift}} = -\mu z\, C\, \frac{dV}{dx}, \tag{1.2}$$

where $V(x)$ [volts] is the potential at point x, z is the valence of the ion, and μ is mobility [cm^2/volt s]. The total flux, J_{t}, across the membrane is given by the sum of these two:

$$J_{\text{t}} = -D\frac{dC}{dx} - \mu z\, C\, \frac{dV}{dx}\,. \tag{1.3}$$

Einstein's relation, also known as the electrical mobility equation for diffusion of charged particles, connects the mobility with the diffusion coefficient:

$$D = \frac{kT}{q}\mu, \tag{1.4}$$

where k is Boltzmann's constant [J K^{-1}], T is the absolute temperature [K], and q is the charge of the particle in coulombs. Substituting Eq. (1.4) in (1.3), we rewrite the total flux as:

$$J_{\text{t}} = -\mu\left(\frac{kT}{q}\right)\frac{dC}{dx} - \mu z\, C\, \frac{dV}{dx}\,. \tag{1.5}$$

The Nernst equation is obtained by setting the total flux to zero, for a given ion species. Replacing kT/q with RT/F, where $R = 8.314$ J K^{-1} mol^{-1} is the ideal gas constant and $F = 9.648 \times 10^4$ C mol^{-1} is the Faraday constant, we are able to convert this equation expressed in terms of the number of individual molecules into its molar equivalent:

$$FC\, z\frac{dV}{dx} = -RT\frac{dC}{dx} \tag{1.6}$$

which can be integrated [22] through the following equation:

$$\int_{V_{\text{out}}}^{V_{\text{in}}} dV = -\frac{RT}{zF}\int_{C_{\text{out}}}^{C_{\text{in}}}\frac{dC}{C}, \tag{1.7}$$

where C_{out} and C_{in} are ion concentrations outside and inside the cell, respectively, and V_{out} and V_{in} represent the membrane potential. Equation (1.7) can be solved to give

$$V_{\text{m}} = V_{\text{in}} - V_{\text{out}} = -\frac{RT}{zF} \ln \frac{C_{\text{in}}}{C_{\text{out}}}, \tag{1.8}$$

where V_{m} is the equilibrium potential across the membrane.

Goldman-Hodgkin-Katz equation

For cases where two or more ions are present, to calculate the resting cell potential the Goldman-Hodgkin-Katz (GHK) equation should be used rather than the Nernst equation. In the GHK equation, the relative contribution of each ion to the membrane potential is considered not only through its concentration gradient and valence, but also by its relative permeability [22]. The GHK voltage for cell membrane is given by:

$$V_m = \frac{RT}{F} \ln\left(\frac{P_{\text{Na}}[\text{Na}^+]_{\text{out}} + P_{\text{K}}[\text{K}^+]_{\text{out}} + P_{\text{Cl}}[\text{Cl}^-]_{\text{in}}}{P_{\text{Na}}[\text{Na}^+]_{\text{in}} + P_{\text{K}}[\text{K}^+]_{\text{in}} + P_{\text{Cl}}[\text{Cl}^-]_{\text{out}}} \right) \tag{1.9}$$

where V_m is the membrane potential, P_{ion} is the permeability [cm/s] for a given ion and $[\text{ion}]_{\text{out}}$ and $[\text{ion}]_{\text{in}}$ are the extracellular and intracellular ion concentration, respectively, in [ions/cm^3].

The reversal potential for a given ion is the membrane voltage at which there is no net ion flux through the individual channel, and is identical to the Nernst potential only for the case of a single ion channel being active. Reversal potential and membrane equilibrium are not identical in human neuron membrane, as there are multiple ion channel types. In other words, a membrane potential for which the summation of the ionic currents is zero, does not necessarily correspond to a true reversal potential for each ion channel, as not all ions will be in equilibrium.

To maintain resting potential and to propagate action potentials, neurons are constantly exchanging ions with the extracellular environment. However, the electric potential generated by an individual neuron is too small to be detected by electroencephalography (EEG) scalp electrodes. In fact, a common modelling assumption is that the EEG is the temporally and spatially-averaged local fluctuation of populations of excitatory neurons around their resting potential [13, 90]. However, some researchers (e.g., Hutt et al. [44]) model the soma voltage which results from a membrane integration of all postsynaptic potentials: the excitatory postsynaptic voltages minus the inhibitory postsynaptic voltages.

1.2 Brain activity and the effect of anaesthetic drugs

Because of the complexities of brain structure, modellers limit their focus to those brain areas which are presumed to be most relevant to their research goals. To investigate the brain function affected by anaesthetic agents, two areas are considered to be of primary importance: cerebral cortex and thalamus.

The cortex is grey matter, divided into two almost symmetrical halves called cerebral hemispheres, composed of about 10^{10} excitatory and inhibitory interacting neurons. The cerebral cortex is connected to various subcortical structures such as the thalamus and the basal ganglia, transmitting information to them via efferent connections and receiving information from them through afferent connections. The cerebral cortex directs all forms of conscious experience, including perception, emotion, thought, planning, and memorization. Thalamus is located in the centre of the brain, with nerve fibres branching out to the cerebral cortex in all directions, acting as a relay between subcortical areas and the cerebral cortex. Thalamus plays a major role in regulating arousal, consciousness, and activity [27, 56, 81]. Damage to the thalamus can lead to permanent coma.

To study brain activity, EEG is one of the common methods. EEG scalp electrodes detect the summed electrical activity of excitatory postsynaptic potentials in apical dendrites of pyramidal neurons in the exterior layers of the cortex. The spatiotemporally oscillating EEG forms brain rhythms which reveal brain states that can be distinguished through frequency and amplitude as illustrated in Fig. 1.3.

1.2.1 Normal brain rhythms

EEG electrodes can determine the relative strengths and locations of electrical activity in different brain regions [96]. Brain activity changes in a consistent and recognizable way according to the functional status of the brain, such as alertness, relaxation, sleep, anaesthesia, lack of oxygen and certain neural diseases, such as epilepsy [15]. EEG activity in particular frequency bands can be extracted using spectral analysis of EEG recordings, and are categorized as below [6, 16, 83] illustrated in Fig. 1.3.

Delta is the name given to EEG activity in the frequency range 0.5 to 3 Hz. Delta activity is characterised by high amplitude slow waves, and is observed in central and frontal areas of the cerebral cortex. Delta activity is probably the major EEG pattern of the deeply asleep and anaesthetized human brain.

Theta covers the frequency range 3.5 to 8 Hz and is classified as "slow" activity. Commonly seen in drowsiness, theta activity is associated with relaxed, meditative, and creative states. Theta response is the most stable component in frontal regions of the cortex.

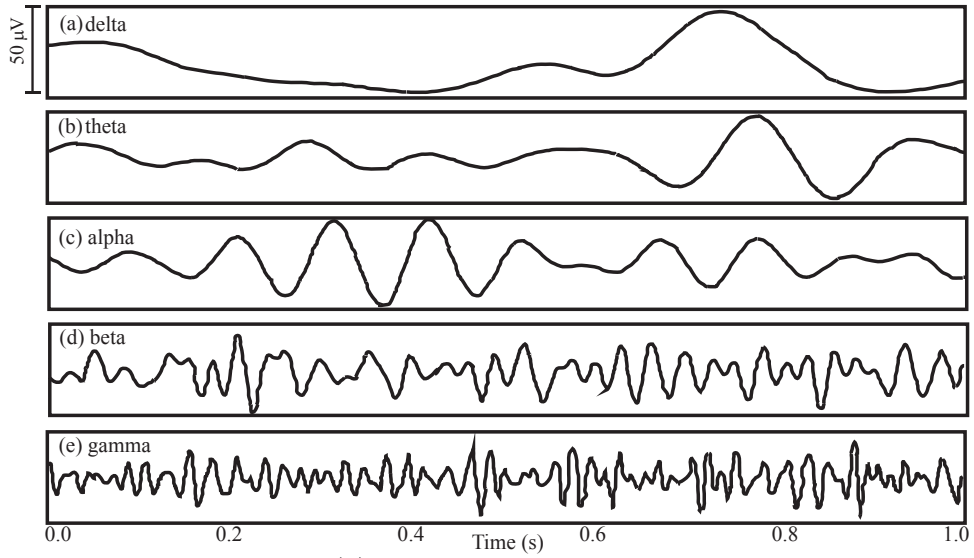

Figure 1.3. EEG brain rhythms. (a) Delta waves $0.5 - 3$ Hz, deep sleep and anaesthesia; (b) Theta waves $3 - 8$ Hz, extreme relaxation and drowsiness; (c) Alpha waves $8 - 14$ Hz, just before falling asleep and hypnosis; (d) Beta waves $12 - 30$ Hz, awake and normal alert consciousness; (e) Gamma waves $30 - 100$ Hz, high level information processing (modified from different figures in [16]).

Alpha activity ranges from 8 to 14 Hz. It is seen in the posterior regions of the cortex. It emerges with closing of the eyes and with relaxation, and attenuates with eye opening or mental exertion. It is the major rhythm seen in normal relaxed adults.

Beta has a frequency range from 15 to about 30 Hz. Beta is seen usually on both sides in symmetrical distribution and is most evident frontally. Beta activity is closely linked to motor behaviour and is generally attenuated during active movements.

Gamma is the name given to EEG activity above 30 Hz. Gamma rhythms are distributed in different cortical and subcortical structures [7, 16], and are thought to represent binding of different populations of neurons together into a network for the purpose of carrying out a particular cognitive or motor function.

1.2.2 Pathological brain rhythms

Seizures are the clinical manifestation of the pathological synchronous electrical activity in the brain. They emerge from a hyperexcitable focus within the brain where synchronized electrical activity originates. Seizures are mainly classified into three different types [19]:

1. **Focal seizures** affect one hemisphere of the brain.
2. **Generalized epilepsy** is characterised by global seizures with no apparent cause.
3. **Unclassified epileptic seizures** which are of unknown origin and may not have distinct clinical and electrical features that allow easy classification.

Figure 1.4(a) presents brain activity in the presence of seizures, while Fig. 1.4(b) shows brain activity in the absence of seizures.

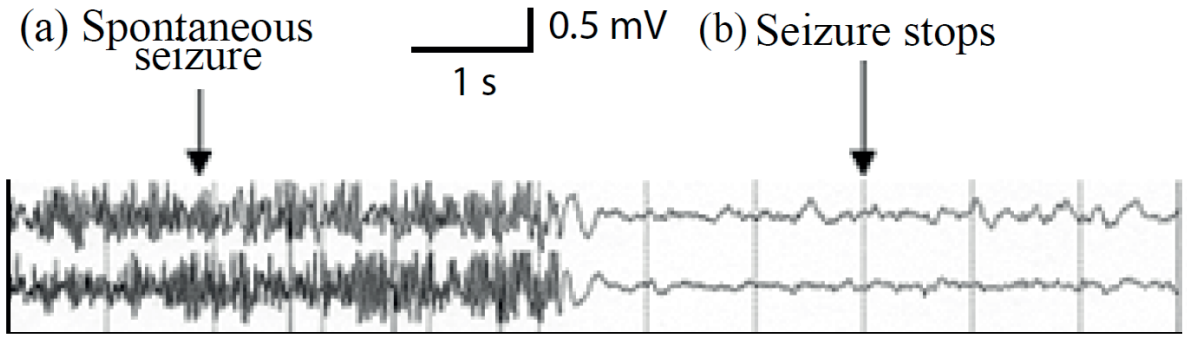

Figure 1.4. Recorded EEG activity in the presence and the absence of seizures, from Fig. 1 of [12].

Approximately 10% of the population has a single convulsive episode during their lifetime. In this situation, the use of anticonvulsants is not indicated. If there are recurrent seizures, and the diagnosis of epilepsy is confirmed, routine treatment with antiepileptic drugs is initiated [68]. The mechanism of action of these drugs is not fully explained, but appears to be related to the decrease of sodium ion current (blocking voltage-dependent sodium channels), increasing the inhibitory effects of GABA, and blocking the NMDA and AMPA receptors.

Anaesthesiologists are frequently faced with seizures in epileptic and nonepileptic patients in the surgical theatre. Some anaesthetic drugs used during anaesthesia possess proconvulsant properties that may trigger clinical seizures at induction or emergence. Anaesthetic-induced epilepsy has been reported during anaesthesia with sevoflurane, isoflurane, etomidate, and opioids as well as propofol [111]. In Chapter 4, we aim to investigate the effects of anaesthetic drugs on brain activity and also the possible underlying mechanism of seizure activity in an anaesthetised brain.

1.2.3 Stages of anaesthesia

Attempts at producing a state of general anaesthesia can be traced throughout recorded history in the writings of the ancient Persian, Egyptian, Greek, Roman, and Chinese scholars [74, 94]. During the Middle Ages scientists made significant advances in medicine in the Eastern world, while their European counterparts also made important advances. By the middle of the seventeenth century, narcotic drugs become more popular as Nicolas Bailly administered a narcotic potion to a patient before an operation; however, Bailly was arrested and fined for practising witchcraft. In 1846, William Morton first introduced ether anaesthesia. This was followed shortly after by nitrous oxide and chloroform. Within a few decades, surgical anaesthesia was being used around the world. Although anaesthetic drugs and delivery techniques have changed, the principles of anaesthesia and

its stages have remained largely unchanged since 1937 when Guedel developed a categorization of the stages of general anaesthesia [34]. These include [34, 38]:

1. **Induction** The period between the administration of anaesthetic drugs and loss of consciousness (LOC). At this stage the patient experiences pain relief and dizzy, dreamy disorientation.
2. **Excitement** The time following LOC associated with intense activity like uncontrolled movement and possibly irregular heart rate and breathing. Due to risks for some patients, the ideal anaesthetic protocol yields a quick and smooth progression to stage 3, which also results in a more rapid recovery.
3. **Surgical anaesthesia** Muscles are relaxed, breathing becomes regular and surgery can begin.
4. **Recovery** The effects of anaesthetic drugs are eliminated and the patient wakes up.

1.2.4 Anaesthetic drug effects on brain activity

Anaesthesia controls pain and produces unconsciousness and loss of memory by interfering with neuron communication. In an active brain, the dominant frequency of the EEG lies between 12.5 and 30 Hz, while after administration of anaesthetic drugs it drops to very low δ-band frequencies ($0.5 - 4$ Hz) in phase 2 of anaesthesia Fig. 1.5(B); this is very similar to the EEG pattern for the naturally sleeping brain in non-REM stage 3 sleep; see Fig. 1.5(C).

Although different groups of general anaesthetics act through distinct molecular targets and therefore via different mechanisms, all produce the same clinical outcome which is unconsciousness [26]. Two common molecular targets of anaesthetic drugs are GABA and NMDA receptors [21, 90]:

- GABAergic anaesthetics (e.g., propofol, etomidate, alfaxalone, and thiopental): the anaesthetic molecule binds to a specific site on the GABA receptor of the postsynaptic neuron, causing chloride ion channels to remain open longer, allowing chloride ions to accumulate inside the postsynaptic neuron. Consequently the neuron becomes more hyperpolarized, and therefore less likely to fire, see Fig. 1.6. In general, these anaesthetic agents enhance the inhibitory effect of GABA receptors by increasing the time decay of the inhibitory postsynaptic potential [1, 8, 56, 106].

- NMDAergic anaesthetics (e.g., ketamine and nitrous oxide): this class of agents act on NMDA receptors of the postsynaptic neuron by reducing the amplitude of postsynaptic potential of the excitatory receptor, so are referred to as NMDA-antagonists. Modelling the action of this receptor is not easy as the duration of the excitatory postsynaptic response to a presynaptic action potential depends not

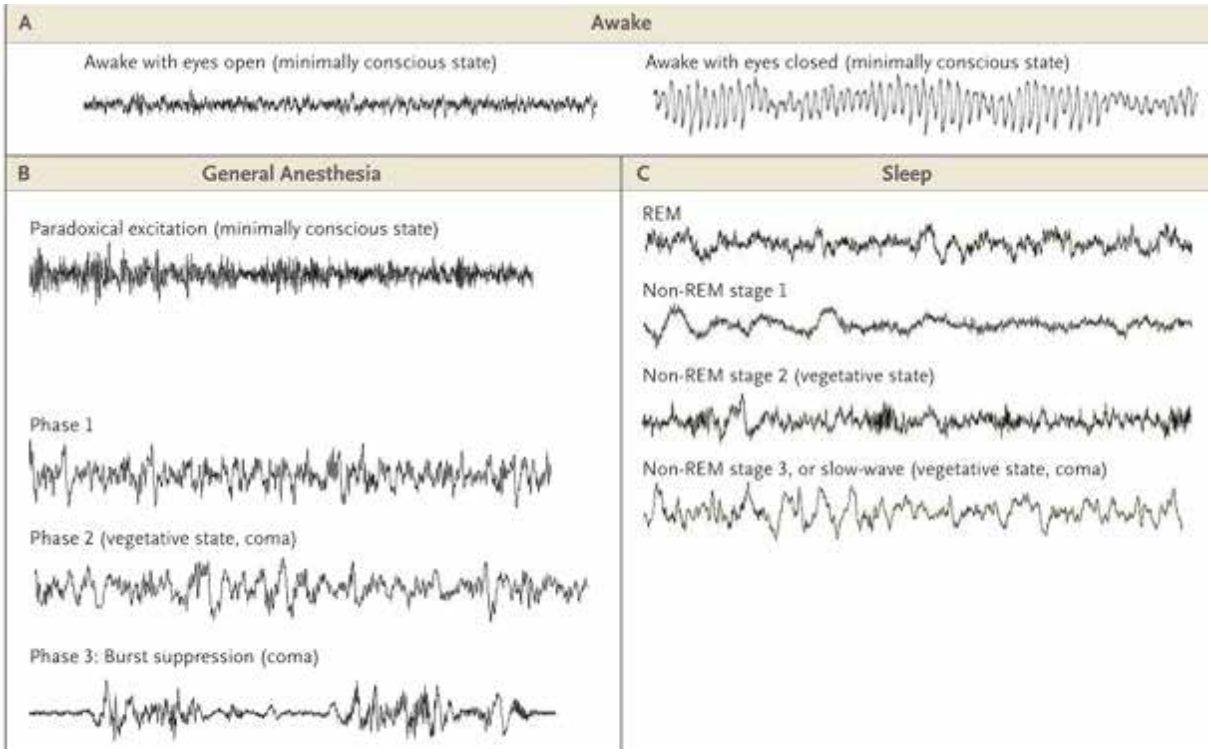

Figure 1.5. Electroencephalographic patterns during the awake state, general anaesthesia, and sleep. Panel A shows the EEG patterns when the patient is awake, with eyes open (left) and the alpha rhythm and with eyes closed (right). Panel B illustrates EEG patterns during the states of general anaesthesia: paradoxical excitation, phases 1 and 2, burst suppression, and the isoelectric tracing. Panel C shows the EEG patterns during the stages of sleep: rapid-eye-movement (REM) sleep; and stages 1, 2, and 3 of non-REM (slow-wave) sleep (EEG tracings during awake and general anaesthesia from Fig. 1 of [83] and EEG tracings during sleep from Fig. 3 of [103]).

only on anaesthetic concentration but also on the voltage state of the receiving neuron [56, 81].

Two significant drug-related phenomena that have attracted researcher attention in the last few decades are the biphasic response and hysteresis.

Biphasic response refers to the dose-dependent changes in EEG activity, with an initial increase at relatively low concentrations, and a subsequent decrease with increasing concentrations [52,59,82]. Figure 1.7 illustrates the biphasic effect of propofol anaesthetic on EEG signal for two different frequency ranges, 0 to 5 Hz and 11 to 15 Hz.

Hysteresis: The blood concentration of anaesthetic agent needed to put a patient to sleep is greater than the concentration observed when the patient returns to consciousness. Figure 1.8 shows EEG signal amplitude as a function of measured propofol blood concentration. There are two distinct surges in activity at distinct drug concentrations: the patient loses consciousness at a considerably higher propofol (about 2.5-fold) concentration than that at which she wakes up. Researchers have identified two possible reasons for this phenomenon. First, it takes some time for the drug to diffuse from the blood (the

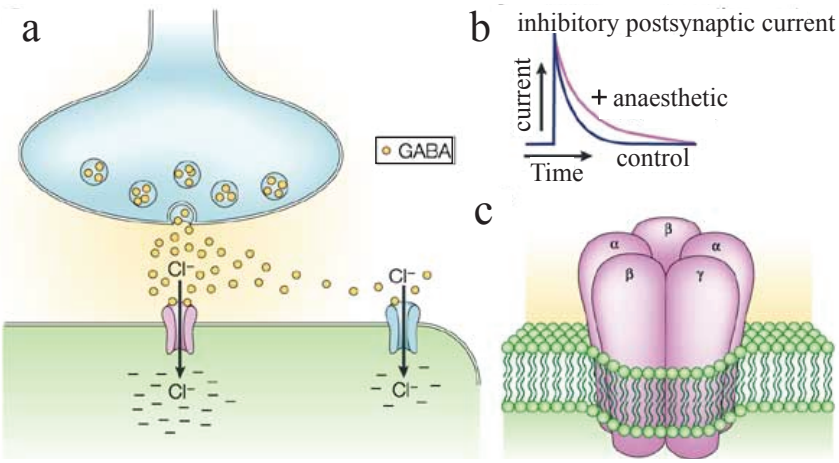

Figure 1.6. GABA receptor and GABAergic anaesthetic drugs. (a) An action potential arriving at the terminal of an inhibitory neuron results in diffusion of GABA neurotransmitter across the membrane where it binds to the pentameric $GABA_A$ receptor, allowing chloride ions flow to the postsynaptic neuron, leading to hyperpolarization. (b) General anaesthetics prolong chloride channel opening and increase postsynaptic inhibition. (c) A pentameric $GABA_A$ receptor complex in the lipid bilayer membrane consists of five protein subunits (from Fig. 3 of [81]).

measurement site) into the brain (the "effect" site), leading to the so-called effect-site displacement error which can be partially compensated for using pharmacokinetic modelling [24, 59, 99]. Second, it has been observed that the central nervous system tends to resist transition between conscious and unconscious states; this is known as the *neural*

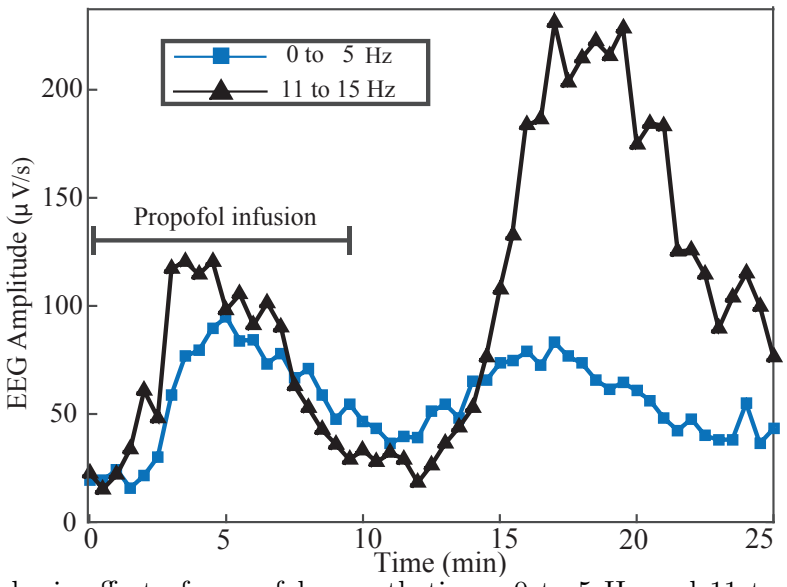

Figure 1.7. Biphasic effect of propofol anaesthetic on 0 to 5 Hz and 11 to 15 Hz EEG signal. During the 10 min of propofol infusion, anaesthetic concentration increases steadily. At low concentrations, the EEG signal shows initial activation, followed by power decrease as concentration is further increased and the patient becomes deeply unconscious. A second EEG activation peak is observed as the anaesthetic concentration reduces and the patient starts to emerge from unconsciousness (graph modified from Steyn-Ross et al [91]; data supplied courtesy of Kuizenga, and reported as "Patient 7" in [59].).

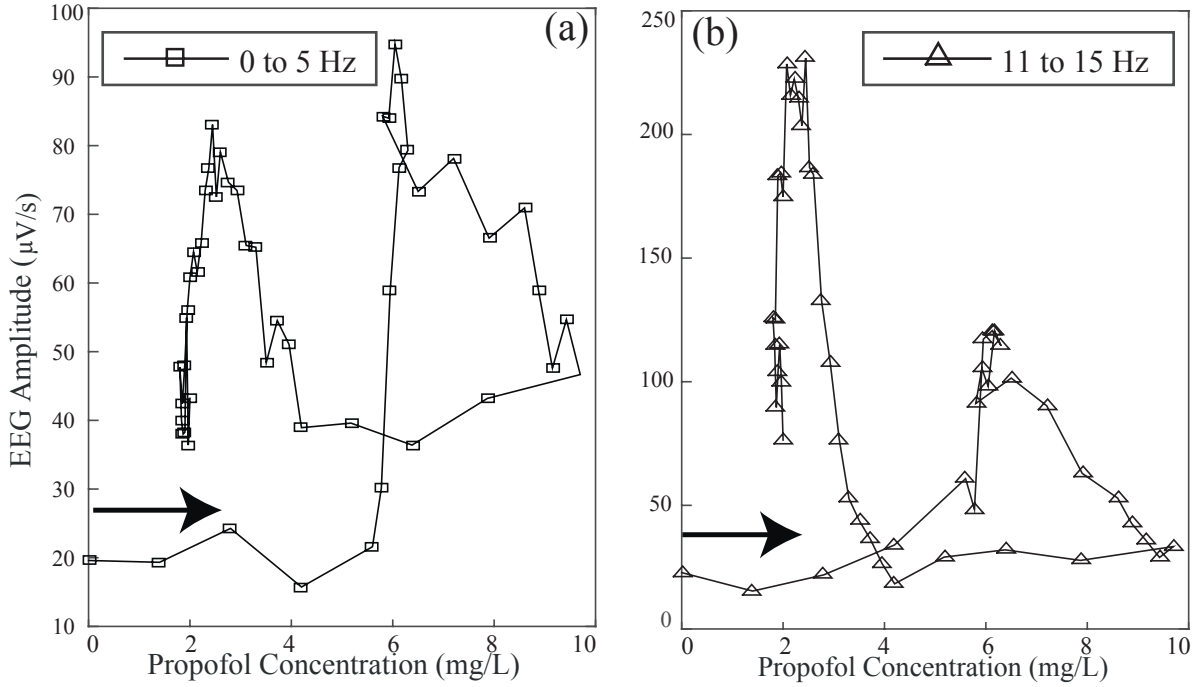

Figure 1.8. EEG "amplitude" data from Fig. 1.7 plotted as a function of measured propofol blood concentration. (a) 0–5 Hz; (b) 11–15 Hz. Each trajectory commences at the lower-left corner at zero concentration. For the 0–5 Hz band, the activation peak is stronger during the induction phase (right-hand peak); for the 11–15 Hz band, the activation peak is considerably stronger at emergence (left-hand peak) (reference as for Fig. 1.7).

inertia effect. It has been found that the forward path from conscious to unconscious and the reverse path from unconscious to conscious are not identical [28].

1.3 Mathematical models for anaesthesia

There are two complementary yet contrasting theoretical approaches to modelling neural activity in the human brain: neural networks and population models.

Spiking neural networks The first experimentally-based mathematical model of a spiking neuron was introduced by Hodgkin and Huxley in 1952 [42]. This model describes the initiation and propagation of action potentials in single neuron, but is not able to explain brain activity associated with higher functions such as memory, learning and pattern recognition, since these functions of nervous system appear to require the coordinated activity of large numbers of neurons. Thus, modellers have been motivated to construct networks of spiking neurons to simulate different brain states. These models are characterized by large numbers of neurons that communicate through synapses with information encoded or decoded through a series of pulse trains [32, 66].

One of the most ambitious attempt in this area is The Blue Brain Project, founded in May 2005 by the Brain and Mind Institute of the Ecole Polytechnique Federale de Lausanne (EPFL) in Switzerland. The long term aim of this project is to study the brain's

architectural and functional principles. The initial goal of the project was simulation of a neocortical macrocolumn, which is about 2 mm tall, has a diameter of 0.5 mm, and contains about 60,000 neurons. The neocortical column represents the basic functional unit of the cerebral cortex in mammals, and these units are repeated millions of times across the cortex. The simulation does not consist simply of an artificial neural network, but involves biologically realistic models of individual neurons and neuron communication [67]. However, the real world application of large scale spiking neural networks has been limited: first, the vast number of neurons and their interconnections make numerical computation of anything close to biological reality impossible; second, many anatomical and physiological parameters which must be incorporated into the model are known only as average properties.

Mean-field models In this approach, researchers investigate the spatial variation and time evolution of the *average* properties of large groups of excitatory and inhibitory neurons. Mean-field models are suited to data which reflect the behaviour of populations of neurons, such as the electroencephalogram (EEG). These models aim to relate well-known microscopic targets of general anaesthetic action to their macroscopic consequences as detected by changes in EEG activity. We now present a brief overview of some mean-field models for anaesthetic action.

1.3.1 Waikato anaesthesia mean-field model (1999)

The first attempt to use mean-field modelling to reproduce the effect of the GABAergic anaesthetic agent propofol on brain activity was by the Cortical Modelling Group at Waikato University [91]. Their work adopted the Liley mean-field model [63] which assumes that neural parameters have been averaged over small volumes of cortex known as macrocolumn elements. These macrocolumns contain two distinct neuron populations (85% excitatory, 15% inhibitory), which interact through chemical synapses. These interactions are either short range (inside the macrocolumn), long range (excitatory inputs from other macrocolumns), or exogenous (input from the thalamus and brain-stem) [90].

Steyn-Ross et al. [91] incorporated the effect of the general anaesthetic agent propofol at the cortex as a modulation of the inhibitory neurotransmitter rate-constant γ_i [s^{-1}] which was paired with an increase in inhibitory postsynaptic strength ρ_i [mV s],

$$\gamma_i = \frac{\gamma_i^0}{\lambda}, \qquad \rho_i = \lambda \rho_i^0 \tag{1.10}$$

where scale-factor $\lambda \geq 1$ represents propofol effect: the zero-anaesthetic background values of inhibitory rate-constant γ_i^0 and synaptic strength ρ_i^0 are scaled by λ after administration of propofol. The original 1999 formulation of the Waikato model proposed an alpha response function to model the inhibitory postsynaptic responses, Fig. 1.9(a);

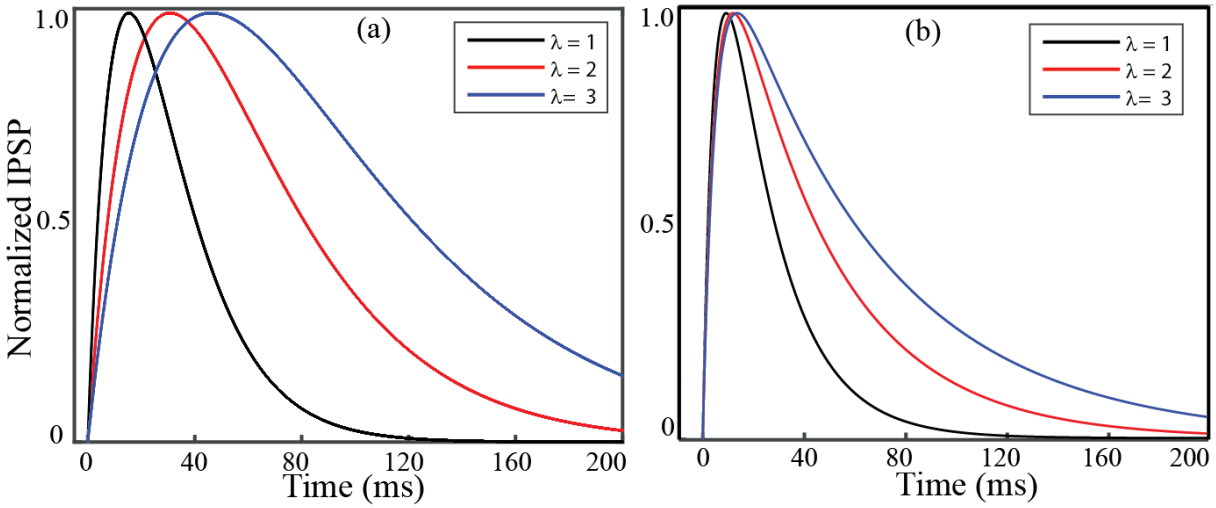

Figure 1.9. Effect of propofol on GABAergic synapses in the Waikato model. The synaptic response function is plotted as a function of time for three different drug concentrations. As the drug effect increases, the decay rate decreases. Model impulse responses for the (a) alpha function $\gamma_i\, te^{-\gamma_i t}$ and (b) biexponential function $\gamma_i\gamma/(\gamma-\gamma_i)(e^{-\gamma_i t}-e^{-\gamma t})$. The symbol λ is a dimensionless anaesthetic-effect scale-factor giving the lengthening of the inhibitory post synaptic potential (IPSP) duration.

however, in the present work we use a biexponential response function, see Fig. 1.9(b); more detailed information is given in Chapter 3.

The model's steady-state voltage distribution V_e as a function of anaesthetic effect λ enabled Steyn-Ross et al to define three distinct regions for the brain under the effect of the anaesthetic agent propofol, Fig. 1.10. For the high levels (region I:"coma") and low levels (region III: "anti-anaesthetic") of anaesthetic effect only a single state was available; while for intermediate values (region II), three steady-state solutions were found.

The model predicts that a first-order transition to the low-firing branch can occur at critical values of the drug concentration $\lambda = 1.53$ from A3 in high firing state (LOC: loss of consciousness); similarly, a transition from the quiescent to the active branch can occur at specific drug concentration $\lambda = 0.28$ from Q1 in the low firing state (ROC: recovery of consciousness). As can be seen in Fig. 1.10, the LOC and ROC correspond to two different levels of anaesthetic effect, predicting a drug hysteresis effect. In other words, the patient will awaken at a lower concentration of anaesthetic than that required to put her to sleep.

In addition to predicting a drug-hysteresis effect, the model also exhibits biphasic behaviour. In Fig. 1.11(a), the induction path shows a power surge at $\lambda = 1.53$, followed by an abrupt decrease in EEG power beyond this point, signalling a transition from the wake to the anaesthetized state. In Fig. 1.11(b) the emergence phase shows a second surge at $\lambda = 0.28$ representing return from wake to consciousness.

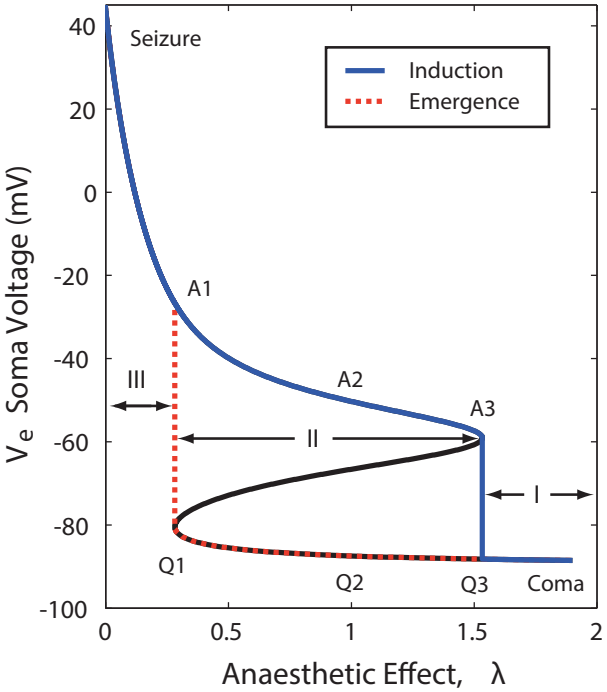

Figure 1.10. Steady-state trajectory for the 1999 Steyn-Ross et al anaesthesia model [91]. In region I for $\lambda > 1.53$, the neural firing is strongly suppressed ("coma"); in region III for $\lambda < 0.3$, the neural firing is maximized ("seizure"). In region II, there are three different values for soma voltage, however only two of these are stable: the upper (active) and lower (quiescent) branches (from Fig. 5 of [90]).

In 2007 Steyn-Ross et al [93] made a significant enhancement to the biophysical fidelity of their cortical model with the inclusion of electrical gap-junction synapses to supplement communication via standard chemical synapses. This change supports the emergence of spatial and spatiotemporal oscillatory modes that are not accessible in the original 1999 equations. Although the predictions of a biphasic effect and drug hysteresis are clear model successes, there are two deficiencies in the original 1999 Waikato model for anaesthesia:

- The biphasic power surge arises from critical slowing associated with close approach to the saddle-node[1] annihilation points at A_3 (induction) and Q_1 emergence, Fig. 1.10, such that the spectral energy becomes focussed to zero frequency. There is no possibility of a Hopf[2] (at say delta or alpha frequencies) tuning of spectral response.
- The recovery of consciousness apparently requires λ-values to be smaller than unity, implying an "anti-anaesthetic" effect.
- The recovery of consciousness apparently requires λ-values to be smaller than unity, implying an "anti-anaesthetic" effect.

[1]Saddle-node bifurcation is a local bifurcation in which two equilibria of a system collide and annihilate each other.

[2]Hopf bifurcation is a critical point where a system's stability changes and a periodic solution arises.

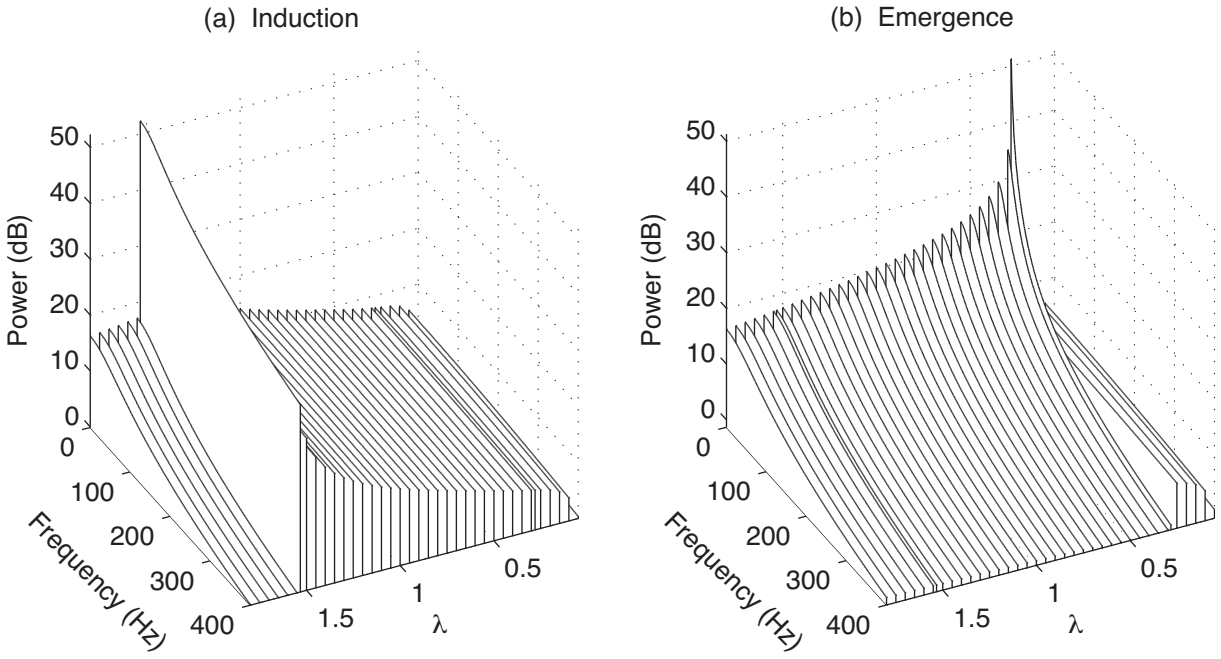

Figure 1.11. Spectral power predictions for Steyn-Ross et al (1999) model. (a) At low concentration of propofol the EEG signal shows an initial increase in power (activation). EEG power falls way as concentration is increased and the patient becomes deeply unconscious. (b) gives a view of the emergence: as the drug concentration is decreased, EEG power increases; EEG power decreases at $\lambda = 0.28$ when patient returns to conciousness (from Fig. 5.7 of [90]). These theoretical power spectra were calculated using linear stochastic theory (e.g., see Eq. (4.5.78) of Gardiner (2008)

Subsequent anaesthetic modelling, including later contributions by the Waikato group and alternative models due to Liley [13], Hutt [44], Hindriks [40], and Molaee-Ardekani [71] have addressed one or both of these limitations. As a part of my thesis research, I have enhanced the 2007 Waikato model by including $\mathrm{GABA_B}$ and NMDA synapses. The revised model predictions are reported in Chapters 3 and 4.

1.3.2 Bojak and Liley (2005) anaesthesia model

Bojak and Liley (2005) presented a mean-field description of the effect of the anaesthetic agent isoflurane on brain activity [13]. Bojak and Liley formulated a set of equations for the peak amplitude, time decay and time rise of the excitatory and inhibitory postsynaptic potential (PSP) as a function of drug concentration. This was done by fitting recorded IPSPs and EPSPs to Hill equations,

$$\Gamma_e(c) \simeq \Gamma_e(0)\frac{0.707^{2.22}}{0.707^{2.22}+c^{2.22}},\ \Gamma_i(c) \simeq \Gamma_i(0)\frac{0.79^{2.6}+0.56c^{2.6}}{0.79^{2.6}+c^{2.6}}\ , \tag{1.11}$$

$$\delta_e(c) \simeq \delta_e(0), \qquad \delta_i(c) \simeq \delta_i(0)\ , \tag{1.12}$$

$$\zeta_e(c) \simeq \zeta_e(0), \qquad \zeta_i(c) \simeq \zeta_i(0)\frac{0.32^{2.7}+4.7c^{2.7}}{0.32^{2.7}+c^{2.7}}, \tag{1.13}$$

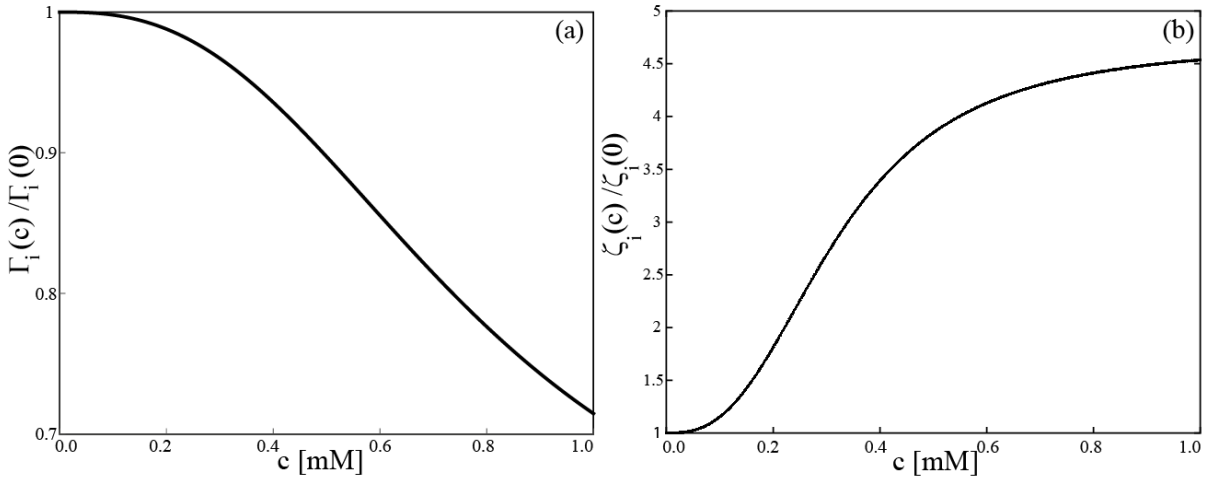

Figure 1.12. Hill equations for isoflurane impact on IPSP amplitude and decay time. (a) Peak amplitude of inhibitory postsynaptic responses decreases as the drug concentration increases. (b) Time decay of inhibitory postsynaptic responses increases as the drug concentration increases.

where $\Gamma(c)$ indicates that the peak amplitude is a function of drug concentration, c, for both excitatory (e) and inhibitory (i) PSPs. Figure 1.12(a) illustrates a decrease in the peak amplitude of inhibitory postsynaptic response as drug concentration increases. While the time rise, δ, shows negligible dependence on concentration, Eq. (1.12), the time decay, ζ, (time required for the PSP to fall to e^{-1} of the maximum amplitude) of Eq. (1.13) shows that the IPSP decay increases with isoflurane concentration, see Fig. 1.12(b). Bojak and Liley proposed a biexponential response function $R(t)$ [mV] to model the postsynaptic responses

$$R(t) = e^{\beta\delta}\Gamma\ \alpha\frac{e^{-\beta t} - e^{\alpha t}}{\alpha - \beta}\ , \tag{1.14}$$

$$\beta \equiv \frac{\epsilon}{e^{\epsilon} - 1}\frac{1}{\delta}\ , \tag{1.15}$$

$$\alpha \equiv e^{\epsilon}\beta\ , \tag{1.16}$$

where R specifies the biexponential fit in terms of δ, the rise time to maximum, and a control parameter ϵ, a remarkably complicated nonlinear function of PSP decay time $\zeta(c)$,

$$\epsilon \simeq \underbrace{\overbrace{e^{2.5466-1.3394k}}^{A'}\overbrace{\sqrt{k-1}}^{A''}}_{A} + \underbrace{\overbrace{\left[e^{-1.2699(k-1)} - 1\right]}^{B'}\overbrace{\left[\frac{1}{k^2} + W_{-1}\left(\frac{e^{-\frac{0.236}{k^2}}}{1 - 3.146k}\right)\right]}^{B''}}_{B}, \tag{1.17}$$

with

$$k = \frac{\zeta(c)}{\zeta(0)}$$

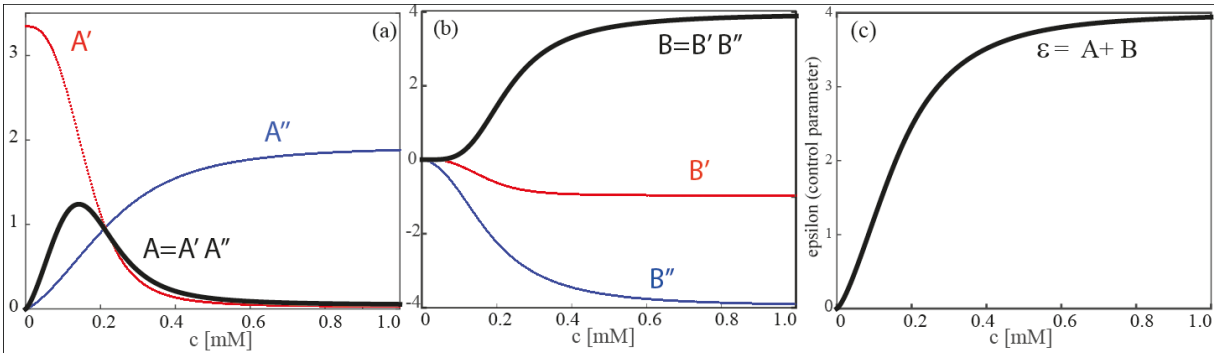

Figure 1.13. Epsilon control parameter for Bojak and Liley model. ϵ-function decomposed into two simpler parts: A and B, see Eq. (1.17). (a) illustrates A and its component parts: A' A''; (b) corresponds to B which is a multiplication of B' and B''. Panel (c) illustrates epsilon control parameter, the summation of A and B. Epsilon increases with drug concentration, approaching saturation at $c = 1$ mM.

To better understand this function, I have decomposed it into two simpler functions A and B. Figure 1.13 illustrates construction of the ϵ-function in terms of its component parts. Here W_{-1} is the Lambert W function (see Chap. 2.2 for more details). Figure 1.13(c) shows that the epsilon control parameter increases monotonically with drug concentration. However, for $\epsilon = 0$ (i.e., no anaesthetic drug), the response reduces to a simple alpha function

$$R_0(t) = e\Gamma\alpha\, te^{-\alpha t} \; . \tag{1.18}$$

The authors employed swarm searches to identify 73454 suitable cortical parameter sets shown in Fig. 1.13 using the full nonlinear model. Since these sets all allowed a quasi-linear approximation, the very majority of parameters sets was identified in a massive Monte Calo search using a linear approximation. The first criterion was the existence of at least one stable equilibrium solution with firing rates between 0.1 and 20 [spike/s] at $c = 0$. In the case of multiple solutions, they chose the one corresponding to the lower membrane potential. This corresponds to the bottom branch of the Steyn-Ross et al model of Fig. 1.10. Cortical parameter sets were then classified into two different categories, non-biphasic and biphasic.

Non-biphasic set: Theoretical power spectra were computed. Acceptable spectra required 15–50% of the total power in δ-band (0–4 Hz), 10–25% in θ (4–8 Hz), 15–40% in α-band (8–13 Hz), and 15–40% in β–band (13–30 Hz). In addition, the power ratios were required to follow the relations

$$\frac{\theta}{\delta} < 0.6 \qquad \text{and} \qquad \frac{\theta}{\alpha} < 0.7 \; .$$

Then they checked the 90% spectral edge frequency (SEF_{90}), which is defined as the

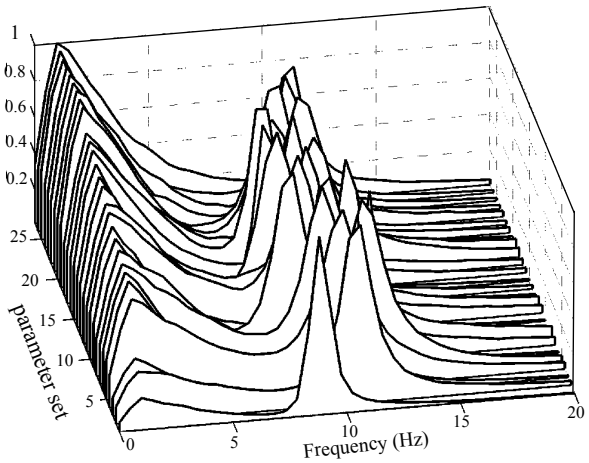

Figure 1.14. Spectral power for biphasic sets. Power spectra obtained through full grid simulations with 27 parameters sets. A biphasic response was always observed in the alpha frequency band (from Fig. 6 of [13]).

frequency below which 90% of the power resides. Then, they computed the quality of the α peak, requiring

$$Q = \Delta f_\alpha / f_\alpha > 5.5 \,, \tag{1.19}$$

where Δf_α is the full width at half maximum.

Afterwards, they checked the extremal values of the spectra in the θ, δ, and α bands. They required that the α maximum be not larger than five times, and not smaller than one-third, the δ maximum. Furthermore, the θ minimum could not be larger than half of either the α or δ maxima, and not larger than 90% of the δ minimum.

Biphasic set: In addition to all requirements defined for non-biphasic sets, biphasic sets needed to fulfil one more requirement. If the total power at $c = 0.24$ mM rose to at least 1.4 times its value at $c = 0$ mM, that parameter set was classified as biphasic. Only 86 parameter sets exhibited a biphasic response, see Fig. 1.14.

Here, we highlight three main aspects of their work:

- The biphasic effect in EEG activity at low drug concentrations could occur without requiring a transition between two distinct states.
- Although the non-biphasic sets vastly outnumbered the biphasic sets, the biphasic sets provided a better agreement with experimental data [13].
- The model was not able to address the issue of hysteresis in the EEG. The PSP responses were defined based on experimental data recorded during administration of anaesthetic drugs. In order to investigate hysteresis, access to PSP recordings during the recovery phase of anaesthesia is necessary.

1.3.3 Molaee-Ardakani (2007) anaesthesia model

For Molaee-Ardakani et al. (2007), the main focus was on slow EEG oscillations observed during deeper levels of desflurane-induced general anaesthesia. While the main building

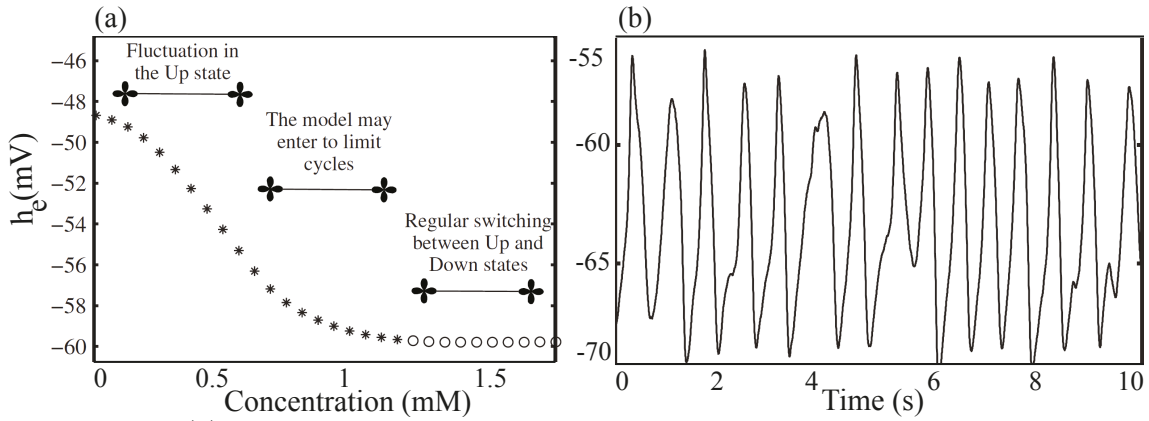

Figure 1.15. (a) Equilibrium solutions of excitatory membrane voltage h_e when anaesthetic drug concentration is varied between 0 and 1.8 mM. Stars are stable and circles are unstable solutions of a linear stability analysis. (b) Ten seconds of simulated h_e signals at anaesthetic concentration 1.5 mM (from Figs 11 and 6(d) of [71]).

elements of the Molaee-Ardakani model [71] are taken from the Steyn-Ross et al [91] and Bojak and Liley [13] mean-field cortical models, the authors incorporated a new slow ionic modulation of the sigmoidal voltage-to-firing rate transfer function for the excitatory neural population. This sigmoid modulation was driven by a slow gating variable that depolarized excitatory neurons when they were in the low firing state, and hyperpolarized them when they were in high firing state.

At higher drug concentrations the slow mechanism induced neural cells to alternate between two levels of activity referred to as Up and Down states, see Fig. 1.15(b), corresponding to enhanced delta activity. The Molaee-Ardakani model results indicated that at low drug concentration the simulated EEG showed low power across a broad range of frequencies, while at the high range of drug concentration, the EEG showed a significant increases in the energy of delta activity, Fig. 1.16. The model was not able to reproduce other typical EEG rhythms such as spindles and alpha.

1.3.4 Hutt and Longtin (2010) anaesthesia model

The Hutt and Longtin mean-field model [44] describes the effective membrane potential and involves excitatory pyramidal cells and inhibitory interneurons, excitatory and inhibitory synapses, non-local spatial interactions and an axonal conduction speed with the inclusion of time-delay. Excitatory and inhibitory synapses can occur on both dendritic branches of excitatory and inhibitory cells. The activity of synapses and neurons are represented as averages over the population in small areas of some millimetres square and short time windows. Hutt and Longtin investigated the effect of the anaesthetic agent propofol which increases the decay time of inhibitory synapses. They predicted the occurrence of a saddle-node bifurcation at a critical propofol concentration. This

bifurcation models the transition between consciousness and unconsciousness during the administration of general anaesthetics.

In their study, two different biexponential functions $h_e(t)$ and $h_i(t)$ represent the response of the mean postsynaptic potential for excitatory and inhibitory populations, respectively,

$$h_i(t) = a_i f\,(p)\,\frac{\beta_1\beta_2}{\beta_2-\beta_1}\left(e^{-\beta_1 t}-e^{-\beta_2 t}\right)\,, \tag{1.20}$$

$$h_e(t) = a_e\frac{\alpha_1\alpha_2}{\alpha_2-\alpha_1}\left(e^{-\alpha_1 t}-e^{-\alpha_2 t}\right)\,. \tag{1.21}$$

These response functions are based on experimental recordings of the responses of single synapses [57]. Here, $a_{i,e}$ are the synaptic gains for inhibitory and excitatory populations; the rise times of the response functions for excitatory and inhibitory synapses are $1/\alpha_2$ and $1/\beta_2$, and $1/\alpha_1$ and $1/\beta_1$ are the corresponding decay times. The function $f(p)$ indicates the action of different concentrations of propofol on the inhibitory synapses as specified by the anaesthetic weighting factor $p \geq 1$

$$f(p) = r^{\frac{-r}{r-1}}(rp)^{\frac{rp}{rp-1}} \qquad \text{with} \quad r = \frac{\beta_2}{\beta_1}\,, \tag{1.22}$$

which guarantees a near constant height of the impulse response function $h_i(t)$ and yields

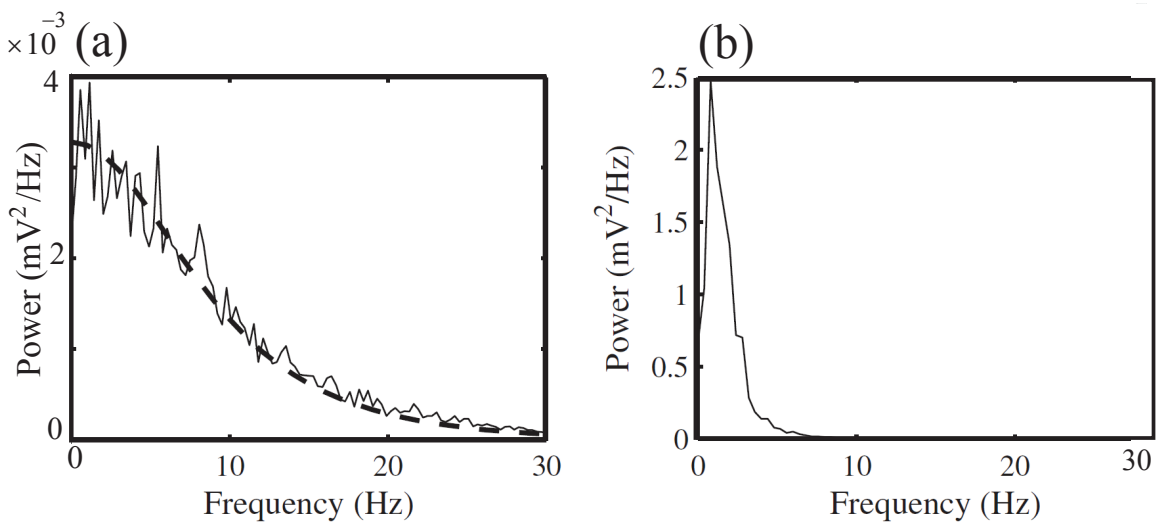

Figure 1.16. Power spectra of simulated h_e signals at different drug concentrations. (a) For very low drug concentration $c = 0.2$ mM, the power spectrum extends to high frequencies. The eigenspectrum (dashed line) corresponding to this drug concentration is a descending function that is reminiscent of the background spectrum of a real EEG signal in the waking period. (b) Appearance of slow waves at $c = 0.75$ mM increases the power of the slow delta-band (from Fig. 7 of [71]).

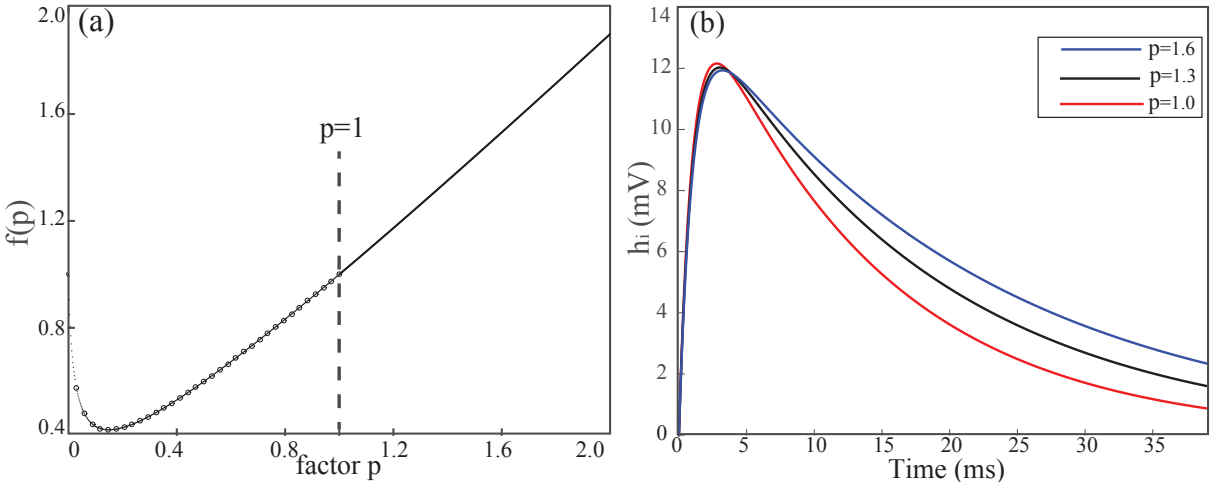

Figure 1.17. (a) The action of anaesthetic drug concentration on inhibitory synapses $f(p)$ is plotted as a function of the weighting factor $p \geq 1$. (b) Effect of propofol on inhibitory synapses in the Hutt (2010) model. The synaptic response function is plotted as a function of time for three different drug concentrations. As drug effect increases, the decay rate decreases.

an increasing charge transfer of the synapse with increasing p. Unlike previous models [13, 40, 71, 91] which treat the conversion of EPSP and IPSP at the soma separately, this model presumes the somatic conversion of the *difference* of excitatory and inhibitory postsynaptic potentials.

They reported two different sets of steady-states: a single stationary solution and three-root solutions. However, these results were possible only for a certain range of firing threshold voltages. The single stationary solution $V_- = V_e - V_i$ occurred for all values of p provided that the firing threshold of excitatory neurons is equal to or lower than the threshold of inhibitory neurons, $\Theta_E \leq \Theta_I$. In contrast, three stationary solutions occurred for some values of p if $\Theta_E > \Theta_I$. However, these solutions occur only for $V_- < 0$ and for stronger inhibition than excitation.

Figure 1.18(a) represents EEG power for a single solution case, showing increasing power in the θ and α-band and a sequential increase then decrease of power in the δ-band. In the case of multi-valued steady-state, they focused on the top branch, Fig. 1.18(b). The increase and decrease of the EEG-power represents biphasic behaviour, but there were some significant differences with EEG power from clinical general anaesthesia. Their results predict that δ-power should increase and decrease *before* the θ- and α-power biphasic surges, while the power spectra in general anaesthesia reveals the power enhancement and attenuation at high frequencies precedes that at low frequencies.

Interestingly, their results support both the findings of Bojak and Liley that biphasic power spectra may emerge in the presence of a single resting state, and also the results of Steyn-Ross et al. who suppose an instability as the origin of biphasic behaviour.

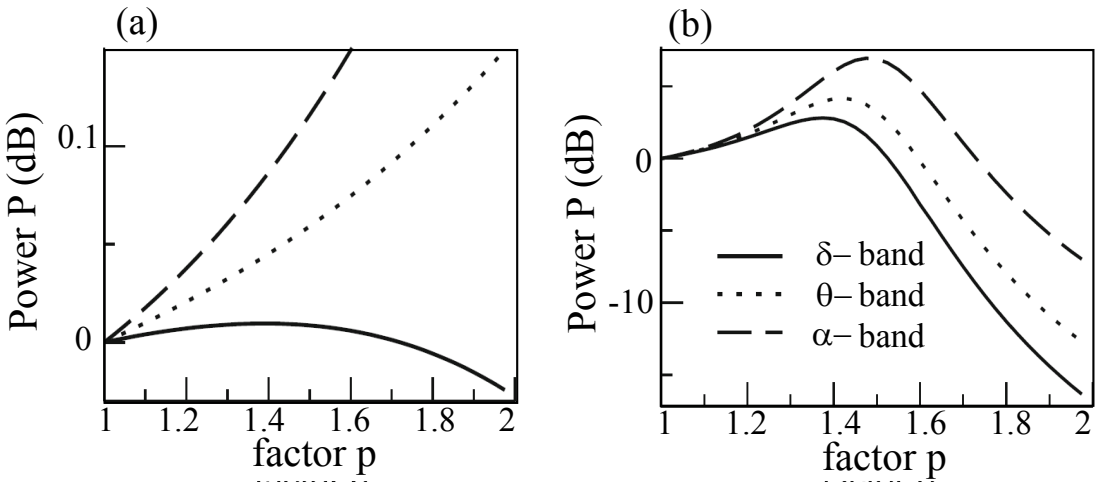

Figure 1.18. Spectral power in different frequency bands for the Hutt (2010) model . The frequency bands are defined in the intervals [0.1 to 4] Hz (δ-band), [4 to 8] Hz (θ-band) and [8 to 12] Hz (α-band). (a) Spectral power in different frequency bands in the single solution case with $\Theta_E = \Theta_I = -60$ mV and $c_e = c_i = 0.06$ $(\text{mV})^{-1}$. (b) Spectral power enhancement on the top branch of the triple stationary solutions. Parameters are $\Theta_E = -50$ mV, $\Theta_I = -60$ mV, $c_e = c_i = 0.114$ $(\text{mV})^{-1}$ (from Figs 9 and 11 of [44]).

1.3.5 Hindriks and van Putten (2012) anaesthesia model

Hindriks and van Putten's 2012 anaesthetic mean-field model [40] is based on the Robinson thalamocortical equations [80]. The HvP model predicts increases in delta and alpha power for moderate (up to 15%) prolongation of $\text{GABA}_\mathbf{A}$ inhibitory response, corresponding to light anaesthetic sedation, as can seen in Fig. 1.19. This mean-field model describes the dynamics of locally averaged membrane potentials of five distinct populations of neurons within a thalamo-cortical system: pyramidal and inhibitory neurons in

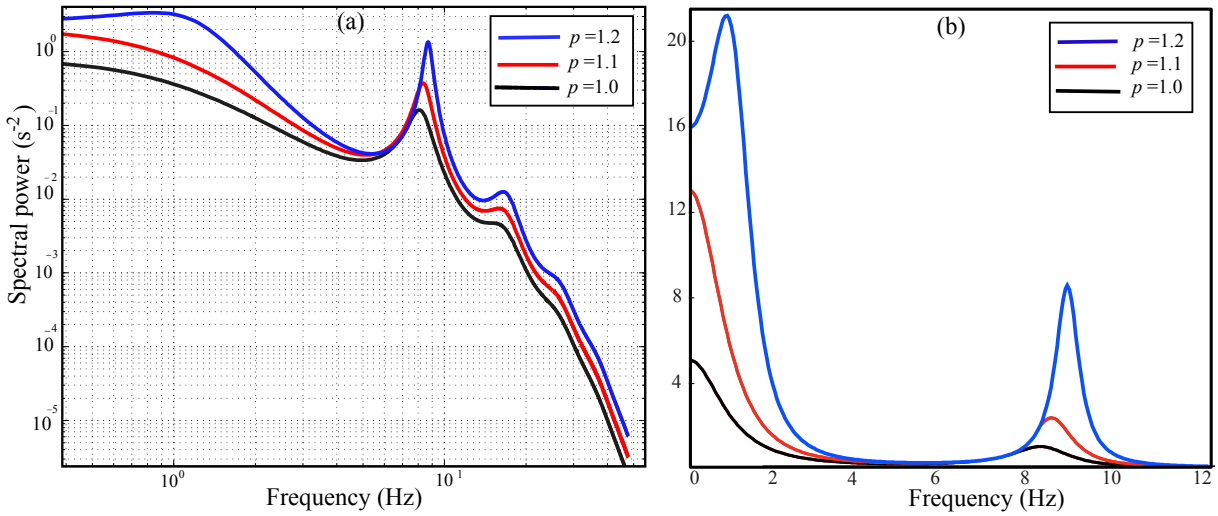

Figure 1.19. Power spectrum predicted by HvP model for baseline condition (black) and in the anaesthesia condition in red and blue. Affinities for cortical excitatory and thalamic relay neurons set to $\epsilon_e = \epsilon_s = 0.5$, while affinity for cortical inhibitory neuron is left at unity, $\epsilon_i = 1$. (a) is the illustration of the power spectrum on a log-log scale, while (b) is power spectrum plotted on a linear scale (based on Fig. 6(a) of [40]).

cortex, relay and reticular neurons in thalamus, and sensory neurons which provide input to the thalamo-cortical system. There is a time delay $\tau/2 = 40$ ms for neural activity propagation from thalamic relay neurons to cortical populations, and vice versa. See Fig. 1.20.

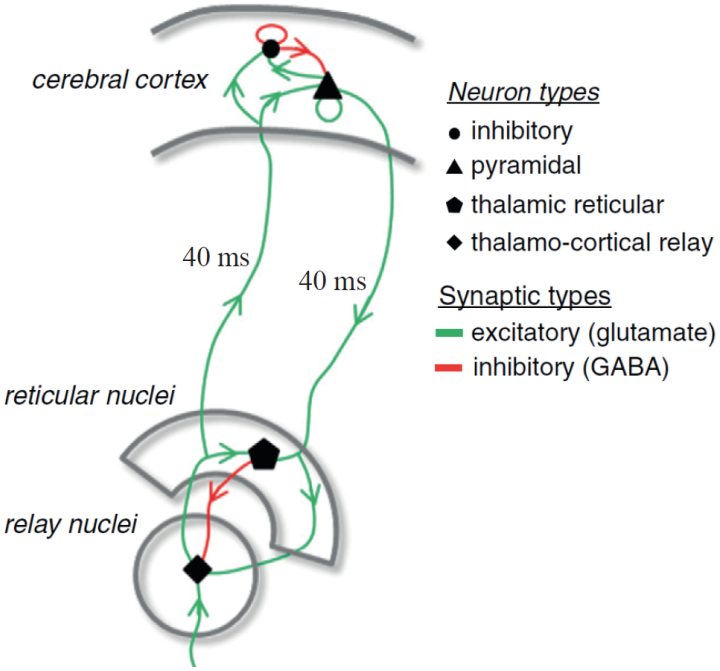

Figure 1.20. Synaptic connections of the HvP thalamo-cortical model. The diagram illustrates the synaptic pathways that connect the different neuronal populations. The model presents four types of neuronal populations: cortical pyramidal neurons and interneurons, thalamo-cortical relay neurons and thalamic reticular neurons and a time delay $\tau/2 = 40$ ms for neural activity propagate from thalamic sensory relay neurons to cortical populations, and vice versa (from Fig. 1 of [41]).

For modelling the action of propofol, Hindriks and van Putten considered the fact that the binding of propofol molecules to $GABA_A$ receptors potentiates their response by decreasing the time constant of receptor deactivation, increasing the duration of inhibitory synaptic transmission [1,8,27]. Therefore, the action of propofol is modelled as a decrease in the decay rate α of $GABA_A$ inhibitory synaptic response

$$\alpha_{ab} = \alpha/p_a \qquad (a,b) \in \{(i,i),(e,i),(s,r)\}\,, \tag{1.23}$$

where e, i, s, and r denote pyramidal, inhibitory, relay, and reticular neurons, respectively, and p_a is the drug effect. Unlike other models, Hindriks and van Putten assumed the inhibitory synaptic responses of the different neuron types have differential sensitivity to propofol and so introduced a drug affinity, ε, such that

$$p_a = 1 + \varepsilon_a(p_i - 1), \qquad a \in \{i,e,s\} \tag{1.24}$$

where the ε_a are positive dimensionless constants. Thus the HvP model has three different inhibitory synaptic responses $\bar{h}_{\rm ii}$, $\bar{h}_{\rm ei}$ and $\bar{h}_{\rm sr}$ for the three distinct inhibitory connections,

$$\overline{h}_{\rm ab}(t) = \frac{\alpha_{ab}\beta}{\beta - \alpha_{ab}}\left(e^{-\alpha_{ab}t} - e^{-\beta t}\right). \tag{1.25}$$

Computing the stationary state trajectories reveals multi-valued steady-state regions. However, Hindriks and van Putten restricted their investigations to only the lowest steady-state voltages. Surprisingly, their results showed that increasing drug effect causes an *increase* in the firing rates in all four populations. Further details regarding this model are presented in Chapter 6.

1.3.6 Hutt (2013) anaesthesia model

In 2013, Hutt introduced a modified anaesthesia model [43] which was based on his previous work in 2010 [44]. He modelled the effect of anaesthetic drug using the clinical results reported by Kitamura et al [56]: the decay time-constant increases with increasing anaesthetic concentration, while the amplitude of the responses remains constant, thus net charge transfer increases with drug concentration.

Hutt replaced the biexponential response function of his earlier [44] model with a single exponential function to describe drug effect at the inhibitory synapse,

$$h(t) = H_0\, e^{-t/\tau_i(p)} \qquad \text{with} \quad \tau_i(p) = p\,\tau_i(1) \tag{1.26}$$

where p is a scale factor representing drug concentration; here H_0 is a constant parameter and the absence of anaesthetic drug is indicated with $p = 1$.

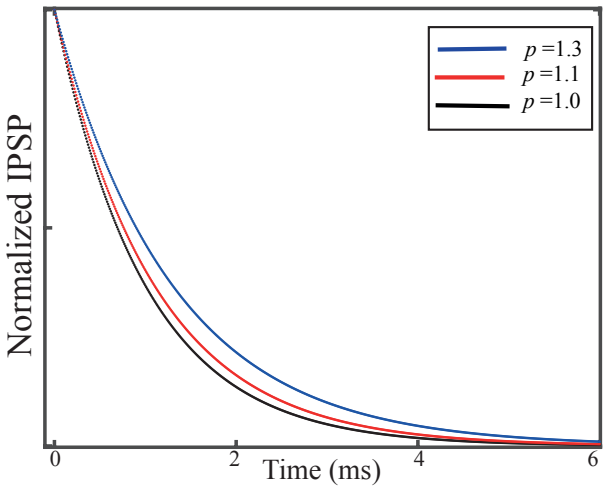

Figure 1.21. Effect of propofol on GABAergic synapses in the Hutt (2013) model. The synaptic response function is plotted as a function of time for three different drug concentrations Eq. (1.26). As the drug effect increases, the decay rate decreases.

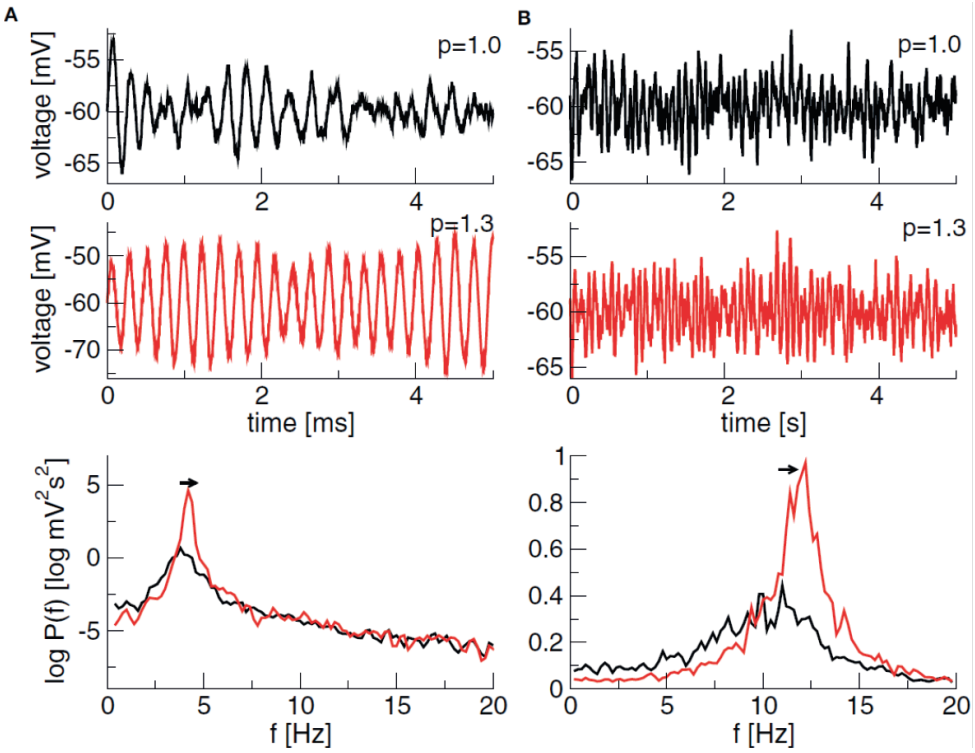

Figure 1.22. Simulated time-series of excitatory voltages and corresponding power spectra in the Hutt (2013) model. Two different model parameters are applied; results for each set are presented separately on the left (A) and right (B) side of the diagram. Simulations were run for 200 ms for two different drug concentrations for each set. With increasing drug concentration, power increases and the peak of maximum power moves to larger frequencies in the β-band for the first set and α-band for the second set of parameters (from Fig 5 of [43]).

Hutt showed that the frequency of maximum power may increase or decrease with increasing anaesthetic concentration relative to changes in the assumed values of particular physiological constants. However, he reported that close to oscillatory instability, the frequency of maximum power increases with increasing p, while far from the stability threshold the maximum power frequency may also decrease. Figure 1.22 shows the results for two different model parametrizations in columns A (left) and B (right). The top pairs of panels correspond to simulations for two different drug concentrations: $p = 1$ and $p = 1.3$; the bottom panel illustrates power spectra. Analytical results predict increase of power in the β-band for the first set, and in the α-band for the second set with increases of anaesthesia. These results illustrate a very strong dependency on the values assumed for the physiological parameters.

1.4 Review of anaesthesia models

The theoretical mean-field descriptions introduced in Section 1.3 follow two approaches to modelling the EEG features observed in the anaesthetised brain: either cortical [**?**, 13, 71, 91] or thalamo-cortical [40, 43].

The first attempt to reproduce the effect of GABAergic anaesthetic drug (such as propofol) was by Steyn-Ross et al [91]. They incorporated the effect of general anaesthetic drug at the cortex as a modulation of the inhibitory neurotransmitter rate-constant, predicting three distinct states for an anaesthetized brain, enabling the brain to switch between awake and anaesthetized states at critical values of the drug concentration.

Liley and Bojak [13] investigated the anaesthetic drug isoflurane and its effect on brain activity. They, however, ignored the multiple-root steady state regions in their research results. They showed that a power surge in EEG activity at low drug concentrations (biphasic effect) without requiring a transition between two distinct states.

Molaee-Ardakani et al [71] incorporated a slow ionic modulation of the sigmoidal voltage-to-firing rate mapping for the excitatory cortical population by introducing a gating variable that depolarizes excitatory neurons when they were in the low firing state, and hyperpolarized them when they were in high firing state. Their model exhibited bistable behaviour.

Hutt and Longtin [44] derived a spatiotemporal field equation for two coupled neural populations consisting of pyramidal cells and GABAergic neurons that inhibit terminal neurons under the administration of propofol. They derived an analytical expression for the EEG power spectrum, showing biphasic behaviour for the EEG power spectrum for both single and multi-valued steady states.

Hindriks and van Putten [40] employed Robinson's model equations [79] to investigate general anaesthesia in the thalamo-cortical system. They applied the Hutt and Longtin method [44] to insert drug effect into the system equations. In contrast to other studies [13, 44, 71, 91], which assumed the same affinity for drug effect in all populations, Hindriks and van Putten defined different affinities for different neuron populations. They compared model predictions for propofol effect on brain activity with clinical EEG recordings, reporting a small increase in the alpha frequency, accompanied by increases in delta and theta frequencies, with increased propofol concentration.

In 2013, Hutt introduced a new response function by replacing the biexponential function of his earlier [44] model with a single exponential to describe drug effect at the inhibitory synapse. He was able to show that the frequency of maximum power may increase or decrease with increasing anaesthetic concentration depending on the values assumed for particular physiological constants [43].

For this thesis, we have chosen to investigate the Waikato and HvP models of anaesthesia. Our goal is to investigate the drug effects on brain dynamics and in particular the effect of anaesthetic drugs. For the Waikato model, we will extend the equations to include the effects of NMDA (excitatory) and $GABA_B$ (inhibitory) synapses.

A notable deficiency in the Waikato model is the lack of an alpha rhythm. The Robinson model includes a thalamo-cortical loop as the source of alpha frequency. Hindriks and

van Putten are the only researchers to apply anaesthesia to the Robinson model. For this reason, we elected to investigate the HvP equations in detail.

Chapter 2

Elements of mathematics

2.1 Introduction

The theory of dynamical systems that arises in many areas of technology and natural science emphasizes the time evolution of the state of a system. The goal when dealing with a dynamical system is to be able to analyse, describe and make predictions about the behaviour of the individual variables and of the complete system.

In this thesis, the focus is not only on dynamical systems described by ordinary differential equations (ODEs), as discussed in Chapters 3 and 4, but also on *delay* differential equations (DDEs) (Chapters 5, 6 and 7). The first reason for choosing differential equations rather than their integral formulations is that integral equations are slow to compute numerically and typically require a large amount of storage. The second reason is that differential equations allow us to locate steady states and this is essential for quantifying stability properties.

In this chapter, a brief survey is provided of the major elements of mathematics that are require for the subsequent chapters. We start by describing the various methods available to solve and analyse ODEs and DDEs. Then, the noise function and its significance for modelling biological systems is discussed. I conclude with a discussion of spectral methods which can be used to analyse the dominant modes of dynamical systems.

Solving DDEs is similar to ODEs in some respects, but there are significant differences:

- In ODEs the function and its derivatives are all evaluated at the same time, while DDEs contain additional derivatives which depend on the solution obtained at previous times.
- In ODEs, gradient discontinuities are not a common issue, while they can be present in DDEs,

$$\frac{d\,y(a^-)}{dt} \neq \frac{d\,y(a^+)}{dt} \qquad \text{if } a = n\,\tau \text{ with } n = \{0, 1, 2, ...\} \tag{2.1}$$

  where τ is the time-delay. In other words, due to the existence of delays, discontinuities can appear at time τ and at multiples of τ.
- Another obvious difference between ODEs and DDEs is the initialization. In DDEs, we have to provide not only the value of the solution at the initial point, but also

the solution at historical times prior to the initial point. In contrast, the solution for ODEs is completely determined by its value at the initial point (see Appendix A.1).

2.2 Delay differential equations

Delay-differential equations arise when a dynamical system induces effects of delayed actions; or in general the model involves responses with non-zero delays. From the mathematical view, delay-differential equations can be expressed as some derivatives of $\vec{y}$ at a time t in terms of $\vec{y}$ at a time t and an earlier time. We restrict our discussion to differential equations with a single fixed delay τ

$$\vec{y}^{(n)} = \vec{F}\left(t, \underbrace{y(t), y'(t), \cdots y^{(n-1)}(t)}_{y \text{ and its derivatives at time } t}, \underbrace{y(t-\tau), y'(t-\tau), \cdots, y^{(n-1)}(t-\tau)}_{y \text{ and its derivatives at time } t-\tau}\right), \tag{2.2}$$

where $\vec{y}^{(n)}$ is an explicit system of delay differential equations of order n with dimension m. We apply the same notation as in Section A.1, where $\vec{y}$ has m dimensions and each has an n-th order differential equation, which can be rewritten as a sets of $k = n \times m$ first-order differential equations

$$\frac{d\vec{V}(t)}{dt} = \vec{F}(\vec{V}(t), \vec{V}(t-\tau)), \tag{2.3}$$

where $\vec{V}$ depends on the value and derivatives of $\vec{y}$ at some time $t-\tau$ in the past, as well as the current value of $y(\vec{t})$ and its derivatives.

2.2.1 Solving DDEs

Simple DDEs can be solved analytically in a stepwise fashion. However, most "useful" DDEs are too complicated to be solved analytically, so we have to resort to numerical methods such as the `dde23` function in MATLAB. Consider a simple first-order DDE with a single delay and fixed coefficients,

$$\begin{aligned} \frac{d\,y(t)}{dt} &= Ay(t) + A_\tau y(t-\tau), & t \geq 0 \\ y(t) &= h(t), & t < 0 \end{aligned}$$

where $h(t)$ defines the "history". As illustrated in Fig 2.1, for such equations the value of the derivative at any time depends on the solution at a previous "lagged" time.

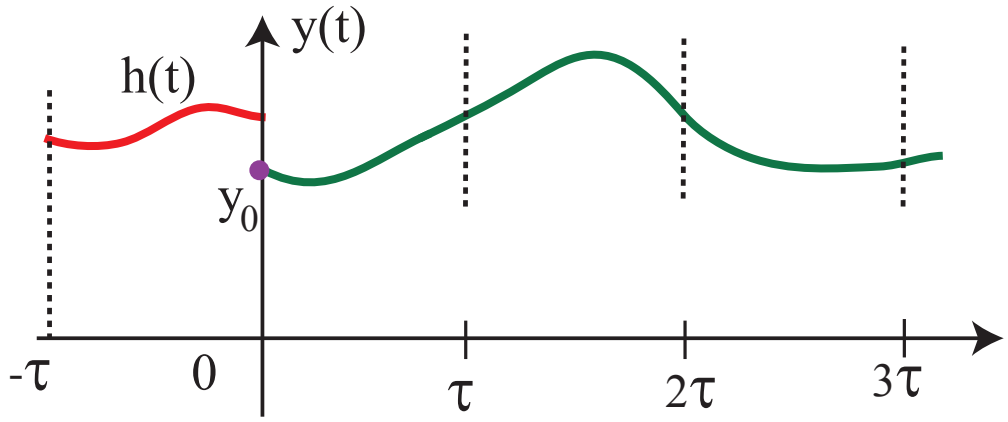

Figure 2.1. For a DDE, the solution $y(t)$ for the future time $0 \leq t < \tau$ depends on the history $h(t)$ defined at previous times, $-\tau < t < 0$.

2.2.2 Method of steps

This method converts the DDE on a given interval to an ODE over that interval by using the known history function for that interval. The resulting equation is solved, and the same process is repeated in the next interval with the latest found solution serving as the history function for the next interval. Although this method may have been discovered by several researchers [10, 107], it is usually attributed to Myshkis [73].

Example: Suppose

$$\frac{dy(t)}{dt} = -y(t-\tau), \quad \text{for} \quad t \geq 0 \tag{2.4}$$

$$y(t) = h(t) = 1, \quad \text{for} \quad t < 0 \tag{2.5}$$

where we will set the constant delay to unity: $\tau = 1$.

To solve Eq. (2.4), first we find the solution for the interval $0 \leq t \leq \tau$. We map the current time interval to the previous time interval which belongs to the history by subtracting τ from $0 \leq t \leq \tau$

$$0 \leq t \leq \tau \quad \Longrightarrow \quad -\tau \leq t-\tau \leq 0 \quad \overset{\tau=1}{\Longrightarrow} \quad -1 \leq t-1 \leq 0\,. \tag{2.6}$$

From Eq. (2.4), the history is

$$y(t) = 1, \quad \text{for} \quad t \leq 0 \tag{2.7}$$

which can be extended to the previous interval

$$y(t-1) = 1, \quad \text{for} \quad -1 \leq t-1 \leq 0\,. \tag{2.8}$$

We rewrite Eq. (2.4) in the interval $0 \leq t \leq \tau$

$$\frac{dy}{dt} = -y(t-1) \quad \Rightarrow \quad \frac{dy}{dt} = -1\,, \tag{2.9}$$

which has solution

$$y(t) = \int_0^t -y(t'-1)dt' + y(0) = \int_0^t -dt' + y(0) = 1 - t, \qquad 0 \leq t \leq \tau\,. \tag{2.10}$$

Now we look for the solution for the next time interval, $\tau \leq t \leq 2\tau$. Using the same method as the previous step

$$\tau \leq t \leq 2\tau \quad \Longrightarrow \quad 0 \leq t-1 \leq 1 \quad \Longrightarrow \quad y(t-1) = 1 - (t-1)\,.$$

For the interval $\tau \leq t \leq 2\tau$ the following derivative is obtained

$$\frac{dy}{dt} = -(1-(t-1))\,, \tag{2.11}$$

whose solution is gained by direct integration

$$y(t) = \int_1^t -y(t-1)dt + y(1) = \frac{t^2}{2} - 2t + 1.5, \qquad \tau \leq t \leq 2\tau\,. \tag{2.12}$$

We continue the function solution for two more time intervals:

$$y(t) = -\frac{t^3}{6} + \frac{3\,t^2}{2} - 4\,t + 3.33, \qquad 2\tau \leq t \leq 3\tau\,,$$

$$y(t) = \frac{t^4}{24} - \frac{2\,t^3}{3} + \frac{15\,t^2}{4} - 9\,t + 7.875, \qquad 3\tau \leq t \leq 4\tau\,,$$

and we note the increase in solution complexity with each interval iteration.

Fig. 2.2(a) shows the solution over the extended period $0 \leq t \leq 8\tau$. The different colours indicate the different function solutions for each delay interval. It is possible to automate this process using, say, MATLAB's symbolic integration function `int` inside a `for`-loop iteration, but only if the initial history function $h(t)$ is a constant value. If the history is a function of time, after just a few delay intervals the integration rapidly becomes unwieldy, leading eventually to failure of the symbolic engine [23, 86].

Difficulties in method of steps

First, the integral arising may not be expressible in terms of known functions. In some cases these integrals result in very long formulae making the solution expensive to compute. Second, the method is inherently finite, so that the long-time behaviour of the

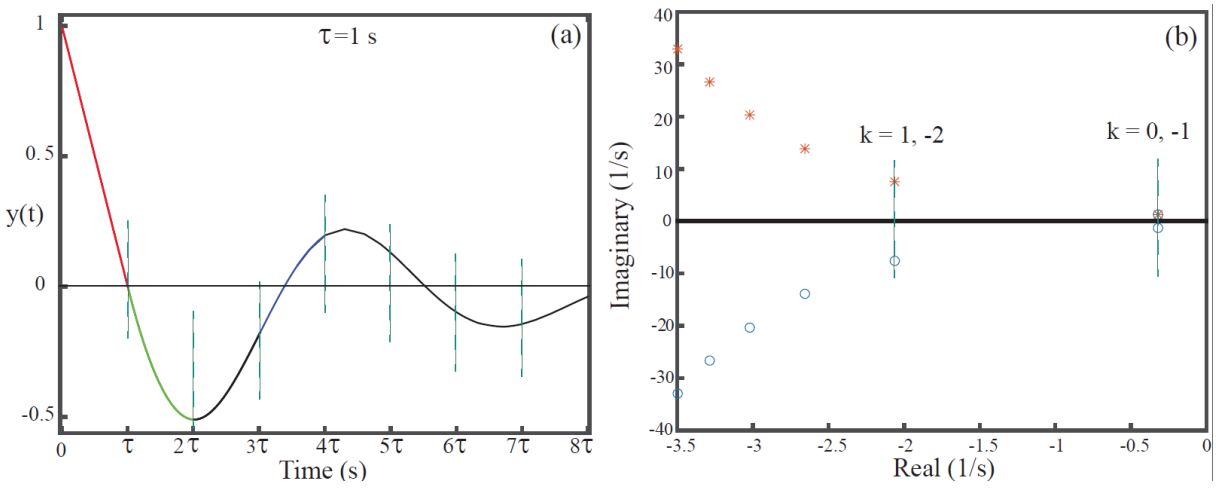

Figure 2.2. Solution of Eq. (2.4) by the method of steps and solution stability by the Lambert method. (a) The solution obtained by applying the method of steps, with each colour indicating different time intervals with different integration functions. (b) Eigenvalues plotted on the complex plane. The eigenvalues obtained using the principal branch, $k = 0, -1$, are dominant and determine the stability of the system with $\lambda = -0.31 + 1.33\,i$. Here, k represents different branches of the Lambert function.

solution is not always evident from the first few analytical steps.

We find that this method is not applicable for our modelling purposes since we are dealing with a high number (typically 13) of first-order delay differential equations. This level of complexity makes it impossible to apply this analytical method to our cortical equations.

2.2.3 The method of characteristics

The stability properties of linear DDEs with discrete delays can be deduced using the characteristic equation. As an example, the characteristic equation for the DDE

$$\frac{d\,\vec{y}(t)}{dt} = \mathbf{A}\vec{y}(t) + \mathbf{A}_\tau \vec{y}(t-\tau)\,, \tag{2.13}$$

is

$$\det(-\lambda\mathbf{I} + \mathbf{A} + \mathbf{A}_\tau e^{-\tau\lambda}) = 0\,, \tag{2.14}$$

where λ are the characteristic roots or eigenvalues of the solution set. Because of the exponential in the characteristic equation, the DDE has, unlike the ODE case, an *infinite* number of eigenvalues, making stability analysis more involved. Even though there are an infinite number of eigenvalues, there is only one pair of eigenvalues with a dominant real part, and these determine the stability of the system [4]. It is important to note that the characteristic equation can only be formed when the differential equation is linear and homogeneous, and has a constant time delay.

Asl and Ulsoy [4] introduced an analytical method for solving systems of DDEs such as Eq. (2.13) using the matrix Lambert W function.[1] However, their method is applicable only when the matrix coefficients $\mathbf{A}$ and $\mathbf{A}_\tau$ commute. In 2006, Yi, Ulsoy and Nelson [109] extended the matrix Lambert W approach to handle the case of non-commuting $\mathbf{A}$ and $\mathbf{A}_\tau$ matrices. Here, we summarise their method.

Rearranging Eq. (2.13),

$$\frac{d\,\vec{y}(t)}{dt} - \mathbf{A}\,\vec{y}(t) - \mathbf{A}_\tau\,\vec{y}(t-\tau) = 0 \qquad \text{for} \quad t < 0\,. \tag{2.15}$$

We assume there is a solution for Eq. (2.13) in the form

$$\vec{y}(t) = \vec{y}_0 e^{\mathbf{S}t}\,, \tag{2.16}$$

where $\mathbf{S}$ is an $m \times m$ matrix. Substituting Eq. (2.16) into (2.15)

$$\mathbf{S}\vec{y}_0 e^{\mathbf{S}t} - \mathbf{A}\,\vec{y}_0 e^{\mathbf{S}t} - \mathbf{A}_\tau\,\vec{y}_0 e^{\mathbf{S}(t-\tau)} = 0\,,$$

which factorizes to

$$\left(\mathbf{S} - \mathbf{A} - \mathbf{A}_\tau\, e^{-\mathbf{S}\tau}\right)\,\vec{y}_0 e^{\mathbf{S}t} = 0\,.$$

As $\vec{y}(t) = \vec{y}_0 e^{\mathbf{S}t}$ is a non-zero solution, then for every moment of time t, we must have,

$$\mathbf{S} - \mathbf{A} - \ \mathbf{A}_\tau\, e^{(-\mathbf{S}\tau)} = 0 \tag{2.17}$$

In the special case $\mathbf{A}_\tau = 0$, the delay term disappears and the DDE collapses to an ODE with

$$\mathbf{S} - \mathbf{A} = 0 \iff \mathbf{S} = \mathbf{A}\,, \tag{2.18}$$

giving the matrix exponential solution

$$\vec{y}(t) = \vec{y}_0 e^{\mathbf{A}t}\,. \tag{2.19}$$

[1] In mathematics, the Lambert-W function is a set of functions defining the branches of the inverse relation of the function $f(z) = ze^z$ where e^z is the exponential function and z is any complex number:

$$z = f^{-1}(ze^z) = W(ze^z)$$

By substituting $z = W(z)$ in the above equation, we get the defining equation for the W function:

$$z = W(z)e^{W(z)}$$

for any complex number z.

Returning to the Eq. (2.17) for $\mathbf{A}_\tau \neq 0$, we multiply $\tau e^{\mathbf{S}\tau} e^{-\mathbf{A}\tau}$ on both sides of Eq. (2.17) and rearrange to obtain

$$\tau e^{\mathbf{S}\tau} e^{-\mathbf{A}\tau}(\mathbf{S}-\mathbf{A}) = \tau e^{\mathbf{S}\tau} e^{-\mathbf{A}\tau}(\mathbf{A}_\tau\, e^{(-\mathbf{S}\tau)})\,. \tag{2.20}$$

In the general case, when the matrices S and A do not commute

$$\tau(\mathbf{S}-\mathbf{A}) e^{\mathbf{S}\tau} e^{-\mathbf{A}\tau} \neq \tau(\mathbf{S}-\ \mathbf{A}) e^{(\mathbf{S}-\mathbf{A})\tau}\,. \tag{2.21}$$

We need to fix the inequality in Eq. (2.21). We take advantage of the following property of the matrix Lambert W function

$$W(\mathbf{H}) e^{W(\mathbf{H})} = \mathbf{H}\,. \tag{2.22}$$

We introduce an unknown matrix $\mathbf{Q}$ that satisfies,

$$\tau(\mathbf{S}-\mathbf{A}) e^{(\mathbf{S}-\mathbf{A})\tau} = -\mathbf{A}_\tau \tau \mathbf{Q} \tag{2.23}$$

then compare Eqs. (2.22) and (2.23) to obtain,

$$(\mathbf{S}-\mathbf{A})\tau = W(-\mathbf{A}_\tau \tau \mathbf{Q})\,, \tag{2.24}$$

which can be solved for $\mathbf{S}$ to give

$$\mathbf{S} = \frac{1}{\tau} W(-\mathbf{A}_\tau \tau\ \mathbf{Q}) - \mathbf{A}\,. \tag{2.25}$$

Substituting Eq. (2.25) into (2.20) yields the following condition which can be used to solve for the unknown matrix $\mathbf{Q}$

$$W(-\mathbf{A}_\tau\, \tau\ \mathbf{Q})\, e^{W(-\mathbf{A}_\tau \tau \mathbf{Q}) - \mathbf{A}\tau} = -\mathbf{A}_\tau\, \tau\,. \tag{2.26}$$

Equation (2.26) always has a unique solution $\mathbf{Q}$ for each branch k [109]. The solution can be obtained numerically for a variety of initial conditions, using the `fsolve` function in MATLAB. Having $\mathbf{Q}$, we can calculate $\mathbf{S}$ through Eq. (2.25), and hence deduce the stability properties of system.

Example: We apply the method of characteristics to the previous example solved via the method of steps

$$\begin{aligned} \frac{d\,y(t)}{dt} &= -y(t-\tau), \quad \text{for} \quad t \geq 0 \text{ and } \tau = 1\,, \\ y(t) &= h(t) = 1, \qquad \text{for} \quad t < 0\,, \end{aligned} \tag{2.27}$$

has characteristic equation

$$-\lambda - e^{-\lambda} = 0\,. \tag{2.28}$$

There are an infinite number of solutions to this equation for complex λ

$$\lambda = W_k(-1)\,, \tag{2.29}$$

where W_k is the k^{th} branch of the Lambert-W function. In Fig. 2.2(b), the complex plane is plotted for the solution of Eq. (2.29) with the imaginary and real parts of λ displayed on the vertical and horizontal axes respectively. As shown in the graph, as k increases, the corresponding real part decreases; this indicates that the lowest branch usually quantifies the stability properties. Here, $k = 0, -1$ are dominant and determine the stability of the system with $\lambda = -0.31 \pm 1.33\,i$ and for $k = 1, -2$ the solution is $\lambda = -2.06 \pm 7.58\,i$.

Applying the method of characteristics for the delay dynamical system which is presented in Chapters 5, 6 and 7 leads us to find out the limitation of this method. Our mentioned system consists of 13 first-order delay differential equations, leading to 13×13 matrices for $\mathbf{A}$ and $\mathbf{A}_\tau$. The `fsolve` function in MATLAB is used, with the aim of solving Eq. (2.26) for the unknown matrix $\mathbf{Q}$. Using `fsolve` requires an accurate initial guess for matrix $\mathbf{Q}$, a 13×13 matrix with a total of 169 elements. Choosing a good initial guess for such a large matrix is almost impossible.

In the second attempt, the symbolic `solve` function in `Maple` was tried. This method leads us to a very unwieldy expression which was not usable.

To solve our delay thalamo-cortical equations, two numerical methods, `dde23` and Euler, was applied successfully and the transfer function was used to analyse the system stability. In the following sections, more detailed explanations are given on these methods.

2.2.4 Numerical methods for solving DDEs

In this section we discuss some aspects relevant to the numerical solution of DDEs. A popular approach is to extend one of the explicit Runge-Kutta methods [87]. The MATLAB function `dde23`, and its companion `ddesd`, take this approach by extending ODE solver `ode23`. The step size is chosen by algorithm to be as small as necessary to get an accurate solution. The `dde23` and `ddesd` solvers have been designed for DDE systems with constant delays.

The idea is similar to the method of steps described in Chap. 2.2.2. In solving for $0 \leq t \leq \tau$, the DDE reduces to an initial value problem for an ODE with $y(t-\tau)$ equal to the given history $h(t-\tau)$ and initial value $y(0) = h(t)$. We can solve this ODE numerically using any of the standard methods. The analytical solution of the DDE on the next interval $\tau \leq t \leq 2\tau$ is handled the same way as the first interval, but subject

to the challenge of keeping track of how the discontinuity at the initial point propagates because of the delays [87].

The second method we applied to solve DDEs is the Euler algorithm, a numerical procedure usually applied to solving ODEs with a given initial value. For our application we have two sets of equations: the first set which behave as ODEs for times less than the time delay τ, and the second set, behaving as DDEs for times bigger than the delay time. For the first time interval $t_n \leq \tau$, the standard formula of the Euler method is applied

$$y(t_{n+1}) = y(t_n) + y'(t_n)\,\Delta t \qquad\qquad t_n = n\Delta t\,, \tag{2.30}$$

then for $t_n > \tau$, we use

$$y(t_{n+1}) = y(t_n) + \left[y'(t_n + y'(t_n - \tau))\right]\Delta t \qquad\qquad \tau = k\Delta t,\, 0 < m < k\,. \tag{2.31}$$

2.3 Stochastic dynamical system

A stochastic dynamical system can be viewed as a deterministic system subjected to the effects of noise. In fact, adding low-intensity noise is supposed to represent the continuous random fluctuations which are natural events occurring in all living systems. In nonlinear systems noise acts as a driving force that can drastically modify deterministic dynamics [89]. In modelling brain activity, neuronal noise is an inseparable phenomenon that is present continuously. Noise-driven fluctuations can lead to non-trivial effects such as causing transitions between coexisting deterministic stable states, stabilizing unstable equilibria, and shifting bifurcation points. At the very least, noise can excite the internal modes of oscillation in both ODEs and DDEs [45].

2.3.1 Noise

Noise as a random variable is a quantity that fluctuates aperiodically in time. For our modelling, we wish to analyse noise evoked fluctuations in excitatory soma voltage and so assume the existence of a continuous wash of stochastic variability entering from non-specific populations. We consider state variables that are perturbed by one or more sources of white noise. The noise contribution is classified according to the way it interacts with the dynamical variable of interest. If the noise intensity, b, is independent of the state of the system, the noise is said to be "additive". In other words, the noise $\zeta(t)$ is simply added to the deterministic part of the system equations

$$\frac{dy}{dt} = F(y) + b\,\zeta(t)\,. \tag{2.32}$$

Alternatively, one can have "multiplicative" noise, for which the coefficient of the noise depends on the value of one or more state variables. In such a case, the evolution equation would take the form

$$\frac{dy}{dt} = F(y) + b(y)\zeta(t)\,, \tag{2.33}$$

where the strength of the noise is dependent on the state of the system, $y(t)$.

In the present work, we adopt the simplest case of additive white noise, that is, noise that is uncorrelated in space and time.

2.3.2 Incorporating noise into a dynamical system

By incorporating noise into the model equations, we transform the ordinary differential equations into stochastic form, also known as Langevin form. When adding noise to the system, we need to ensure that the stochastic mapping is dimensionally consistent with the evolution equations. For our modelling purposes, the noise function is defined as a rapidly varying random fluctuation function of time about its mean

$$\widetilde{p(t)} = b\,\xi(t)\,, \tag{2.34}$$

where $\xi(t)$ is white noise with zero mean

$$\langle \xi(t) \rangle = 0\,, \tag{2.35}$$

and delta-function covariance

$$\langle \xi_m(t)\,\xi_n(t') \rangle = \delta_{mn}\,\delta(t-t')\,. \tag{2.36}$$

Taking the integral of Eq. (2.36), we obtain

$$\int_{-\infty}^{\infty} \langle \xi_m(t)\,\xi_n(t') \rangle \rangle\, dt = \delta_{mn} \int_{-\infty}^{\infty} \delta(t-t')\, dt = 1\,. \tag{2.37}$$

Equation (2.37) shows that the Dirac delta-function, $\delta(t)$, carries units of inverse time, since the Kronecker delta δ_{mn} does not carry any units. Therefore, $\xi(t)$ must have units of inverse square-root of time [$s^{-1/2}$]. The coefficient b of Eq. (2.34) must not only fulfil the requirements of dimensional consistency, but also control the strength of the noise in the system equations. In this thesis, we wish to incorporate white noise as the non-specific subcortical flux input.

In our stochastic simulations, we approximate white noise by drawing samples from MATLAB's Gaussian-distributed unit-variance random-number generator, `randn`, such

that

$$\xi(t) \;=\; \frac{\texttt{randn}}{\sqrt{\Delta t}}\,, \tag{2.38}$$

where the numbers taken from `randn` are taken to be dimensionless, and where Δt is the simulation time-step. Thus $\xi(t)$ has variance $1/\Delta t$, giving the correct white-noise limit as $\Delta t \;\to\; 0$.

Here, it is important to mention that noise can only be added to a fixed time-step integrator (e.g., Euler); adding noise to a variable time-step integrator (e.g., `dde23`, `ode45`) will give unreliable results because the step-adjustment algorithm necessarily assumes a fully deterministic system. Integration of stochastic differential equations requires considerable care.

2.4 Power spectral density

In all brain modelling, detecting the dominant frequency components is one of the key goals as these can be referred to specific states of rhythmic brain activity. Fourier transform methods are applied to quantify the frequency content of clinical recordings and of modelling equation predictions. The relevant Fourier theory is summarised in Appendix A.2. We now give a brief overview of how to estimate the input–output transfer function for a linear system of equations. This is relevant to our analysis of the Robinson (Ch 5) and HvP models (Chs 6, 7).

2.4.1 Transfer function

Transfer functions are commonly used in the analysis of systems such as single-input single-output filters, typically within the fields of signal processing, communication theory, and control theory [36]. Transfer functions relate the output or response of a system such as a filter circuit to the input or stimulus. We can compute the transfer function for any dynamical system which can be described as a set of linear partial differential equations, even of very high order. The transfer function is a convenient representation of a linear time-invariant dynamical system. The order of the differential equations is of no concern as we do not work directly with these equations, and this property is considered to be one of the advantages of using transfer function instead of standard linear stability analysis.

The transfer function is defined as a relation between the output and input of the linear system, and is usually presented in the (k, ω) frequency domain, where $k = 2\pi/\lambda$ and $\omega = 2\pi f$. After suitable rearrangement of the system equations, we obtain

$$H(k,\omega) = \frac{F(k,\omega)}{G(k,\omega)}\,, \tag{2.39}$$

where $F(k,\omega)$ is the output function and $G(k,\omega)$ is the input to the system; both are expressed as polynomial equations. To calculate the power spectral density, one computes the mod-square,

$$\text{PSD} \equiv |H(k,\omega)|^2 \ . \tag{2.40}$$

Here, it is important to mention that the roots of the numerator function $F(k,\omega)$ indicate the zeros of the system, while setting $G(k,\omega)$ to zero, also known as the dispersion curve, determines the poles of the system. In fact, poles are eigenvalues and they describe the main dynamics of the system. If we assume λ is one of the poles in the frequency domain, written as $\lambda = \alpha + i\,\omega$, then the corresponding eigenvalue expression in the time domain follows the relation $U = -i\,\lambda$. Thus the imaginary part of the eigenvalue in frequency domain corresponds to the real part of the time-domain eigenvalue, i.e., the damping rate. For more details see [36]. We use the transfer function in Chapters 6 and 7 to analyse the stability of a delay dynamical system.

Chapter 3

Theoretical investigation of anaesthetic effects in the extended Waikato model

3.1 Introduction

Continuum models of the cortex aim to describe the interactions of the neural populations that generate the electrical perturbations and rhythms which can be detected with scalp and cortical EEG (electroencephalogram) electrodes.

In the continuum (mean-field) model, neural parameters have been averaged over the population of neurons in a small volume of cortex. However, the basic frame for delivering the effect of spikes in the mean-field model is the same as that for an individual neuron: presynaptic flux activity travels along the axon to the synaptic terminals; these presynptic inputs generate postsynaptic potentials. Activity entering the dendritic tree is integrated at the soma, producing a fluctuation in the soma voltage. In the standard Waikato mean-field model, the net neuron voltage is determined by axon-dendritic activity at the chemical synapses; excitatory inputs are mediated by AMPA receptors and inhibitory inputs by $GABA_A$ receptors.

The aim of the current work is to investigate the effect of anaesthetic drugs on the extended Waikato model. The model is extended by incorporating additional physiological detail: we now include four receptors ($GABA_A$, $GABA_B$, NMDA, AMPA) rather than just two ($GABA_A$, AMPA). Two classes of neural synapses are modelled: the first is the excitatory AMPA and NMDA synapse in which the nerve impulse in a presynaptic cell tends to increase the probability that the postsynaptic cell will fire an action potential; the second, the inhibitory synapses $GABA_B$ and $GABA_A$, tend to suppress postsynaptic firing.

This chapter starts with a discussion of the mathematical formulation of the cortical model developed by Prof Moira Steyn-Ross and colleagues at Waikato University. The effect of increasing $GABA_B$ and NMDA gain factors on cortical activity is investigated through linearised dispersion curve predictions and fully nonlinear dynamical grid simulations.

In 2012, Steyn-Ross et al [92] showed that in the standard Waikato model the Turing spatial mode, set by gap-junction diffusion, is protective against entering oscillatory modes; and weakening the Turing mode by reducing gap conduction can release an uncontrolled Hopf oscillation and hence an increased propensity for seizure and simultaneously an increased sensitivity to $GABA_A$ergic anaesthesia. Following the previous work, we examine the gap-junction diffusion effect on the extended Waikato model. We investigate the effect of Cx36 reduction on seizure activity while simultaneously altering the cooperation of $GABA_B$ergic and NMDAergic anaesthetic agents.

3.1.1 The extended Waikato cortical model

The cortex is modelled as a two-dimensional continuum of excitable tissue containing interlinked populations of excitatory and inhibitory neurons. Each neuron is represented as an RC integrator of membrane resistance R_m and capacitance C, with the resting membrane potential acting as a battery in series with the membrane resistance, Fig. 3.1. The total entering currents are the sum of the synaptic current I^{syn} due to the spike activity at the chemical synapses, plus diffusive current I^{gap} due to gap junction connections. This is equal to the membrane resistance current, $(V^{\text{rest}} - V)/R_m$ plus the membrane displacement current, $C\,dV/dt$,

$$C\frac{dV}{dt} + \frac{V(t) - V^{\text{rest}}}{R_m} = I^{\text{syn}}(t) + I^{\text{gap}}(t) \tag{3.1}$$

Multiplying through by membrane resistance R_m gives

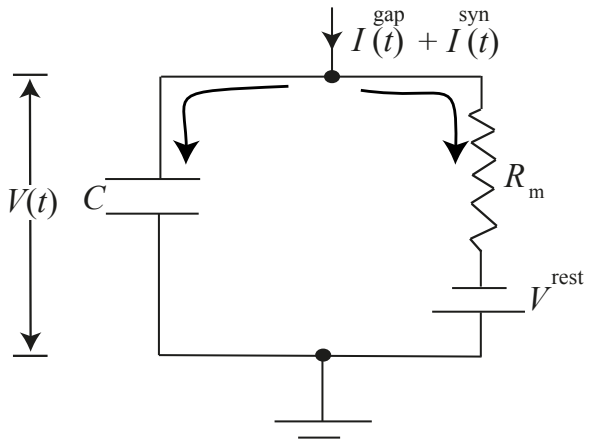

Figure 3.1. Mapping of a membrane onto an equivalent electrical circuit. The soma membrane behaves like a capacitor of capacitance C and the ion channels are modelled as resistors R. Synaptic current due to the spike activity at the chemical synapses is denoted by I^{syn}, the diffusive current due to gap junction connections by I^{gap}. V^{rest} is the resting membrane potential for the neuron.

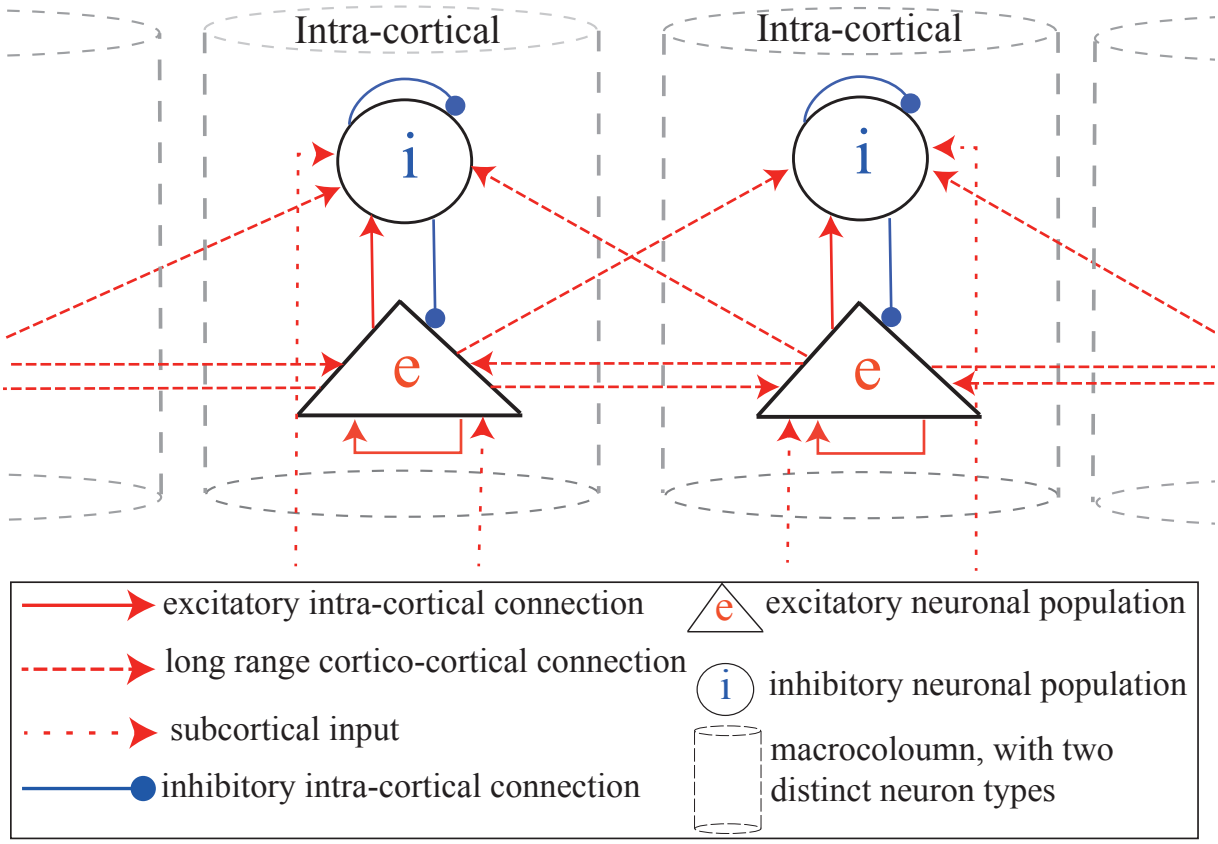

Figure 3.2. Schematic representation of the connective topology within and between cortical macrocolumns. The shape of neurons follows their appearance under microscope: pyramidal excitatory neurons are triangles; inhibitory neurons are circles.

$$\tau \frac{dV}{dt} = V^{\text{rest}} - V(t) + \delta V^{\text{syn}}(t) + \delta V^{\text{gap}}(t) \tag{3.2}$$

where $\tau = R_{\text{m}}C$ is the cell time-constant, δV^{syn} is the voltage perturbation due to chemical synaptic inputs, and δV^{gap} is the voltage change due to gap-junction currents.

Following the work of Liley et al [62, 63], cortical neurons are aggregated into small columnar structures called *macrocolumns* (see Fig. 3.2) of volume $\sim$1 mm^3 containing $\sim 10^5$ neurons. Each macrocolumn consists of two distinct neuron populations, with 85% being excitatory and 15% inhibitory. Neuron interactions are divided into three different types:

1. Short range (intracortical) interactions limited to inside the macrocolumn and between the inhibitory and excitatory cells;
2. Long range (cortico-cortical) interactions represent input to excitatory and inhibitory populations from a distance;
3. Exogenous (subcortical) interactions represent input from the thalamus and brainstem.

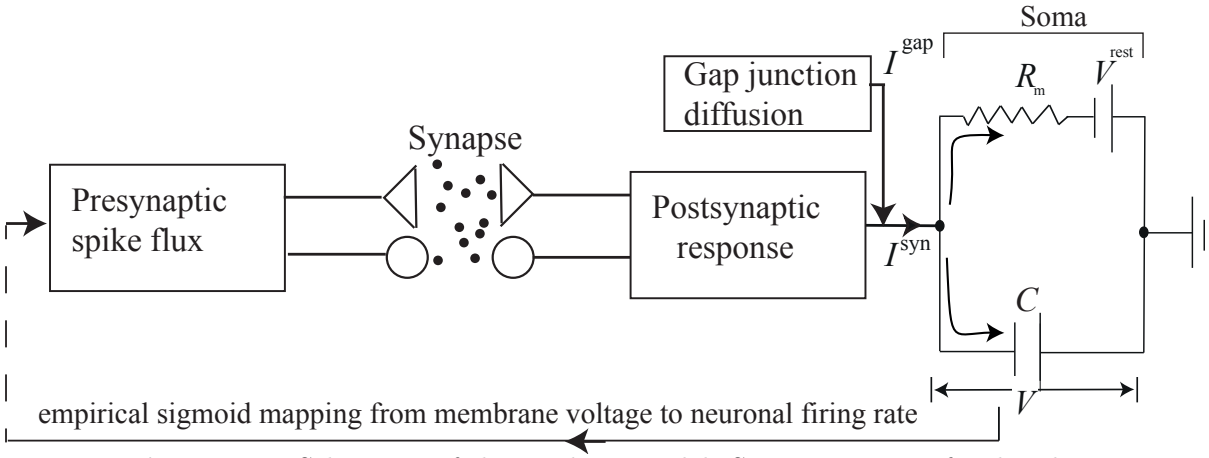

Figure 3.3. Schematic of the Waikato model. See Figs 3.4–3.7 for details.

The standard Waikato mean-field cortical model is a population aggregate of the single neuron model. Incoming fluxes induce postsynaptic dendrite potentials that are integrated at the soma, driving a time-dependent perturbation about the soma resting potential. This is illustrated in Fig. 3.3.

3.1.2 Presynaptic flux inputs

Long range flux inputs ϕ_{ek}^{N} and ϕ_{ek}^{A} are generated by distant excitatory sources $Q_e^{N,A}$, mediated by NMDA (N) and AMPA (A) receptors respectively, and obey 2D damped wave equations [80] while travelling to the destination populations, which can be either excitatory (e) or inhibitory (i),

$$\left[\left(\frac{\partial}{\partial t}+\nu\Lambda_{ek}^{A}\right)^{2}-(\nu\bigtriangledown)^{2}\right]\phi_{ek}^{A}(\vec{r},t)=(\nu\Lambda_{ek}^{A})^{2}Q_{e}^{A}(\vec{r},t), \qquad k=i,e \tag{3.3}$$

$$\left[\left(\frac{\partial}{\partial t}+\nu\Lambda_{ek}^{N}\right)^{2}-(\nu\bigtriangledown)^{2}\right]\phi_{ek}^{N}(\vec{r},t)=(\nu\Lambda_{ek}^{N})^{2}Q_{e}^{N}(\vec{r},t) \tag{3.4}$$

Here, the square brackets donate an operator, $\nabla^2 = \dfrac{\partial^2}{\partial x^2} + \dfrac{\partial^2}{\partial y^2}$ is the Laplacian differential operator in Cartesian coordinates, ν is the axonal conduction speed, and $\Lambda_{ek}^{N,A}$ is the inverse-length scale for axonal connections in cm^{-1}. Subscript ek is read left to right indicate a connection *from* presynaptic neuron type e (either NMDA or AMPA) *to* postsynaptic neuron type k. Equations (3.3) and (3.4) (second-order) can be reformulated as a set of eight coupled first-order DEs for both NMDA and AMPA receptors.

Short-range inputs $\phi_{ik}^{a,b}$ (inhibitory flux reaching $\mathrm{GABA_A}$ and $\mathrm{GABA_B}$ receptors) and $\phi_{ek}^{N,A}$(local) are produced locally (i.e., within the macrocolumn) so are assumed to propagate instantaneously. Therefore these fluxes can be replaced by their sources: Q_i

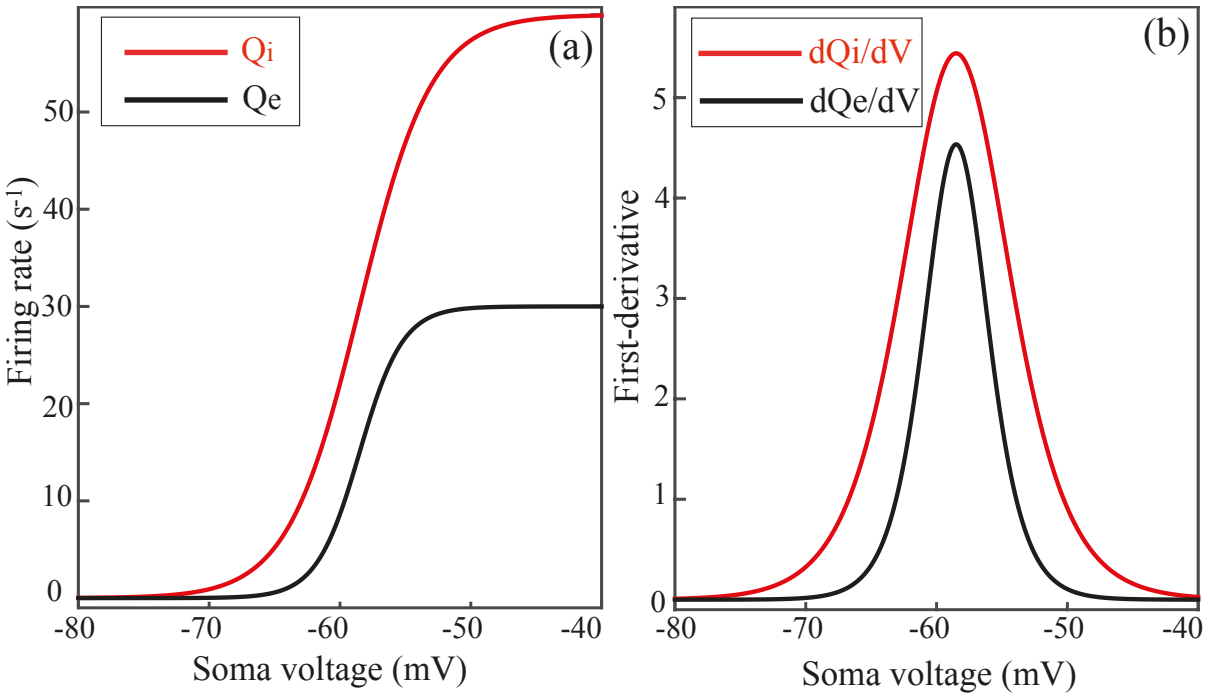

Figure 3.4. Sigmoidal functions relating firing rate to average soma potential. (a) Sigmoid curves of Eq. (3.7): excitatory sigmoid Q_e (black curve); inhibitory sigmoid Q_i (red). (b) First derivative of sigmoid functions: dQ_e/dV_e (black curve); dQ_i/dV_i (red).

inhibitory and Q_e for excitatory,

$$\phi_{ik}^{a,b}(\text{local}) = Q_i^a = Q_i^b = Q_i \tag{3.5}$$

$$\phi_{ek}^{N,A}(\text{local}) = Q_e^A = Q_e^N = Q_e \tag{3.6}$$

The spike-rate is represented by a sigmoidal mapping from membrane voltage V_k to the firing rate Q_k, see Fig. 3.4,

$$Q_k = \frac{Q_k^{\max}}{1 + e^{-c(V_k - \theta_k)/\sigma_k}} \tag{3.7}$$

where $Q_k^{\max}$ is the maximum firing rate, θ_k is the sigmoid threshold voltage for firing and σ_k is the standard deviation with $c = \pi/3$; see Table 3.1 for values.

Subcortical inputs ϕ_{ek}^{sc} are added into the system equations to provide a source of low-intensity random fluctuations. The subcortical excitation is modelled as a spatiotemporal Gaussian distributed white noise, $b\,\xi_{ek}(\vec{r}, t)$ which is superimposed on a background level of excitation $\langle \phi_{ek}^{sc} \rangle$,

$$\phi_{ek}^{sc}(\vec{r}, t) = \langle \phi_{ek}^{sc} \rangle + b\,\xi_{ek}(\vec{r}, t) \tag{3.8}$$

where b is a constant scale-factor for subcortical drive to tune the level of subcortical excitation and also to fulfil the requirements of dimensional consistency, and ξ_{ek} is the Gaussian-distributed white-noise source generated by the MATLAB command `randn`, see

Chap. 2.3.

The total presynaptic input for each population is the sum of long-range, short-range and subcortical inputs,

$$M_{ek}^{N}(\vec{r},t) = \underbrace{N_{ek}^{N}\phi_{e}^{N}(\vec{r},t)}_{\text{long-range}} + \underbrace{n_{ek}^{N}Q_{e}^{N}(\vec{r},t)}_{\text{local}} + \underbrace{\phi_{ek}^{sc}(\vec{r},t)}_{\text{subcortical}} \tag{3.9}$$

$$M_{ek}^{A}(\vec{r},t) = \; N_{ek}^{A}\phi_{e}^{A}(\vec{r},t) \; + \; n_{ek}^{A}Q_{e}^{A}(\vec{r},t) + \; \phi_{ek}^{sc}(\vec{r},t) \tag{3.10}$$

where capital letter N_{ek} and small n_{ek} distinguish the number of long-range and local input connections; see Table 3.1. Inhibitory inputs include only the short range connections,

$$M_{ik}^{a}(\vec{r},t) = n_{ik}^{a}Q_{i}(\vec{r},t) \tag{3.11}$$

$$M_{ik}^{b}(\vec{r},t) = n_{ik}^{b}Q_{i}(\vec{r},t) \tag{3.12}$$

where n_{ik} is the short-range axonal connectivity numbers for inhibitory ($\mathrm{GABA_A}$, $\mathrm{GABA_B}$) receptors.

3.1.3 Postsynaptic responses

Presynaptic flux M_{lk} releases neurotransmitters into the synaptic cleft, changing the postsynaptic dendrite voltage via charge transfer through opened ion channels. We assume that the resulting voltage fluctuation at the dendrite, U_{lk}, is given by the temporal convolution of the dendrite impulse response $H_{lk}(t)$ with presynaptic input M_{lk}, scaled by the synaptic reversal potential, ψ_{lk} and gain factor ρ_l,

$$U_{lk}(\vec{r},t) = \rho_l\,\psi_{lk}\,\Phi_{lk}(\vec{r},t) \quad \text{where} \quad \begin{matrix} l = e,i \\ k = a,b,A,N \end{matrix} \tag{3.13}$$

and,

$$\Phi_{lk}(t) = [H_{lk}(t) \otimes M_{lk}(t)] \equiv \int_0^t H_{lk}(t-t')\,M_{lk}(t')\,dt'$$

where subscript l indicate the coming fluxes can be either excitatory or inhibitory and k defines flux destinations which can be one of receptor populations (a,b,A,N).

Experimental measurements of the postsynaptic potential (PSPs) show a rapid-rise, slow-decay curve which is well approximated by a biexponential function $H(t)$. However, there is a difference between the excitatory and inhibitory response functions. Excitatory response function is assumed not to be effected by anaesthetic drug concentration,

$$H_{ek}^{m}(t) = \frac{\alpha^m\beta^m}{\beta^m-\alpha^m}\left(e^{-\alpha^m t} - e^{-\beta^m t}\right), \qquad m = A,\ N \tag{3.14}$$

Table 3.1. Definitions and values for cortico-cortical and intracortical parameters

Symbols	Description	Value	Unit
$\Lambda_{eb}^{A,\,N}$	inverse-length scale for axonal connection	4	cm^{-1}
ν	axonal conduction speed	140	$\mathrm{cm\,s}^{-1}$
$Q_{e,\,i}^{max}$	maximum firing rate	30, 60	s^{-1}
$\theta_{e,i}$	sigmoid threshold voltage	-58.5,-58.5	mV
$\sigma_{e,i}$	standard deviation for threshold	3, 5	mV
c	sigmoid constant (see Eq (3.7))	$\pi\sqrt{3}$	
$N_{ek}^{A,\,N}$	long-range axonal connectivity	2000	
$n_{ek}^{A,\,N}$	short-range axonal connectivity	800	
$n_{ik}^{a,\,b}$	short-range axonal connectivity	600	
$\langle\phi_{eb}^{sc}\rangle$	tonic flux entering from subcortex	500	s^{-1}
$V_{i,e}^{\mathrm{rev}}$	reversal potential at dendrite	-70, 0	mV
$V_{i,e}^{\mathrm{rest}}$	neuron resting voltage	-64, -64	mV
(α^b, β^b)	$\mathrm{GABA_B}$ (decay, rise) rates	$(10, 30)$	s^{-1}
(α^a, β^a)	$\mathrm{GABA_A}$ (decay, rise) rates	$(20-40, 200)$	s^{-1}
(α^A, β^A)	AMPA (decay, rise) rates	$(50, 200)$	s^{-1}
(α^N, β^N)	NMDA (decay, rise) rates	$(15, 120)$	s^{-1}

while inhibitory response functions are dependent on drug concentration factor p,

$$H_{ik}^{m}(t) = \frac{\alpha^m(p)\,\beta^m}{\beta^m - \alpha^m(p)}\left(e^{-\alpha^m(p)\,t} - e^{-\beta^m\,t}\right), \qquad m = a,\, b \tag{3.15}$$

where β^m and α^m are the rate of rise and decay respectively. As shown in Table 3.1 and Fig. 3.7, the rise and decay rates for each receptor type (a, b, A, N) are quite distinct.

Before defining the postsynaptic fluxes of Eq. (3.14), we simplify the equation set by assuming particular symmetries in the inhibitory fluxes,

$$\Phi_{ii}^{a}(t) = \Phi_{ie}^{a}(t), \qquad \Phi_{ii}^{b}(t) = \Phi_{ie}^{b}(t) \tag{3.16}$$

and similarly for the excitatory fluxes,

$$\Phi_{ei}^{A}(t) = \Phi_{ee}^{A}(t), \qquad \Phi_{ei}^{N}(t) = \Phi_{ee}^{N}(t) \tag{3.17}$$

Invoking these symmetries halves the number of second-order DEs from eight to four.

Taking derivatives (for detailed calculation see Appendix B.1) of all postsynaptic inputs, the excitatory fluxes Φ^A_{ek} and Φ^N_{ek} (units: spikes/s) obey second-order differential equations. Excitatory fluxes are received by the target neural populations k,

$$\left[\frac{d}{dt}+\alpha^A\right]\left[\frac{d}{dt}+\beta^A\right]\Phi^A_{ek}(t)=\alpha^A\beta^A M^A_{ek}(t) \tag{3.18}$$

$$\left[\frac{d}{dt}+\alpha^N\right]\left[\frac{d}{dt}+\beta^N\right]\Phi^N_{ek}(t)=\alpha^N\beta^N M^N_{ek}(t) \tag{3.19}$$

and Φ^a_{ik}, Φ^b_{ik} are inhibitory flux inputs coming from inhibitory populations,

$$\left[\frac{d}{dt}+\alpha^a\right]\left[\frac{d}{dt}+\beta^a\right]\Phi^a_{ik}(t)=\alpha^a\beta^a M^a_{ik}(t) \tag{3.20}$$

$$\left[\frac{d}{dt}+\alpha^b\right]\left[\frac{d}{dt}+\beta^b\right]\Phi^b_{ik}(t)=\alpha^b\beta^b M^b_{ik}(t) \tag{3.21}$$

Reversal function ψ_{lk} is a dimensionless weighting factor which captures the dendritic response sensitivity to reversal potential for all receptors,

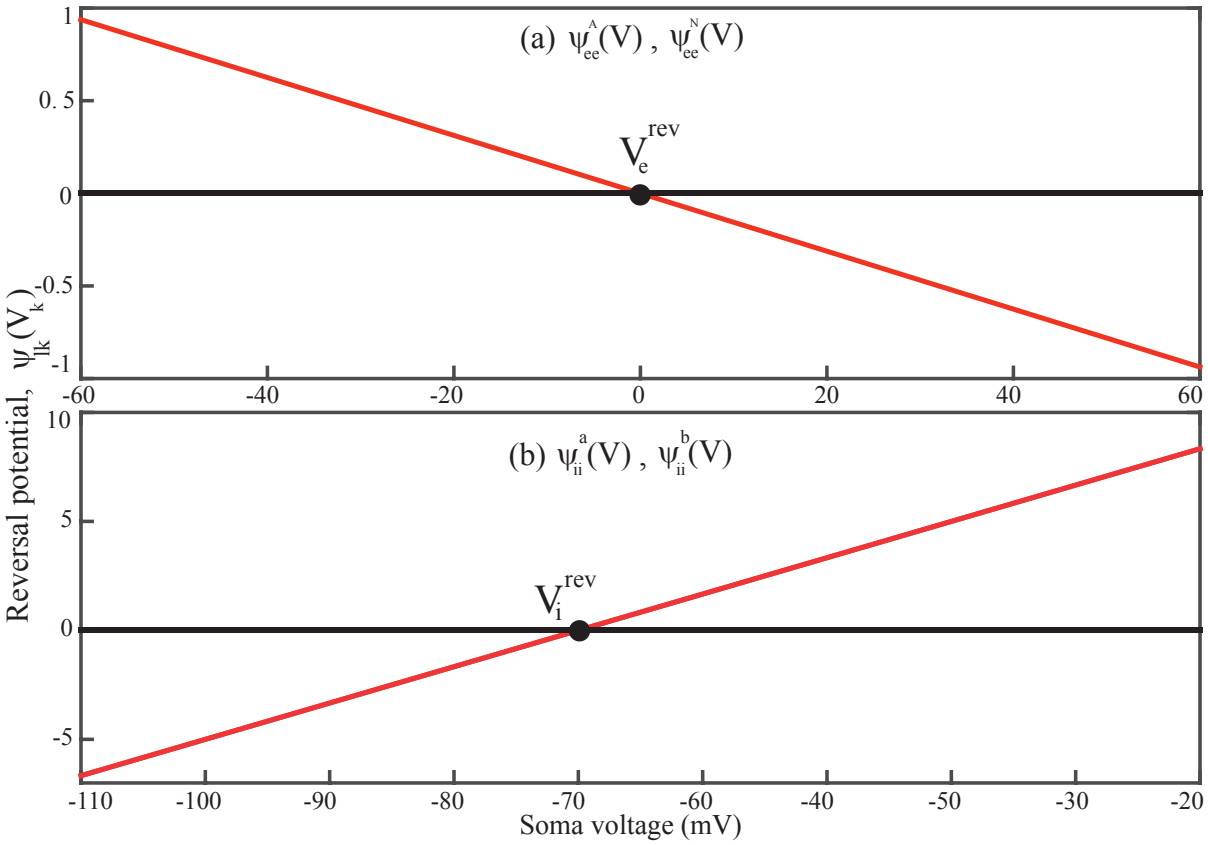

Figure 3.5. Reversal potential functions for (a) excitatory and (b) inhibitory populations defined by Eqs (3.22) and (3.23) respectively.

$$\psi_{ek}^{m}(V_k) = \frac{V_e^{\text{rev},m} - V_k}{V_e^{\text{rev},m} - V_k^{\text{rest}}}, \qquad m = A,\, N \tag{3.22}$$

$$\psi_{ik}^{m}(V_k) = \frac{V_i^{\text{rev},m} - V_k}{V_i^{\text{rev},m} - V_k^{\text{rest}}}, \qquad m = a,\, b \tag{3.23}$$

where V_k^{rest} and V_k^{rev} represent the rest and reversal potentials respectively; a, b denote inhibitory populations GABA_A, GABA_B; A, N denote excitatory populations AMPA, NMDA; see Fig. 3.5.

Soma voltage from chemical synapses is modelled as postsynaptic potentials (PSPs) summing at the neuron somatic capacitor,

$$\begin{aligned} V_k(t) &= (\text{soma resting potential}) + (\text{input perturbation}) \\ &= V_k^{\text{rest}} + (\text{soma impulse response}) \otimes (\text{excitatory and inhibitory voltage inputs}) \\ &= V_k^{\text{rest}} + L_k \otimes [e_k(t) + i_k(t)] \end{aligned} \tag{3.24}$$

where the excitatory and inhibitory voltage inputs are given by,

$$e_k(t) = \rho_e^A \psi_{ek}^A \Phi_{ek}^A(t) + \rho_e^N \psi_{ek}^N \Phi_{ek}^N(t) \tag{3.25}$$

$$i_k(t) = \rho_i^a \psi_{ik}^a \Phi_{ik}^a(t) + \rho_i^b \psi_{ik}^b \Phi_{ik}^b(t) \tag{3.26}$$

The soma response $L_k(t)$ is a single exponential decay with time-constant τ_k (see Fig. 3.6),

$$L_k = \frac{1}{\tau_k} e^{-t/\tau_k} \tag{3.27}$$

where $\tau_k = R_m C$. By taking the derivative (see Appendix B.2) of Eq. (3.24), we obtain:

$$\tau_k \frac{dV_k}{dt} = V_k^{\text{rest}} - V_k(t) + e_k(t) + i_k(t) \tag{3.28}$$

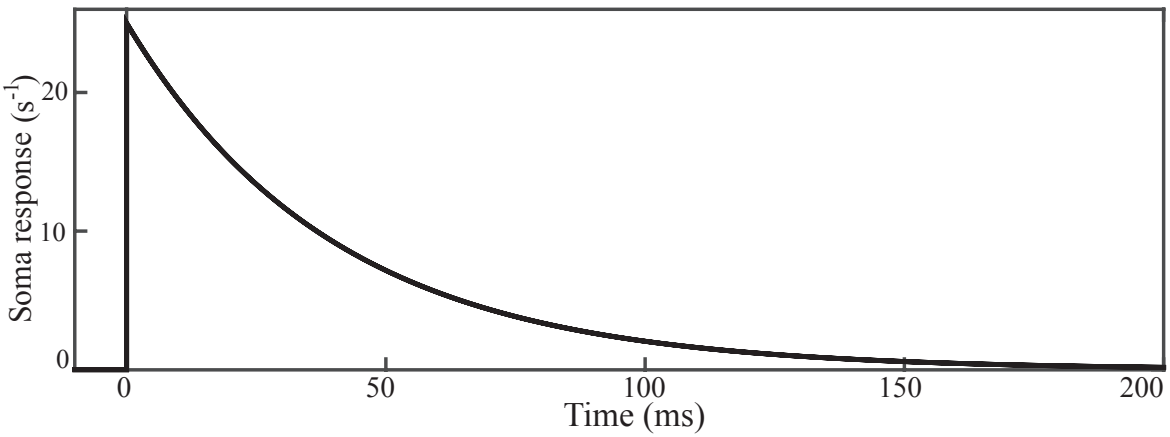

Figure 3.6. Soma impulse response of Eq. (3.27) for cell time-constant $\tau = 40$ ms.

which is similar to Eq. (3.1) for the membrane voltage equation for a single neuron.

Soma voltage from electrical synapses Gap-junctions form resistive linkage between adjacent cells allowing the passage of ions and small molecules (Fig. 1.2).

Table 3.2. Function definitions for the cortical model

Variable	Symbols	Unit	Equation
Firing rate	Q_k	s^{-1}	(3.4)
Soma filter impulse	L_k	s^{-1}	(3.27)
Dendrite filter impulse	H_{lk}	s^{-1}	(3.33)
Reversal potential at dendrite	ψ_{lk}	–	(3.22), (3.23)

The gap-junction diffusive current is modelled as:

$$I_k^{\text{gap}} = \frac{a}{R} \bigtriangledown^2 V_k \tag{3.29}$$

The incorporation of diffusive coupling within an existing mean-field synaptic model of electrocortical activity is based on the microanatomical measurements of Fukada et al with a defined as the area of the Fukuda-cell and R being the gap-junction resistance; more details are in [29, 77, 93]. Including the gap-junction diffusive current, Eq. (3.28) becomes:

$$\frac{\tau_k}{R_m}\frac{\partial V_k}{\partial t} = \frac{V_k^{\text{rest}} - V_k(t)}{R_m} + I_k^{\text{syn}} + I_k^{\text{gap}} \tag{3.30}$$

where $\tau_k/R_m = C$, the membrane capacitance of Figs 3.1 and 3.3. Multiplying both sides by R_m yields:

$$C\frac{\partial V_k}{\partial t} = V_k^{\text{rest}} - V_k(t) + I_k^{\text{syn}} R_m + D_{kk} \bigtriangledown^2 V_k \tag{3.31}$$

The diffusive coupling strength for inhibitory neurons is defined by $D_2 = D_{ii}$, and $D_1 = D_{ee}$ for excitatory diffusive coupling strength, which is much weaker, $D_1 = D_2/100$. Diffusive coupling D_1, D_2 carry units of area [cm^2], so that $D_{1,2}/\tau$ can be regarded as a diffusion constant [cm^2/s].

3.2 Modelling the action of anaesthetic agents

Different categories of anaesthetic agent can affect cortical neurons through different mechanisms. Here, the main focus is modelling the effect of GABAergic and dissociative anaesthetic agents on cortical activity.

3.2.1 Modelling anaesthetic action of GABAergic agent

The intravenous anaesthetic agent propofol (2.6-diisopropylphenol) is a short-acting general anaesthetic widely used for the induction and the maintenance of anaesthesia. Propofol is classified as a GABA-enhancing drug. GABAergic anaesthetics tend to inhibit brain action by increasing the duration of each inhibitory postsynaptic potential, holding the $GABA_A$ chloride channels open longer, thus allowing an increased number of Cl^- ions to diffuse down their concentration gradient into the cell. As a result, the cortical neurons

Table 3.3. Symbol definitions for postsynaptic equations

Symbols	Description	Value	Unit
$\tau_{e,\,i}$	neuron time constant	0.04, 0.04	s
$V^{\text{rev}}_{A,\,N}$	reversal potential at dendrite	0	mV
$V^{\text{rev}}_{a,\,b}$	reversal potential at dendrite	-70	mV
$V^{\text{rest}}_{e,\,i}$	neuron resting potential	-64, -64	mV
ρ^N_e	NMDA excitatory synaptic gain	1.0×10^{-3}	mV s
ρ^A_e	AMPA excitatory synaptic gain	1.0×10^{-3}	mV s
ρ^a_i	$GABA_A$ inhibitory synaptic gain	-1.03×10^{-3}	mV s
ρ^b_i	$GABA_B$ inhibitory synaptic gain	-1.03×10^{-3}	mV s
D_2	$i \longrightarrow i$ gap-junction diffusive coupling strength	$0 - 1.0$	cm^2
D_1	$e \longrightarrow e$ gap-junction diffusive coupling strength	$D_2/100$	cm^2

become hyperpolarized (more negative) and therefore less likely to fire.

Clinical works show that anaesthetic drugs such as propofol tend to enhance the effectiveness of inhibitory synapses, particularly of the fast-action $GABA_A$ and the slow-action $GABA_B$ receptors [8, 56, 58]. $GABA_B$ synapses are less affected by propofol [84], so have been ignored in previous anaesthesia models.

Propofol prolongs $GABA_A$ response by a dimensionless scale factor p_a representing drug concentration, α^a is the decay rate of postsynaptic potential at zero drug concentration; for non-zero drug effect, the decay rate α^a_p is a function of anaesthetic drug:

$$\alpha^a_p = \frac{\alpha^a}{p_a}, \qquad p_a \geq 1 \tag{3.32}$$

Therefore the action of propofol is modelled as a decrease in the decay rate of the $GABA_A$ or a potentiating of the inhibitory synaptic responses

$$\left[\frac{d}{dt} + \alpha^a_p\right]\left[\frac{d}{dt} + \beta\right]\Phi^a_{ik}(t) = \alpha^a_p \beta\; Q_i(t), \qquad p_a \geq 1 \tag{3.33}$$

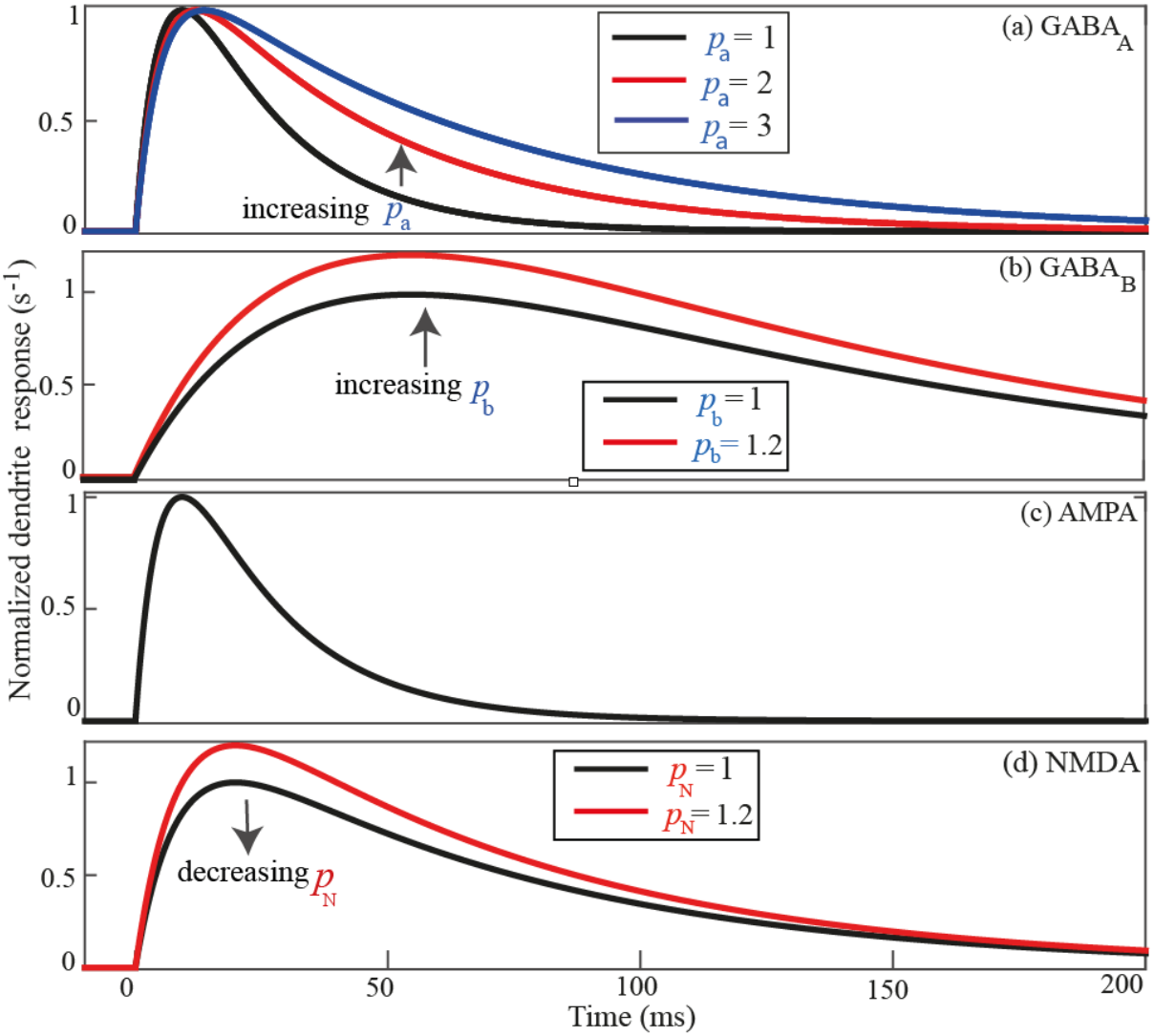

Figure 3.7. Dendrite impulse responses for all four populations in the extended Waikato model. (a) $GABA_A$ response plotted as a function of time; increasing the $GABA_A$ drug concentration p_a prolongs IPSP duration. (b) Gain factor on $GABA_B$ response increases with the $GABA_B$ anaesthetic effect p_b is increased. Panel (c) shows the AMPA response function, which is not affected by anaesthetic agent. Panel (d) indicates drug effect on the gain factor at NMDA receptors.

which contributes to changes of inhibitory fluxes through Eq. (3.34).

For $GABA_B$ receptors, propofol effect is modelled as an increase in IPSP gain [85], obeying $\rho_i^b(p_b) = p_b\, \rho_i^b$; this allows us to control the effectiveness of $GABA_B$ fluxes entering the soma. We highlight the $GABA_A$ and $GABA_B$ contributions to the inhibitory inputs,

$$I_k(t) = \rho_i^a \psi_{ik}^a \underbrace{\Phi_{ik}^a(t)}_{\text{GABA}_\text{A}\text{ effect}} + \underbrace{\rho_i^b(p_b)}_{\text{GABA}_\text{B}\text{ effect}} \psi_{ik}^b \Phi_{ik}^b(t) \tag{3.34}$$

3.2.2 Modelling anaesthetic action of NMDAergic agent

Dissociative agents are a class of anaesthetics that work to antagonize, or inhibit the action of NMDA receptor; the state of anaesthesia they induce is referred to as dissociative anaesthesia, as these agents decrement perceptions of sight and sound and produce feelings of detachment (dissociation) from the environment and self. The most common dissociative drugs are nitrous oxide and ketamine.

Glutamate activates NMDA receptors (slow activation), the slow activation in NMDA is due to the requirement that two agonist molecules glycine and L-glutamate must bind to open the receptor [18, 53, 110]. While L-glutamate is released from specific presynaptic terminals, low concentrations of ambient glycine present at the synapse allow receptor activation.

A unique and significant property of the NMDA receptor channel is its sensitivity to block by physiological concentrations of Mg^{2+} in presynapses [48, 75]. The Mg^{2+} blockage is only cleared when the NMDA receptor channels are sufficiently depolarized, see Fig. 3.8. The conductance of the NMDA receptor is modelled as a sigmoid function of voltage and magnesium concentration [49, 50],

$$g(V) = 1/(1 + e^{(a\,(V-\theta)\,C)}) \tag{3.35}$$

where V is the cell voltage (mV), C is the magnesium concentration (mM), a is a coefficient that changes depending on the magnesium concentration, and θ is the mid-point voltage threshold.

As shown in Fig. 3.8, decreases in extracellular magnesium shift the conductance function to the left of the graph, which corresponds to lower voltage threshold. For all concentrations, the magnesium blockade is cleared at voltages more positive than about +50 mV.

In Fig. 3.9(a), the NMDA gating function $g(V)$ is plotted for four concentrations of magnesium $C = [1, 3, 10, 50]$ mM for an assumed threshold $\theta = 0$ mV. The gating functions become less steep with decreasing magnesium concentration; Fig. 3.8(b) illustrates the gate function as a function of membrane voltage for a setting of voltage threshold $\theta = [-60, -50, -40, 0]$ mV at fixed Mg^{2+} concentration $C = 3.7$ mM. It can be seen that decreasing voltage threshold moves the curves to the left.

The theoretical NMDA conductance function that we will apply for our NMDA modelling obeys the following equation,

$$g(V) = 1/(1 + e^{(-0.062(V+60))}) \tag{3.36}$$

where $aC = -0.062$ mV^{-1} corresponds to a range of drug concentration between 1 and 10 mM; see Fig. 3.8. In Fig. 3.9(c), the gating function g is plotted as a function of

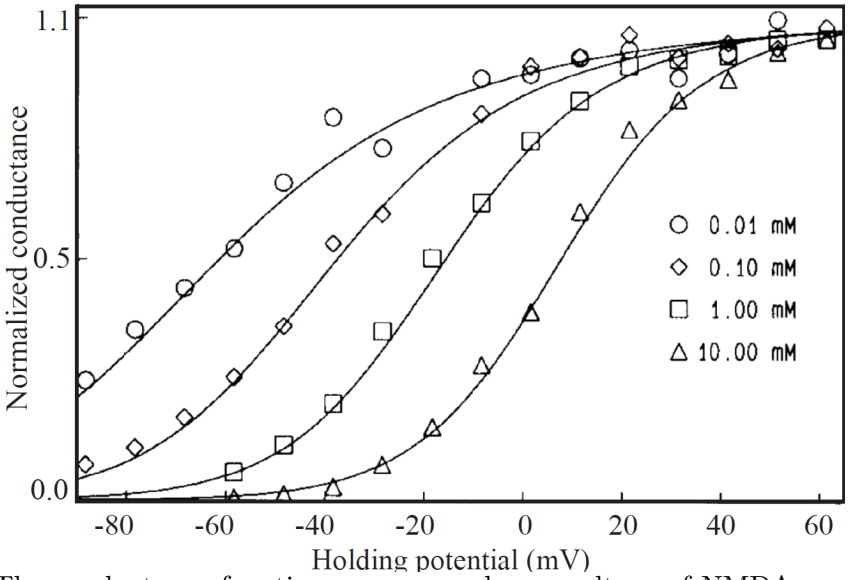

Figure 3.8. The conductance function versus membrane voltage of NMDA receptors for four magnesium concentrations $C = [0.01, 0.1, 1, 10]$ mM. Current amplitudes from the cell converted to conductance, assuming a reversal potential of 0 mV, normalized to maximum conductance, and plotted against holding potential. The data are fitted with curves generated from the gating function derived from Eq. (3.35), from [50]. The conductance versus voltage families shift to the right in an orderly fashion with increasing external magnesium.

voltage.

Dissociative anaesthetics are thought to reduce the effectiveness of NMDA postsynptic event by limiting the influx of sodium ions and consequently lowering the overall level of excitation of the postsynaptic cell [14].

To apply this hypothesis in the Waikato model, the effectiveness of NMDA receptors is altered through the following definition:

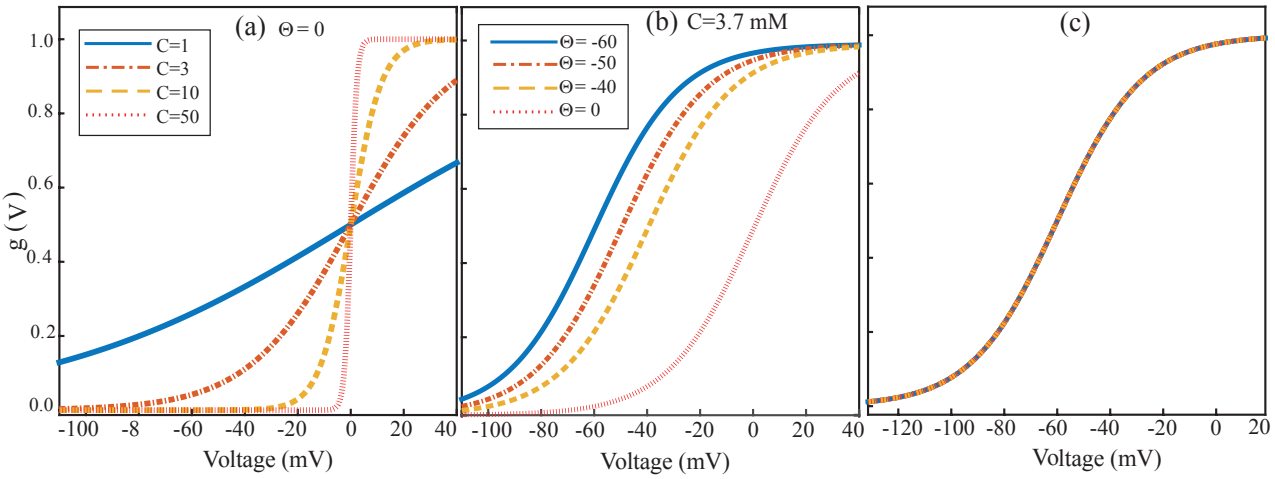

Figure 3.9. The conductance g of NMDA is plotted as a function of voltage for the whole cell (a) for a set of magnesium concentrations $C = [1, 3, 10, 50]$ mM, and (b) for a set of voltage thresholds $\theta = [-60, -50, -40, 0]$ mV. (c) Theoretical conductance function (3.36) for our NMDA modelling.

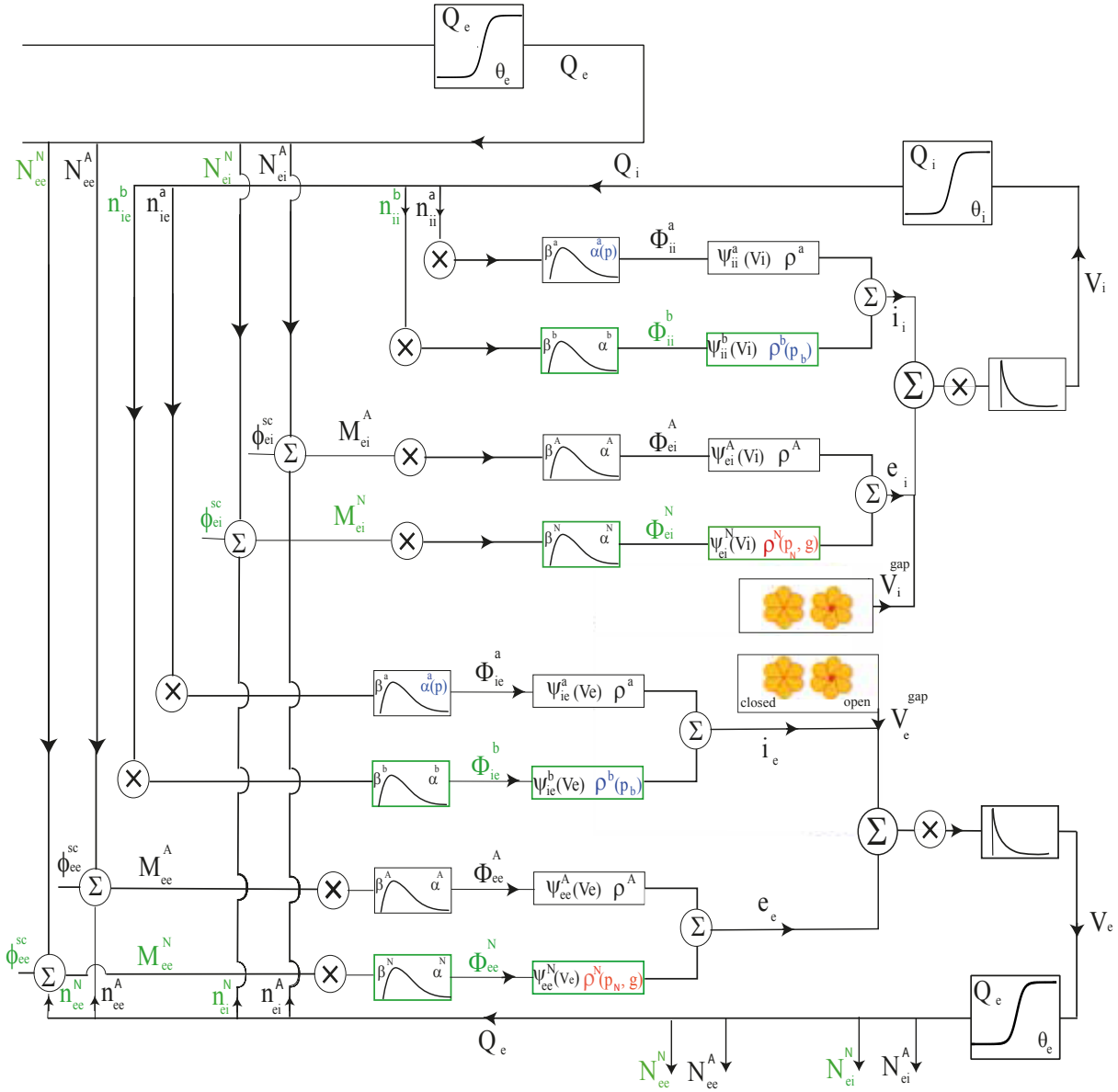

Figure 3.10. The cerebral cortex is pictured as a continuum of macrocolumns interconnected via their excitatory sigmoid outputs. The inter-macrocolumn communication is governed by wave equations to include propagation delay effects. In addition, the entire macrocolumn mass is buffeted by ϕ^{sc}_{ek} exogenous inputs coming up from excitatory sources in the subcortex. All inputs (local, distant, and external) are combined at the summing points to determine the M_{lk} presynaptic inputs. The resulting chemical and electrical synaptic currents are integrated at the soma capacitor to give a soma voltage V_k $(k = e, i)$. The green boxes indicate the extensions to the standard Waikato model, the blue and red text highlight the cooperation of GABAergic and NMDAergic contributions. The Σ summation symbol indicates the integration of all fluxes entering the soma RC compartment of Fig 3.3.

$$E_k(t) = \rho^A_e \psi^A_{ek} \Phi^A_{ek}(t) + \rho^N_e \psi^N_{ek} \Phi^N_{ek}(t) \tag{3.37}$$

$$\rho^N_e(p_N) = \rho^N_e p_N \, g(V), \qquad p_N \geqslant 1 \tag{3.38}$$

where p_N is the drug effect in NMDA receptors. To increase the effect of dissociative drug in the model, we decrease the effectiveness of NMDA receptors p_N.

Figure 3.10 summarizes the cortical connectivities for the Waikato model.

3.3 Results

In the current study, we present the anaesthetized model dynamical behaviour due to alteration of $GABA_A$, $GABA_B$ and NMDA receptor effectiveness. The effect of Cx36 gap junction blockade during anaesthesia is also investigated.

Before exploring the full two-dimensional behaviour due to anaesthetic effect, it is useful to calculate the homogeneous steady states of the model. To locate the steady states, all temporal and spatial derivatives are set to zero, and the noise source ϕ_{ek}^{sc} is removed. Then, the steady-state membrane voltage and firing rates for both the inhibitory and excitatory neural populations are computed numerically as a function of the anaesthetic effect p_a. Here, it is important to emphasize that the all steady-state manifolds illustrated in the current chapter are completely independent of the D_2 inhibitory and D_1 excitatory diffusion coefficients, as their Laplacian operators ∇^2 have been zeroed.

We focus attention in the vicinity of a general anaesthetic phase transition where the equilibrium trajectory displays multiple steady states: an awake "top state", and an anaesthetized "bottom state", separated by an unstable intermediate "mid state".

A linear stability analysis is performed through linearisation of voltages about the equilibrium state at the fixed anaesthetic drug effect p_a, where the awake state of the cortex is close to a critical point (loses the stability).

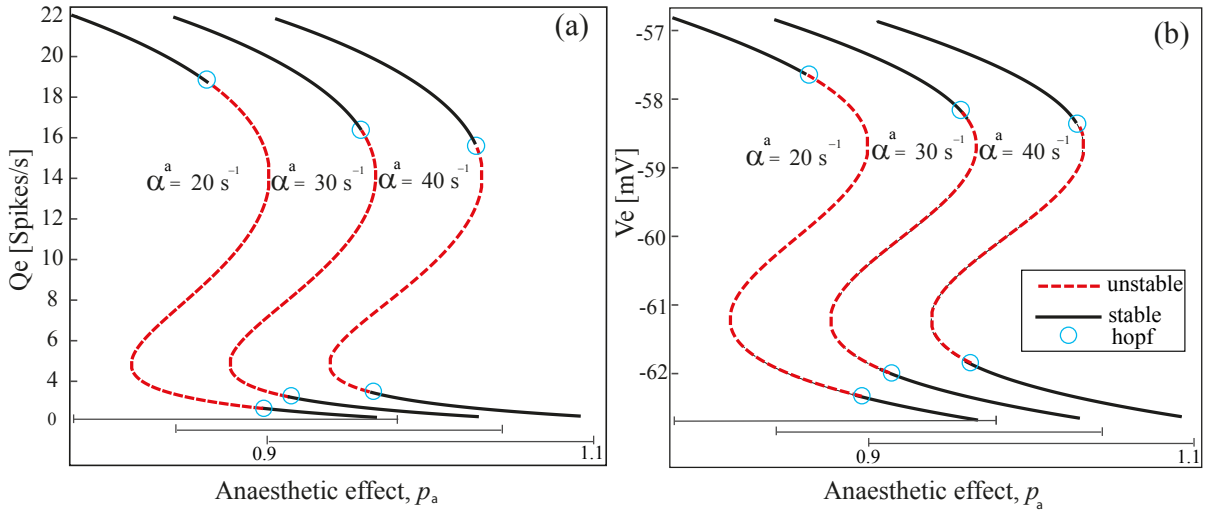

Figure 3.11. $GABA_A$ effect on distribution and stability of cortical equilibrium states expressed as (a) excitatory firing rate Q_e, and (b) excitatory membrane voltage V_e. Anaesthetic drug effect is varied over the range $0 \leqslant p_a \leqslant 1.1$ as indicated by horizontal scale bars. Region of instability (dashed red lines) increases as the background $GABA_A$ decay-rate α^a is stepped to lower values. V_e and Q_e are linked through the sigmoid mapping of Eq. (3.7).Steady states were found using `fzero` in Matlab; stability was assessed from linear eigenvalue analysis.

3.3.1 Numerical considerations

In the homogeneous limit, the cortical Eqs (3.3, 3.18 and 3.31) are equivalent to 12 first-order differential equations (DEs). The stochastic DEs were integrated using a forward-time, centred-space (FTCS) Euler-Maruyama [39] algorithm custom-written in MATLAB with time step mostly $\Delta t = 0.1$ ms. In all 2D numerical simulations, the cortex is a square grid of side-length 25 cm which is joined at the edges to give toroidal boundaries. All state variables were initialized at their homogeneous steady state values. The time step was set sufficiently small that the dominant spatial feature advanced by less than the spacing between adjacent grid points in time, thereby ensuring numerical stability. For example the large diffusive coupling and fine spatial resolution mandate a very small time step in order to ensure numerical stability.

3.3.2 $GABA_A$ and the extended Waikato model

Steady state distribution

To include GABAergic anaesthetic effect on $GABA_A$ receptors, the decay rate of $GABA_A$ response function is assumed to be the main target via Eq. (3.33). Decay-rate alterations control $GABA_A$-mediated postsynaptic charge transfer. To explore the effect on the cortex stability, the distribution of equilibrium states of membrane voltages V_e^0 and firing rates Q_e^0 of the excitatory neural population are plotted as a function of anaesthetic drug p_a for three inhibitory rate constants $\alpha^a = [20, 30, 40]$ s^{-1}.

As shown in Fig. 3.11, reducing the α^a decay rate of $GABA_A$ response increases the region of instability in the cortex.

Linear stability analysis

To predict the dynamical behaviour of the cortex about the awake state equilibrium, the LSA calculations are performed in the presence of weak inhibitory diffusion $D_2 = 0.2$ cm^2, for different decay-rates. Fig. 3.12 illustrates representative dispersion curves, plotted as a function of scaled wave number $q/2\pi$, corresponding to a fixed value of anaesthetic drug effect $p_a = 1.0$. Three settings of $GABA_A$ decay rate $\alpha^a = [20, 25, 30]$ s^{-1} are selected. Although the homogeneous cortex has access to three steady states, only the top- and bottom-branch dispersion curves are plotted since the mid-branch is always unstable state and the brain can never switch to that state. As the rate of decay decreases, a temporal (Hopf) mode develops in both branches, but no spatial (Turing) mode is predicted. In Fig. 3.13, the linear stability prediction of low frequency temporal oscillations is tested in the cortical model through fully nonlinear grid simulations. It is important to mention that in this thesis, the terms Hopf and Turing instability respectively refer to the regions in which linear stability analysis predicts a dominant eigenvalue with a positive real part

and a non-zero imaginary part (Hopf) or a positive real part, zero imaginary part and a non-zero wavenumber (Turing).

GABA$_A$ numerical simulations

To confirm the dispersion prediction several simulations were run. Scanning Fig. 3.13 from top to bottom, one can observe that the pattern of cortical dynamics is very sensitive to to the value of GABA$_A$ decay rate: for small decay rates $\alpha^a \leq 20$ s^{-1}, the Hopf instability drives large-scale ∼1 Hz oscillations which are highly synchronized. For an intermediate range $20 \leq \alpha^a \leq 25$ s^{-1}, the oscillations become slower and less synchronized. For $\alpha^a \geq 27$ s^{-1}, these oscillations become weaker and finally disappear.

Figure 3.14 shows bird's-eye snapshots of the evolution of spontaneous pattern formations in excitatory firing rates at ∼2 s intervals (left to right) for step increases in the

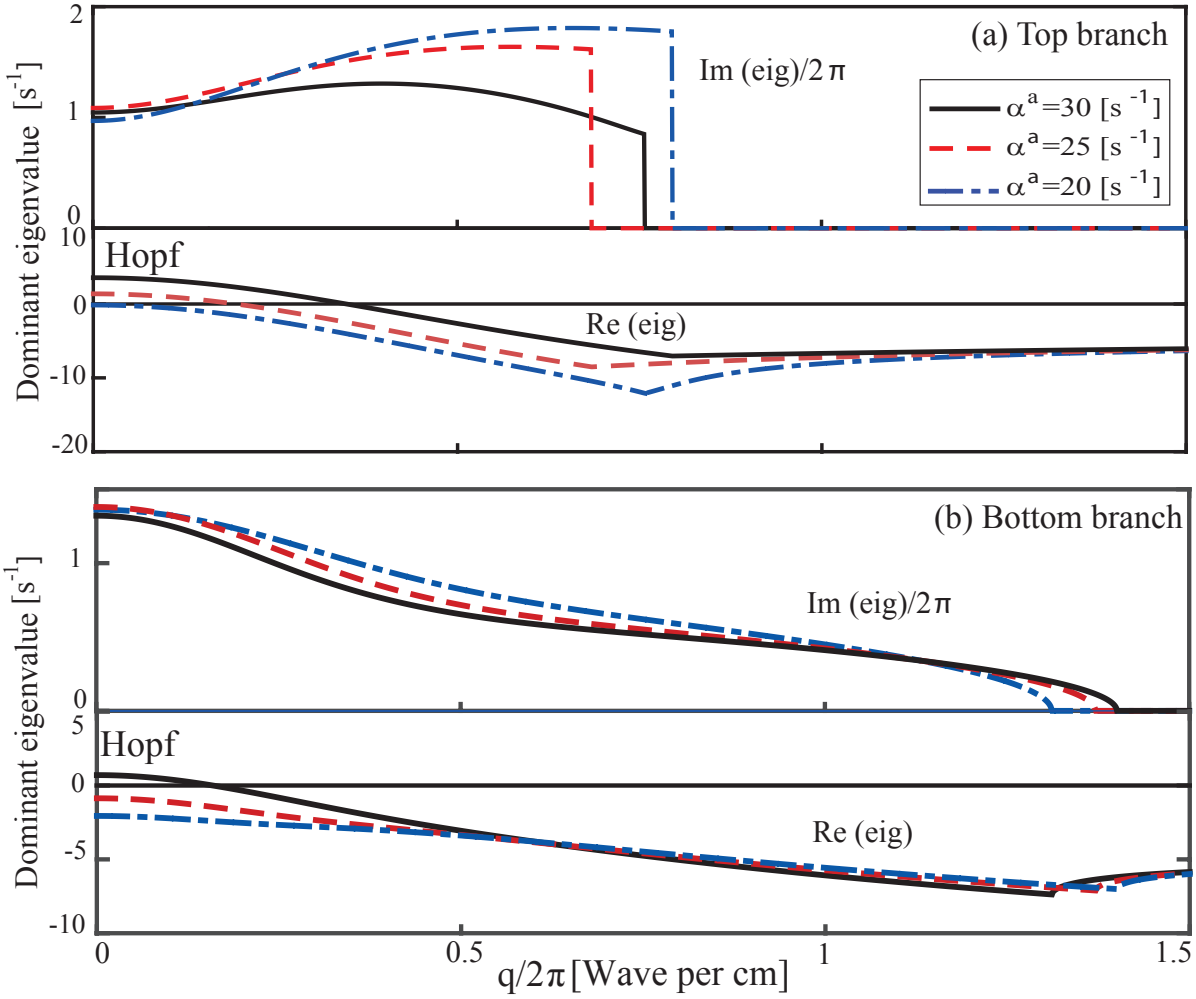

Figure 3.12. Eigenvalue distribution curves with respect to various α^a at fixed inhibitory diffusion $D_2 = 0.2$ cm^2. Predicted dispersion curves for spatially homogeneous cortex for (a) top-branch, (b) bottom-branch at $p_a = 1.0$ for selected inhibitory GABA$_A$ decay rate values $\alpha^a = [20, 25, 30]$ s^{-1}. In each panel the top traces show oscillation frequency (in Hz) and the lower traces indicate the real part of the dominant eigenvalue, Re(eig), as a function of scaled wave number $q/2\pi$.

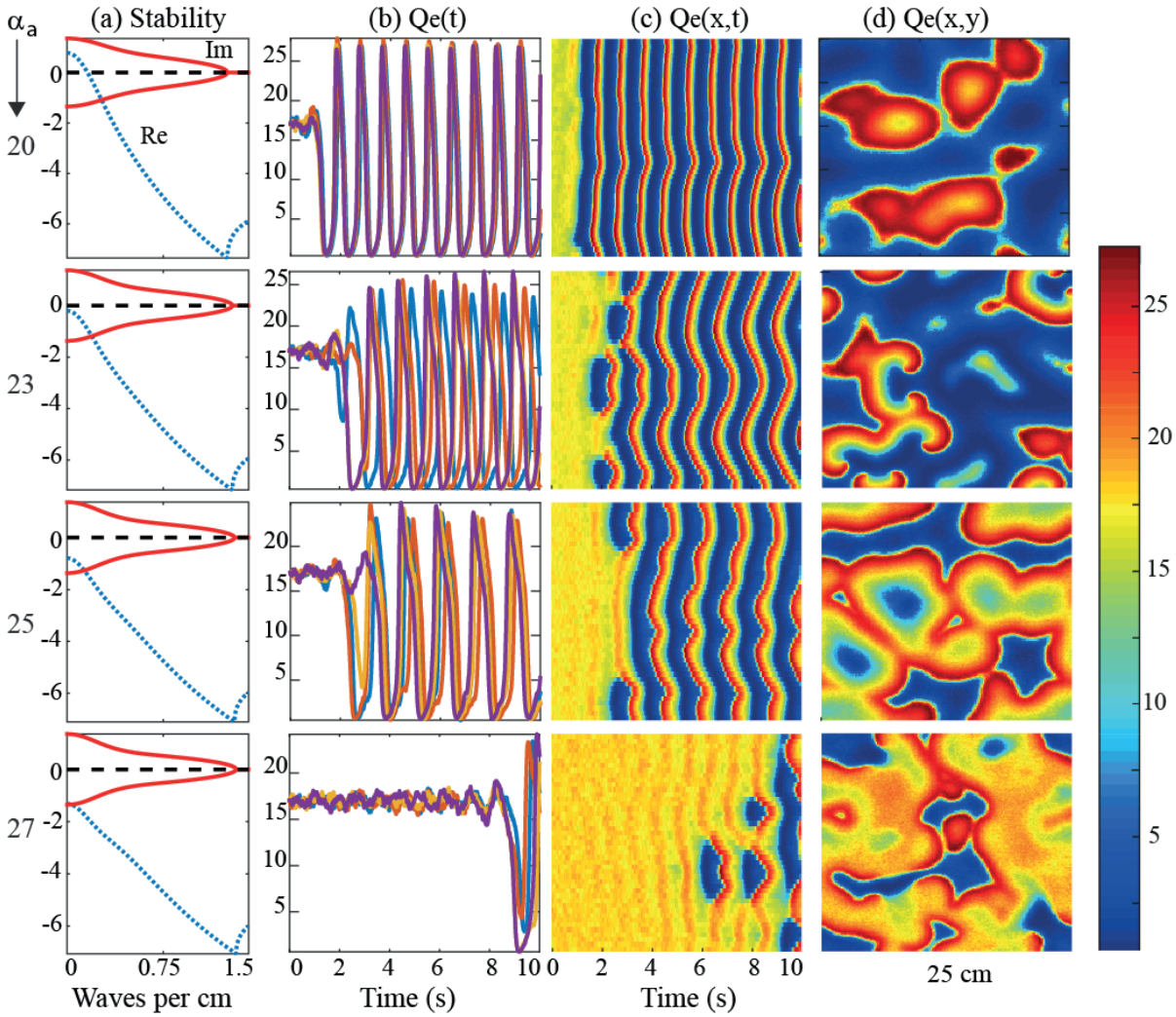

Figure 3.13. Grid simulations of the cortical model launching from the top branch for a set of $GABA_A$ inhibitory decay-rates $\alpha^a = [20, 23, 25, 27]$ s^{-1} with a fixed $GABA_B$ effect of $p_b = 25\%$. In the dispersion curves (first column), solid-red and dashed-blue curves are respective real and imaginary parts of the dominant eigenvalues in the up branch. The second column is the time-series of five points along the centred-vertical line (y=90) of the 180×180 grid. The third column is the 10-s space-time stripchart extracted from the centred-vertical axis of the simulated cortex with a side length 25 cm and a 180×180 grid; time step was $\Delta t = 10^{-4}$ s. Grid was continuously stimulated by low-intensity spatio-temporal white noise. The fourth column is a snapshot of the grid activity at final time step.

α^a $GABA_A$ decay rates (top to bottom), presented as a 5×5 gallery. Model parameters match these used for Fig. 3.13.

The seizure promoting impact of gap-junction closure due to $GABA_A$ergic anaesthetic agent was reported by Steyn-Ross et al. [92]. In the following sections, we investigate the effect of gap-junction closure on seizure activity while simultaneously altering the cooperation of $GABA_B$ergic and NMDAergic anaesthetic agents.

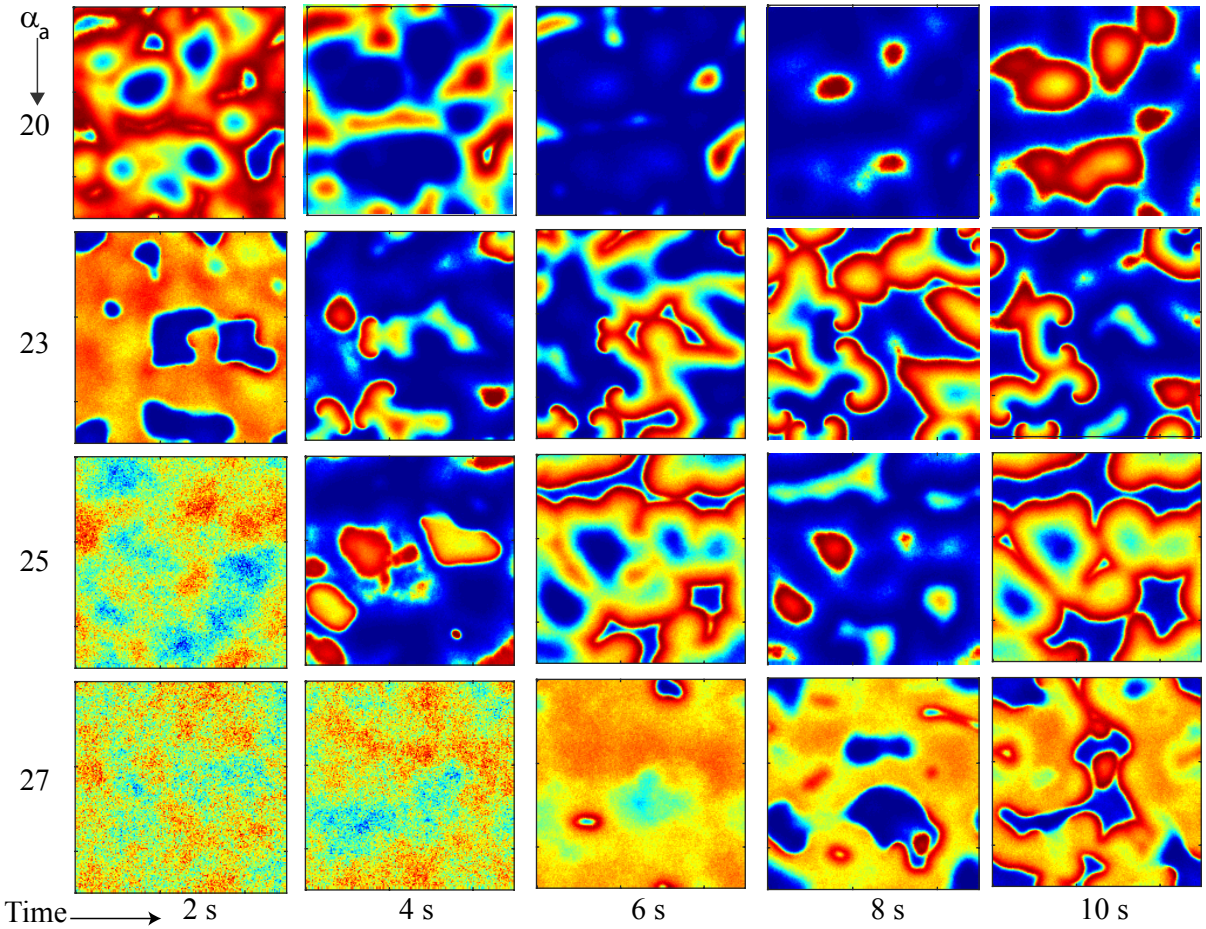

Figure 3.14. Evolution of firing activity for stepped values of α^a $GABA_A$ decay rate (vertical axis). Cortical sheet is initialised at the homogeneous steady state stimulate by subcortical white noise. Colour indicates the activation of cortical tissue: red, high firing activated and blue low firing suppression; see Fig. 3.13 for colour bar.

3.3.3 $GABA_B$ and the extended Waikato model

Cortical steady states and $GABA_B$ effect

We now investigate the effect of $GABA_B$ activation (enhancement) with $GABA_A$ decay-rate fixed at $\alpha^a = 25\ s^{-1}$, and other parameters set to the default values listed in Tables 3.1 and 3.3).

Figures 3.15(a) and (b) graph the distribution of Q_e^0 and V_e^0 equilibrium values as a function of the anaesthetic drug p_a for three $GABA_B$ gain factors, $p_b = [15\%, 25\%, 35\%]$. In each trajectory, a multi-state region is observed for a specific range of anaesthetic drug p_a. Increasing the $GABA_B$ gain factor decreases excitation of the cortex and shifts the steady state trajectories to the left, while increasing the region of instability in both upper and bottom branches.

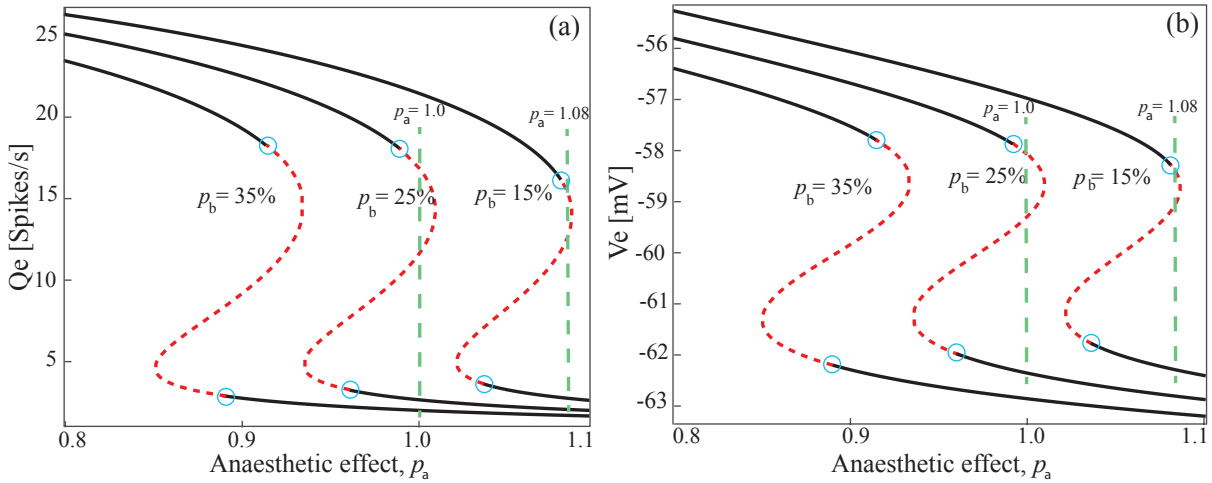

Figure 3.15. $GABA_B$ effect on steady states distribution. As shown in panel (a) increasing the $GABA_B$ effect enhances the unstable regions for the steady state trajectories for the excitatory cortical populations. Panel (b) shows the corresponding voltage membrane V_e to the firing rate presented in (a), see Fig. 3.11 for more details.

$GABA_B$ linear stability analysis

To investigate the $GABA_B$ effect on the dynamical behaviour of the cortex at the equilibrium state, a linear stability analysis is performed and compared for two $GABA_B$ settings: $p_b = 15\%$ and 25%; simultaneously the gap-junction diffusion effect on the extended Waikato model is tested.

To have a reliable comparison between dispersion curve predictions of these $GABA_B$ settings, it is desirable to have similar instability conditions on the upper branch. At the chosen drug effects $p_a = 1.08$ ($p_b = 15\%$) and $p_a = 1.0$ ($p_b = 25\%$), the homogeneous cortex has access to three steady states, see Fig. 3.15. We present dispersion curves for the top branch only (we did not observe significant sensitivity to $GABA_B$ on the bottom branch). Figure 3.16(a) and (b) show dispersion curves plotted for $p_b = 15\%$ and 25% respectively. Each panel is divided into the upper and lower parts present the imaginary ($\pm\omega$) and real parts (α) of the leading eigenvalue $\Lambda_{\text{dom}} = \alpha \pm i\omega$ respectively (the non-dominant eigenvalues have more negative real parts, therefore make a negligible contribution to cortical stability). In each panel four settings of gap-junction diffusion are plotted: $(D_1, D_2)/\text{cm}^2 = (0.003, 0.3)$; (0.004, 0.4); (0.005, 0.5); (0.006, 0.6).

As shown in Fig. 3.16, the dispersion curves predict a Hopf instability for all gap-junction values: at $q = 0$ (infinite wavelength) the real part of the leading eigenvalues are positive with $\omega \simeq 1$ Hz. A Turing instability appears at the highest diffusion setting $D_2 = 0.6$ cm^2 for both $GABA_B$ values. In the case of $p_b = 15\%$, a Turing instability is predicted at $q/2\pi = 0.3$ cm^{-1} ($\lambda = 3.33$ cm); while for $p_b = 25\%$, the instability develops at $q/2\pi = 0.44$ cm^{-1}, corresponding to wavelength $\lambda = 2.27$ cm. These results indicate a stronger Turing instability with a bigger wavelength for the lower $GABA_B$ effect.

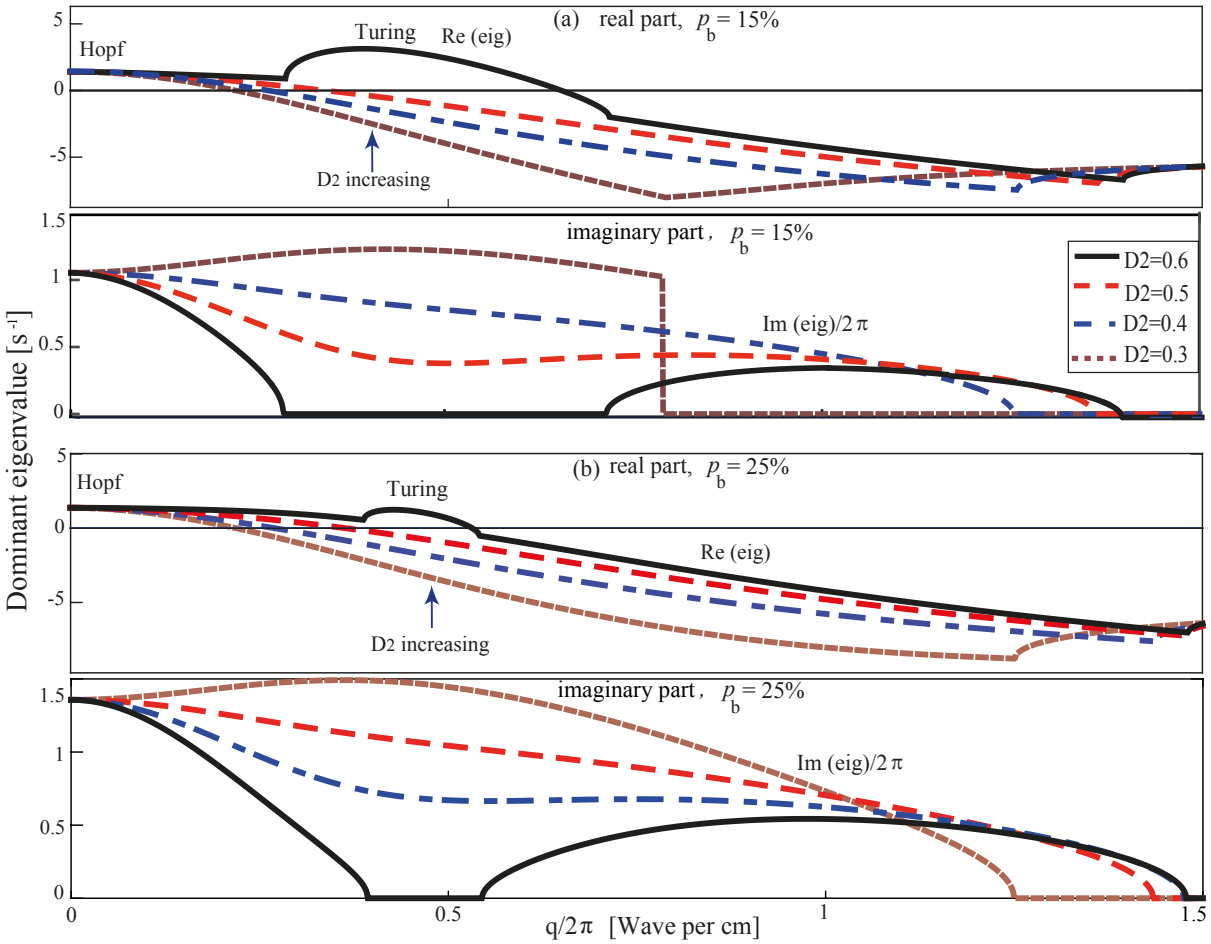

Figure 3.16. $GABA_B$ effect and model dispersion curves. Linear stability predictions are illustrated for the top branch of homogeneous cortical system for (a) $p_b = 15\%$ and (b) $p_b = 25\%$. In each panel the lower boxes show the real part of the dominant eigenvalue, Re(eig), as a function of wave number $q/2\pi$; the upper traces indicate oscillation frequency (in Hz), $\omega = \text{Im(eig)}/2\pi$. The Turing instability near 0.35 wave/cm (for $D_2 = 0.6$ cm^2) is considerably weakened when $GABA_B$ effect is boosted from $p_b = 15\%$ to 25%.

LSA predicts both Hopf and Turing instabilities on the upper branch for the strong diffusion effect $D_2 > 0.5$ cm^2. Increasing $GABA_B$ unbalance the spatial mode (Turing) in favour of the temporal mode (Hopf) on the top branch; for $p_b > 25\%$, the Turing instability vanishes.

$GABA_B$ numerical simulations

The linear stability predictions of Fig. 3.15 indicate that increases in $GABA_B$ enhance instability, with the cortex becoming destabilized for a wider range of anaesthetic drug. And Fig. 3.16 shows that increasing the $GABA_B$ effect and closing gap junction unbalances the spatial mode (Turing) in favour of the temporal mode (Hopf), allowing a seizure oscillation to develop.

To test these predictions, a series of grid simulations of the full nonlinear cortical equations was ran. Firing rates and soma voltages are initialized to the steady-state

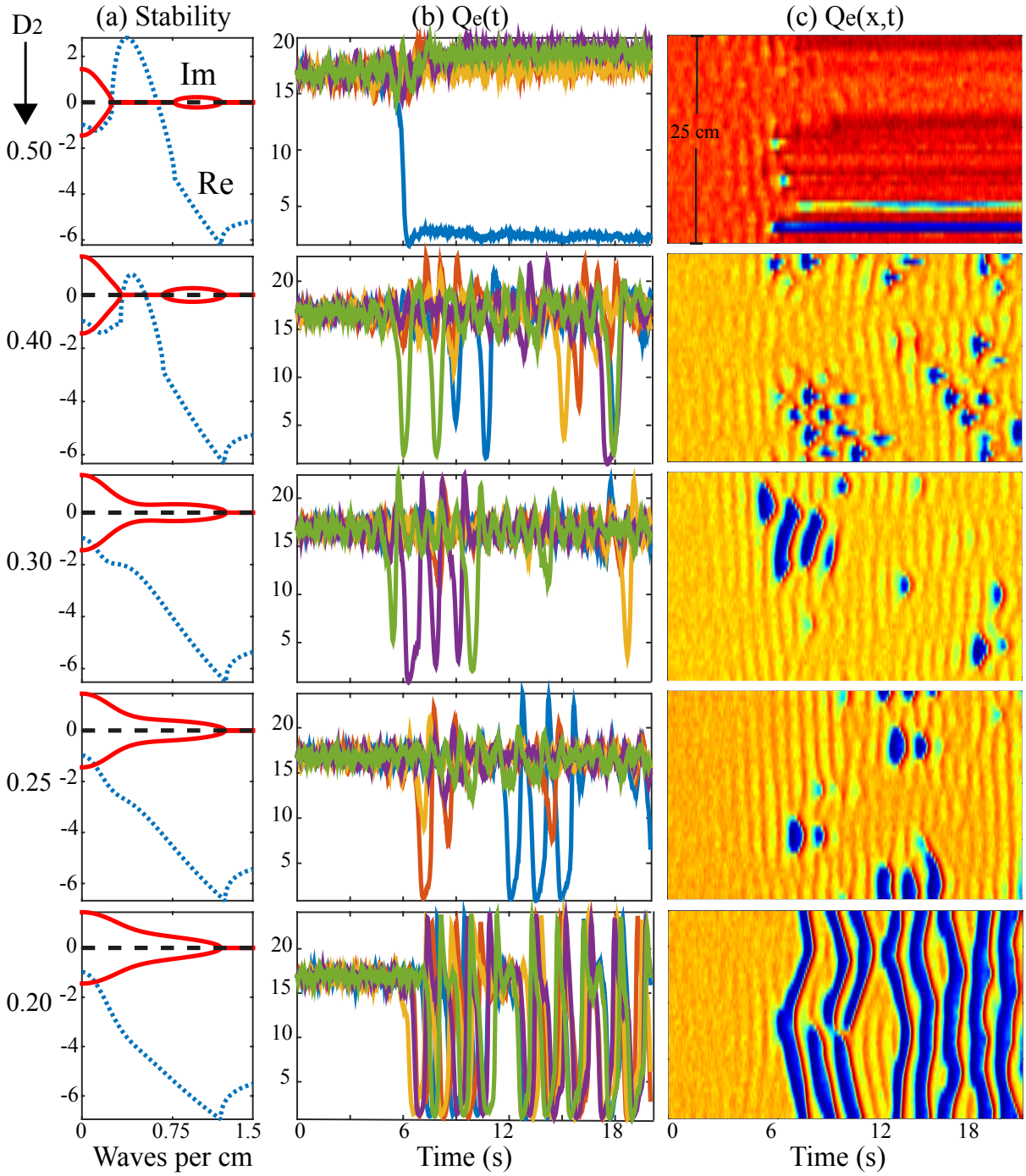

Figure 3.17. Effect of inhibitory diffusion on "awake" cortex with $GABA_B$ effect $p_b = 15\%$ and $GABA_A$ decay rate $\alpha^a = 25\ s^{-1}$. (a) Dispersion curve for equilibrium top branch (solid-red and dashed-blue curves are real and imaginary parts of dominant eigenvalue); (b) time-series for excitatory firing rate $Q_e(t)$ of five points along the centred-vertical line (y=90)of the 180×180 grid; (c) $Q_e(t, x)$ space-time strip-charts of activity along the midline. For $D_2 = 0.5\ cm^2$ (top row), a stationary Turing pattern emerges; smaller diffusion values lead to oscillating patterns of firing activity (see Fig. 3.19 for time-evolution snapshots).

values on the top branch. All grid points are then perturbed continuously by random subcortical white noise, and the subsequent evolution of the cortical sheet is traced for

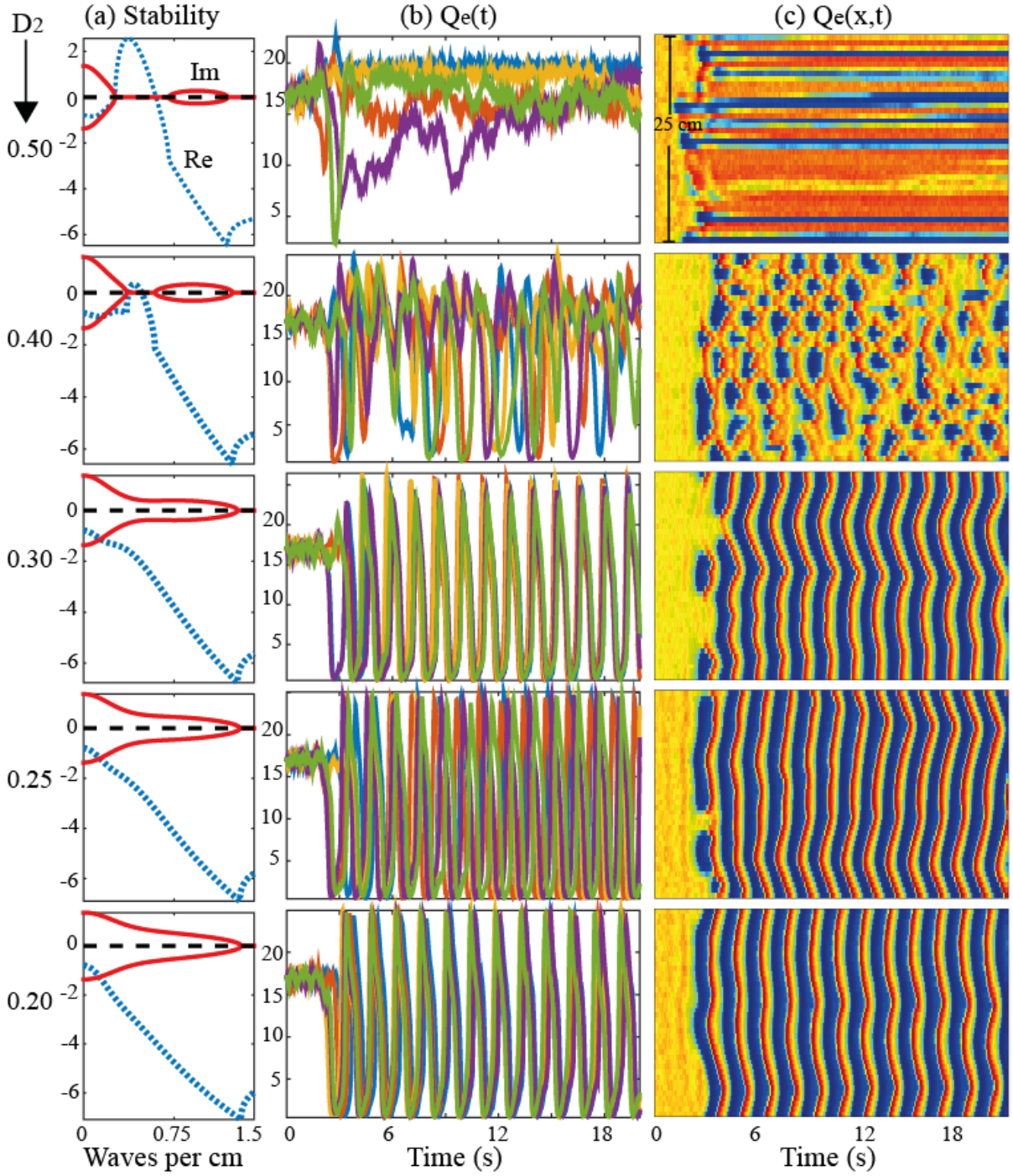

Figure 3.18. Effect of inhibitory diffusion on "awake" cortex with $GABA_B$ effect $p_b = 25\%$. (See Fig. 3.17 caption for further details, and Fig. 3.19 for time-evolution gallery.)

a total time of 20 s with grid resolution of 2.7 mm and time step of 0.1 ms. Each full-resolution 20 s run required almost 2 h. Here, the pattern dynamics of the cortex for two $GABA_B$ gain factors are investigated. Figures 3.17 and 3.18 illustrate the dynamical effect of the reduction in inhibitory diffusion on pattern formation on the "awake" state of the cortex for $p_b = 15\%$ and 25% respectively. Each figure contains five rows corresponding to five values of gap-junction strength. There are three columns: the first column indicates the dispersion curves for the dominant eigenvalue; the second shows a 20-s time-series of

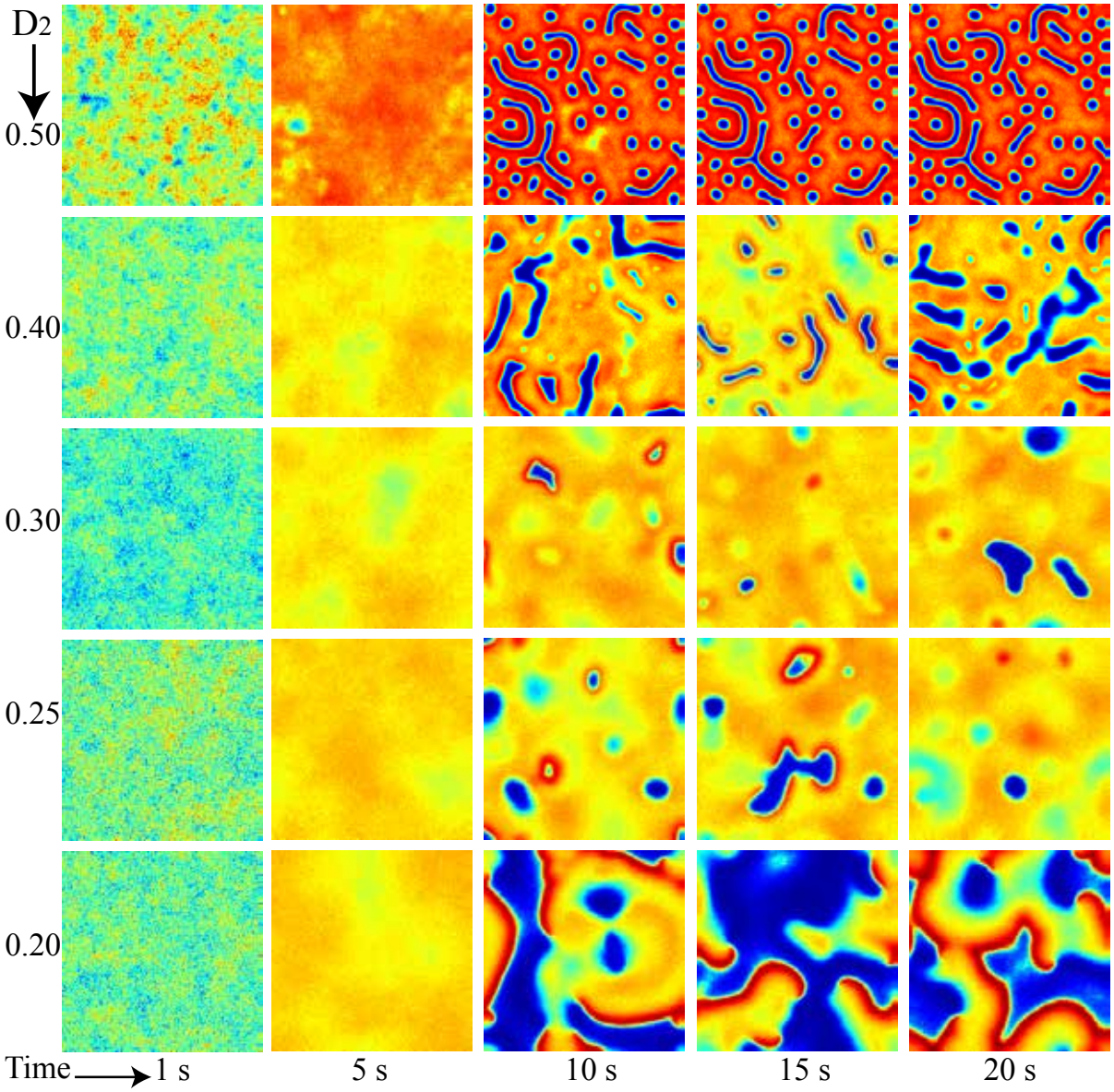

Figure 3.19. Evolution of $Q_e(x, y)$ firing pattern ($GABA_B$ effect $p_b = 15\%$, $GABA_B$ decay-rate $\alpha^a = 25\ s^{-1}$) for Fig. 3.17. The five rows correspond to five values of inhibitory diffusion D_2. Only the top row evolves to a stationary Turing pattern. Colour indicates level of activation: red, high firing; blue, low firing.

five grid points along the vertical midline $y = 90$ of the of the 180×180 grid; the third column is the corresponding space-time strip-chart extracted from the centred-vertical axis.

Scanning Figs. 3.17 and 3.18 from top to bottom shows that stability and the cortical pattern are strongly sensitive to changes in inhibitory diffusion strength D_2. Moreover, changes in $GABA_B$ setting create different dynamical characteristics in the cortical model for each D_2. As shown in Fig. 3.17 in the presence of $p_b = 15\%$, for strong diffusion $D_2 = 0.5\ cm^2$, the Turing instability dominates to form a Turing pattern which is frozen in space with no temporal oscillation. For intermediate inhibitory diffusions $0.2 < D_2/cm^2 < 0.5$, a strong competition between spatial (Turing) and temporal (Hopf) modes is observed,

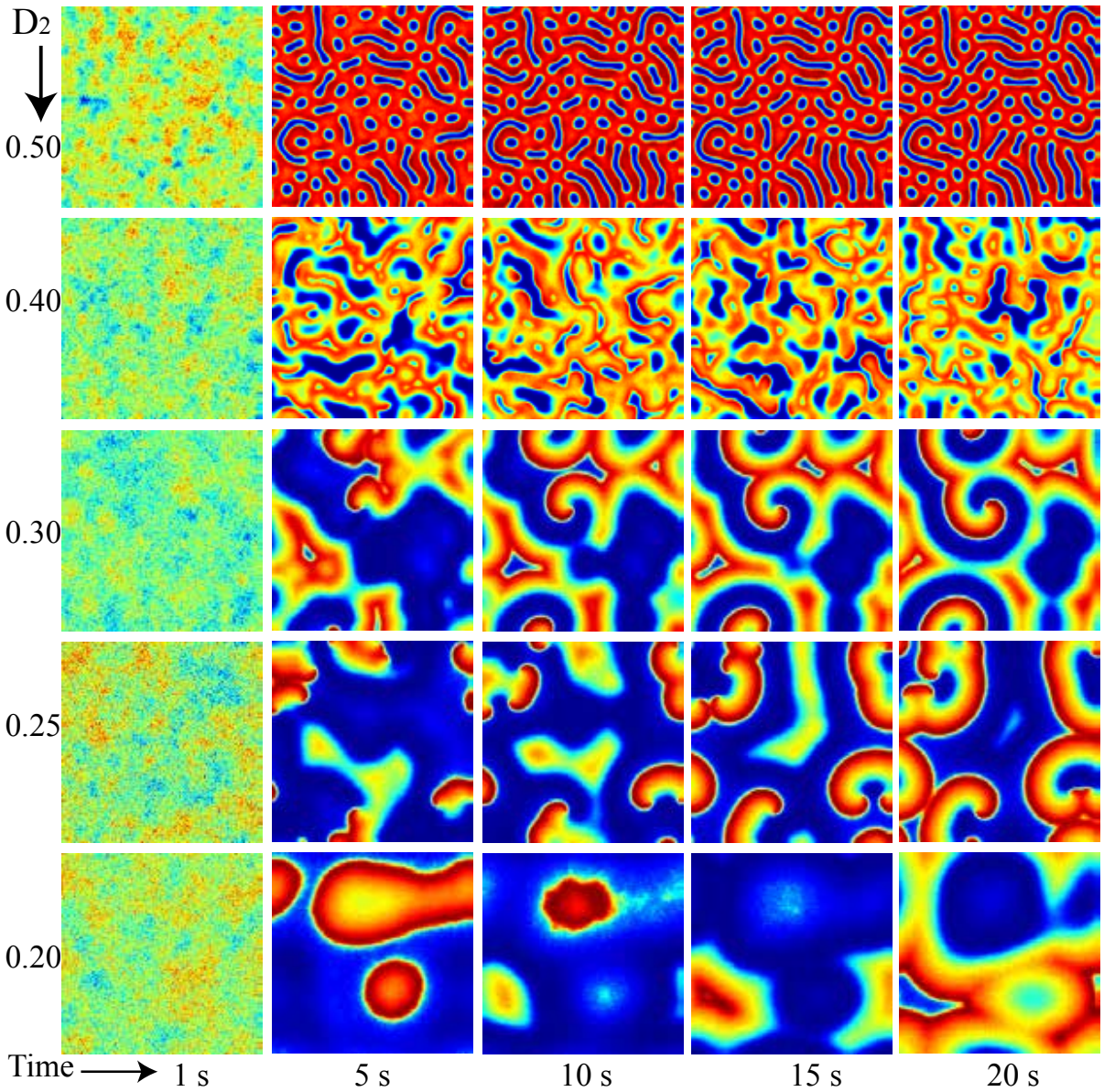

Figure 3.20. Evolution of $Q_e(x, y)$ firing patterns ($p_b = 25\%$, $\alpha^a = 25\ \mathrm{s}^{-1}$) for Fig. 3.18. (See Fig.3.19 caption for other details.)

resulting in a chaotic spatiotemporal pattern with irregular oscillations between up and down states; for weak diffusions $D_2 \leq 0.2\ \mathrm{cm}^2$, the temporal instability dominate to drive large, slow oscillations.

For the greater $\mathrm{GABA_B}$ effect of $p_b = 25\%$ in Fig. 3.18, closing gap junctions unbalances the spatial mode earlier, allowing seizure oscillations to develop at weaker gap-junction connectivity. For intermediate inhibitory diffusions $0.2 < D_2/\mathrm{cm}^2 < 0.5$, while $p_b = 15\%$ creates chaotic dynamics, $p_b = 25\%$ develops mostly temporal instabilities and for the weak diffusion $D_2 \leq 0.2$, the greater $\mathrm{GABA_B}$ gain factor develops a fully synchronized oscillation. Therefore, one can conclude that for both $\mathrm{GABA_B}$ settings the resulting patterns are an interaction between Turing and Hopf. Increasing $\mathrm{GABA_B}$ tends to destabilize the stationary Turing structure in favour of large-scale oscillations. This prediction

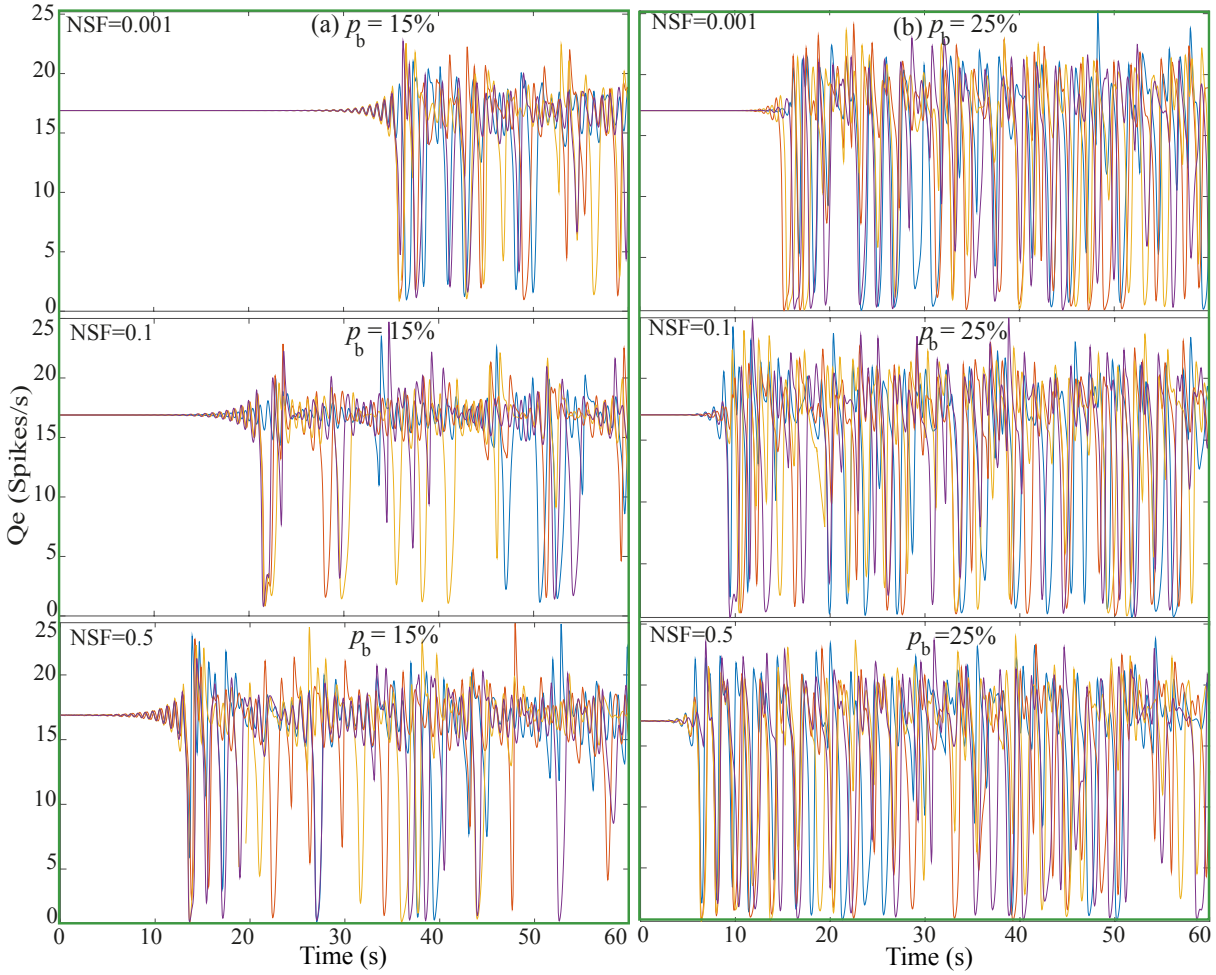

Figure 3.21. Noise intensity impact on simulations. The effect of three different NSF= [0.001, 0.1, 0.5] on simulation results (a) $p_b = 15\%$ and (b) $p_b = 25\%$. As the noise intensity increases, the time required to develop seizure-like chaotic oscillations decreases.

of increased instability is consistent with findings from clinical experiments [9, 11].

Figures 3.19 and 3.20 show bird's-eye snapshots of the evolution of pattern formations for the excitatory activity. In Fig. 3.19 ($p_b = 15\%$), one can see that by time $t = 5\,\mathrm{s}$, a cloud-like pattern appears, indicating slow spatial fluctuations (second column), and by 10 s, the cortex has largely organized itself into its final spatiotemporal configuration.

With strong diffusion for $t \geq 10\,\mathrm{s}$ (the upper row $D_2 = 0.5\ \mathrm{cm}^2$), the Turing pattern appears as high-amplitude island-like regions surrounded by valleys of low amplitudes with maximum contrast between the higher and lower firing rates. As a result of closing gap-junctions (reductions in inhibitory diffusion strength), the width of the inactive (blue) regions increases and travelling-wave patterns appear.

Comparing with the evolution for $p_b = 25\%$ in Fig. 3.19, we see that the cortex organises to the final configuration in less than 5 s; as the gap-junction strengths decrease, the cortex moves from Turing to temporal pattern without being in a chaotic state for a large range of diffusion strength: the full temporal pattern for $p_b = 25\%$ happens at

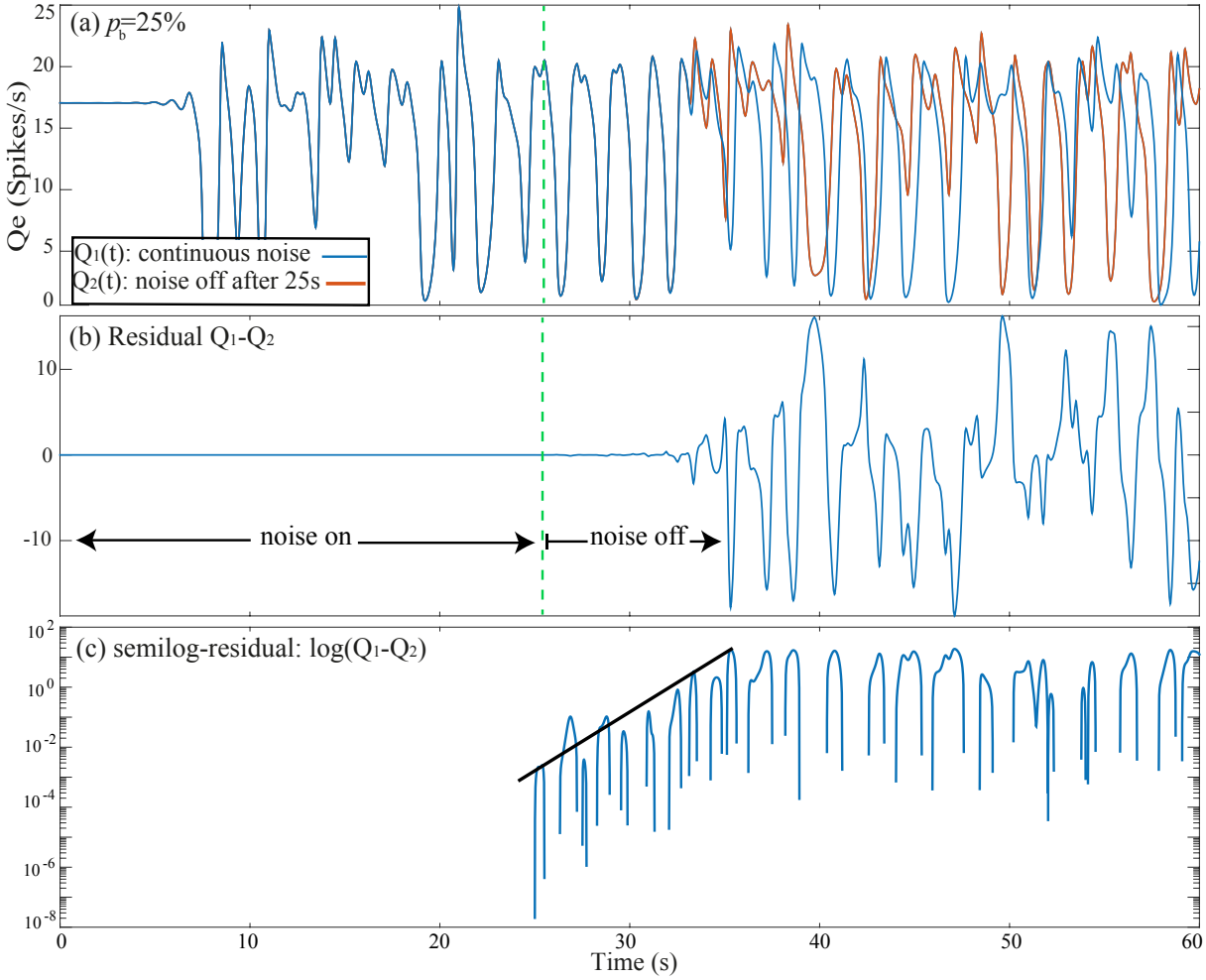

Figure 3.22. Evidence for chaotic behaviour of the Waikato cortical equations. (a) Blue trace Q_1 shows cortical evolution for continuous white noise with NSF = 0.5, $p_b = 25\%$ (corresponding to one of the four traces in Fig. 3.21, bottom right panel). Red trace Q_2 is a repeat run with identical noise up until time $t = 25$s, at which point noise is turned off (vertical dashed line). (b) Residual for $Q_1 - Q_2 = 0$ shows that traces are identical up until $t = 25$s. (c) Thereafter, residual grows exponentially with Lyapunnov exponent $\lambda = 0.92$ s^{-1} until saturation occurs for $t \gtrsim 35$s.

$D_2 = 0.3$ cm^2; while in the case of $p_b = 15\%$, the temporal pattern formation is completed at $D_2 \leq 0.2$ cm^2.

To test the effect of the noise scale factor (NSF) on our results, a series of simulations of the Waikato cortical equations for three different noise intensities for two values for $GABA_B$ effect ($p_b = 15\%$ and $p_b = 25\%$) was ran using Euler-Maruyama integration with time step of 0.3 ms in MATLAB, see Figs. 3.21 to 3.23. The system equations were perturbed continuously by identical sequences of subcortical white noise, but the scale factor of the noise intensity was set at one of three different values (see Fig. 3.22). The evolution of the cortical sheet was traced for a total time of 60 s. Cortical equations were initialized to the top-branch steady-state values. Figure 3.21 shows that increasing noise intensity reduces the time of onset of seizure-like activity. Once large-scale oscillations have developed, the noise has little or no effect on oscillation dynamics. In contrast,

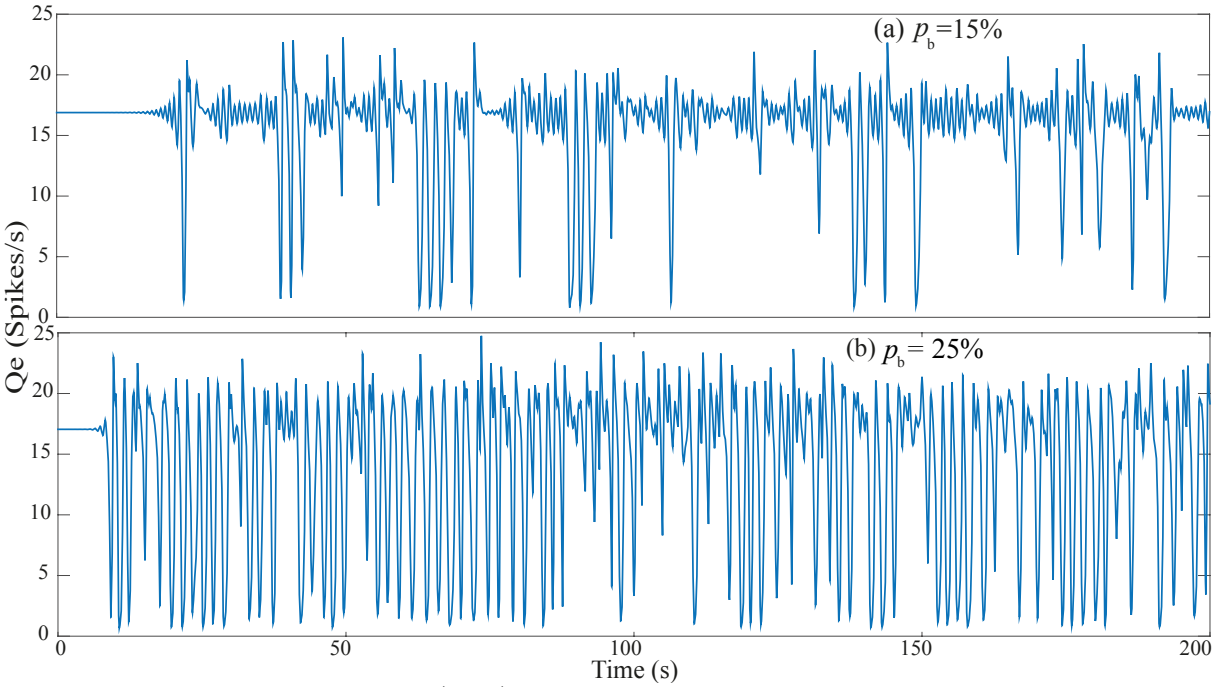

Figure 3.23. Seizure-like event (SLE) activity enhanced in a theoretical Waikato mean-field model as $GABA_B$ effect is increased. (a) The minimal effect of $GABA_B$ for $p_b = 15\%$ is considered as a baseline and (b) the greater $p_b = 25\%$ impact as a modelling drug effect.

increasing the modelled $GABA_B$ effect from $p_b = 15$ to 25% has a marked qualitative impact on the duration of oscillatory bursts, see Fig. 3.23. We conclude that the activity bursts seen in Figs. 3.21 to 3.23 are not noise-driven events. In fact, these are chaotic oscillations as demonstrated in Fig. 3.22. A pair of simulations with the identical sequences of white noise was run; for the blue trace, the noise is continuous, while noise is turned off at 25 s for the red trace (see Fig. 3.22(a)). The red trace shows that large-scale oscillations persist even in the absence of noise. Figure 3.22(b) and (c) present the residual of these two traces on a linear and semi-log scale respectively. The exponential divergence in Fig. 3.22(c) demonstrates exquisite sensitivity to changes in initial conditions, and provides strong evidence of the chaotic nature of these oscillations.

3.3.4 NMDA and the Waikato model

The mean-field model is characterised by excitatory neurotransmitters (AMPA), and inhibitory neurotransmitters ($GABA_A$, $GABA_B$); in the current section, the model is modified by including NMDA as another excitatory neurotransmitter. The results presented in the following sections are due to the existence of all four receptors (AMPA, NMDA, $GABA_A$, $GABA_B$).

NMDA cortical steady states

Inclusion of NMDA neurotransmitter via Eq. (3.37) alters both the distribution of soma-voltage steady states and the extent of cortical instability. Figure 3.24 shows that the

inclusion of the NMDA term increases the level of excitation, pushing the steady-state manifolds to the right and increasing excitation in the upper branch. For example, for $p_a = 1.8$, the upper-branch firing rate increases with NMDA effect: $Q_e = 17$ s^{-1}($p_{\rm N} = 100\%$), $Q_e = 28$ s^{-1}($p_{\rm N} = 200\%$); $Q_e = 32$ s^{-1}($p_{\rm N} = 300\%$)); note that the latter two values are beyond the displayed range of Fig. 3.24(a).

NMDA stability analysis and dispersion curves

To predict the dynamical behaviour of the cortical model, a sample of dispersion curves for anaesthetic drug effect $p_a = 1.08$ and $p_a = 2.56$ are plotted as a function of wave number for two NMDA gain factors p_N =[100%, 200%]; results are presented in Fig. 3.25 for the top and bottom branches. Four settings of gap junction diffusions are chosen $D_2 = [0.2, 1, 2, 3]$ cm^2. The real part of the leading eigenvalues are plotted, since these determine system stability.

Comparing Fig. 3.25(a) and (c) at $q = 0$, the real part of the dominant eigenvalues are very similar [Re(eig)= 0.6 ($p_N = 100\%$) and Re(eig)= 0.5 ($p_N = 200\%$)]; providing us with reasonable initial instability conditions to allow comparison between LSA of the two NMDA settings for the non-zero wave numbers. As shown in Fig. 3.25(a) at the NMDA gain factor $p_N = 100\%$, the Turing instability is prominent only for very strong diffusion coefficients $D_2/\text{cm}^2 \gtrsim 2.0$, while the temporal instabilities are predicted for all inhibitory diffusion strengths. Boosting NMDA effect to $p_N = 200\%$ in Fig. 3.25(c), dispersion curves predict that Turing peaks either decrease ($D_2 = 3$ cm^2) or vanish ($D_2 = 2$ cm^2), so the Hopf temporal modes will dominate on the upper branch. Comparing panels (a) and (c) of Fig. 3.25 for strong gap-junction diffusion, increasing NMDA effect unbalances the spatial mode (Turing) in favour of the temporal mode (Hopf) on the top branch.

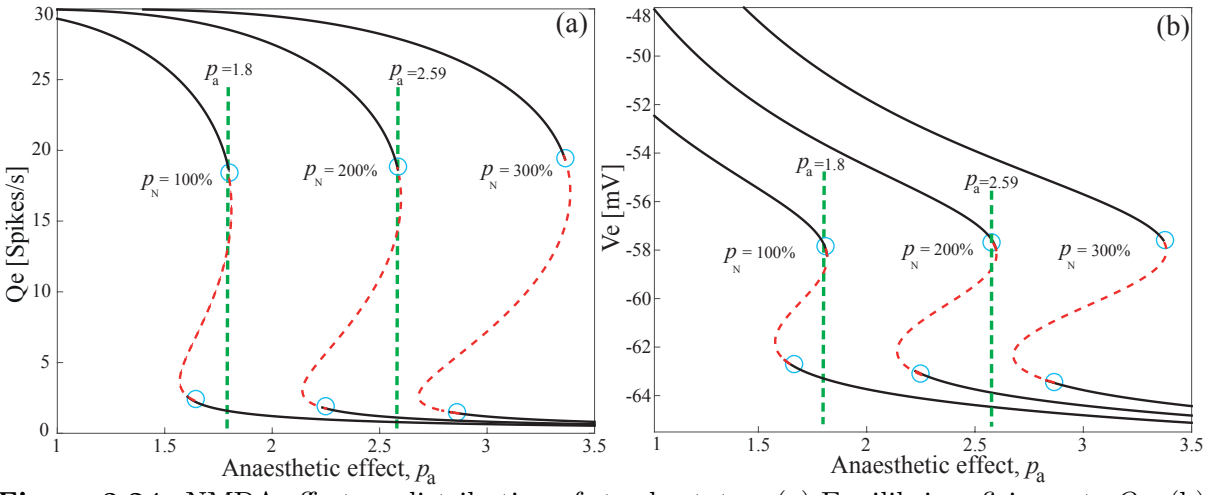

Figure 3.24. NMDA effect on distribution of steady states. (a) Equilibrium firing rate Q_e; (b) membrane voltage V_e for the excitatory population as a function of anaesthetic effect for the different values of NMDA effect $p_N = [100\%, 200\%, 300\%]$.

NMDA numerical simulations

In order to verify the numerical correctness of the model predictions, fully nonlinear stochastic simulations were run for the full cortical system equations in Chap. 3.1. The pattern dynamics of the cortex for two NMDA gain factors are investigated.

Figures 3.26 and 3.27 illustrate the dynamical effect of the reduction of the gap-junction diffusion for the awake state of the cortex for $p_N = 100\%$ and 200% respectively. Each figure contains four rows corresponding to four values of gap-junction diffusion

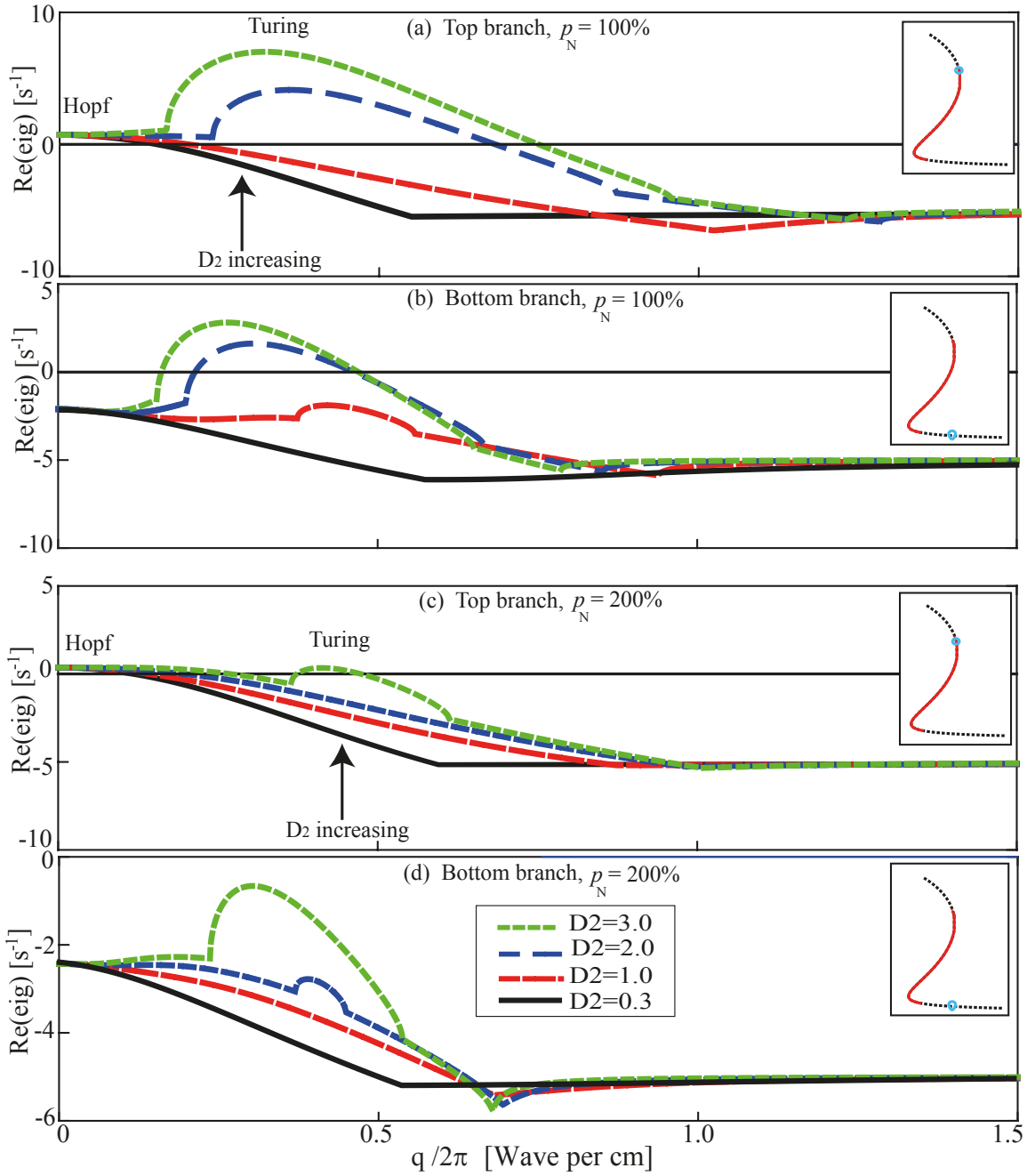

Figure 3.25. NMDA effect dispersion curves. (a, b) NMDA effect $p_N = 100\%$ with anaesthetic effect $p_a = 2.59$ and $p_b = 20\%$ for (a) top branch and (b) bottom branch. (c, d) Dispersion curves for NMDA effect $p_N = 200\%$, anaesthetic effect $p_a = 1.8$ and $p_b = 20\%$.

strengths. Scanning Figs 3.26 and 3.27 from up to bottom show that the cortical patterns are strongly impacted by changes in inhibitory diffusion values D_2 for both NMDA settings. A comparison between Figs 3.26 and 3.27 shows for intermediate inhibitory diffusion $0.3 < D_2/\text{cm}^2 < 0.5$, while $p_N = 100\%$ creates a chaotic dynamical behaviour for $p_N = 200\%$ mostly temporal instabilities are developed over time and for the weak diffusion, the greater NMDA gain factors develop a synchronized oscillation with slower oscillations in comparison to $p_N = 200\%$, the dynamical pattern is not in full synchronized state. Scanning Column (d) from up to down indicates a Turing pattern with maximum contrast between the higher and lower firing rates for strong diffusion value. Reductions in inhibitory diffusion strength increases the separation between activated area and travelling-wave temporal patterns appear.

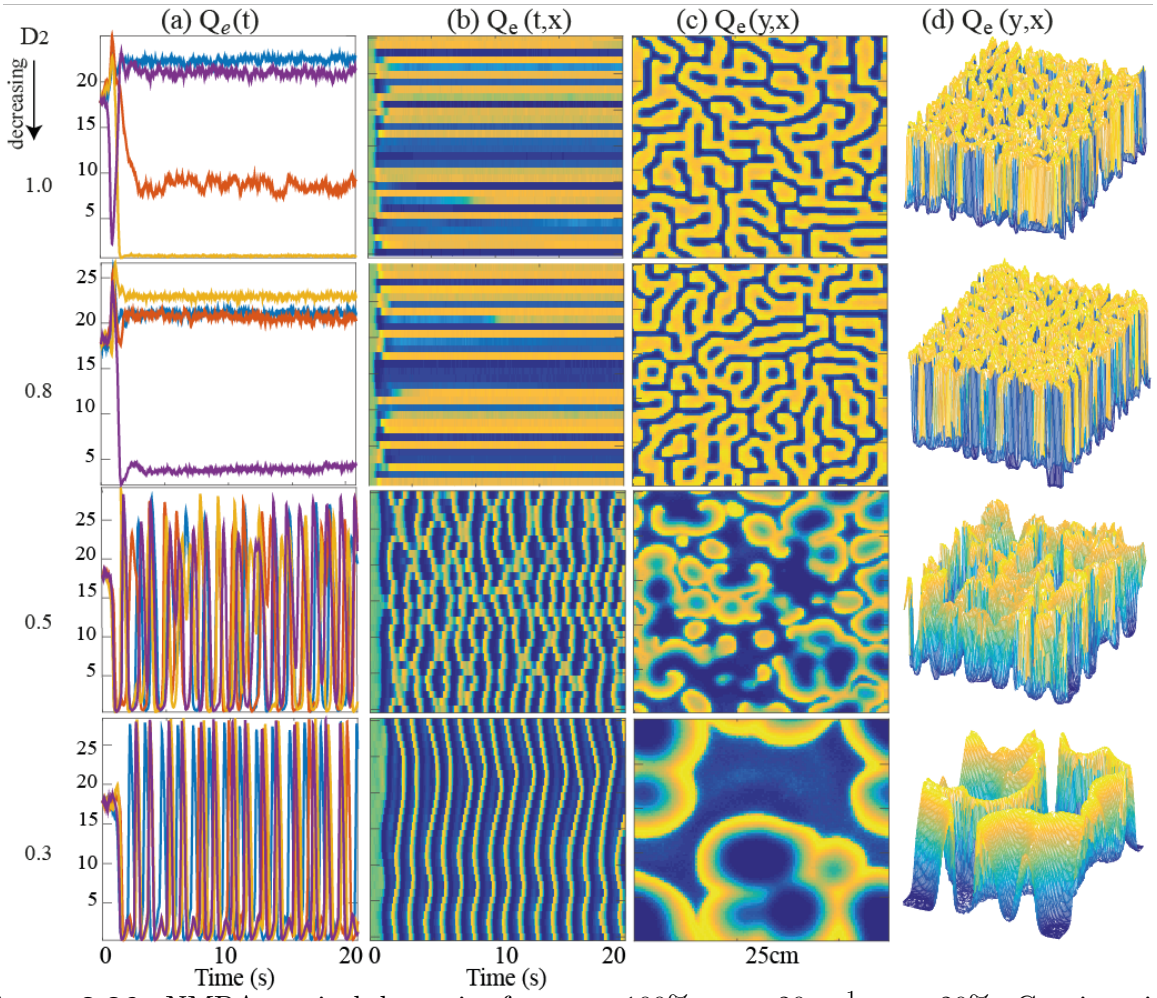

Figure 3.26. NMDA cortical dynamics for $p_N = 100\%, \alpha_a = 20\ \text{s}^{-1}$, $p_b = 20\%$. Gap-junction strength D_2 is stepped from 0.9 (top row) to 0.3 cm^2 (bottom). Cortex is initialised at the $p_a = 1.8$ awake state. (a) Time-series of excitatory firing-rate $Q_e(t)$ for 20 sec. (b) $Q_e(t, x)$ space-time chart representing the 20-sec time-evolution of cortical activity along the $y = 60$ midline strip. Firing rate (y-axis) ranges from 0 to 33 s^{-1}, colour scale from blue to orange indicates the numerical range from low to high. (c) Bird's eye snapshot $Q_e(y, x)$ at $t = 20$ sec. (d) Mesh images $Q_e(y, x)$ of the cortex when $t = 20$ sec. Grid resolution is 2.4 mm and time step is 0.1 ms. Grid size is 120×120.

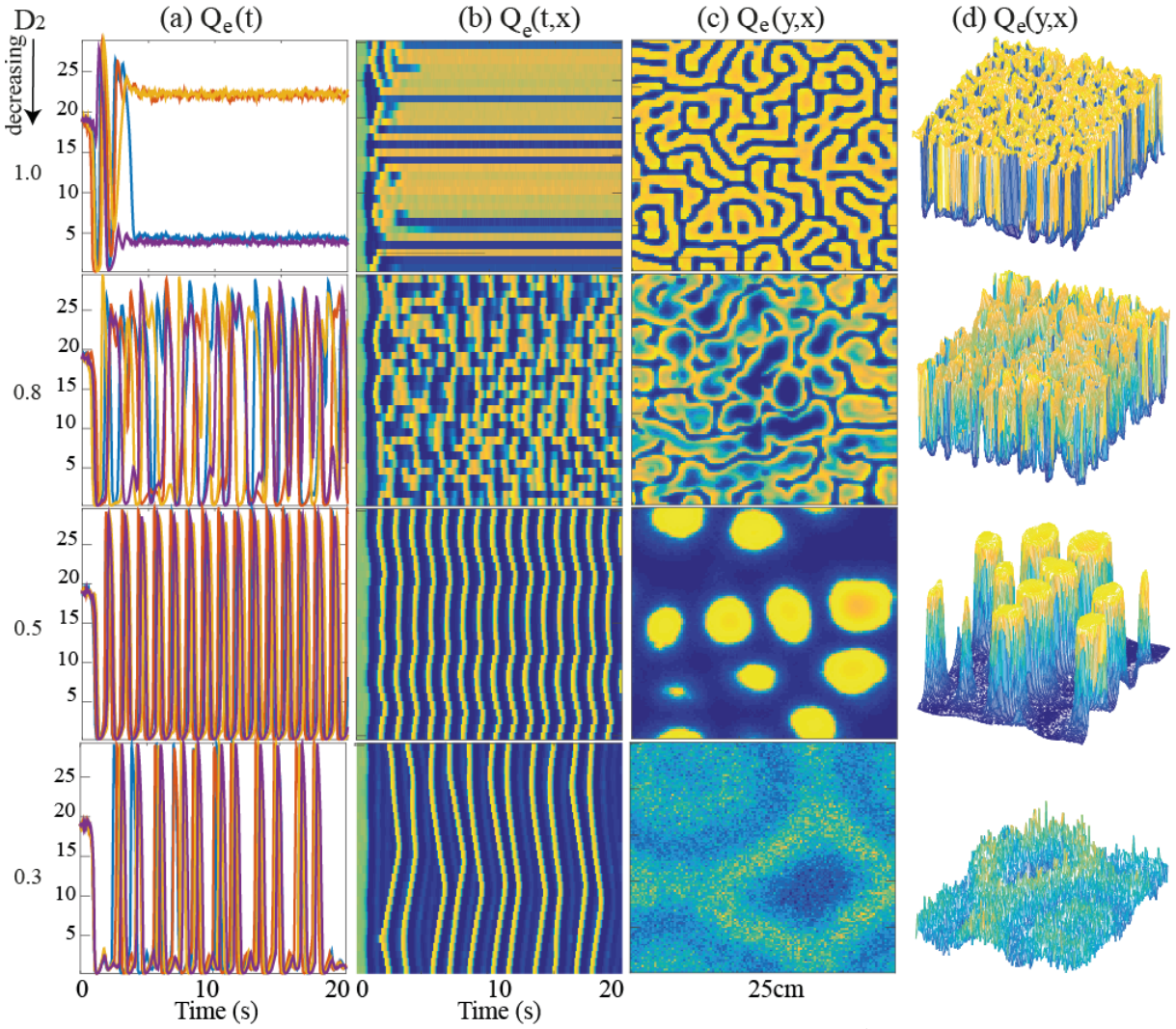

Figure 3.27. NMDA cortical dynamics for $p_N = 200\%, \alpha_a = 20\ \mathrm{s}^{-1}$, $p_b = 20\%$ see Fig. 3.26 caption for simulation details.

Here, it is important to mention that our simulation result is not in agreement with our finding from dispersion curve prediction in Fig. 3.25. For a specific range of gap-junction $D_2 < 1$, the Hopf oscillation on the upper branch loses stability through Turing bifurcation on the lower branch which cannot be discerned from linear stability analysis. Nevertheless, we can conclude that increased NMDA effectiveness (and hence increased excitation) tends to weaken the spatial mode (Turing) and enhance slow temporal oscillations (Hopf).

3.4 Conclusion

Anaesthetic agents from the inductive class (e.g., propofol) affect $\mathrm{GABA_A}$ receptors through potentiating $\mathrm{GABA_A}$-induced ionic currents; this is modelled as a prolongation of the tail of the unitary IPSP. These agents also interact with $\mathrm{GABA_B}$ receptors through increasing inhibitory synaptic neurotransmission [85], this modelled as an increase of inhibitory synaptic gain. Dissociative drugs (e.g., ketamine, nitrous oxide) affect excitatory

synaptic neurotransmitter through the modulation of NMDA receptor function [33, 97], the effect of these agents is modelled as a voltage-dependent alteration of excitatory synaptic gain.

Linear stability analysis predicts that reducing the decay rate (i.e., prolonging the decay duration) of $GABA_A$ destabilises the temporal stability in both awake and anaesthetised states of the cortex. Increases in $GABA_B$ gain enhance the instability in the upper branch, while the lower branch does not show significant sensitivity to the $GABA_B$ changes; while NMDA effectiveness affects the stability on both awake and anaesthetised states. Dispersion curves predict that increasing $GABA_B$ and NMDA effectiveness tends to destabilize Turing patterns in favour of a temporal mode (Hopf) with large-scale synchronized oscillations that may represent a seizure state.

In both cases of $GABA_B$ and NMDA inclusion, strong gap-junction diffusivity activates a natural mechanism for Turing bifurcation that accelerates to the spontaneous formation of spatial patterns of high and low neural activity over the whole cortex. Simulation pattern and linear stability prediction are in agreement in the case of $GABA_B$. However, in the case of NMDA modelling, for a specific range of gap-junction $D_2 < 1$, Hopf pattern in upper branch loses stability through a Turing instability on the lower branch. The Waikato model indicates that the cortex may be susceptible to seizures when Cx36 gap junctions are blocked during anaesthesia. This may explain why some anaesthetics cause seizures, as many of these agents also block gap junctions [105].

Previous clinical work has shown that Cx36 gap junctions are crucial in determining cortical stability [98]. However, there is a contradiction between experimental results about gap-junction blocking agents: some report suppression of seizure activity [30,51,54], while others provide evidence that these drugs enhance seizure activity [47, 76, 100, 108]. Some reports suggest that the excitation and suppression effects may be dependent on concentration [31,100]. Moreover, there is some evidence that there is interaction between gap-junctions closure and GABA [29] and NMDA activity [14, 102].

However, to date no clinical experiments on either people or animals have investigated the propensity for gap junction blockade to cause seizure activity during anaesthesia.

In the next chapter, we will test this hypothesis by designing two experiments, the first using in vitro cortical brain slices and the second using in vivo EEG recording. The first experiment studies the effect of $GABA_B$ on cortical slice activity (applying baclofen); and the second experiment (EEG recording) examines whether anaesthetising mice with a commonly used general anaesthetic (propofol)-while simultaneously blocking Cx36 gap junctions with mefloquine-induces signs of seizure activity in brain.

Chapter 4

Experimental investigation of $GABA_B$ enhancement and gap-junction closure

4.1 Effect of $GABA_B$ on in vitro cortical slice activity

Anaesthetic drugs, such as propofol, enhance the effectiveness of inhibitory synapses, particularly of the fast-acting $GABA_A$ receptors. The much slower acting $GABA_B$ receptors are little affected by propofol, so have been ignored in previous anaesthesia models.

In Chap. 3, we extended the Waikato cortical model to investigate the effect of propofol on brain activity in the presence of both $GABA_A$ and $GABA_B$ synapses. The model predicts that enhancement of $GABA_B$ should have a seizure-promoting effect on brain activity. To test this prediction, a set of experiments were designed based on *in vitro* cortical brain slices[1] [60] using the $GABA_B$ agonist[2] baclofen. The popularity of the in vitro brain slice method is due to high controllability of experimental conditions and its ease of use. This method has been applied to the study of anaesthetic drug effect by Voss [101] and many others [64, 69].

Baclofen has been shown previously to enhance seizure-like activity in adult *hippocampal* rat slices at a dose of 0.1–1.5 μM in normal aCSF [61] and in activated hippocampal tissue (4-AP[3], zero-Mg and electrically stimulated) at a range of doses 1–50 μM [72, 95, 104]. In the stimulated protocols, baclofen enhances ictal (seizure) activity, while abolishing interictal (between seizure) activity. Baclofen given to neocortical slices strongly inhibits no-magnesium *interictal activity* at a dose of 1–50 μM [55].

In this study the aim is to investigate the effect of baclofen on *ictal-like activity* in the *anaesthetised* neocortex (in the previous clinical experiments, no anaesthetic drug was administered). Consistent with the Waikato cortical model predictions, the hypothesis is that $GABA_B$ activation with baclofen should enhance seizure-like activity in the anaesthetised cortex.

[1] Tissue slices are used to quantify metabolic reactions of tissues

[2] Agonist is a chemical that binds to and activates a receptor to produce a biological response

[3] 4-Aminopyridine ($C_5H_6N_2$) is an organic compound used to characterize subtypes of the potassium channel

4.1.1 Method

This section describes the methods employed in these experiments such as solutions preparation, slicing, recording and data analysis. This work was carried out under the supervision and guidance of physiologist Dr Logan Voss.

Solutions

Two artificial cerebrospinal fluid solutions were prepared. These solutions are similar to cerebrospinal fluid and are designed to keep the slices in a functioning condition for several hours. Made with double distilled water, the solutions are stored at 1–4 ℃ for no longer than 7 days. All solutions were bubbled with carbogen (95% O_2 and 5% CO_2) for at least 15 minutes before use. The two solutions used were:

- **Normal aCSF**: NaCl (125 mM), KCl (2.5 mM), $MgCl_2$ (1 mM), $CaCl_2$ (2 mM), NaH_2PO_4 (1.25 mM), $NaHCO_3$ (26 mM) and D-glucose (10 mM)
- **Zero-magnesium aCSF** lacking magnesium ions: NaCl (124 mM), KCl (5 mM), $CaCl_2$ (2 mM), NaH_2PO_4 (1.25 mM), $NaHCO_3$ (26 mM) and D-glucose (10 mM)

Normal aCSF was applied for brain extraction and tissue slicing, while zero-magnesium aCSF was used to stimulate seizure-like event (SLE) activity from slices.

Removing magnesium from the aCSF unblocks and therefore activates excitatory NMDA channels, resulting in increased tissue excitability and generation of seizure-like activity. This is a commonly used method for inducing "seizures" in neocortical slices [101].

Slicing

Adult male and female wild-type (129 sv[4]) mice aged between 4 to 14 weeks were used to obtain neocortical brain slices. The mice were anaesthetized with carbon dioxide (approximately 30 s exposure) before decapitation and brain dissection. The brain was freed from adjacent tissue and placed into ice-cold normal aCSF. The delay between brain removal and slicing was not more than 10 minutes. Immediately before slicing, the anterior and posterior 1–2 mm of cerebral cortex was removed with a razor blade. The tissue block was glued to a stainless steel stage for slicing in ice-cold normal aCSF. The brain was sectioned in the coronal plane (see Figure 4.1) into 6–8 slices with a thickness of 400 μM, and then given a minimum of one hour for recovery at room temperature, 25℃ in carbogenated zero-magnesium aCSF.

Recording

For electrical recording, slices were transferred (three slices at a time) to an immersion-style recording bath (Tissue Recording System, Kerr Scientific Instruments, New Zealand);

[4]common inbred strain of laboratory mouse

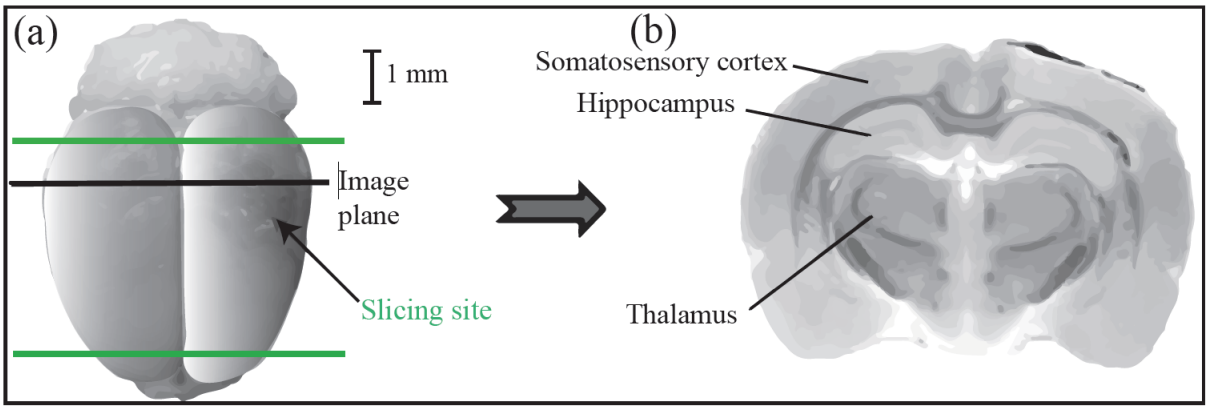

Figure 4.1. Coronal brain cuts as indicated by bold green lines (a) Mouse brain viewed from above showing the region of slicing (bold green lines); (b) a single coronal slice taken from the region of the black line.

see Fig. 4.2. Zero-magnesium aCSF solution with addition of carbachol (33 μM), was delivered via gravity feed at a flow rate of 5.0 ml/min at room temperature (24–26°C).

Swartzwelder et al (1987) [95] reported that in the hippocampus the enhancing effect of baclofen is observed only on ictal (seizure) activity, while interictal activity is suppressed. Based on these findings carbachol was added to the bath solution to optimise prolonged ictal-like SLE events in zero-magnesium solution [99].

Spontaneous local field potential activity was recorded from the cerebral cortex using a 50 μm teflon-coated tungsten electrode, one in each slice. The electrode was referenced to a silver/silver-chloride disc, which served as a common reference. The signal was amplified by a factor of 250, with 16-bit resolution and bandpass filtered between 1.0 and 3000 Hz and the sampling rate was 10 kHz. The data were collected using `LabChart6` and saved for later analysis using custom-written MATLAB (R2014b) codes.

To protect the recordings from contamination by electrical artifacts, all experiments were carried out in a double-shielded room which strongly attenuates external electromagnetic fields; however, total elimination of noise is impossible.

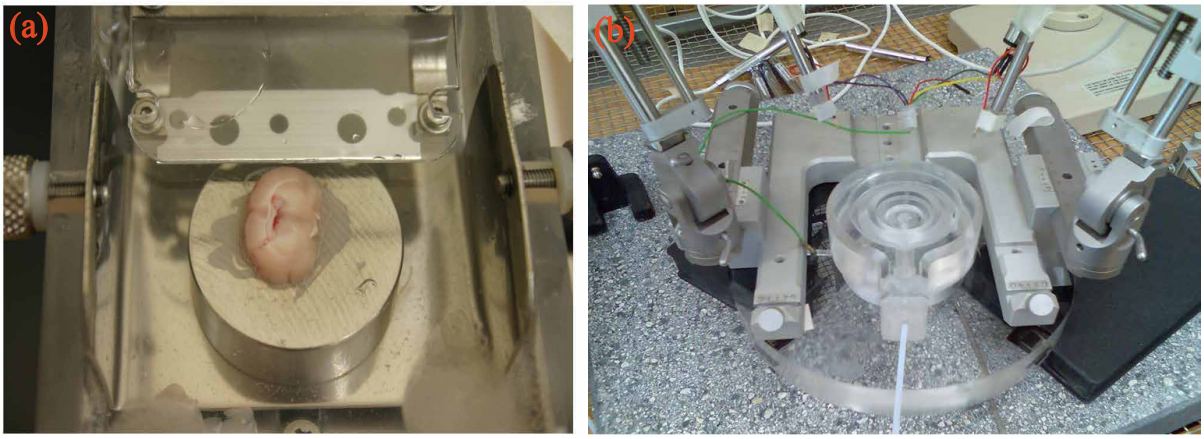

Figure 4.2. Experimental setup for recording local field potentials from mouse brain slice in vitro; (a) for 400-μm coronal brain slices, and (b) the recording chamber with electrode holders.

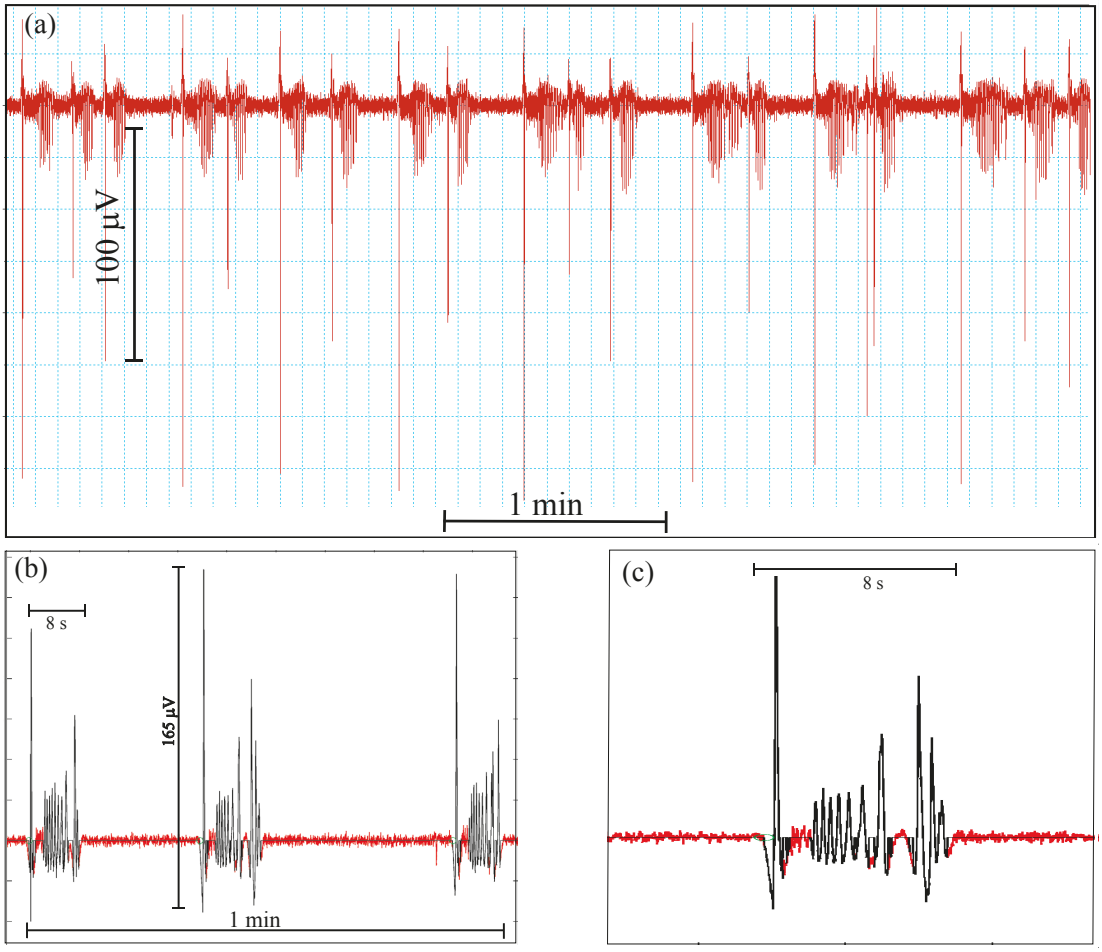

Figure 4.3. (a) Profile of seizure-like event (SLE) activity induced in a single cortical slice from a wild-type (129 sv) mouse during perfusion with zero-magnesium artificial cerebrospinal fluid (0-Mg aCSF), 33 μM carbachol plus 50 μM baclofen. Each of the high-amplitude vertical lines indicates a single SLE. (b) Expanded view of three SLEs. In this example the peak-to-peak amplitude was approximately 165 μV, SLE length was $\sim$8 s and the frequency (the number of SLEs per minute) was 3 min^{-1} (c) Expanded view of one SLE. The red and black colours indicate the base line and SLE activity respectively. Compare with human seizure recording in Fig. 1.4.

Procedure

The study was divided into experimental and control sections. In the experimental part the effect of baclofen on SLE length, frequency and amplitude was quantified. There were three stages to the procedure with a total duration of approximately 105 minutes:

- **Baseline**: Cortical slices are perfused with zero-magnesium aCSF, and 33 μM carbachol for 30 min.
- **Drug effect**: Baseline solution is replaced with zero-magnesium aCSF, 33 μM carbachol plus 50 μM baclofen. The collected solution is discarded for the first 10 minutes

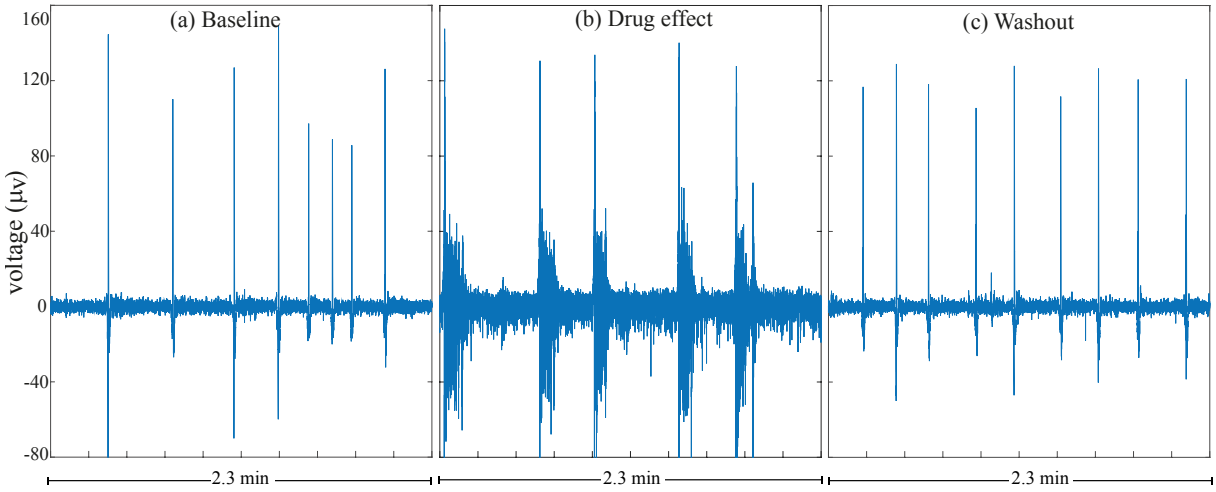

Figure 4.4. Seizure-like event (SLE) activity induced in a single slice during (a) baseline; (b) baclofen effect; and (c) washout.

to allow wash-in of the drug, and thereafter recirculated. This step maintains a constant drug concentration in the recirculated solution. Baclofen is perfused for 45 min.

- **Washout**: Slices are returned to baseline solution for 30 min. Collected solution is discarded for first 10 min before recirculating to prevent drug contamination during the 30-min washout. The aim is to determine whether SLEs revert to pre-drug baseline characteristics.

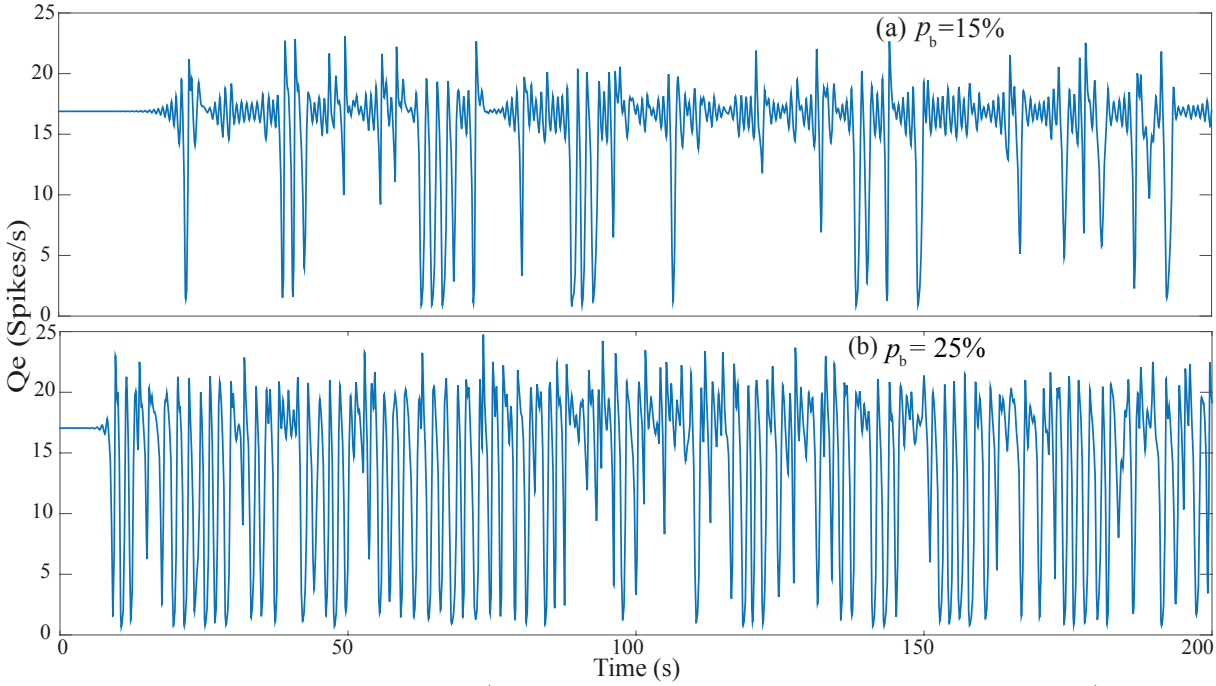

Figure 4.5. Duplicate of Fig. 3.23 (simulation of $GABA_B$ effect in Waikato model) for convenient comparison with slice results of Fig. 4.4. We note that the propensity for prolonged large-scale oscillations is boosted by strengthened p_b .

For ease of comparison with the numerical modelling for $GABA_B$ effect reported in Chap. 3, Fig. 4.5 is a duplicate of Fig. 3.23. If the large oscillations in the model correspond to seizure events in the slice, then we see that SLEs are prolonged at larger $GABA_B$ values, consistent with the slice experiments of Fig. 4.4.

Control experiments

In the second section, a series of control experiments were designed to confirm the validity of the outcomes from the baclofen experiments. Three control experiments were undertaken.

1. **Time control** This part was carried out by perfusing only zero-magnesium aCSF and 33 μM carbachol for the full 105 min. The purpose was to determine the effect of time on SLE characteristics.
2. **Drug control: saclofen + baclofen** The aim was to investigate whether the effect of baclofen on seizure-like events is consistent with action at the $GABA_B$ receptor. This was done by adding the $GABA_B$ antagonist[5] saclofen to the baseline solution. The procedure was as follows:
   - Baseline: Perfusion of cortical slices with zero-magnesium aCSF, 33 μM carbachol plus 100 μM saclofen for 30 min.
   - Drug effect: Zero-magnesium aCSF, 33 μM carbachol, 50 μM baclofen plus 100 μM saclofen was applied, recording for 45 min. The aim was to investigate if saclofen eliminates the baclofen effect, since both target $GABA_B$ receptors in the slices.
   - Washout: The baseline solution was applied for 30 min.
3. **Drug control: saclofen** The aim was to investigate the $GABA_B$ antagonist saclofen effect on SLE characteristics. Same procedure as for baclofen, except saclofen was added in place of baclofen.

4.1.2 Data analysis

Data preprocessing was carried out by visual inspection and obvious artefacts were removed manually. In the majority of cases, SLEs were detected and analysed by applying a semi-automated MATLAB algorithm.

SLE **amplitude** was defined as the peak-to-peak activity, that is the difference between the maximum positive and the maximum negative deflection.

SLE **frequency** was computed over a 2-min sliding window with 70-s overlap, and reported as the number of events per minute.

To define SLE **length** a semi-automated method was applied through MATLAB code. First, the standard deviation of an SLE-free segment was calculated. Then for each

[5]A receptor antagonist is a receptor ligand or drug that blocks or dampens agonist-mediated response

detected SLE, using varying window lengths (40–200 samples), the SLE was deemed to continue until the standard deviation of the window did not exceed that of the SLE-free segment. Window lengths were manually tuned for each recording by visual inspection.

For statistical comparisons, SLE length, frequency and amplitude were averaged over the 30 min immediately prior to drug delivery and compared to the average value during the 45 min of drug infusion and the average value during 30 minutes of washout (drug-free solution).

In some cases (7 recordings out of 16 for baclofen, and 1 of 16 for saclofen), SLE characteristics were analysed manually because the automated algorithm failed to accurately quantify SLE length. This was due primarily to inconsistencies in SLE features in some recordings, and occasionally large delays between the initial SLE field potential deflection and subsequent oscillation. In these cases SLE length was quantified by visual inspection of five SLEs during baseline, drug and washout periods.

Comparisons were analysed using the non-parametric repeated measures analysis of variance (ANOVA) Friedman test[6]. This test was used because not all data were normally distributed. A p-value < 0.05 was interpreted as statistically significant, in which case the Dunn multiple comparison test[7] was used.

4.1.3 Results

An example of the pattern of SLE activity obtained from one slice is illustrated in Figs. 4.3 and 4.4. The main finding was that SLE duration increased during the infusion of baclofen. The mean (SD) SLE length increased from 7.5 (9.6) s during baseline to 14.5 (19.7) s during baclofen infusion ($p < 0.01$). This effect reversed during drug washout. Thus mean SLE duration during baclofen infusion doubled compared to baseline (Fig. 4.6).

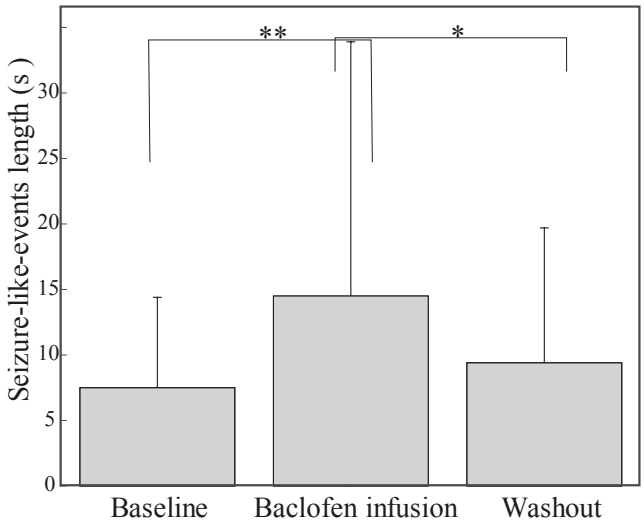

Figure 4.6. Effect of baclofen on the *length* of seizure-like events: Comparison between Baseline and Drug infusion shows a very significant difference ($p^{**} < 0.01$); comparison between Washout and Drug infusion shows a significant difference ($p^{*} < 0.05$). There is no significant difference between Washout and Baseline, confirming that SLE length reverted to Baseline after stopping baclofen infusion. The error bars indicate standard deviation.

[6]The Friedman test is a non-parametric test to compare three or more matched groups

[7]Dunn's test is a non-parametric pairwise multiple comparisons procedure based on rank sums, often used as a post hoc procedure following rejection of a Kruskal-Wallis test

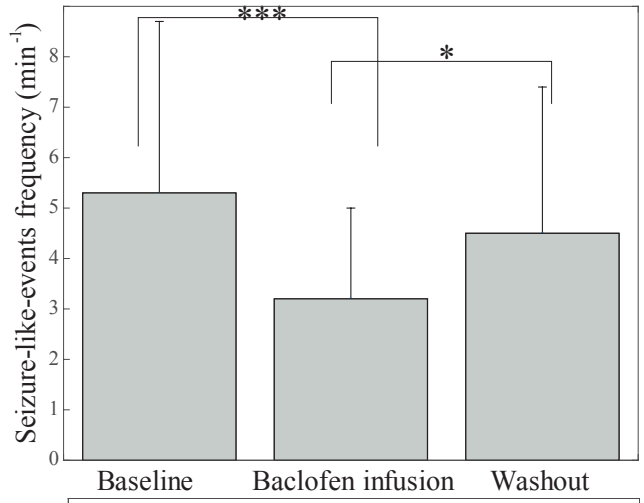

Figure 4.7. Effect of baclofen on the *frequency* of seizure-like events: Comparison between Baseline and Drug infusion shows that there is a highly significant difference ($p^{***} < 0.001$); comparison between Washout and Drug infusion shows a significant difference ($p^{*} < 0.05$).

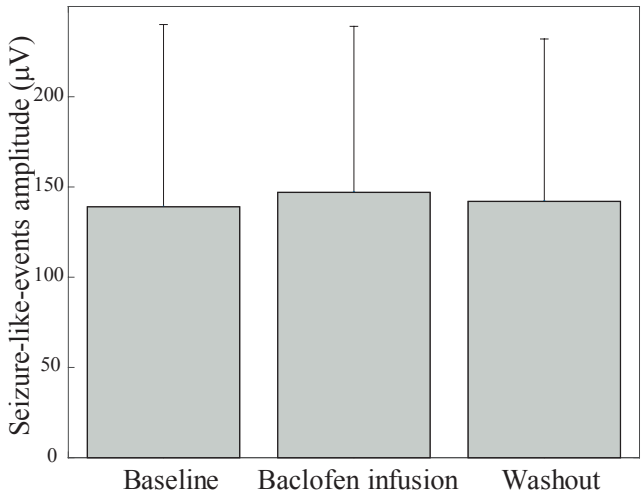

Figure 4.8. Effect of baclofen on the *amplitude* of seizure-like events. There is no significant difference between Baseline, Infusion, and Washout conditions.

Reflecting the increase in SLE length, the frequency of occurrence of seizure-like events was lower during baclofen infusion (3.2 min^{-1}) compared to baseline (5.3 min^{-1}) and washout (4.5 min^{-1}). Thus, the frequency of the SLEs during baclofen infusion reduced by a factor of 40% compared to the mean value in baseline (Fig. 4.7).

There was no significant change in the peak-to-peak SLE amplitude after the inclusion of baclofen into the aCSF (Fig. 4.8). Table 4.1 summarizes the mean values and respective standard deviations (SD) for different experimental stages for SLE characteristics.

The time-control results of Table 4.2 show that SLE characteristics changed over time: SLE length and peak-to-peak amplitude reduced with time (significant difference between the "baseline" and "washout" values ($p < 0.05$)). Also, SLE frequency increased over time (note that these was no change in aCSF composition during this 105 min control experiment). In fact, these results indicate that time has an opposite effect to that of baclofen.

The saclofen control experiment of Table 4.3 revealed that the GABA_B antagonist cancelled the effect of the GABA_B agonist baclofen: there was no significant change in SLE characteristics when saclofen and baclofen were combined ($p > 0.5$). Comparing

Tables 4.1 and 4.3, we see that SLE length in the presence of baclofen was 14.5 s compared to 9.8 s when there was a combination of baclofen and saclofen.

Table 4.1. Effect of baclofen infusion on the characteristics of seizure-like events ($n = 16$ slices)

Condition	length (s)	frequency (min^{-1})	amplitude (μV)
Baseline	7.5 (6.9)**	5.3 (3.4)***	139 (101)
Baclofen infusion	14.5 (19.7)	3.2 (1.8)	147 (92)
Wash out	9.4 (10.3)*	4.5 (2.9)*	142 (90)

Asterisks indicate level of significance relative to baclofen infusion:
$p^* < 0.05, p^{**} < 0.01, p^{***} < 0.001$

Table 4.2. Effect of time on the characteristics of seizure-like events during constant washin of 0-Mg aCSF + carbachol. Here, Baseline, "Drug infusion", and Washout are all equivalent since there is no drug infusion ($n = 9$ slices)

Condition	length (s)	frequency (min^{-1})	amplitude (μV)
Baseline (30 min)	8.9 (4.5)	2.7 (0.6)	132.9 (112)
"Drug infusion" (45 min)	5.6 (2.6)	4.2 (1.5)	65.3 (40.0)
Wash out (30 min)	4.2 (2.1)*	5.6 (3.4)*	52.2 (29)*

Table 4.3. Effect of control infusion (saclofen + baclofen) on SLE characteristics ($n = 9$ slices)

Condition	length (s)	frequency (min^{-1})	amplitude (μV)
Baseline	6.2 (4.2)	5.0 (1.9)	116.5 (84.9)
Saclofen+baclofen	9.8 (11.2)	4.2 (1.9)	98.9 (58.8)
Wash out	6.9 (5.0)	4.8 (2.5)	101.2 (67.1)

Table 4.4. Effect of saclofen infusion on SLE characteristics ($n = 6$ slices)

Condition	length (s)	frequency (min^{-1})	amplitude (μV)
Baseline	3.1 (0.6)	5.1 (2.1)	74.3 (56.4)
Drug infusion	3.4 (1.1)	5.0 (1.5)	67.5 (46.0)
Wash out	3.0 (0.7)	5.1 (1.33)	66.7 (45.2)

Saclofen delivered on its own did not significantly change SLE characteristics ($p > 0.5$). As shown in Table 4.4, SLE length, frequency and amplitude remained stable.

4.1.4 Conclusion

The aim of this first experiment was to investigate the effect of baclofen $GABA_B$ potentiation on seizure-like event activity in cortical brain slices. Our hypothesis from the theoretical modelling is that increasing $GABA_B$ activity should increase the length of seizure like events, without effecting the amplitude. Our experimental results support both modelling predictions, as baclofen infusion significantly enhanced SLE length in the

slices, but had no significant effect on SLE amplitude. That this was a $GABA_B$-mediated effect was confirmed by blocking the baclofen effect with the $GABA_B$ antagonist saclofen.

In both slice observations (Figs 4.3 and 4.4) and model simulations (Fig. 4.5), the duration of the intermittent large-scale oscillations is drug dependent. For the numerical model, there is strong evidence that the oscillations are chaotic in nature (see Fig. 3.22(c)); thus bursting events are not noise-driven (Fig. 3.21). Whether or not the SLEs seen in slice measurements are chaotic or noise-driven is unknown, and would be very challenging to resolve since, unlike numerical simulations, noise in a biological system cannot be suppressed.

4.2 Gap junction blockade during anaesthesia

Blockade of connexin-36 (Cx36) gap junctions during anaesthesia may be important for destabilising brain activity. The extended mean-field Waikato model predicts that blocking gap-junctions enhances seizure activity in an anaesthetised brain (Chap. 3.1). This may explain why some anaesthetics cause seizures, as many of these agents also block gap junctions [105]. Previous work has shown that blockade of Cx36 gap junctions can have excitatory effects in the brain [92, 100]. However, to date the propensity for gap junction blockade to cause seizure activity during anaesthesia has not been investigated.

The present experiment was designed to investigate whether closing Cx36 junctions (the most common type of neuronal gap junction in the brain) during general anaesthesia induces signs of seizure activity in mice. This was done by recording the electroencephalogram while mice are anaesthetised with propofol, with or without pretreatment with the gap-junction-blocking drug mefloquine.

The hypothesis was that closing the gap junctions during general anaesthesia would induce signs of seizure activity.

4.2.1 Method

This section describes the methods employed in these experiments: drug preparation, procedures, data recording and data analysis.

Animals

After obtaining approval (923) from the Waikato Animal Ethics Committee, male and female ($n = 5$) wild-type (c57 and 129sv) mice aged 7–8 weeks, provided by the University of Waikato animal facility, were used for this study.

Drugs

The following drugs were used during the experimental procedures:

- propofol 10 mg/ml (Provive MCT-LCT, Claris, Australia) administered at the dose of 100 mg/kg; in the case that the main dosage did not put the animal to sleep, a top-up dose in the range of 50–100 mg/kg was administered.
- mefloquine 5 mg/ml (Sigma-Aldrich, NZ) was dissolved in H_2O, and administrated at the dosage of 50 mg/kg. This dose of mefloquine is sufficient to block Cx36 gap junctions but on its own does not cause seizure activity, although higher doses can cause seizure activity [3, 70, 102].

Both drugs were administered intraperitoneally (i.e., via injection into the peritoneum).

Data recording

EEG were recorded using a PowerLab 4/30 (AP Instruments, CA, USA), connected to an Animal Bio Amp[8] with three scalp electrodes.

Once the mouse had been anaesthetised, three needle electrodes were inserted under the skin on the scalp to detect EEG activity. The needles were 26 gauge surgical steel, sterilised with ethanol prior to use. Two needles were inserted on the top of the head above each cerebral hemisphere (active electrodes) and the third towards the back of the head (ground electrode). EEG recording was an essential part of this study because it was the only accurate way to robustly identify seizure-like activity that may not be obvious behaviourally. The recording was done over a continuous 20-min period with a 1–100 Hz pass-band and 400-Hz sampling rate with a notch filter set to 50 Hz to eliminate mains artifacts. EEG data were saved to computer for later analysis.

Experimental procedure

The aim of this experiment was to study the anaesthetised brain activity before and after the administration of the gap-junction-blocking agent. This required two sets of EEG recordings: first, monitoring the effect of propofol alone as a control; and the second, monitoring the effect of propofol plus mefloquine on brain activity. The experimental sequence was as follows:

- The experiment began with the injection of H_2O (i.p.) at the same volume as mefloquine
- After waiting for 30 min, propofol was administrated at the dose of 100 mg/kg in a volume up to 300 μL to achieve full anaesthesia (indicated by the loss of righting reflex)
- Scalp electrodes were inserted, then EEG was recorded from the anaesthetized mouse for 20 min
- Waited until animal returned to the normal activity and full consciousness (30–45 min)

[8] Animal Bio Amp is a high-performance software-controlled differential amplifier. The function of the amplifier is to amplify and filter small bioelectrical signals associated with nerve and muscle activity.

- Mefloquine (50 mg/kg) was injected in a volume of 100 μL
- After waiting for 30 min, propofol was injected (same quantity as previously)
- Cortical activity was recorded for 20 min, see Fig. 4.9.

At the end of the experiment, the needle electrodes were removed prior to anaesthesia wake-up and the animals were retained for use in future (unrelated) experiments. The EEG needle electrodes were sharpened and resterilised prior to reuse.

Video recordings were also taken to capture changes in animal behaviour. We were interested to see if there was any signs of seizure activity during the closure of gap-junctions, but none were observed.

4.2.2 Data analysis

The first step was a visual inspection of the raw EEG to detect any seizure activity, either interictal or ongoing oscillatory high-amplitude sharp (ictal) waves.

The second step was to compute the power spectral density for each set of data using MATLAB function `spectrogram`, which is based on the short-time Fourier transform (described in Chap. A.2). The aim was to look for mefloquine effects on anaesthetised brain activity which could be not detected through visual inspection.

4.2.3 Results and discussion

We did not observe any behavioural signs of seizure activity during any phase of the experimental protocol. Visual inspection of raw EEG recording also showed no sign of seizure activities in the anaesthetised brain.

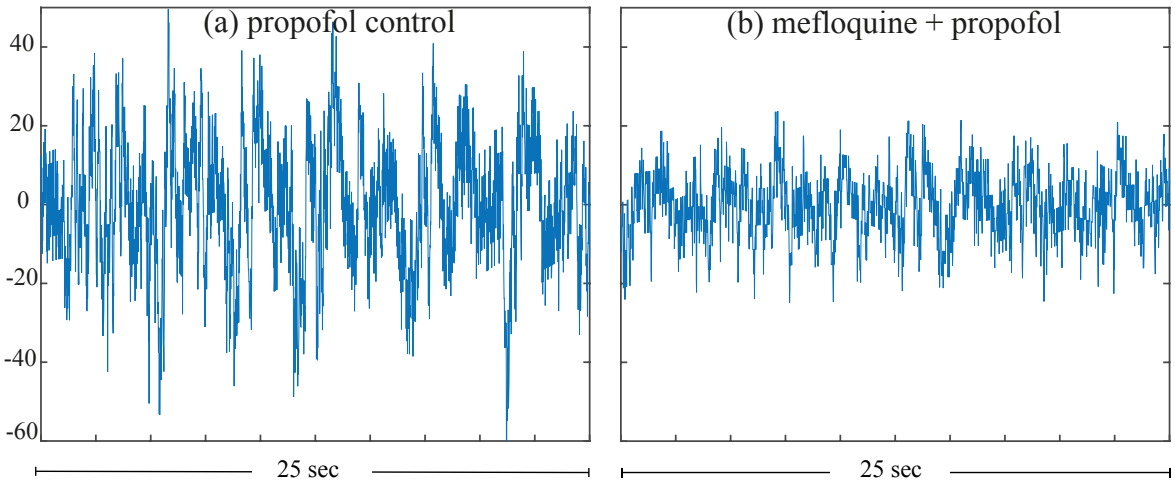

Figure 4.9. 25 s recording of animal EEG activity (a) during propofol exposure and (b) during propofol and mefloquine exposure. Closing gap-junctions reduced the amplitude of the anaesthetised brain activity. Recording was done over a continuous 20-min period with 1–100 Hz pass-band and 400 Hz sampling rate with the notch frequency of 50 Hz.

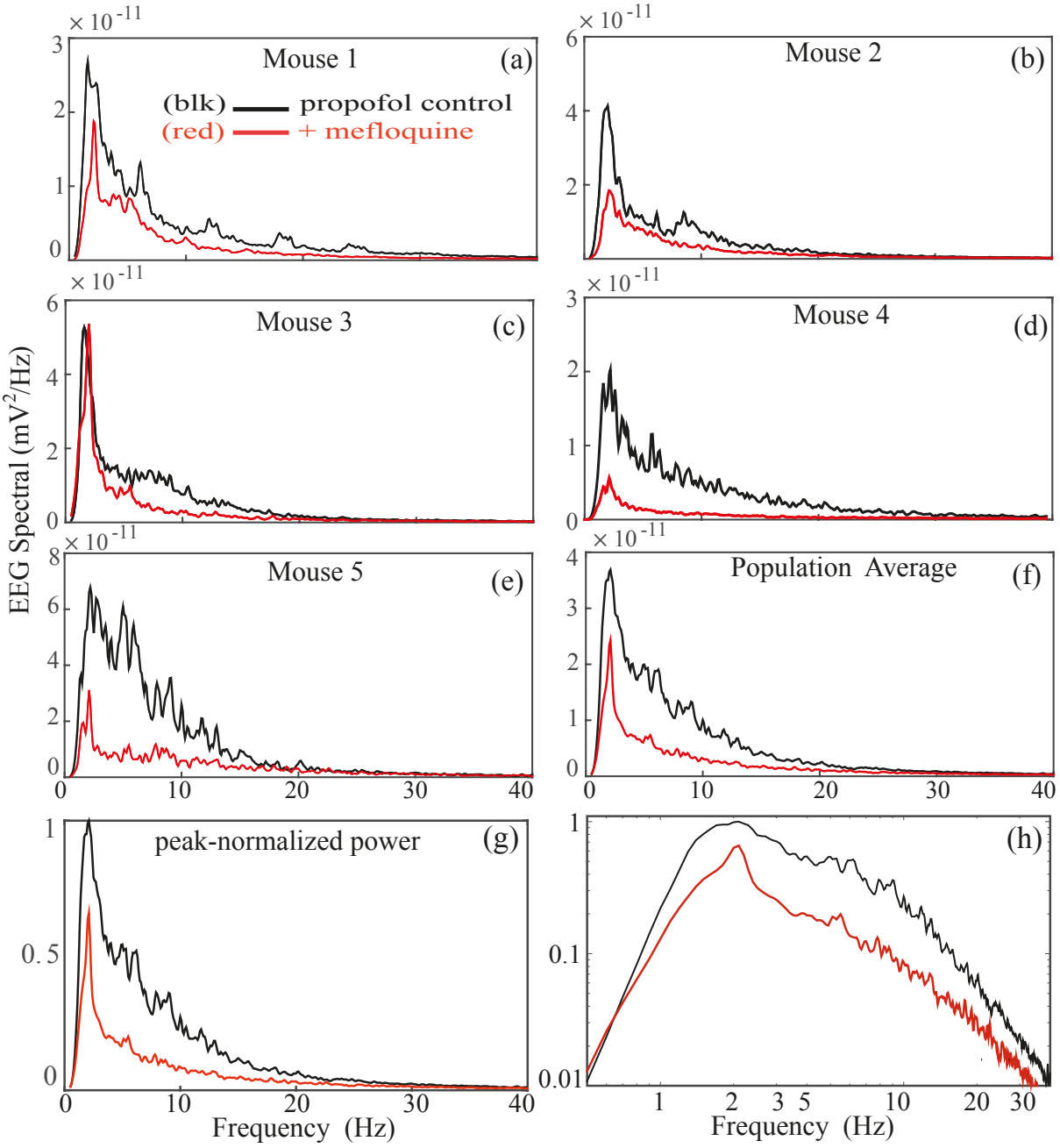

Figure 4.10. EEG spectra for five anaesthetized mice. (a) to (e) Spectra in the presence of mefloquine + propofol (red graph) and propofol only (black graph); (f) average spectral power for all mice; the average normalized EEG spectra on (g) linear and (h) log-log axes.

The EEG power spectral densities of EEG recording for each animal for both protocols (propofol only vs propofol plus mefloquine), are shown in Figs. 4.10 and 4.11. Spectral density peaked at delta (1–4 Hz) and low alpha (6–10 Hz) frequencies for the propofol only protocol. For the propofol plus mefloquine runs, the delta peak remained dominant, but higher frequency activity was strongly suppressed.

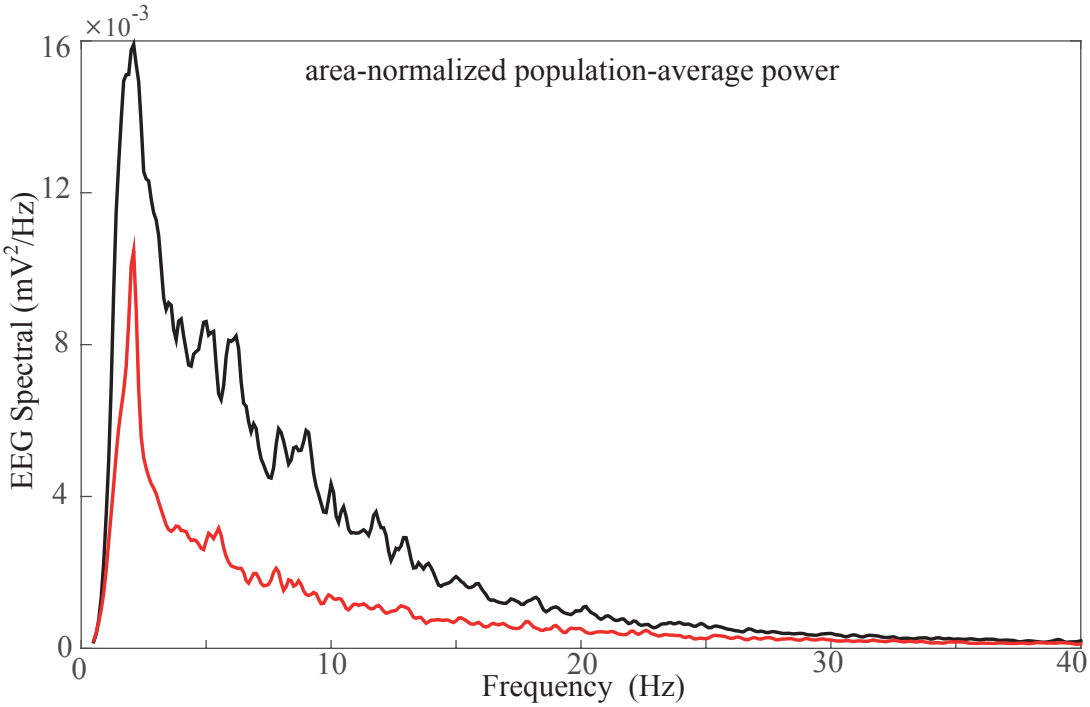

Figure 4.11. The area-normalized population-average EEG spectra, for more details see Fig. 4.10.

4.3 Conclusion

The Waikato model predicts that when the brain is at the boundary between consciousness and unconsciousness, closing gap junctions can cause seizure activity. However, no seizure activity was observed when mefloquine was preadministered to animals undergoing propofol anaesthesia. This may be because the animals in the current experiments transitioned rapidly into a deeply anaesthetized state in which seizure activity would not be expected. In other words, the brain was already on the bottom "comatose" branch of the steady state manifold at the time that EEG recording began.

The lower power in the mefloquine group is consistent and these animals being more deeply anaesthetised, in keeping with studies showing that Cx36 knockout mice require less anaesthetic [46].

In the second part of this thesis, we present a detailed analysis of the Hindriks and van Putten thalamocortical (TC) mean-field model [40] for propofol anaesthesia, an enhancement of the Robinson TC brain model.

Chapter 5

The Robinson thalamocortical model

5.1 Introduction

We now proceed to the second part of this thesis: a detailed investigation of the Hindriks and van Putten (HvP) model for propofol anaesthesia. The present chapter introduces the Robinson thalamocortical (TC) mean-field equations on which the HvP model is based. We will examine the properties and limitations of the HvP anaesthesia model (Chap. 6), then seek to remedy these shortcomings (Chap. 7).

5.2 Robinson thalamocortical model

We now give an overview of the thalamocortical model of Robinson, Rennie and Rowe [79]. Like the Waikato cortical model [90], the Robinson mean-field equations describe population-averaged neural activity, but unlike the Waikato formulation, the Robinson model incorporates two-way delayed connections between cortex and thalamus. The transmission delay is set at a fixed value of 80 ms, and, as we shall demonstrate in Sec. 5.3, is responsible for generating the ∼8-Hz alpha rhythm. Our demonstration proceeds via two theoretical experiments: first, by eliminating the thalamus; then by varying the TC round-trip delay from 0 to 100 ms.

The Robinson model [79] describes the dynamics of locally averaged membrane potentials of five distinct neural populations within the TC system in a mean-field representation:

- cortical pyramidal neurons (e) with large axonal ranges; these neurons form excitatory connections to cortical and thalamic neurons
- cortical inhibitory neurons (i) with short axon ranges; these form inhibitory synapses onto pyramidal and inhibitory cortical neurons
- thalamic sensory relay neurons (s); these excitatory neurons link activity in the thalamus to the cortex
- thalamic reticular neurons (r) which form inhibitory connections to the main body of the thalamus and are responsible for regulating thalamic activity
- non-specific neurons (n) are the excitatory populations lying outside the TC system

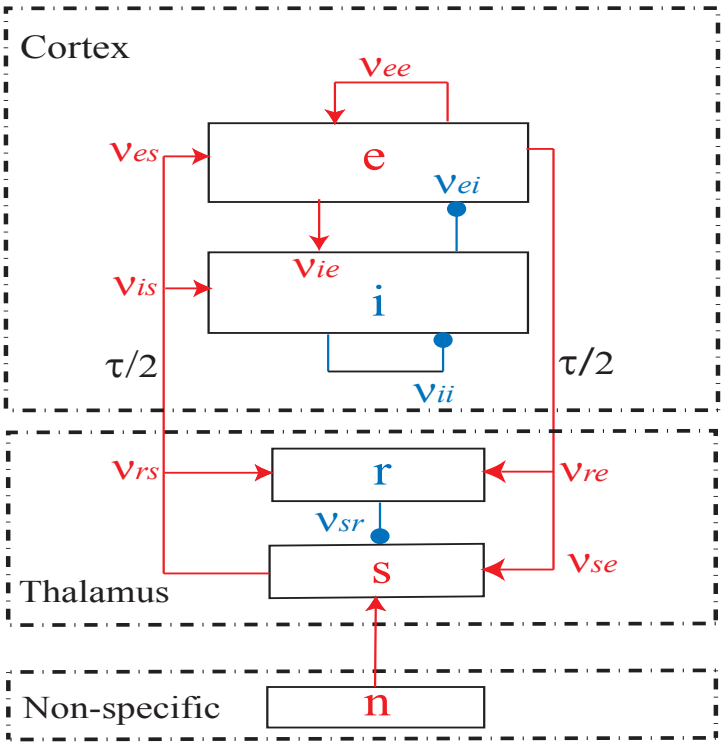

Figure 5.1. Robinson model connectivity. The model contains cortex and thalamus with two distinct excitatory and inhibitory populations in each: cortical pyramidal (e) and inhibitory (i) in cortex, thalamic reticular nucleus (r) and thalamic sensory nuclei (s) in thalamus. Non-specific neurons (n) lie outside the thalamocortical system. Arrowheads represent excitatory connections; solid circles show inhibitory connections. The round-trip loop delay of $\tau = 80$ ms from cortex to thalamus is assumed to be split symmetrically so that the $\tau/2$ propagation delay for signals to travel from cortex to thalamus matches that for the return path from thalamus to cortex.

These neural populations and their interconnections are illustrated in Fig. 5.1. There is a round–trip loop delay of $\tau = 80$ ms from thalamus to cortex to thalamus, split symmetrically between the forward and reverse branches. Symbol ν_{ab} defines the synaptic strength linking neural population b to neural population a (note that the double subscripts are read from right to left). The averaged effect of a sequence of action potentials on a neural population type a is represented as a sigmoidal mapping from voltage to average spike-rate,

$$Q(V_a) = \frac{Q^{\max}}{1 + \exp(-(V_a - \theta)/\sigma)}, \qquad a = e, i, r, s \tag{5.1}$$

where $Q^{\max}$ is the maximal firing rate in spike/s, V_a is the voltage (mV) at the cell body of given population a, θ is the average activation threshold (mV) at which the function has maximum sensitivity to small changes in the soma potential, and σ is proportional to the standard deviation of activation thresholds over the neural population. Here, it is important to mention that all four firing rate modulation functions Q_a (corresponding

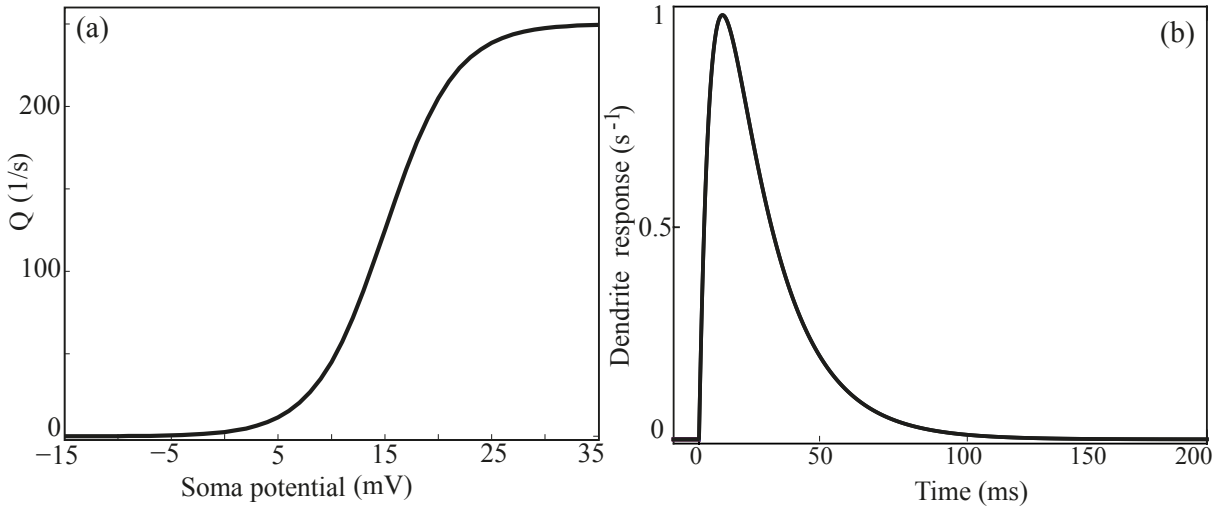

Figure 5.2. Firing rate and dendrite response functions. (a) Sigmoid curve relating average soma potential to average firing rate, defined by Eq. (5.1). (b) Synaptic response is modelled as a biexponential function, corresponding to Eq. (5.3). The sigmoid and synaptic response functions for all excitatory and inhibitory populations are identical in the Robinson model. (Note that soma potential is measured relative to resting potential.)

to four different populations) are identical in the Robinson model; see Fig. 5.2(a). However, clinical results have shown that different neuron populations have distinct threshold voltages [57] presenting different firing rate sigmoidal curves.

Robinson model equations

The soma voltage $V_a(t)$ is the sum of postsynaptic potentials $P_{ab}(t)$, generated by activity received from afferent (sending) populations b,

$$V_a(t) = \Sigma_b P_{ab}(t),$$

where postsynaptic potential $P_{ab}(t)$

$$\begin{aligned} P_{ab}(t) &= h_{ab}(t) \otimes \nu_{ab}\phi_b(t - \tau_{ab}) \\ &\equiv \int_0^t h_{ab}(t - t')\nu_{ab}\ \phi_b(t - t' - \tau_{ab})\ dt' \end{aligned} \tag{5.2}$$

is the result of convolving the input flux ϕ_{ab}, scaled by synaptic strength ν_{ab}, with the dendritic response function, $h_{ab}(t)$, modelled here as a biexponential of rise-rate β_{ab} and decay-rate α_{ab} ($\beta_{ab} > \alpha_{ab}$),

$$h_{ab}(t) = \frac{\alpha_{ab}\beta_{ab}}{\beta_{ab} - \alpha_{ab}} \left(e^{-\alpha_{ab}t} - e^{-\beta_{ab}t} \right) \tag{5.3}$$

The average membrane potentials V_e, V_i, V_r and V_s for the four distinct populations are written as follows:

$$V_e(t) = h_{ee}(t) \otimes \upsilon_{ee}\phi_e(t) + h_{es}(t) \otimes \upsilon_{es}Q_s(t - \tau/2) + h_{ei}(t) \otimes \upsilon_{ei}Q_i(t) \tag{5.4}$$

$$V_i(t) = h_{ie}(t) \otimes \upsilon_{ie}\phi_e(t) + h_{is}(t) \otimes \upsilon_{is}Q_s(t - \tau/2) + h_{ii}(t) \otimes \upsilon_{ii}Q_i(t) \tag{5.5}$$

$$V_s(t) = h_{sn}(t) \otimes \upsilon_{sn}\phi_n(t) + h_{se}(t) \otimes \upsilon_{se}\phi_e(t - \tau/2) + h_{sr}(t) \otimes \upsilon_{sr}Q_r(t) \tag{5.6}$$

$$V_r(t) = h_{re}(t) \otimes \upsilon_{re}\phi_e(t - \tau/2) + h_{rs}(t) \otimes \upsilon_{rs}Q_s(t) \tag{5.7}$$

where all of the $h_{ab}(t)$ are identical. Figure 5.1 illustrates the connectivity between separate cortical and thalamic populations, with time delay $\tau/2 = 40$ ms for long-range excitatory neural activity to travel between cortex and thalamus. A damped wave equation describes the propagation of the pyramidal neural activity $Q_e(t)$ within the cortex:

$$D_e\phi_e(t) = Q_e(t), \tag{5.8}$$

$$D_e = \left(\frac{1}{\gamma}\frac{\partial}{\partial t} + 1\right)^2 - \ell_e^2\,\nabla^2 \tag{5.9}$$

where D_e denotes the wave operator, ℓ_e is the mean range of cortical excitatory axons in meters, $\gamma = v/\ell_e$ is the damping rate in s^{-1}, and v is the axonal propagation velocity in $\mathrm{m\,s}^{-1}$. Table 5.1 lists the Robinson parameter values.

5.3 Source of alpha rhythm in Robinson model

To identify the source of alpha frequency in the Robinson model, two theoretical experiments are performed: the first examines the dynamical behaviour of the reduced Robinson model resulting from the elimination of the thalamus; the second investigates the effect of varying the TC time-delay τ. To our knowledge, such an investigation has not been reported previously.

5.3.1 Significance of thalamus

To confirm the importance of thalamus in the Robinson model, the cortex is isolated by cutting all connections between thalamus and cortex. Then Eqs (5.4) and (5.5) reduce to,

$$V_e(t) = h_{ee}(t) \otimes \upsilon_{ee}\phi_e(t) + h_{ei}(t) \otimes \upsilon_{ei}Q_i(t) \tag{5.10}$$

$$V_i(t) = h_{ie}(t) \otimes \upsilon_{ie}\phi_e(t) + h_{ii}(t) \otimes \upsilon_{ii}Q_i(t) \tag{5.11}$$

To determine the stability of the isolated cortex, we assume the system has achieved a steady state, then perform a linear stability analysis. For the isolated cortex, LSA predicts

Table 5.1. Parameter values for Robinson model constants. Excitatory (inhibitory) connections have positive (negative) synaptic strength, and are shown on Fig. 5.1 in red (blue).

Parameter	Symbol	Robinson and HvP	Unit
Maximal firing-rate	$Q^{\max}$	250	s^{-1}
Synaptic strength from e to e neurons	ν_{ee}	1.2	mV s
Synaptic strength from i to e neurons	ν_{ei}	-1.8	mV s
Synaptic strength from s to e neurons	ν_{es}	1.2	mV s
Synaptic strength from i to i neurons	ν_{ii}	-1.8	mV s
Synaptic strength from e to i neurons	ν_{ie}	1.2	mV s
Synaptic strength from s to i neurons	ν_{is}	1.2	mV s
Synaptic strength from r to s neurons	ν_{sr}	-0.8	mV s
Synaptic strength from e to s neurons	ν_{se}	1.2	mV s
Synaptic strength from s to r neurons	ν_{rs}	0.2	mV s
Synaptic strength from e to r neurons	ν_{re}	0.4	mV s
Average noise level	$\nu_{sn}\langle\phi_n\rangle$	1	mV
Rest potential (e, i, r, s)	V_a^{rest}	0	mV
Thalamocortical delay	τ	80	ms
Cortical damping rate	γ	100	s^{-1}
Synaptic rise rate	β	200	s^{-1}
Synaptic decay rate	α	50	s^{-1}
Sigmoid threshold voltage	θ	15	mV
Standard deviation for threshold	σ	3.3	mV

very strong stability in the cortex with dominant eigenvalue the $\Lambda_{\mathrm{dom}} = -50\ \mathrm{s}^{-1}$ with no possibility of oscillation; therefore the cortex-only reduced model cannot generate an alpha rhythm.

5.3.2 Effect of time-delay

Although Robinson et al [79] describe the thalamus as being the source of the alpha rhythm, no information is given regarding to the significance of the magnitude of the time-delay. Alteration of the time-delay does not affect the steady-state manifold, but the value of τ has a pronounced impact on system stability. Standard linear stability analysis is not applicable in the presence of time-delay. Instead, we need to compute the dispersion curves by transforming the system equations to the Fourier domain; see Appendix C for details.

Figure 5.3 presents the dispersion predictions for linear stability due to alteration of the time-delay. This figure provides clear insights as to the source of the alpha rhythm in the Robinson model. As time-delay is increased, the stability of the system decreases (the real part of the dominant eigenvalue becomes less negative) and the dominant frequency changes from delta to alpha band.

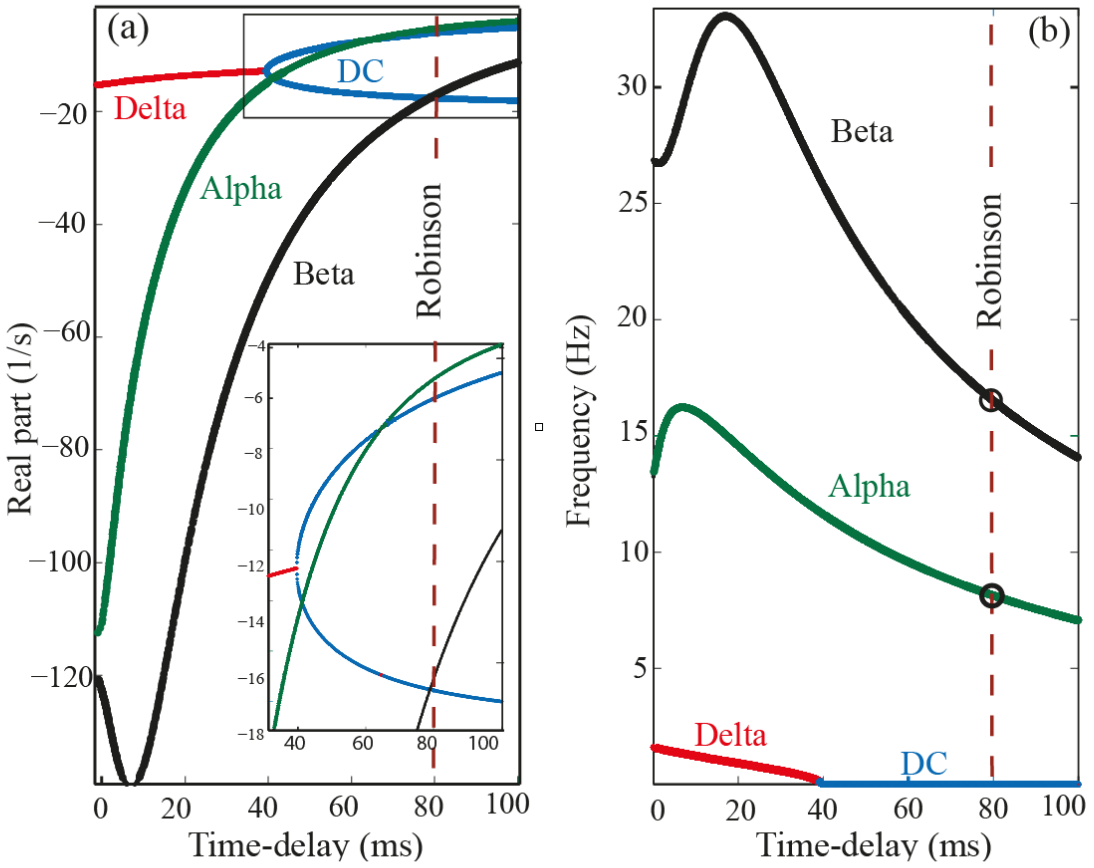

Figure 5.3. Effect of loop-delay τ on the linear stability of the original Robinson TC model (no propofol effect). Shown are (a) the damping rates and (b) frequencies of the TC system. The standard Robinson model fixes $\tau = 80$ ms, giving alpha oscillations ∼8 Hz as the dominant mode. Delta band mode is dominant for $\tau < 40$ ms, while alpha band is favoured for $\tau > 62$ ms.

Thus the loop delay time between cortex and thalamus plays a critical role in producing the alpha rhythm in this model. In fact, for $\tau > 62$ ms the alpha rhythm is dominant, while for $\tau < 40$ ms, the delta rhythm is preferred.

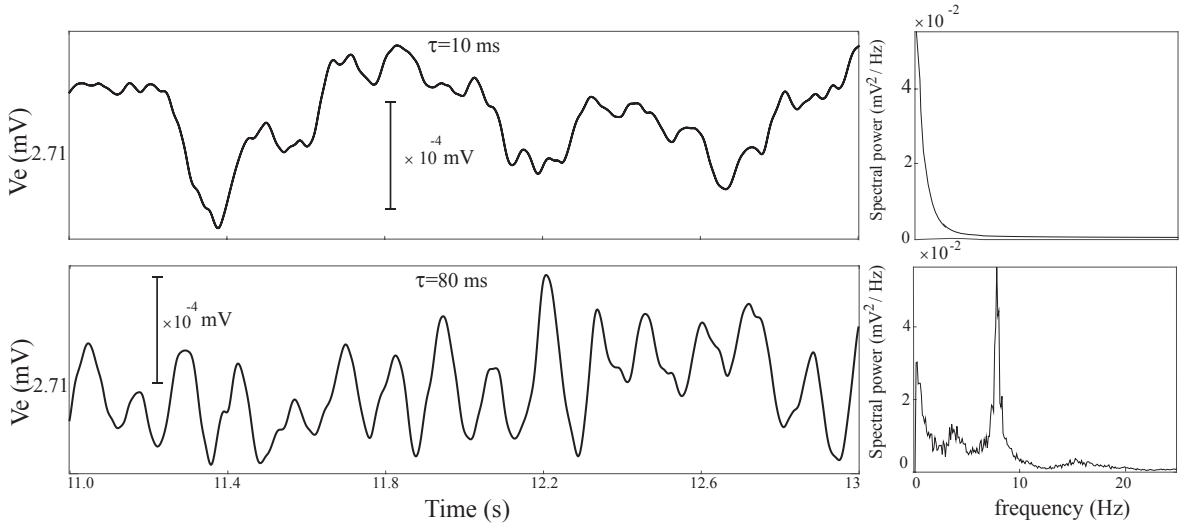

Figure 5.4. Simulation of Robinson model for two values of time delay (a) Setting $\tau = 10$ ms results in a dominant δ frequency; (b) Setting $\tau = 80$ ms gives a dominant α frequency.

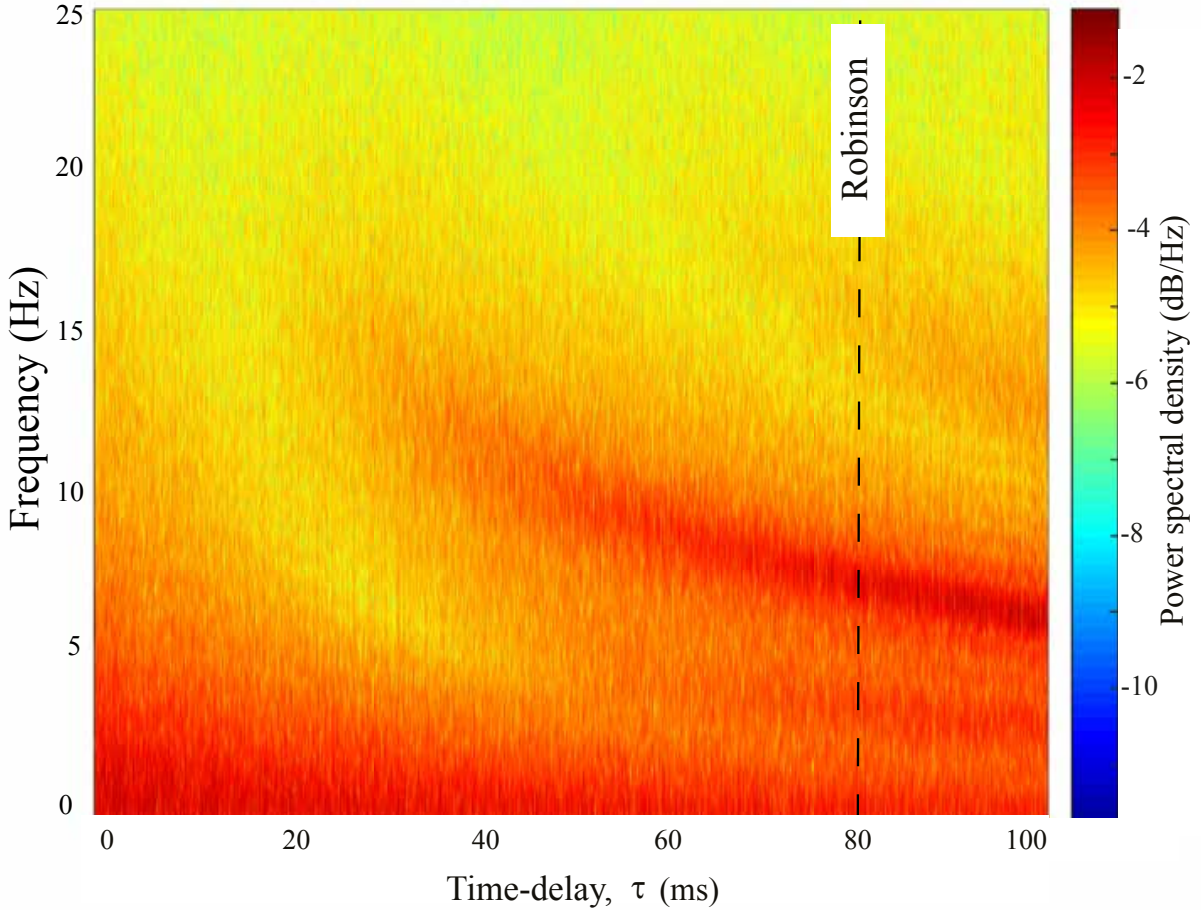

Figure 5.5. Effect of loop-delay τ on the fluctuation power spectral density in the Robinson TC model. This a spectrogram plot of the noise-evoked V_e spectral power as the TC delay is smoothly varied from 0 to 100 ms over a time interval 2000 s with Euler time-step $\Delta t = 10^{-4}$ s. These results confirm the stability predictions of the Fig. 5.3. Note that the zero-frequency component has been removed by applying a 0.5 Hz high-pass filter prior to Fourier analysis. Spectral power is normalized by noise power, which has a variance of 10^{-6}V^2; see Table 5.1.

To check the validity of these dispersion predictions, several numerical simulations were run for different time-delay settings. Figure 5.4(a) exhibits a very slow delta oscillation $f \approx 1$ Hz in the presence of the small value of time-delay $\tau = 10$ ms. Meanwhile, Fig. 5.4(b) shows that raising the TC time-delay to $\tau = 80$ ms raises the system frequency to $f \approx 8$ Hz. These findings are consistent with the dispersion predictions of Fig. 5.5.

Figure 5.5 plots a spectrogram of the white-noise-evoked V_e spectral power as the time delay is varied from 0 to 100 ms over a time interval 2000 s with Euler time-step $\Delta t = 10^{-4}$ s. These results confirm the dispersion stability predictions of Fig. 5.3: the beta and alpha-band frequencies reduce smoothly as τ is increased.

5.4 Conclusion

It is clear that the Robinson TC model is very sensitive to the time-delay for signals travelling between thalamus and cortex. Increases in time-delay tend to destabilize the

TC system. Emergence of alpha activity is crucially dependent on the existence of a sufficiently large thalamocortical loop delay. The standard Robinson model sets $\tau = 80$ ms, giving alpha oscillations $\sim$8 Hz as the dominant mode.

Chapter 6

Hindriks and van Putten anaesthesia model

6.1 Introduction

This chapter presents a detailed analysis of the Hindriks and van Putten (HvP) thalamocortical mean-field model for propofol anaesthesia [40]. As reported by Hindriks and van Putten, their model predicts increases in delta and alpha power for moderate (up to 130%) prolongation of $GABA_A$ inhibitory response, corresponding to light anaesthetic sedation [40]. However, we will show that for deeper anaesthetic effect, the model jumps from a low-firing state to an extremely high-firing stable state ($\sim$250 spikes/s), and remains locked there even at $GABA_A$ prolongations as high as 300% which would be expected to induce full comatose suppression of all firing activity.

Hindriks and van Putten [40] investigated general anaesthesia in the thalamocortical (TC) system by applying the Hutt and Longtin [44] drug mechanism to the mean-field TC equations of Robinson et al [79]. In marked contrast to other studies [13, 44, 71, 91], which assumed the same affinity for drug effect in all populations, Hindriks and van Putten enforced differing sensitivities for the different neural populations. They compared model predictions for propofol effect on brain activity with clinical EEG recordings, reporting a small increase in the alpha frequency, accompanied by increases in delta and theta power, as propofol concentration was raised to sedative levels.

The chapter begins with an introduction on the HvP model; then the link between the Robinson and HvP systems is elucidated. The HvP system behaviour across the full physiological range of anaesthetic effect ($1.0 \leq p_i \leq 3$) is compared against the originally reported results which were restricted to light anaesthetic sedation only ($1.0 \leq p_i < 1.29$) [40]. This comparison highlights a shortcoming of the HvP model under deepening anaesthesia: the sedated state loses stability, causing the TC system to jump to an extremely high-firing stable state at $p_i \gtrsim 1.298$.

6.2 Modelling propofol drug effect: HvP equations

For modelling the action of propofol, Hindriks and van Putten considered the fact that the binding of propofol molecules to $GABA_A$ receptors potentiates their response by decreasing the time constant of receptor deactivation, thereby increasing the duration of inhibitory synaptic transmission [1, 8, 25]. Thus the action of propofol is modelled as a decrease in the decay rate α_{ab} of the $GABA_A$ inhibitory response,

$$\alpha_{ab}(p_a) = \alpha_{ab}/p_a \qquad (a,b) \in \{(i,i),(e,i),(s,r)\} \tag{6.1}$$

where p_a is assumed to vary across the i, e, s populations based on distinct propofol *affinities* ε_{ab} for different $GABA_A$ receptor,

$$p_a = 1 + \varepsilon_{ab}(p_i - 1) \quad \text{with} \qquad a \in \{i,e,s\} \tag{6.2}$$

and $\varepsilon_{ii} = 1$, $\varepsilon_{ei} = \varepsilon_{sr} = 0.5$ (see Table 6.1). Thus cortical inhibitory neurons are assumed to be more strongly impacted by propofol than either cortical excitatory and relay neurons. This leads to three distinct inhibitory synaptic responses $\bar{h}_{ii}$, $\bar{h}_{ei}$ and $\bar{h}_{sr}$,

$$\bar{h}_{ab}(t) = \frac{\alpha_{ab}\beta}{\beta - \alpha_{ab}}\left(e^{-\alpha_{ab}t} - e^{-\beta t}\right), \qquad (a,b) \in \{(i,i),(e,i),(s,r)\} \tag{6.3}$$

where α_{ab} is a function of p_a. Equation (6.3) shows that the peak-height is not constant (it is a function of anaesthetic effect); however, based on the clinical finding reported by Bai et al [8] and Kitamura et al [56], the peak of amplitude of synaptic responses in the

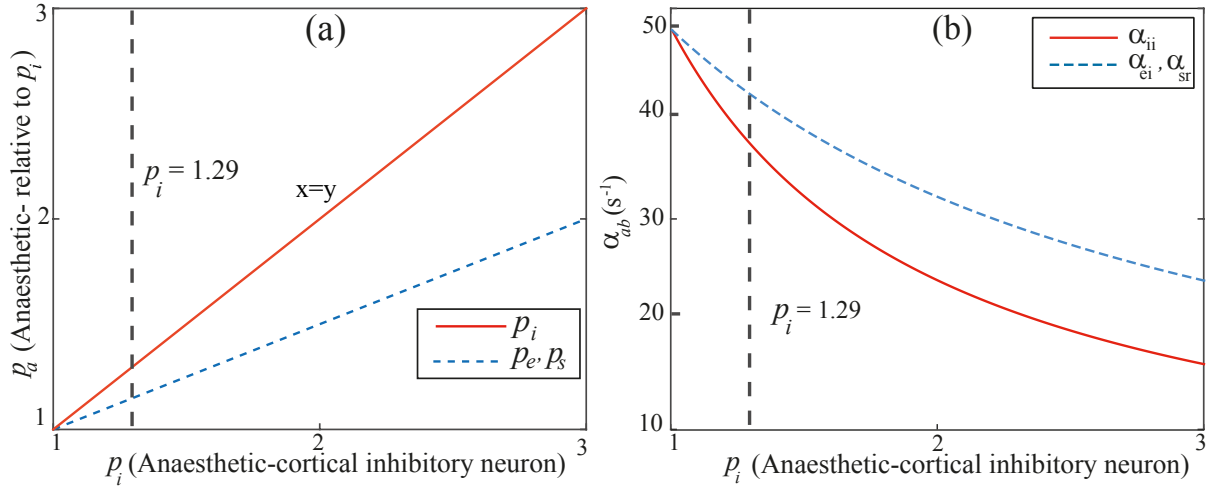

Figure 6.1. Drug effect and the decay rate for different synapses. Panel (a) presents different sensitivity of $GABA_A$ receptors to anaesthetic agents relative to affinity for cortical inhibitory neurons p_i. Panel (b) shows the decay rate α_{ab} for different synaptic responses due to increasing anaesthetic effect p_i.

HvP model are set to be constant by reparameterizing Eq. (6.3),

$$h_{ab}(t) = \frac{H}{\eta\left(\alpha_{ab}, \beta\right)} \bar{h}_{ab}(t) \tag{6.4}$$

where H is introduce as the synaptic efficacy, and $\eta(\alpha_{ab}, \beta)$ is the maximum value of $\bar{h}_{ab}$ obeying Eq. (6.5),

$$\eta\left(\alpha_{ab}, \beta\right) = \frac{\alpha_{ab}\beta}{\beta - \alpha_{ab}} \left[\exp\left(- \alpha_{ab} \frac{\ln \frac{\beta}{\alpha_{ab}}}{\beta - \alpha_{ab}} \right) - \exp\left(- \beta \frac{\ln \frac{\beta}{\alpha_{ab}}}{\beta - \alpha_{ab}} \right) \right] \tag{6.5}$$

Note that the maximum height of h_{ab} indeed equals H and hence is independent of the rate constants.

Figure 6.2 shows the h_{ii}, h_{ei} and h_{sr} IPSP response curves. As highlighted in Fig. 6.3, the red graphs indicate inhibitory responses that are modulated by anaesthetic effect. The average membrane potentials V_e, V_i, V_r and V_s are

$$V_e(t) = h_{ee}(t) \otimes \upsilon_{ee}\phi_e(t) + h_{es}(t) \otimes \upsilon_{es}Q_s(t - \tau/2) + h_{ei}(t) \otimes \upsilon_{ei}Q_i(t) \tag{6.6}$$

$$V_i(t) = h_{ie}(t) \otimes \upsilon_{ie}\phi_e(t) + h_{is}(t) \otimes \upsilon_{is}Q_s(t - \tau/2) + h_{ii}(t) \otimes \upsilon_{ii}Q_i(t) \tag{6.7}$$

$$V_s(t) = h_{sn}(t) \otimes \upsilon_{sn}\phi_n(t) + h_{se}(t) \otimes \upsilon_{se}\phi_e(t - \tau/2) + h_{sr}(t) \otimes \upsilon_{sr}Q_r(t) \tag{6.8}$$

$$V_r(t) = h_{re}(t) \otimes \upsilon_{re}\phi_e(t - \tau/2) + h_{rs}(t) \otimes \upsilon_{rs}Q_s(t) \tag{6.9}$$

with blue symbols indicating all inhibitory connections affected by anaesthetic. Setting drug effect $p_i = 1$ collapses the HvP model to the standard Robinson case. Note that

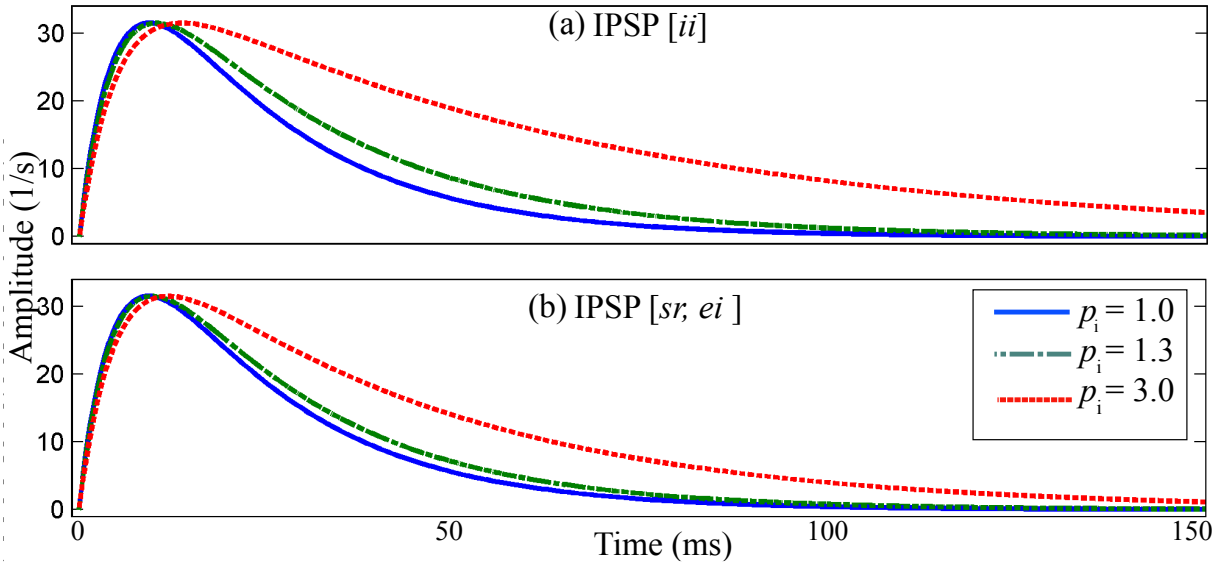

Figure 6.2. Synaptic responses in the HvP model. Panels (a) and (b) show the synaptic response due to increasing anaesthetic effect p_i on the (ii) and (ei, sr) connections respectively.

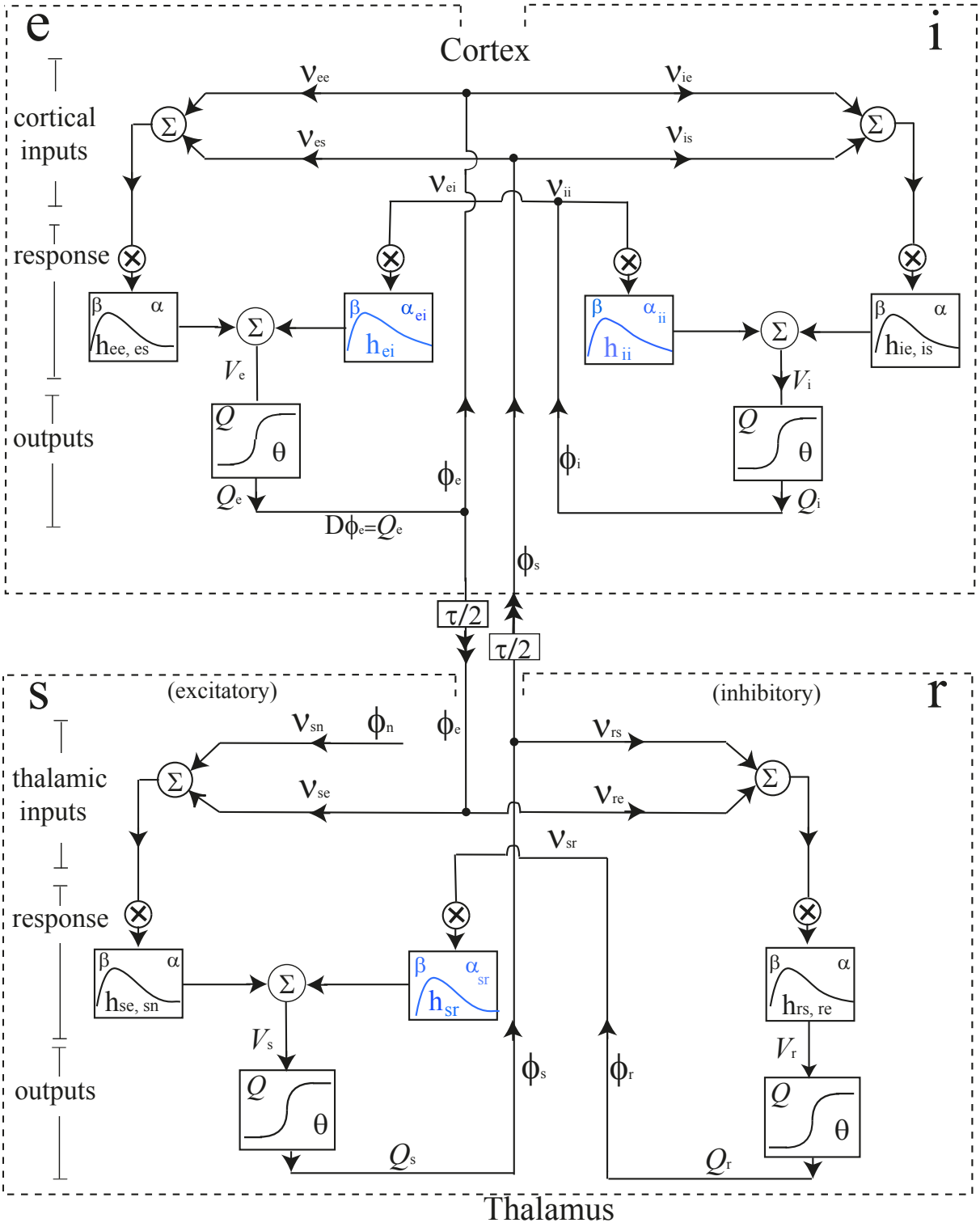

Figure 6.3. Schematic representation of cortical and thalamic connections in the HvP model. Excitatory neural populations appear on the left (e, s) and inhibitory populations (i, r) on the right; black boxes illustrate excitatory responses with no drug effect and blue graphs represent inhibitory responses due to drug effect. Input fluxes ϕ_b are scaled by synaptic strengths ν_{ab}, then convolved $(\otimes)$ with response functions h_{ab} and mapped to firing rates Q_a. The one-way transmission delay between cortex and thalamus is $\tau/2$.

Table 6.1. Parameter values for efficacy, affinity and synaptic rates in different neuronal populations

Parameter	Symbol	HvP	Unit
Synaptic efficacy	H	31.5	s^{-1}
Differential affinity of propofol (type i)	ϵ_{ii}	1	–
Differential affinity of propofol (type e)	ϵ_{ei}	0.5	–
Differential affinity of propofol (type s)	ϵ_{sr}	0.5	–
Synaptic rise rate	β_{ab}	200	s^{-1}
Synaptic decay rate	α_{ab}	50	s^{-1}

in the Robinson model all dendritic responses are identical with a fixed rate of decay $\alpha_{ab} = 50\ s^{-1}$.

6.3 Detailed examination of the HvP model

6.3.1 HvP model steady-state

Clinical results show relative increases in potentiation of inhibitory postsynaptic currents of up to 300% as propofol concentration is raised to a level sufficient to induce unconsciousness; this can be mapped to drug effect ranges $1.0 \leq p_i \leq 3.0$ [1, 106]. HvP system behaviour is investigated with respect to this extended but physiological range of anaesthetic effect.

The steady states are calculated by setting the spatial and temporal derivatives in the model equations to zero ($\nabla = 0$ & $\frac{\partial}{\partial t} = 0$ and $D_e = 1$). Since the homogeneous steady-state firing rates $(Q_e^*, Q_i^*, Q_s^*, Q_r^*)$ are not dependent on time and space, they satisfy,

$$\begin{aligned} y(t) &= h_{ab}(t) \otimes \upsilon_{ab} Q_b^* \\ &= \int_0^\infty h_{ab}(t) \upsilon_{ab} Q_b \, dt \\ &= \upsilon_{ab} Q_b \int_0^\infty h_{ab}(t) \, dt \\ &= \frac{H}{\eta_{ab}} \upsilon_{ab} Q_b^* \qquad \text{while} \qquad \int_0^\infty \bar{h}_{ab}(t) \, dt = 1 \end{aligned} \tag{6.10}$$

Substituting Eq. (6.10) in Eqs (6.6–6.9) gives:

$$V_e^* = \frac{H}{\eta}\upsilon_{ee}Q_e^* + \frac{H}{\eta}\upsilon_{es}Q_s^* + \frac{H}{\eta_{ei}}\upsilon_{ei}Q_i^* \tag{6.11}$$

$$V_i^* = \frac{H}{\eta}\upsilon_{ie}Q_e^* + \frac{H}{\eta}\upsilon_{is}Q_s^* + \frac{H}{\eta_{ii}}\upsilon_{ii}Q_i^* \tag{6.12}$$

$$V_s^* = \frac{H}{\eta}\upsilon_{sn}\phi_n + \frac{H}{\eta}\upsilon_{se}Q_e^* + \frac{H}{\eta_{sr}}\upsilon_{sr}Q_r^* \tag{6.13}$$

$$V_r^* = \frac{H}{\eta}\upsilon_{re}Q_e^* + \frac{H}{\eta}\upsilon_{rs}Q_s^* \tag{6.14}$$

Computing the stationary state trajectories as a function of anaesthetic effect p_i reveals multi-valued regions; these were not reported in the HvP results [40]. For the ranges $1.0 < p_i < 1.55$ and $2.7 < p_i < 3.0$, soma voltages (and firing rates) can take on three different values, either stable (shown in black) or unstable (red) (Fig. 6.4).

The pyramidal and reticular neural populations exhibit very high soma membrane potentials on the top branch B1 (corresponding to near maximal firing rates $Q \approx 250$ Hz), even at a deep anaesthesia corresponding to $\mathrm{GABA_A}$ prolongation as high as 300%. However, a different behaviour is observed for the relay and cortical inhibitory neurons: although the B1 top branch starts at maximum firing rates at $p_i = 1$, the high firing rates in relay neurons drop dramatically to almost zero at $p_i = 2.4$, while the high firing rates in cortical inhibitory neurons falls more smoothly to a lower range ($\sim 100\ \mathrm{s}^{-1}$). It is important to note that Hindriks and van Putten [40] reported only the low activity B3 branch; see the zoomed view on the second and fourth rows of Fig. 6.4.

6.3.2 Linear stability analysis, dispersion relation

To determine the stability of a dynamical system in the presence of a time-delay, the dispersion method in Fourier domain is applied. This transforms a delay τ in time to a phase shift $e^{i\omega\tau}$ in frequency space, and time-domain convolutions become products in Fourier space. Thus the temporal convolution between a time-delayed signal $Q_b(t - \tau_{ab})$ and the dentritic response $h_{ab}(t)$ maps to Fourier space as given by

$$P_a(t) = h_{ab}(t) \otimes Q_b(t - \tau_{ab}) \longleftrightarrow \widetilde{P}_a(\omega) = L_{ab}(\omega)\widetilde{Q}_b(\omega)\, e^{-i\omega\tau_{ab}}, \tag{6.15}$$

where ω denotes complex angular frequency. The Fourier transform of the synaptic response $h_{ab}(t)$ given the frequency response $L_{ab}(\omega)$,

$$L_{ab}(\omega) = \left(1 + \frac{i\omega}{\alpha_{ab}}\right)^{-1}\left(1 + \frac{i\omega}{\beta}\right)^{-1}$$

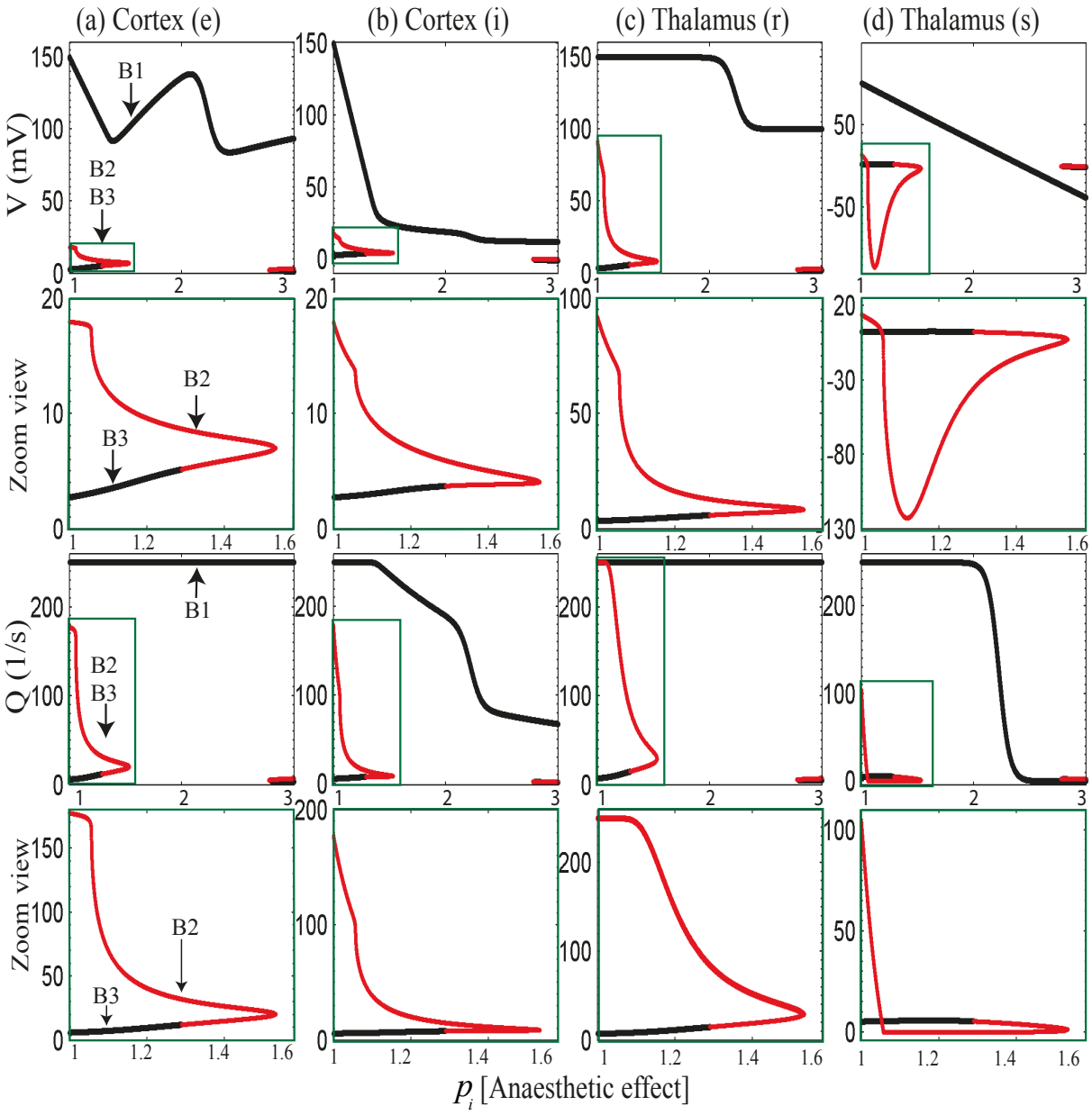

Figure 6.4. HvP model steady-states for soma voltages $V_{e,i,r,s}$ (first two rows) and firing rates $Q_{e,i,r,s}$ (bottom two rows). Boxed regions in first and third rows are expanded in the zoomed views of the second and forth rows. Black and red colours indicate stable and unstable equilibrium points respectively. Branch labels: B1 = top branch (high activity, always stable); B2 = mid branch (always unstable); B3 = bottom branch (low activity, becomes unstable). Note that only the stable solutions on the low activity B3 branch are reported in the HvP paper [40].

The transfer function relates the input $\tilde{\phi}_{\mathrm{n}}(\omega)$ to the output $\tilde{\phi}_{\mathrm{e}}(\omega)$ of the system equations (see Chap 2.4.1). For pairs of neuron types (a, b) both located either within cortex or within thalamus [*i.e.*, $(a, b) \in (e, e), (e, i), (i, e), (i, i), (r, s), (s, r)$] the frequency response from neuron type b to neuron type a is given by,

$$\zeta_{ab}(\omega) = \frac{H}{\eta(\alpha, \beta)} \upsilon_{ab} Q'(V_a^*) \left(1 + \frac{i\omega}{\alpha_{ab}}\right)^{-1} \left(1 + \frac{i\omega}{\beta_{ab}}\right)^{-1} \tag{6.16}$$

For pairs of neuron types separated by a time delay [*i.e.*, $(a,b) \in (e,s),(r,e),(i,s),(s,e)$] the frequency response from neurons of type b contains a phase shift from the propagation delay $\tau/2$ between cortex and thalamus,

$$\zeta_{ab}(\omega) = \frac{H}{\eta(\alpha,\beta)} \upsilon_{ab} Q'(V_a^*) \left(1 + \frac{i\omega}{\alpha_{ab}}\right)^{-1} \left(1 + \frac{i\omega}{\beta_{ab}}\right)^{-1} (e^{-i\omega\tau/2}) \tag{6.17}$$

In the HvP model, ϕ_e is taken to be proportional to the EEG [79]. To derive the transfer function, we linearise the sigmoid function about the steady state $(V_e^*, V_i^*, V_s^*, V_r^*)$ in the time domain for Eqs. (6.6–6.9). Then the system equations are rewritten in frequency domain. In Appendix C, we show how to derive the transfer function from $\widetilde{\phi}_n$ to $\widetilde{\phi}_e$ giving

$$\frac{\widetilde{\phi}_e}{\widetilde{\phi}_n} = \frac{\zeta_{eisn} + (1-\zeta_{ii})\zeta_{esn}}{[(\widetilde{D} - \zeta_{ee})(1-\zeta_{srs}) - \zeta_{ese} - \zeta_{esre}](1-\zeta_{ii}) - \zeta_{eie}(1-\zeta_{srs}) - \zeta_{eise} - \zeta_{eisre}} \tag{6.18}$$

The dispersion relation is obtained from the poles of the transfer function. This is equivalent to setting the denominator in Eq. (6.18) to zero, giving,

$$[(\widetilde{D} - \zeta_{ee})(1-\zeta_{srs}) - \zeta_{ese} - \zeta_{esre}](1-\zeta_{ii}) - \zeta_{eie}(1-\zeta_{srs}) = \zeta_{eise} + \zeta_{eisre} \tag{6.19}$$

In the HvP model, we restrict our attention to the spatially-homogeneous dynamic ($k = 0$) as it simplifies the analysis of dispersion relation. A solution for ω of Eq. (6.19) corresponds to a thalamocortical resonance of damping rate $\mathrm{Im}(\omega)$, angular frequency $\mathrm{Re}(\omega)$. Stable resonances are characterized by $\mathrm{Im}(\omega) < 0$ and unstable resonances are characterized by $\mathrm{Im}(\omega) > 0$.

LSA shows that B1 branch is strongly stable, while B2 is strongly unstable. Our focus here is the low activity B3 branch, since only the B3 solutions are considered in the HvP paper [40]. Figure 6.5(b) indicates at $p_i = 1.298$ the B3 stable branch loses stability.

To prove the validity of LSA predictions, simulations are run at three different levels of propofol: $p_i = 1$, stable; $p_i = 1.329$, marginal; $p_i = 1.48$, strongly unstable. Run (1) shows small fluctuations about equilibrium. Run (2) transitions to growing limit cycle, while run (3) jumps to an extreme high firing state. Our investigation shows the HvP system is not able to return to low activity after jumping to a high activity state, and it remains there even after reducing the drug effect, as shown in the hysteresis results of Fig. 6.6.

Our numerical simulations confirm the existence of the B1 pathological high firing state, and the abrupt transition from B3 to B1 branches at drug effect $p_i \gtrsim 1.37$ (Fig. 6.6). Simulation begins at the $p_i = 1.0$ equilibrium point on the stable portion of the low-activity B3 branch (see Fig. 6.4), then p_i is slowly ramped to 3.0 over 2000 s in an

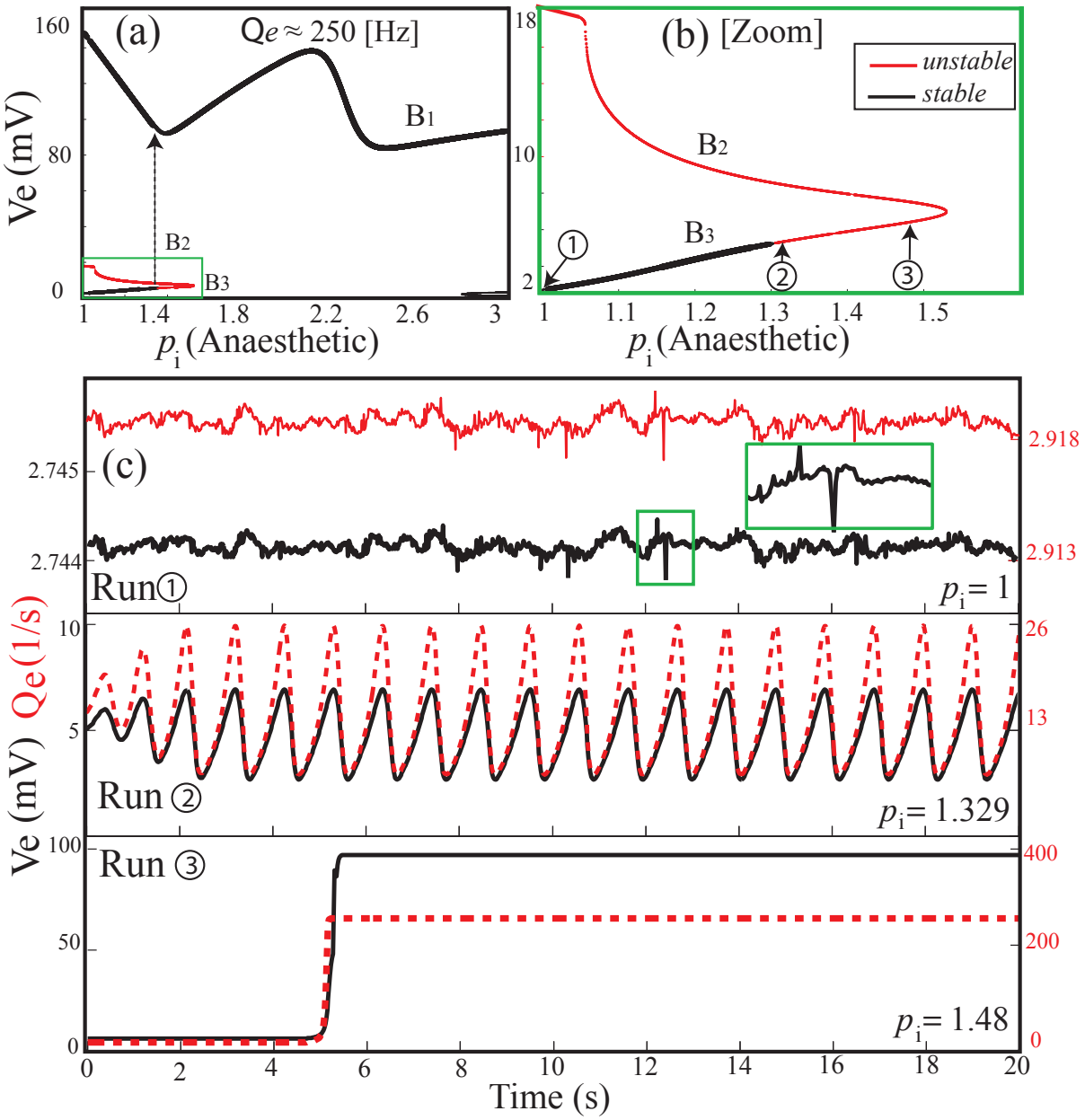

Figure 6.5. Distribution of HvP model pyramidal steady states voltages under anaesthetic effect and thalamocortical simulation results at three nominated p_i values. (a) Steady states and (b) zoom view of B2 (unstable) and B3 (mixed stability) branches. (c) Stochastic simulations are run for 20 s at three locations on the B3 branch: (1) $p_i = 1.0$ (stable); (2) $p_i = 1.329$ (weakly unstable); (3) $p_i = 1.48$ (strongly unstable). Simulation settings: Euler integrator, $\Delta t = 10^{-4}$ s, low-intensity white noise to V_e, V_i, V_r, V_s. Note that (a) and (b) replicate the top left panels of the first two rows of Fig. 6.4.

attempt to simulate induction of anaesthesia. Rather than suppressing cortical activity, increasing drug effect (red curves) leads to increasing voltage and firing rate, culminating in an abrupt transition to a pathologically high-firing state for $p_i \simeq 1.37$, subsequent to loss of B3 stability for $p_i \simeq 1.29$ (see Fig. 6.4). The cortex remains stuck on the pathological B1 branch, even when p_i is reduced (dashed-black curves) from 3.0 back to 1.0. Once the hyperexcited state has been reached, there is no mechanism for recovering

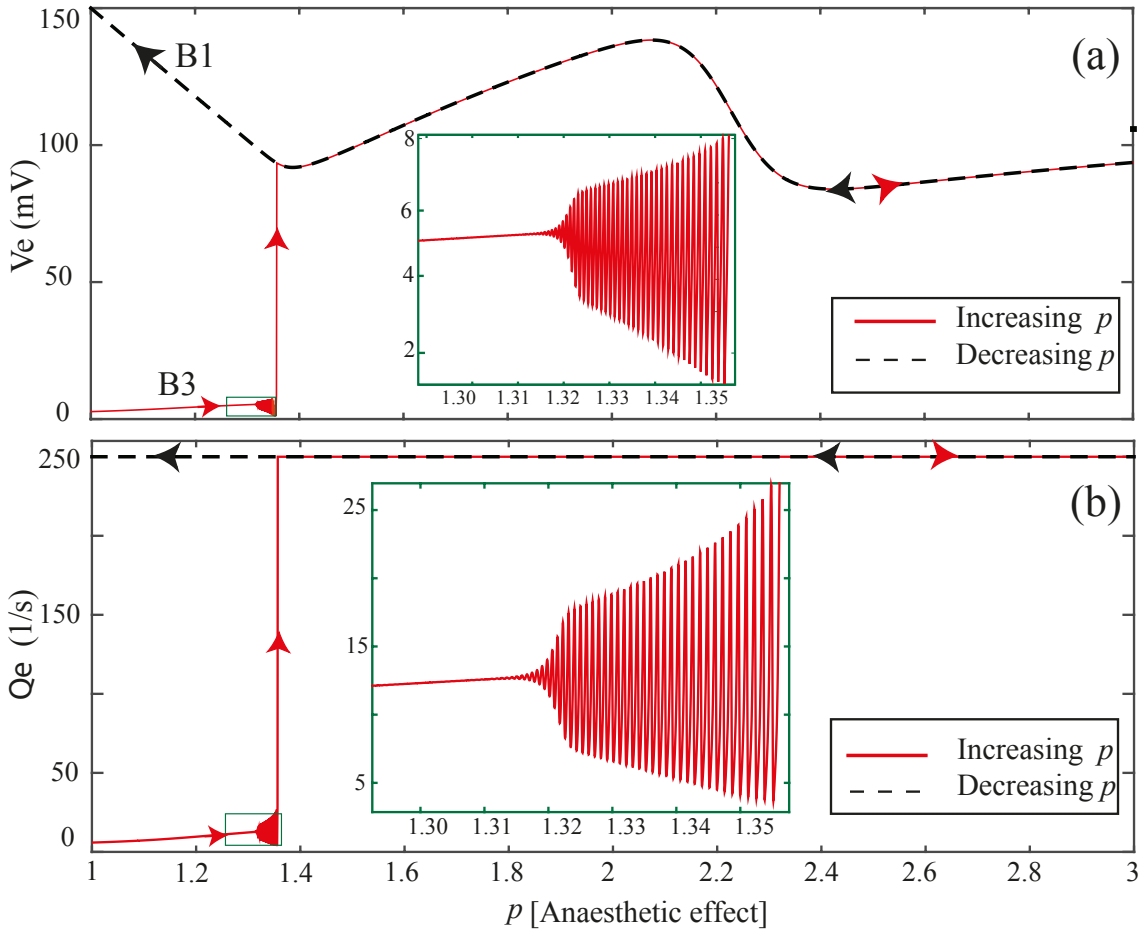

Figure 6.6. Numerical simulations showing pathological phase transition and hysteresis for the HvP model for anaesthesia. (a) V_e soma voltage and (b) Q_e firing rate of excitatory cortical neurons for increasing (red) and decreasing (dashed black) levels of anaesthetic effect p_i for $1.0 \leq p_i \leq 3.0$. Simulation begins at the $p_i = 1.0$ equilibrium point on the stable portion of the low-activity B3 branch (see Fig. 6.4), then p is slowly ramped to 3.0 over 2000 s (Euler simulation, time-step $\Delta t = 10^{-4}$ s). Increasing drug effect (red curves) leads to *increasing* voltage and firing rate, culminating in an abrupt transition to a pathologically high-firing state for $p_i \simeq 1.37$, subsequent to loss of B3 stability for $p_i \simeq 1.29$.

normal firing rates.

6.4 Source of alpha rhythm in the HvP model

6.4.1 Effect of time-delay

In Chap 5.3.2, we showed that the setting of thalamocortical delay is fundamental to the generation of the alpha rhythm in the Robinson model. The standard Robinson model sets $\tau = 80$ ms, giving alpha oscillations ~8 Hz as the dominant eigenvalue mode (see Fig. 5.3). To investigate the significance of the time-delay on the generation of the alpha rhythm in the HvP model, we performed a new set of theoretical experiments. Fig. 6.7 presents the effect of the time-delay variation on the linear stability of the HvP model.

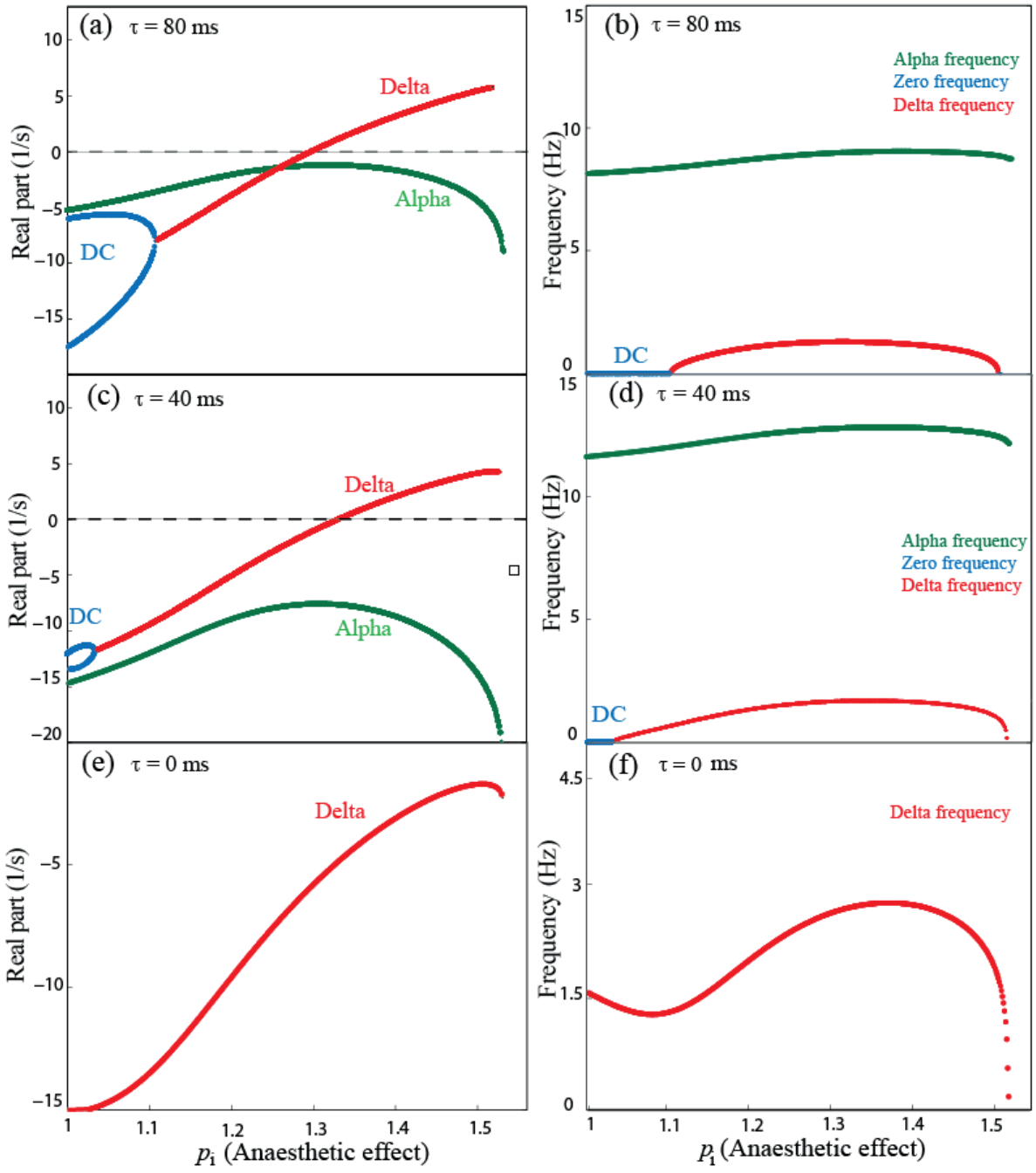

Figure 6.7. Effect of thalamocortical time delay τ on linear stability of the HvP model for the low-activity branch B3. Shown are the damping rates on the left and frequencies on the right for three different values of the time delay $\tau = 0, 40, 80$ ms. Reducing the time delay increases the stability of the system (left graphs), changing the dominant mode from alpha to delta frequencies. At $\tau = 0$, lower branch B3 is completely stable and the system no longer has access to the extreme high-firing branch B1. DC refers to the zero-frequency eigenvalue.

We see that as time delay decreases, system stability increases and the frequency of dominant mode rises.

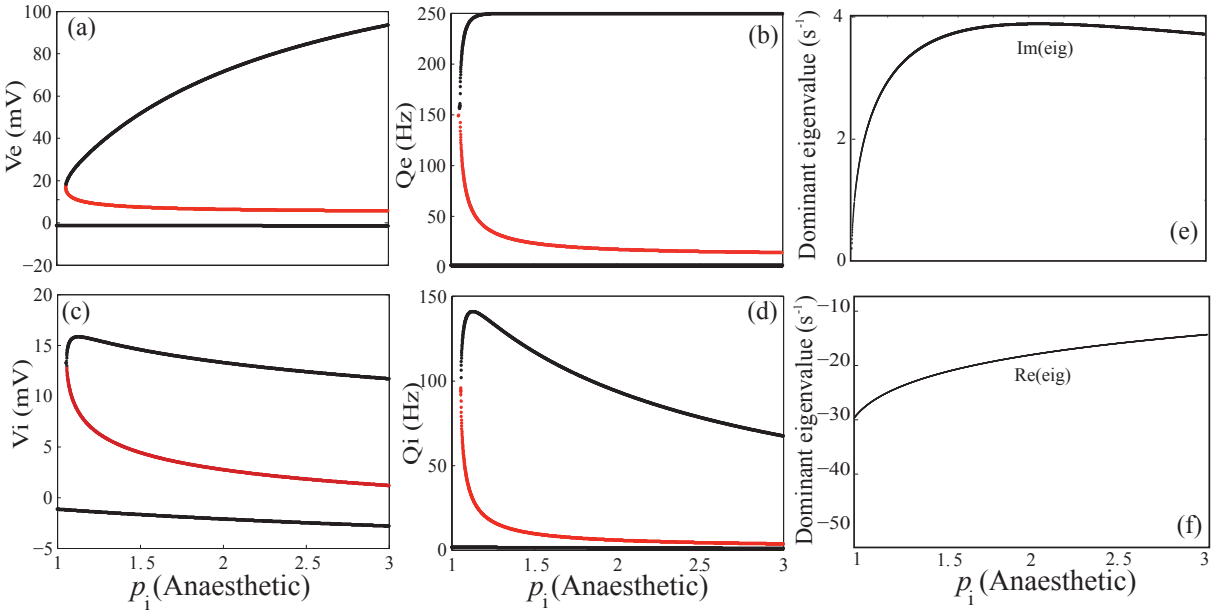

Figure 6.8. Distribution of steady states in the cortex-only HvP model. Panels (a) and (b) represent trajectories of the excitatory voltage and firing rates respectively; panels (c) and (d) are the corresponding inhibitory values. Panel (e) shows the real part of the dominant eigenvalue in the lower branch, and (f) illustrates the imaginary part (damping).

6.4.2 Significance of thalamus

To confirm the importance of thalamus in the HvP model, the cortex is isolated by cutting all connections between thalamus and cortex. Then Eqs (6.11) and (6.12) reduce to,

$$V_e(t) = h_{ee}(t) \otimes \upsilon_{ee}\phi_e(t) + h_{ei}(t) \otimes \upsilon_{ei}Q_i(t) \tag{6.20}$$

$$V_i(t) = h_{ie}(t) \otimes \upsilon_{ie}\phi_e(t) + h_{ii}(t) \otimes \upsilon_{ii}Q_i(t) \tag{6.21}$$

To determine the stability of the isolated cortex, we assume the system has achieved a steady state; Figs 6.8(a) and (c) indicate the equilibrium membrane voltages for the

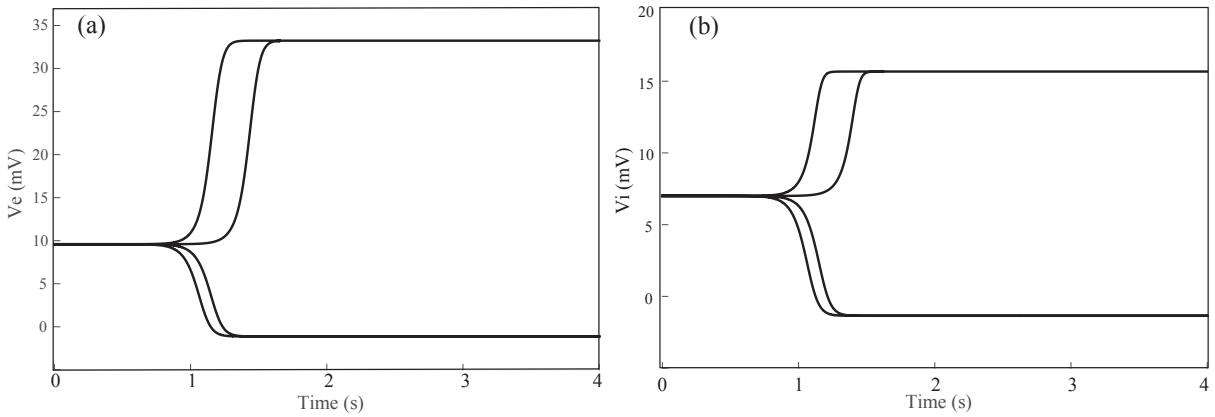

Figure 6.9. Simulations of the cortex-only reduced HvP model. Four-second time development of the cortical excitatory (a) and inhibitory (b) populations; all simulations are launched from the unstable middle branch.

excitatory and inhibitory cortical populations respectively.

A linear stability analysis for the isolated cortex predicts very strong stability in both upper and lower branches, and strong instability in the middle branch. Figure 6.8(e) and (f) show the imaginary and the real parts of the dominant eigenvalue for the lower branch; we note that the cortex-only reduced HvP anaesthetised model cannot generate an alpha rhythm.

To confirm our linear stability predictions, we ran several simulations, all starting from unstable-middle branch at the anaesthetic effect fixed at $p_i = 1.2$. As shown in Fig. 6.9, the isolated cortex leaves the unstable middle branch after less than 1 s and switches either to the upper or lower branch, both of which are strongly stable.

6.5 Conclusion

We have compared the HvP system behaviour across the full physiological range of anaesthetic effect ($1.0 \leq p_i \leq 3$) against the originally reported results [40] which were restricted to light anaesthetic sedation only ($1.0 \leq p_i < 1.29$). This comparison highlights a shortcoming of the HvP model under deepening anaesthesia: the sedated state loses stability, causing the TC system to jump to a pathologically high-firing stable state at $p_i \gtrsim 1.298$.

The high voltage state exists for both pyramidal and reticular neurons even at $GABA_A$ prolongation as high as 300%. In fact, setting the propofol affinity in pyramidal and reticular dendrites at half that for cortical inhibitory cells markedly *decreases* inhibition in the anaesthetised brain.

We find that the HvP model dynamics is highly sensitive to the value selected for τ, the TC loop delay: decreasing the time delay not only changes the resonance frequency, but also increases system stability, (Fig. 6.7). As we showed in Fig. 5.3, the loop delay is crucial for the production of alpha rhythm.

In the next chapter, we investigate some possible solutions to eliminate the pathological behaviour of the HvP model for deep anaesthetic effect.

Chapter 7

Modified Hindriks and van Putten model

7.1 Introduction

In chapter 6, we compared the HvP system behaviour across the full physiological range of anaesthetic effect ($1.0 \leq p_i \leq 3$) against the originally reported results which were restricted to light anaesthetic sedation only ($1.0 \leq p_i < 1.29$) [40]. This comparison highlighted a shortcoming of the HvP model under deepening anaesthesia. We now suggest some modifications to overcome the unphysiological behaviour of extreme high firing rates observed in Fig. 6.4.

In this chapter we attempt to restore biophysical fidelity with suitable adjustments to drug efficacy, and by including synaptic reversal potentials:

- **Standard drug modelling** In the HvP model, the pyramidal and relay populations are assumed to be less sensitive to propofol ($\epsilon_{ei} = \epsilon_{sr} = 0.5$) compared with cortical inhibitory neurons ($\epsilon_{ii} = 1$). We investigate the impact of equalizing drug sensitivity across populations by setting all efficacies equal ($\epsilon_{ii} = \epsilon_{ei} = \epsilon_{sr} = 1$).
- **Inclusion of reversal potential** We alter HvP model by incorporating reversal potentials, adjusting the excitatory sigmoid parameters, and eliminating the population-dependent anaesthetic efficacies.

7.2 Effect of efficacies in the HvP model

To gain a better understanding of how different efficacies of $GABA_A$ receptors impact HvP system characteristics, we examine the effect of pyramidal and relay neuron efficacy on steady-state trajectories and stability.

As shown in Fig. 6.4, the HvP model loses stability on bottom branch B3 at drug effect $p_i = 1.3$ and jumps to the high-firing branch B1. Since $p_i = 1.3$ is considered as the critical point, we are interested to learn how efficacy alterations influence system steady states and stability at this point.

Fig. 7.1 shows the effect of pyramidal efficacy variation on the system equilibrium points. The efficacy for pyramidal cells varies over the valid range $0 \leq \epsilon_{ei} \leq 1.0$, while the efficacy for relay neurons remains unchanged as shown in Table 7.1; the drug effect is set to $p_i = 1.3$. We observe a single-valued steady-state region with extremely high-firing rate for $\epsilon_{ei} < 0.32$. As the pyramidal efficacy ϵ_{ei} is increased above 0.32, multi-valued steady-states emerge. (The parameter set corresponding to the HvP model is marked with a dashed vertical line.)

For the low range $\epsilon_{ei} < 0.32$, system excitation increases, leading to extremely high firing for all populations. Conversely, increasing ϵ_{ei} decreases excitation (e.g., at $p_i = 1.3$, the pyramidal membrane voltage is $V_e = 160$ mV in the original HvP model, but this drops to 53 mV when $\epsilon_{ei} = 1$). The dispersion curve predicts very strong stability for the top branch with no interesting dynamics. For the bottom branch B3, an instability

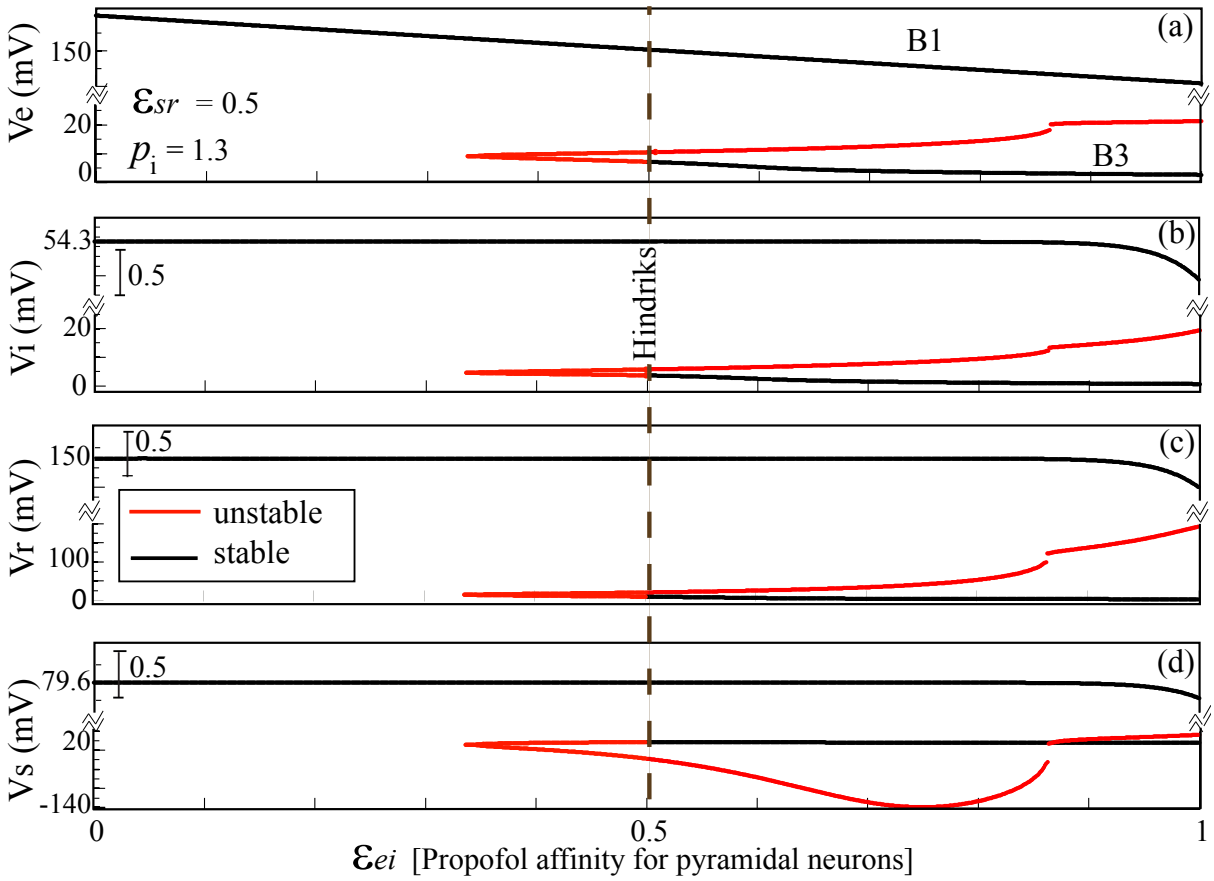

Figure 7.1. Effect of pyramidal efficacy (ϵ_{ei}) on steady state trajectories and stability for the HvP model. Shown are steady states for all populations, with the drug effect and the relay efficacy remaining fixed at $p_i = 1.3, \epsilon_{sr} = 0.5$. Increasing pyramidal efficacy from 0 to 1.0 not only alters the number of steady states from one to three but also increases system stability. Dashed line marks the HvP set; we note that the low-activity B3 branch becomes stable as it crosses the $\epsilon_{ei} = 0.5$ Hindriks marker (the discontinuity in the unstable branch near $\epsilon_{ei} = 0.86$ disappears if an extremely fine root search is undertaken).

observed for the range of pyramidal efficacies $0.32 < \epsilon_{ei} < 0.5$, but as efficacy is increased ($\epsilon_{ei} \geqslant 0.5$) the bottom branch becomes completely stable.

The effect of relay neuron efficacy on the system equilibria is illustrated in Fig. 7.2. Relay neuron efficacy is varied over the range of $0 \leq \epsilon_{sr} \leq 1.0$, while the efficacy for pyramidal neurons fixed at $\epsilon_{er} = 1$ and the drug effect is set to $p_i = 1.3$. Increasing relay efficacy does not have any significant effect.

We can conclude that the effect of pyramidal efficacy on HvP model characteristics is much stronger than that from relay neurons. These results are reasonable as pyramidal neurons are long-range and are able to propagate in the TC system through the wave equation so their contribution to soma voltages in all populations is more significant.

7.3 Modified HvP model

To correct the HvP model, we propose two modifications: first, we present the HvP model under standard drug modelling $\epsilon_{ii} = \epsilon_{ei} = \epsilon_{sr} = 1$; second, we introduce reversal

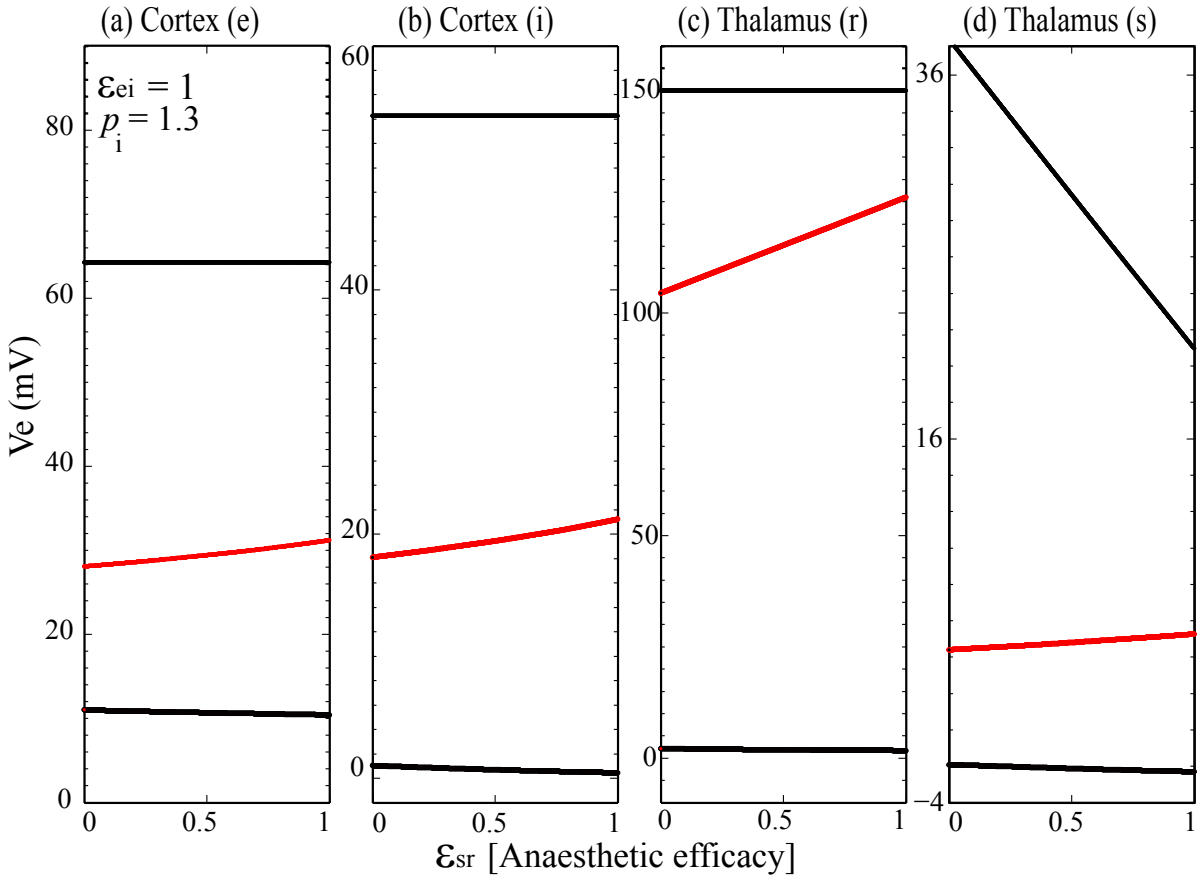

Figure 7.2. Effect of the relay efficacy (ϵ_{sr}) on steady state stability for the HvP model. Shown are steady states for all populations, with the drug effect and the relay efficacy remaining fixed at $p_i = 1.3$, $\epsilon_{ei} = 1$. Increasing the relay efficacy from 0 to 1.0, does not have any significant effect on the number of steady states and system stability.

potentials. Since the mid-branch is always unstable and the thalamocortical system can never move to that state, it is ignored in the following sections.

7.3.1 Standard drug modelling

Setting all efficacies to the maximum value ($\epsilon_{ei} = \epsilon_{ii} = \epsilon_{sr} = 1$) switches the HvP drug modelling to the standard method [13, 44, 71, 91]. We calculated the steady states under the new conditions, then performed a linear stability analysis of the top branch B1 and bottom branch B3; see Figs 7.3 and 7.4. For each figure, panel (a) illustrates steady-states trajectories with one highlighted branch; panels (b) and (c) show the real part and frequency of the dominant eigenvalues for the considered branch respectively.

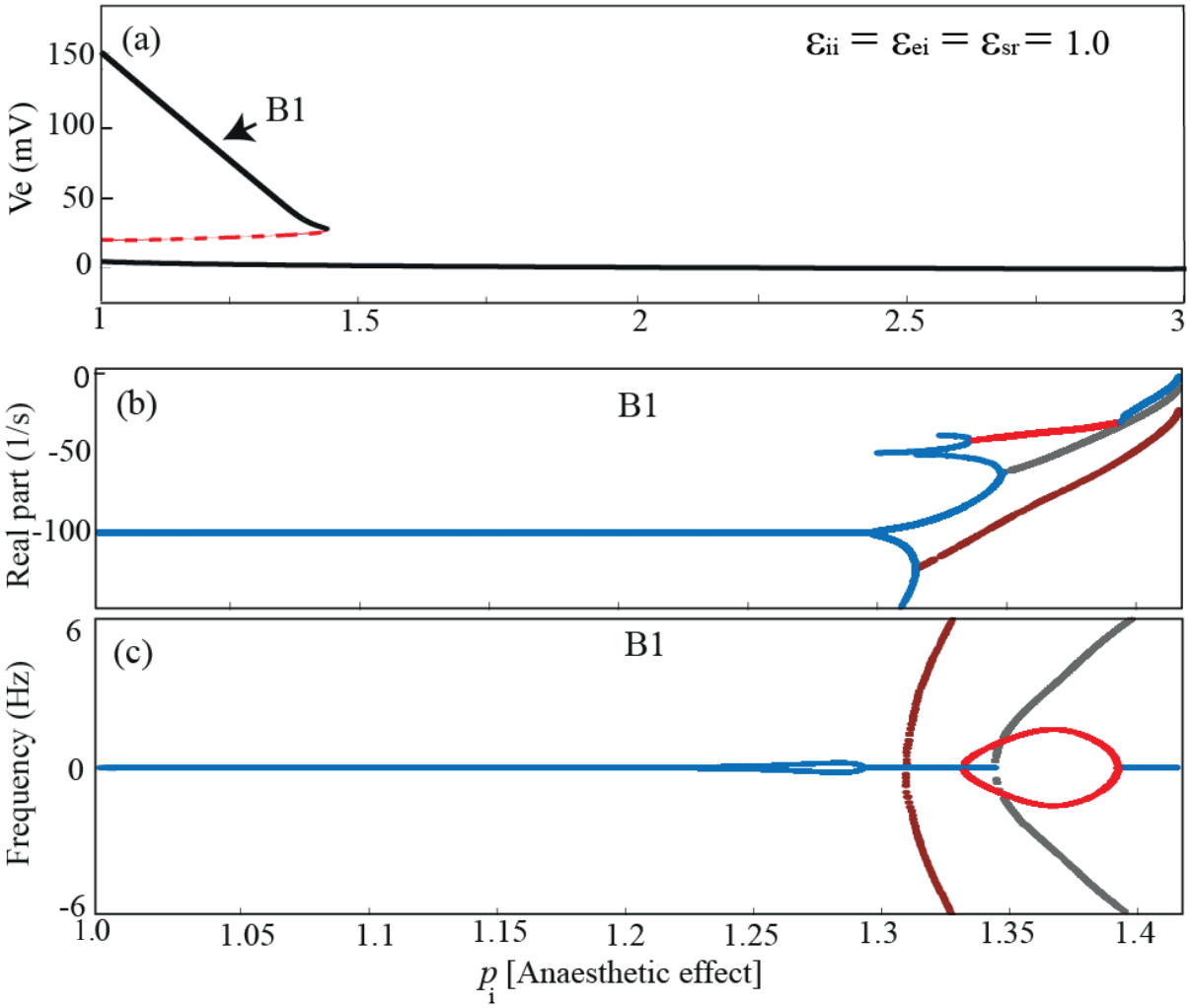

Figure 7.3. Effect of setting all efficacies to maximum value ($\epsilon_{ii} = \epsilon_{ei} = \epsilon_{sr} = 1$) on the HvP dynamical behaviour, B1 branch. Shown are (a) the steady state voltages for pyramidal populations, (b) the damping rates and (c) frequencies. (a) Increasing all efficacies to unity changes the steady state trajectories and decreases the range of high voltages on B1, but still B1 corresponds to extremely high firing rates. (b) Linear stability predicts a strongly stable behaviour. Although increasing anaesthetic effect eventually decreases the stability of B1, it never loses stability. As shown in (b) and (c) the dominant eigenvalue is mostly of zero frequency.

Figure 7.3(a) shows that increasing the efficacies to unity changes the steady state trajectories and decreases the range of high voltages on B1; however, B1 still corresponds to extremely high firing rates. The dispersion curves predict a strong stability with mostly zero frequency for the B1 branch, Fig. 7.3(b) and (c).

The dispersion curve for bottom branch B3 is presented in Fig. 7.4. In contrast with what we observed in the original HvP model, steady state voltages for pyramidal populations *decrease* as the drug effect increases, see Fig. 7.4(a). Increasing drug effect makes the system more stable, since the real part of dominant eigenvalues becomes more negative (Fig. 7.4(b)). It is important to note that alpha frequency decreases as the drug effect increases Fig. 7.4(c).

Unifying the efficacies alters the behaviour of the HvP significantly, constraining the anaesthetized brain into a plausible range, since the thalamocortical system now has a access to bottom branch B3 which is always stable and so never forces a jump to the

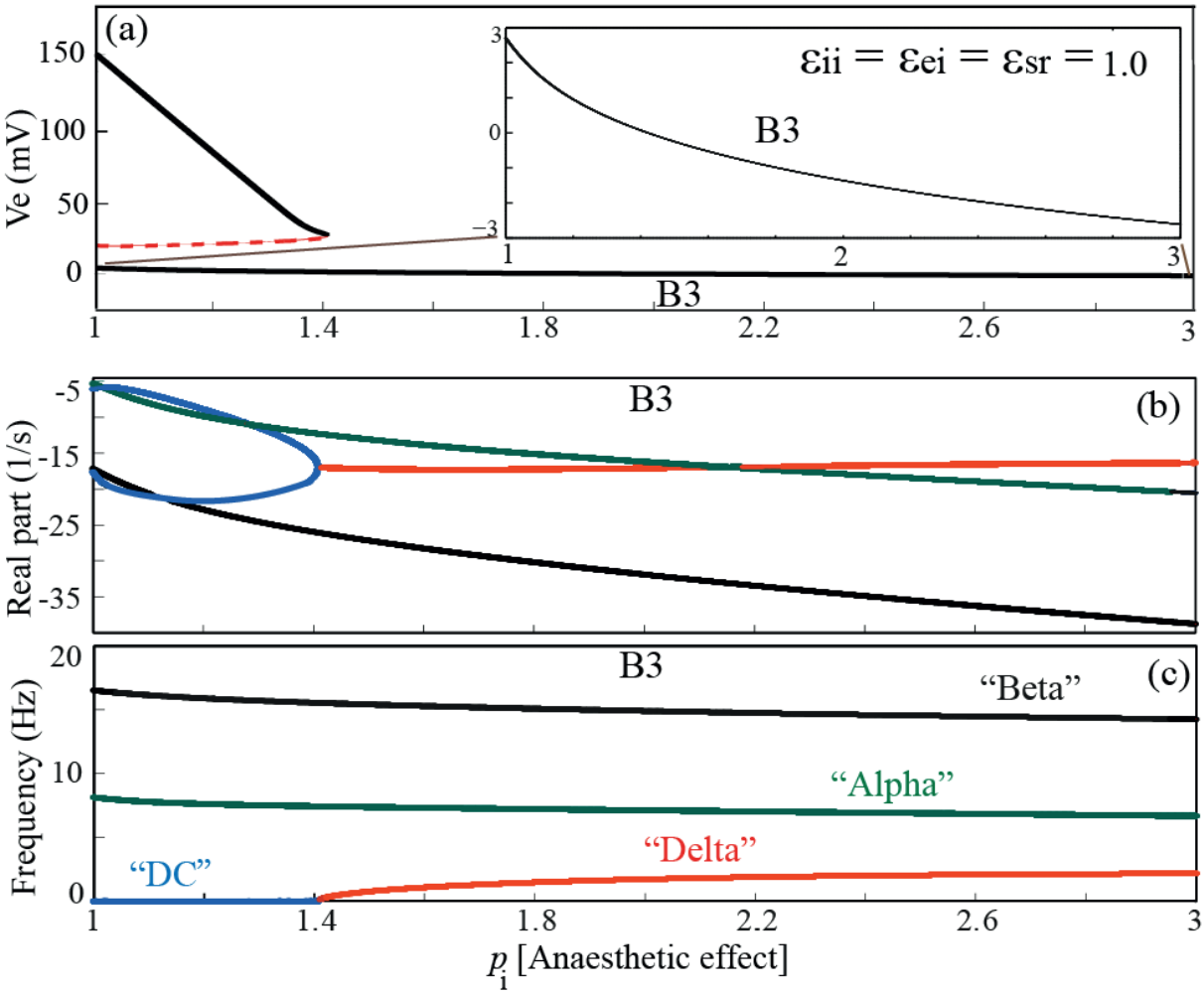

Figure 7.4. Effect of setting all efficacies to maximum value ($\epsilon_{ii} = \epsilon_{ei} = \epsilon_{sr} = 1$) on HvP model dynamical behaviour, B3 bottom branch. (a) Increasing all efficacies to unity changes the steady state trajectories and decreases membrane voltages on B3. (b) Linear stability predicts a strongly stable behaviour. Increasing anaesthetic effect increases the stability of B3. (c) Alpha frequency *decreases* as the drug effect increases.

B1 branch. But the firing rates on the B1 branch are implausibly high, never dropping below ~ 200 spikes/s (even at the B1 turning point; see sigmoid mapping in Fig. 7.6(a)). If the B1 firing rates were lower, then the upper branch could possibly be interpreted as the "conscious" branch, with the turning point near $p_i = 1.4$ representing the point of transition into coma. In an effort to tame the B1 behaviour, we now examine the consequences of including reversal potentials in the HvP equations.

7.3.2 Inclusion of reversal potential

We believe the HvP model should be modified to satisfy the following requirements:

- First, having distinct states for awake and anaesthetized so that increasing (decreasing) the drug effect switches the state of the thalamocortical system from awake (anaesthetized) to anaesthetized (awake). Studies conducted by Destexhe et al [20] and Steriade et al [88] to determine the mean histogram of neural cell membrane potentials also support the idea of cortical "up" and "down" states. This multi-state idea has been adopted in previous modelling works [44, 71, 91].
- Second, ensuring that brain activity decreases under deepening propofol levels rather than increasing.
- Third, constraining the upper-branch firing rate to biologically plausible values.

Reversal potential functions $\psi_{ab}(V_b)$ are incorporated into the model equations to constrain the incoming fluxes. The modified model parameters are presented in Table 7.1. While the inhibitory sigmoid parameters are similar to the original values, the excitatory threshold has been lowered so that the excitatory populations activate at lower voltages than the inhibitory populations, Fig. 7.6(a). This ensures an appropriate inverse-S distribution of steady states over the desired drug range.

Unlike HvP, in the modified model all neurons have the same inhibitory synaptic response due to the drug effect, Fig. 7.6(b). We note that there is no experimental evidence supporting the HvP assumption of different efficacies in different neuronal types.

Modified HvP (mHvP) system equations

The weighting function ψ_{ab}, Eq. (7.1), is dimensionless factor that scales the effectiveness of the ϕ_b incoming flux in proportion to the difference between the cell voltage V_a of the receiving neuron and the relevant ionic reversal potential V_b^{rev},

$$\psi_{ab}(V_a) = \frac{V_b^{\text{rev}} - V_a}{V_b^{\text{rev}} - V_a^{\text{rest}}}, \tag{7.1}$$

where V_a^{rest} represent the reversal potentials and $V_a^{\text{rest}} \equiv 0$ is the resting voltage in the Robinson and HP models. See Table 7.1 and Fig. 7.5.

After incorporating reversal potentials in the model equations, the average membrane potentials V_e, V_i, V_r and V_s in the modified model obey the following set of coupled equations,

$$V_e = h(t) \otimes \Big[\upsilon_{ee}\psi_{ee}(V_e)\phi_e(t) \Big] + h(t) \otimes \Big[\upsilon_{es}\psi_{es}(V_e)Q_s(t-\tau/2) \Big] \tag{7.2}$$
$$+ h_{ei}(t) \otimes \Big[\upsilon_{ei}\psi_{ei}(V_e)Q_i(t) \Big]$$
$$V_i = h(t) \otimes \Big[\upsilon_{ie}\psi_{ie}(V_i)\,\phi_e(t) \Big] + h(t) \otimes \Big[\upsilon_{is}\psi_{is}(V_i)Q_s(t-\tau/2) \Big] \tag{7.3}$$
$$+ h_{ii}(t) \otimes \Big[\upsilon_{ii}\psi_{ii}(V_i)Q_i(t) \Big]$$
$$V_s = \; h(t) \otimes \upsilon_{sn}\phi_n + h(t) \otimes \Big[\upsilon_{se}\psi_{se}(V_s)\,\phi_e(t-\tau/2) \Big] \tag{7.4}$$
$$+ h_{sr}(t) \otimes \Big[\upsilon_{sr}\psi_{sr}(V_s)\,Q_r(t) \Big]$$
$$V_r = h(t) \otimes \Big[\upsilon_{re}\psi_{re}(V_r)\,\phi_e(t-\tau/2) \Big] + h(t) \otimes \Big[\upsilon_{rs}\psi_{rs}(V_r)\,Q_s(t) \Big] \tag{7.5}$$

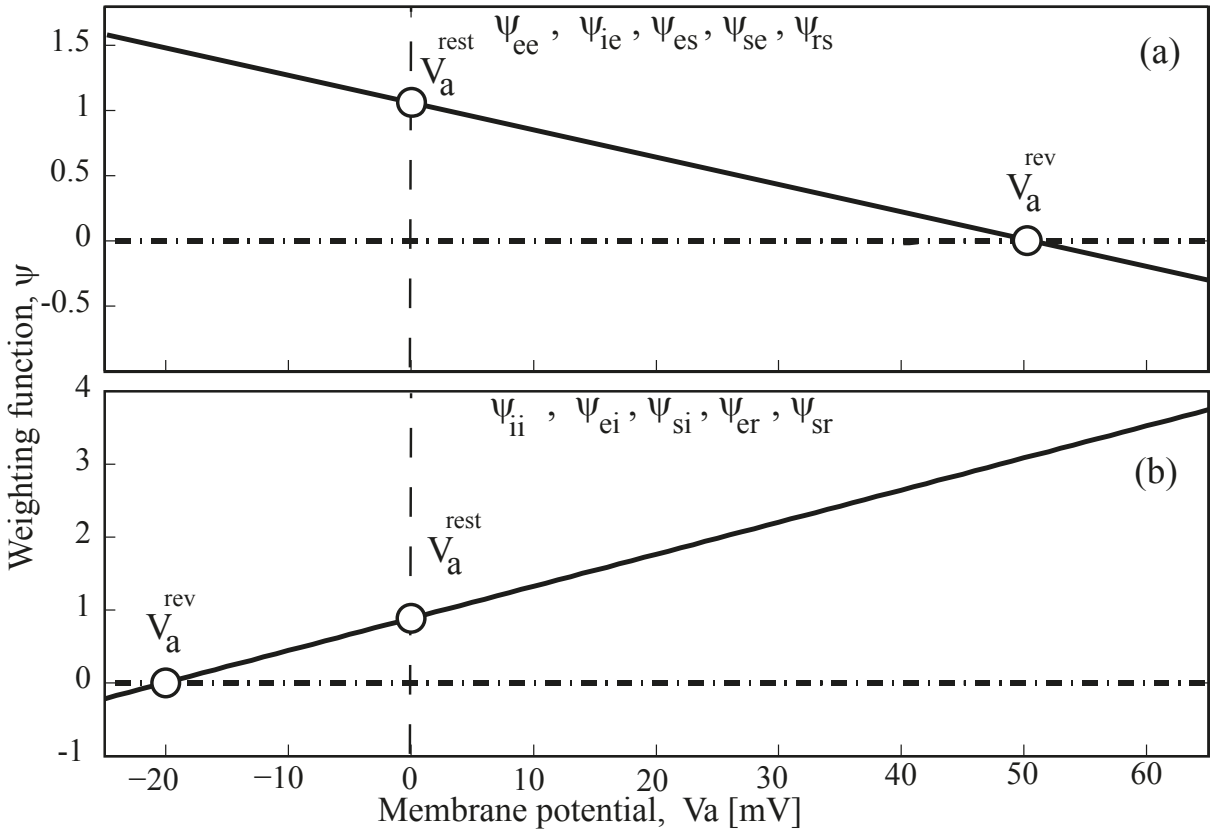

Figure 7.5. Reversal potential weighting Eq. (7.1) functions for modified HvP. We set $V_a^{\text{rest}} = 0$ for all populations (the same as the HvP model). Graph (a) plots the five weighting functions for flux entering excitatory populations (e, s), while graph (b) shows the corresponding weighting functions for flux entering inhibitory populations (i, r), see Table 7.1.

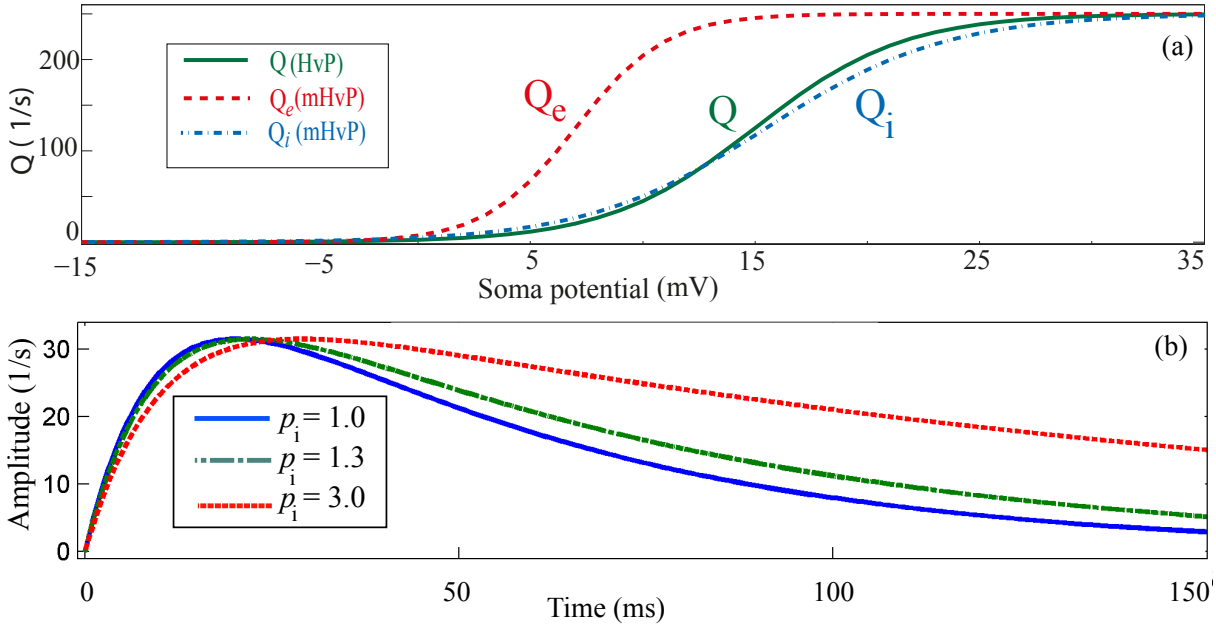

Figure 7.6. Transfer functions and synaptic responses. (a) Sigmoid curve relating average soma potential to firing rate. In the HvP model, the sigmoid functions for all populations are identical (green curve). However in the modified HvP model, the sigmoid functions for excitatory (red curve) and inhibitory (blue curve) neural populations are made distinct. (b) Curves show effect of increasing anaesthetic drug for the inhibitory populations. Unlike HvP, here we assume that all three inhibitory populations (ii, ei, sr) have identical efficacy.

(See Table 5.3.2 for parameter values.)

As can be seen in Eqs (7.3)–(7.5), the reversal potential acts directly in the incoming flux, which is then convolved with the synaptic response. Figure 7.6(b) shows the $\mathrm{GABA_A}$ synaptic response function; identical synaptic responses all inhibitory connections (ii, ei, sr) are assumed in the mHvP model. Increasing the $\mathrm{GABA_A}$ergic drug concentration p_i prolongs the IPSP duration. Table 7.1 presents the parameter values for the mHvP model constants for the sigmoid and response functions.

Table 7.1. Parameter values for HvP and mHvP model constants. Excitatory (inhibitory) connections have positive (negative) synaptic strength. Note that reversal potentials are expressed relative to an assumed resting potential of 0 mV.

Parameter	Symbol	HvP	Modified HvP	Unit
Rest potential (e, i, r, s)	V_a^{rest}	0		mV
Synaptic decay rate	α	50	30	s^{-1}
Average spike-threshold	$\theta_{e,i}$	15	$7, 15$	mV
Spike-threshold deviation	$\sigma_{e,i}$	3.3	$2, 3.8$	mV
Differential affinity of propofol (type i)	ϵ_{ii}	1	1	–
Differential affinity of propofol (type e)	ϵ_{ei}	0.5	1	–
Differential affinity of propofol (type s)	ϵ_{sr}	0.5	1	–
Reversal potential for excitatory (e, s)	$V_{e,s}^{\mathrm{rev}}$	–	$+50$	mV
Reversal potential for inhibitory (i, r)	$V_{i,r}^{\mathrm{rev}}$	–	-20	mV

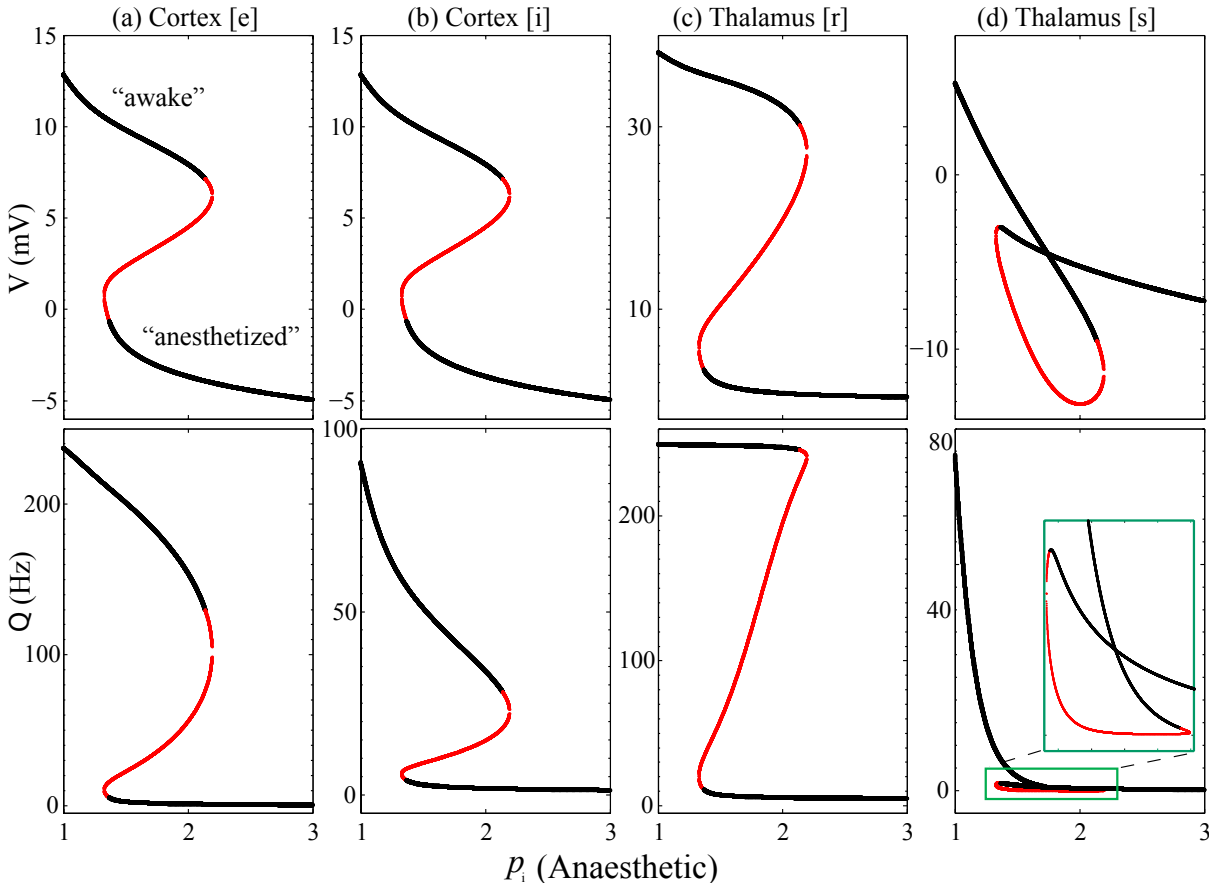

Figure 7.7. Steady-state distribution for the modified HvP model as a function of propofol effect. The modified model predicts that the TC system now has access to a high firing state and a low firing state such that the brain can switch from "awake " to "anaesthetized" at a critical level of drug concentration. The black and red colours indicate respectively stable and unstable equilibrium points.

7.3.3 Results

Steady-states for modified HvP

A similar methodology as used for the HvP model is applied to find the steady-state solutions for the modified HvP. The following equations define the steady-state manifold,

$$V_e^* = \psi_{ee}(V_e^*)\, h(t)\upsilon_{ee}Q_e^* + \psi_{es}(V_s^*)\, h(t)\upsilon_{es}Q_s^* + \psi_{ei}(V_e^*)\, h_{ei}(t)\upsilon_{ei}Q_i^* \tag{7.6}$$

$$V_i^* = \psi_{ie}(V_i^*)\, h(t)\upsilon_{ie}Q_e^* + \psi_{is}(V_i^*)\, h(t)\upsilon_{is}Q_s^* + \psi_{ii}(V_i^*)\, h_{ii}(t)\upsilon_{ii}Q_i^* \tag{7.7}$$

$$V_s^* = h(t)\upsilon_{sn}\phi_n + \psi_{se}(V_s^*)\, h(t)\upsilon_{se}Q_e^* + \psi_{sr}(V_s^*)\, h_{sr}(t)\upsilon_{sr}Q_r^* \tag{7.8}$$

$$V_r^* = \psi_{re}(V_r^*)\, h(t)\upsilon_{re}Q_e^* + \psi_{rs}(V_r^*)\, h(t)\upsilon_{rs}Q_s^* \tag{7.9}$$

Figure 7.7 presents the steady-state distribution for all soma voltages as a function of propofol effect in the mHvP model. We can now identify distinct phases of the thalamocortical system: high firing represents the awake state and low firing the anaesthetized state. The fact that the steady-state distribution exhibits multi-valued soma voltages is

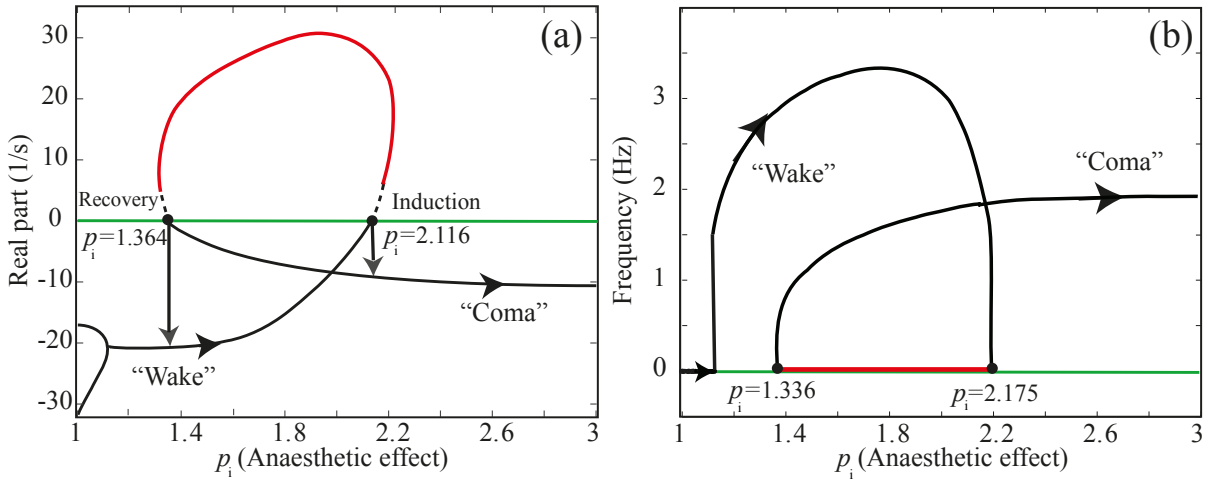

Figure 7.8. Linear stability analysis for the modified HvP model. Shown are the damping rates (a) and frequencies (b) as a function of the percentile increase in the time constant of GABAergic receptors on cortical inhibitory neurons p_i. Emergence of anaesthesia occurs at the critical point $p_i = 1.364$ and induction of anaesthesia happens at $p_i = 2.116$.

very significant as it means the transition from awake (anaesthetized) to anaesthetized (awake) cannot proceed continuously. There must be a sudden switching of state at a certain value of drug concentration.

Dispersion relation for modified HvP

The same method as for HvP is applied on the modified model to derive the dispersion relation; see appendix D for more details. After arranging these equations in Fourier domain, we obtain the transfer function,

$$\frac{\widetilde{\phi}_e}{\widetilde{\phi}_n} = \frac{c_r\,\psi^*_{ei}\,\psi^*_{is}\,\zeta_{eisn} + (c_i - \zeta_{ii})\,c_r\psi^*_{es}\zeta_{esn}}{E} \tag{7.10}$$

where

$$\begin{aligned} E = &\left[F\,(D\,c_e - \zeta_{ee}\,\psi^*_{ee}) - \left[\zeta_{ese}\,c_r\,\psi^*_{se} + \zeta_{esre}\,\psi^*_{sr}\,\psi^*_{re}\right]\psi^*_{es}\right] \\ &\times (c_i - \zeta_{ii}) - \psi^*_{ei}\left[F\,\zeta_{eie}\,\psi^*_{ie} + \psi^*_{is}\left[\zeta_{eise}\,c_r\psi^*_{se} + \zeta_{eisre}\,\psi^*_{sr}\,\psi^*_{re}\right]\right] \\ F = &\,c_s\,c_r - \zeta_{srs}\,\psi^*_{rs}\,\psi^*_{sr} \end{aligned} \tag{7.11}$$

$$\begin{aligned} c_e &= 1 + L_{ee}\,\upsilon_{ee}\left(\frac{\phi^*_e}{V^{rev}_e - V^{ss}_e}\right) + L_{es}\upsilon_{es}\left(\frac{Q^*_s}{V^{rev}_s - V^{ss}_e}\right) + L_{ei}\,\upsilon_{ei}\left(\frac{Q^*_i}{V^{rev}_i - V^{ss}_e}\right) \\ c_i &= 1 + L_{ie}\,\upsilon_{ie}\left(\frac{\phi^*_e}{V^{rev}_e - V^{ss}_i}\right) + L_{is}\upsilon_{is}\left(\frac{Q^*_s}{V^{rev}_s - V^{ss}_i}\right) + L_{ii}\,\upsilon_{ii}\left(\frac{Q^*_i}{V^{rev}_i - V^{ss}_i}\right) \end{aligned}$$

$$c_r = 1 + L_{re}\,\upsilon_{re}\left(\frac{\phi_e^*}{V_e^{rev} - V_r^{ss}}\right) + L_{rs}\upsilon_{rs}\left(\frac{Q_s^*}{V_s^{rev} - V_r^{ss}}\right)$$
$$c_s = 1 + L_{se}\,\upsilon_{se}\left(\frac{\phi_e^*}{V_r^{rev} - V_{ss}^{ss}}\right) + L_{sr}\upsilon_{sr}\left(\frac{Q_r^*}{V_r^{rev} - V_s^{ss}}\right)$$

The dispersion relation is obtained by setting the denominator in Eq. (7.10) to zero, giving

$$\left[F\,(D\,c_e - \zeta_{ee}\,\psi_{ee}^*) - \left[\zeta_{ese}\,c_r\,\psi_{se}^* + \zeta_{esre}\,\psi_{sr}^*\,\psi_{re}^*\right]\psi_{es}^*\right](c_i - \zeta_{ii}) \tag{7.12}$$
$$-\,\psi_{ei}^*\Big[F\,\zeta_{eie}\,\psi_{ie}^* + \psi_{is}^*\left[\zeta_{eise}\,c_r\psi_{se}^* + \zeta_{eisre}\,\psi_{sr}^*\,\psi_{re}^*\right]\Big] = 0$$

As for the HvP model, we restrict attention to spatially homogeneous dynamics ($k = 0$). A solution (ω) of Eq. (7.12) corresponds to a thalamocortical resonance with damping

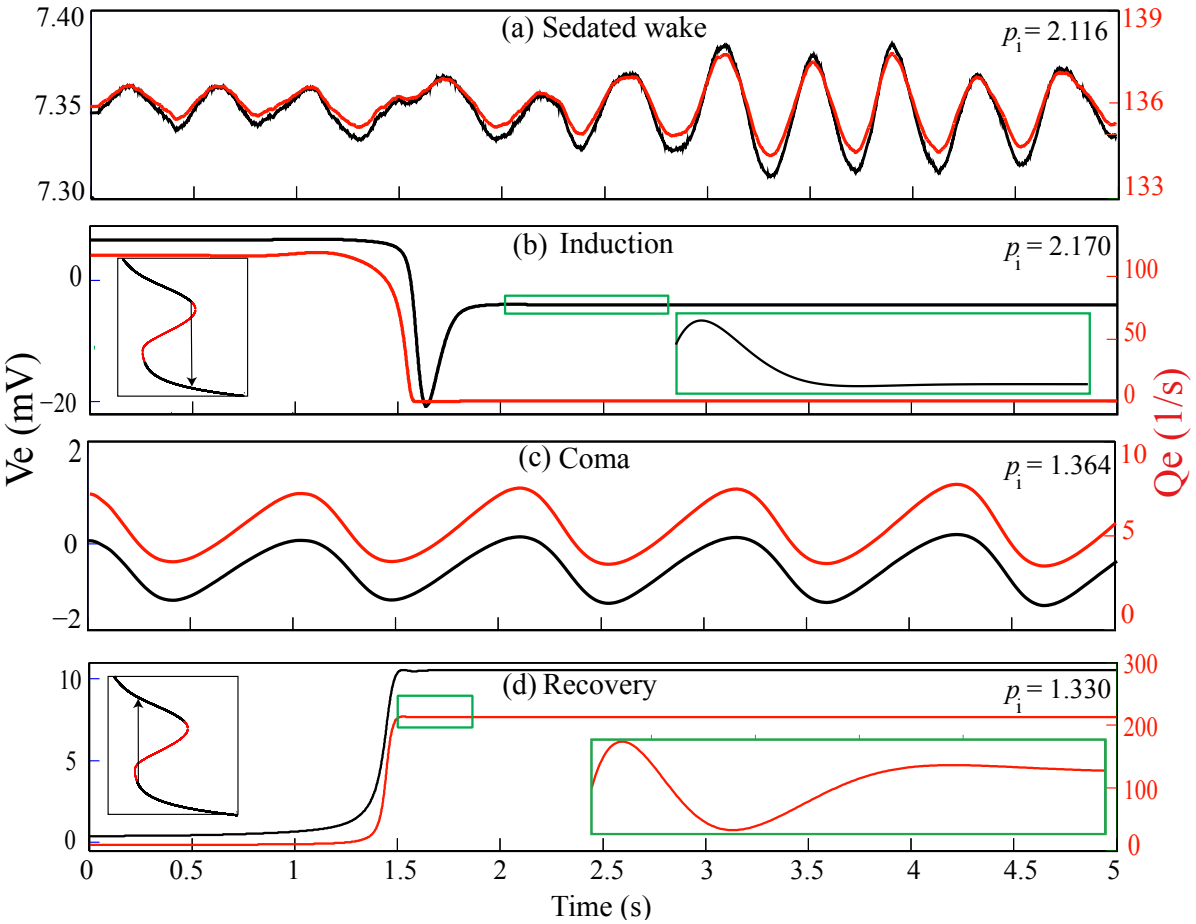

Figure 7.9. Simulations for pyramidal neurons at nominated p_i values in the mHvP model. (a) At the critical point $p_i = 2.116$ ("awake"), TC model is marginally unstable with 2.6 Hz oscillation; for a 600-s simulation, transition from "awake" to "coma" occurs at $t = 400$ s. (b) At $p_i = 2.170$ (close to turning point) induction of anaesthesia occurs, after transition from "awake" to "coma". (c) At critical point $p_i = 1.364$ ("coma"), TC model is marginally unstable with ∼1 Hz oscillation; for a 600-s simulation, transition occurs at $t = 350$ s. (d) The emergence from anaesthesia occurs at $p_i = 1.330$. Simulation settings: Euler integrator, $\Delta t = 10^{-4}$ s, low-intensity white noise to V_s.

rate $\mathrm{Im}(\omega)$, angular frequency $\mathrm{Re}(\omega)$. Stable resonances are characterized by $\mathrm{Im}(\omega) < 0$ and unstable by $\mathrm{Im}(\omega) > 0$.

As shown in Fig. 7.8, linear stability predicts that the top branch loses stability at $p_i = 2.116$, defining a point at which induction of anaesthesia can occur; while in the bottom branch, emergence of anaesthesia occurs at the critical point $p_i = 1.364$. The modified model predicts a drug-effect hysteresis in which the measured drug concentration is larger at induction than at emergence. The prediction of hysteresis is supported by theoretical and clinical works by other research groups [35, 59, 91].

Figure 7.9 shows simulation results for pyramidal neurons at nominated p_i values in the mHvP model. We identify distinct phases of the anaesthetized thalamocortical system with high firing = "awake"; low firing = "anaesthetized". Simulation results are consistent with the stability predictions of Fig. 7.8: at the critical points $p_i = 2.116$ and $p_i = 1.364$, TC model is marginally unstable and for a long simulation, transition from awake (coma) to coma (awake) occurs at $t = 400$ s (350 s). The dominant frequency observed in the awake state is $\sim$3 Hz and $\sim$1 Hz in the anaesthetized state.

7.4 Conclusion and discussion

In this chapter, two solutions were proposed to improve biophysical fidelity of the HvP model: setting all synaptic efficacies equal ($\epsilon_{ii} = \epsilon_{ei} = \epsilon_{sr} = 1$), and imposing reversal potentials.

While equalising synaptic efficacies eliminates the pathological jump into seizure for $p_i \gtrsim 1.3$, this modification also reverses the published HvP alpha-band trends of increasing power and (weakly) increasing alpha frequency during sedation. Instead, the modified HvP shows decreasing alpha power and weakly *decreasing* alpha frequency as propofol effect increases. This mismatch between HvP and mHvP raises the question: what is observed clinically?

Feshchenko et al [24] investigates propofol-induced alpha, and reported decreasing of alpha power with increasing drug concentration. Ching et al [17] found broadband beta-activity which slowed into the alpha-range at the point of induction; the alpha-band frequency and power reduced with further increases of propofol. Gugino et al [35] showed decreasing posterior alpha at light sedation, and increasing frontal predominance with deeper sedation. None of these studies reported an increase in alpha frequency for light sedation.

The second modification (equalizing efficacies, tuning sigmoid parameters and incorporating reversal potentials) alters the steady-state solutions to give bistable behaviour enabling the brain to switch between awake and anaesthetized states at critical levels of drug concentration, predicting a drug-hysteresis effect in which the measured concentration is larger at induction than at emergence. The dominant alpha frequency reported

by Hindriks and van Putten during propofol anaesthesia disappears in favour of delta frequency activity. The dominant frequency observed in the awake state is now ∼3 Hz and ∼1 Hz in the anaesthetized state; the mHvP model no longer supports alpha-band oscillations in the awake state.

Further investigations have shown that the alpha resonance can be reactivated by weakening the inhibition of the thalamocortical loop. The revised HvP model now exhibits a decrease in alpha frequency with deepening anaesthesia, consistent with clinical reports [17, 24]. This new work is being written up for publication.

Chapter 8

Summary and future work

8.1 Summary

In this thesis, we have investigated two mean-field descriptions for the effect of general anaesthetic agents on brain activity: the extended Waikato cortical model (WM) and the Hindriks and van Putten (HvP) thalamocortical model.

8.1.1 Anaesthetic effects in extended Waikato model

The Waikato cortical model represents the cortex as small columnar structures containing $\sim 10^5$ neurons, with 85% being excitatory and 15% inhibitory. In the extended Waikato model, the net neuron voltage is determined by axo-dendritic activity at the chemical synapses (excitatory inputs mediated by AMPA and NMDA receptors; inhibitory inputs by $GABA_A$ and $GABA_B$ receptors), plus input from electrical synapses. Inductive anaesthetic agents affect $GABA_A$ receptors by potentiating $GABA_A$-induced ionic currents, modelled as a prolongation of the IPSP tail. These agents also interact with $GABA_B$-receptors by increasing inhibitory synaptic gain. Dissociative drugs affect excitatory synaptic neurotransmission through modulation of NMDA receptor function, modelled as a voltage-dependent alteration of excitatory synaptic gain.

We investigated the effect of reduced gap junction conductance on cortical activity while simultaneously altering the effectiveness of $GABA_A$-,$GABA_B$- and NMDAergic anaesthetic agents. Linear stability analysis predicts that reducing the decay rate of $GABA_A$ response destabilises the temporal stability in both awake and anaesthetised states of the cortex. Dispersion curves suggest that increasing $GABA_B$ and NMDA effectiveness will tend to destabilize Turing patterns in favour of a temporal mode (Hopf) with large-scale synchronized oscillations that may represent a seizure state.

These extended Waikato model investigations indicate that the cortex may be susceptible to seizures when gap junctions are blocked during anaesthesia. This may explain why some anaesthetics cause seizures, as many of these agents also block gap junctions. The model also predicts that enhancement of $GABA_B$ should have a seizure-promoting effect on brain activity.

We tested these Waikato model predictions with two biological experiments. We found that potentiation of $GABA_B$ receptors, using the $GABA_B$ agonist baclofen in slices of mouse cortical tissue, tended to enhance seizure-like activity. However, our *in vivo* investigation of the effect of closure of gap junctions, using mefloquine, did not reveal any seizure patterns in anaesthetized mouse EEG signals.

8.1.2 Anaesthetic effects in the HvP and mHvP models

The second part of this thesis presented an introduction, examination and modification of the Hindrks and van Putten (HvP) anaesthesia model. First, the Robinson thalamocortical model which provides the foundation equations for the HvP model was introduced. The source of alpha activity was investigated, and we confirmed that the alpha frequency and amplitude is crucially dependent on the existence of a sufficiently long thalamocortical loop delay, τ. The standard Robinson model sets $\tau = 80$ ms, giving alpha oscillations $\sim$8 Hz as the dominant mode.

Hindriks and van Putten applied anaesthetic drug to the Robinson mean-field equations by lengthening IPSPs in a drug-dependent fashion, but enforced differing sensitivities for the different neural populations. The HvP paper limits itself to light sedation levels of anaesthesia only ($p_i \lesssim 1.3$), and is silent about model behaviour at deeper levels. In fact, we found that for deeper anaesthetic effect, HvP jumps from low-firing to an extremely high-firing stable state of$\sim$250 spikes/s, and remains locked there even at $GABA_A$ prolongations as high as 300% which would be expected to induce full comatose suppression. This occurs because the authors set the propofol affinity in pyramidal and reticular dendrites at half that for that of cortical inhibitory cells, thus reducing inhibition in the anaesthetised brain.

To overcome this pathological behaviour, we tested two possible modifications: first, eliminating the population-dependent anaesthetic sensitivity (efficacy) of the HvP model by setting ($\epsilon_{ii} = \epsilon_{ei} = \epsilon_{sr} = 1$); second, incorporating reversal potentials and tuning the excitatory sigmoid defining the mapping from voltage to firing rate. Both modifications eliminate the (pathological) lower-branch instability at $p_i \lesssim 1.3$, and the upper branch now displays a decreasing trend with p_i, terminating at a turning point near $p_i \lesssim 1.4$. Although the first modification results in alpha oscillations on the bottom branch, this alpha component is completely lost when the second set of modifications is applied to HvP.

8.2 Future work

There are several aspects of this thesis that could be extended in future work:

1. **Identification of key parameters**

Working with the Waikato and HvP anaesthesia models, we found that certain parameters played a critical role in determining steady-state and dynamical behaviours. Only a subset of model sensitivities were explored in this thesis. It would be useful to undertake a more comprehensive and systematic sensitivity analysis to identify all key parameters. This knowledge should provide insights and might allow oversimplifications and construction of reduced models.

2. **Gap junctions and seizure**
   The Waikato model predicts that when the brain is at the boundary between consciousness and unconsciousness, closing gap junctions can promote seizure activity. However, no seizure activity was observed when mefloquine, a gap-junction blocker, was preadministered to animals under propofol anaesthesia. Surgery could be performed to implant skull electrodes in mice lacking the gene for connexin-36. These mice could be anaesthetised with propofol and their cortical EEG recorded to capture any seizure activity near transition. This experiment would determine whether our null result was due to the fact that our EEG recording could only begin *after* the animals had been anaesthetized, so were already in coma.

3. **Loss of alpha in modified HvP**
   After inclusion of reversal weighting functions in the modified HvP model the alpha rhythm was lost, being replaced by a dominant delta-band oscillation. Perhaps the modifications have unbalanced the thalamic and cortical contributions such that loop dynamics have been suppressed in favour of cortical delta. This could be investigated further in an endeavour to restore the alpha component.

Appendix A

Elements of mathematics

A.1 Ordinary differential equations

Ordinary differential equations are a set of coupled n^{th}-order differential equations containing functions of one independent variable and its derivatives. An n^{th}-order differential equation is usually solved by reexpressing as a set of n first-order ODEs.

Assume $\vec{y}$ is a vector whose elements are functions of coupled differential equations of a system, and that $\vec{F}$ is a vector function of y and its derivatives; thus

$$\vec{y}^{(n)} = \vec{F}\left(t, y, y', y'', \cdots, y^{(n-1)}\right) \tag{A.1}$$

where $\vec{y}^{(n)}$ is an explicit system of ordinary differential equations of order n with dimension m. In column-vector form:

$$\begin{pmatrix} y_1^{(n)} \\ y_2^{(n)} \\ \vdots \\ y_m^{(n)} \end{pmatrix} = \begin{pmatrix} f_1\left(t, y, y', y'', \cdots, y^{(n-1)}\right) \\ f_2\left(t, y, y', y'', \cdots, y^{(n-1)}\right) \\ \vdots \\ f_m\left(t, y, y', y'', \cdots, y^{(n-1)}\right) \end{pmatrix} \tag{A.2}$$

To solve Eq. (A.1), ordinary differential equations of order n with dimension m can be reshaped to k sets of first-order differential equations where $k = n \times m$. The vectorized form of the first-order differential equations is

$$\frac{d\vec{V}}{dt} = \vec{F}(\vec{V}) \tag{A.3}$$

where $\vec{V}$ is a vector variable containing all elements of y and its derivatives, and $\vec{F}$ is the set of first-order differential equations,

$$\begin{aligned} \overrightarrow{V} &= [v_1 \ v_2 \ ... \ v_k]^{\mathrm{T}} \\ \overrightarrow{F} &= [f_1 \ f_2 \ ... \ f_k]^{\mathrm{T}} \end{aligned} \tag{A.4}$$

where the T superscript denotes transpose.

Taking a multivariate Taylor expansion of the right-hand side of Eq. (A.3) about the equilibrium point $\vec{V}^*$ we obtain,

$$\frac{d}{dt}\vec{V} = \vec{F}(\vec{V}^*) + \left.\frac{\partial \vec{F}}{\partial \vec{V}}\right|_{\vec{V}^*} \delta\vec{V} + \frac{1}{2!}\left.\frac{\partial^2 \vec{F}}{\partial \vec{V}^2}\right|_{\vec{V}^*} \delta\vec{V}^2 + \dots \tag{A.5}$$

where $\delta\vec{V} = \vec{V} - \vec{V}^*$ is the deviation of $\vec{V}$ from its equilibrium value V^*. By definition, at the equilibrium point (steady state), $\vec{V}$ no longer changes with time. This means that the equilibrium point of the system can be calculated by putting to zero the time derivative in Eq. (A.3):

$$\frac{d\vec{V}}{dt} = 0$$

which means $\vec{F}(\vec{V}^*) = 0$.

For very small values of δV, only the first term in Eq. (A.5) is considered significant; thus

$$\frac{d\,\delta\vec{V}}{dt} \approx \left.\frac{\partial \vec{F}}{\partial \vec{V}}\right|_{\vec{V}^*} \delta\vec{V}, \qquad \text{with} \qquad \frac{d\,\delta\vec{V}}{dt} = \frac{d\vec{V}}{dt} \tag{A.6}$$

which has the matrix form,

$$\frac{d}{dt}\begin{bmatrix} \delta v_1 \\ \\ \delta v_2 \\ \vdots \\ \delta v_k \end{bmatrix} = \left.\begin{bmatrix} \dfrac{\partial f_1}{\partial v_1} & \dfrac{\partial f_1}{\partial v_2} & \cdots & \dfrac{\partial f_1}{\partial v_k} \\ \dfrac{\partial f_2}{\partial v_1} & \dfrac{\partial f_2}{\partial v_2} & \cdots & \dfrac{\partial f_2}{\partial v_k} \\ \vdots & \vdots & & \vdots \\ \dfrac{\partial f_n}{\partial v_1} & \dfrac{\partial f_k}{\partial v_2} & \cdots & \dfrac{\partial f_k}{\partial v_k} \end{bmatrix}\right|_{V^*} \begin{bmatrix} \delta v_1 \\ \\ \delta v_2 \\ \vdots \\ \delta v_k \end{bmatrix} \tag{A.7}$$

The partial derivatives in Eq. (A.7) define the elements of the $k \times k$ Jacobian matrix $\mathbf{A}$,

$$\frac{d\,\delta\vec{V}}{dt} = \mathbf{A}^*\delta\vec{V} \tag{A.8}$$

where $\mathbf{A}^*$ is the Jacobian matrix evaluated at the equilibrium point.

In order to assess system stability, the method of characteristics is applied: we assume Eq. (A.8) has a solution of the form $v_i = \xi_i e^{\lambda_i t}$. Substituting in Eq. (A.8) we obtain,

$$(\mathbf{A} - \lambda\mathbf{I})\,\vec{\xi} = 0 \tag{A.9}$$

noting that λ is the eigenvalue of the matrix $\mathbf{A}$ and $\vec{\xi}$ is the corresponding eigenvector. Calculating the determinant of Eq. (A.9) can determine the eigenvalues, which are the

roots of the polynomial equation,

$$\det(\mathbf{A} - \lambda\mathbf{I})\,\vec{\xi} = 0 \tag{A.10}$$

Thus, the general solution for the linear homogeneous system in Eq. (A.8) can be expressed,

$$V(t) = \sum_{i=1}^{n} \xi_i\, e^{\lambda_i t} \tag{A.11}$$

where λ_i is the set of eigenvalues of the Jacobian matrix $\mathbf{A}$. The eigenvalues of the Jacobian are, in general, complex values,

$$\lambda_i = \alpha_i + i\ \omega_i \tag{A.12}$$

where α_i and ω_i are the real and imaginary parts of the eigenvalue respectively. The complex part of the eigenvalue contributes an oscillatory component to the solution. If any real part of the eigenvalues $\alpha_i > 0$, then $\vec{V}^*$ is unstable; this indicates a divergent trajectory which tends to move away from the equilibrium point with time. Provided all the real part of all eigenvalues $\alpha_i < 0$, the steady-state $\vec{V}^*$ is stable, indicating a trajectory which converges towards the equilibrium point. If one eigenvalue has a zero real part and the other eigenvalues have negative real parts, $\vec{V}^*$ will be associated with a long-lived or slow mode, a phenomenon known as critical slowing down.

A.2 Spectral analysis

Spectral analysis is the process of decomposing a stationary time-series into its component harmonics, quantifying power distribution as a function of frequency. To analyse the frequency spectrum for either clinical or model-generated time-sampled signals, the MATLAB function `spectrogram`, based on the short-time Fourier transform, is useful.

Mathematically, for the continuous-time case, the function to be transformed is multiplied by a window function which is nonzero for only a certain period of time. The Fourier transform of the resulting signal is taken as the window is slid along the time-axis, resulting in a two-dimensional representation of the signal [2]. For any normalized window $W(\tau)$, we have

$$\int_{-\infty}^{\infty} W(\tau)\, d\tau = 1\,, \tag{A.13}$$

where Eq. (A.13) can be rewritten as

$$\int_{-\infty}^{\infty} W(t-\tau)\, d\tau = 1\,. \tag{A.14}$$

Thus, a continnuous-time signal $y(t)$ can be approximated by its windowed sample,

$$y(t) \approx y(t) \int_{-\infty}^{\infty} W(t-\tau)\, d\tau = \int_{-\infty}^{\infty} y(t)\, W(t-\tau)\, d\tau\,. \tag{A.15}$$

The continuous Fourier transform of $y(t)$ is

$$Y(\omega) = \int_{-\infty}^{\infty} y(t)\, e^{-j\omega t}\, dt\,. \tag{A.16}$$

Substituting Eq. (A.15) into Eq. (A.16), we obtain

$$Y(\omega) = \int_{-\infty}^{\infty} \left[\int_{-\infty}^{\infty} y(t)\, W(t-\tau)\, e^{-j\omega t}\, dt \right] d\tau\,, \tag{A.17}$$

allowing us to define

$$Y(\tau, \omega) = \int_{-\infty}^{\infty} y(t)\, W(t-\tau)\; e^{-j\omega t}\, dt\,. \tag{A.18}$$

Here $Y(\tau, \omega)$ is the Fourier transform of $y(t)\, W(t-\tau)$, a complex function representing the phase and magnitude of the signal over time and frequency.

However, when analysing time-sampled data, it is necessary to introduce the discrete-time short Fourier transform approach, we need to map the continuous-time method to discrete-time; therefore, we make the following identifications

$$W(t-\tau) \longrightarrow W(m\Delta t - n\Delta t) \;\equiv\; W_{m-n}\,, \tag{A.19}$$

$$y(t) \longrightarrow y(m\Delta t) \;\equiv\; y_m \qquad (m, n \text{ are time indices})\,, \tag{A.20}$$

$$Y(f) \longrightarrow Y(k\Delta f) \;\equiv\; Y_k\,, \qquad (k \text{ is the frequency index}) \tag{A.21}$$

$$T \;=\; N\Delta t \tag{A.22}$$

$$\Delta f \;=\; \frac{1}{T} \;=\; \frac{1}{N\Delta t}\,, \tag{A.23}$$

where T is the length of the data record consisting of N samples taken at regular time intervals $\Delta t = 1/f_s$ with f_s being the sampling rate. Applying these mappings to the time-limited continuous Fourier transform of Eq. (A.17) leads to

$$\begin{aligned} Y(n, k\Delta f) \;&=\; \sum_{m=0}^{N-1} y_m\, W_{m-n}\, e^{\left[-j\, 2\pi (k\Delta f)(m\Delta t)\right]}\, \Delta t\,, \\ &=\; \Delta t \sum_{m=0}^{N-1} y_m\, W_{m-n}\, e^{-j2\pi mk/N}\,, \qquad k = 0,\, 1,\, \ldots,\, N-1\,, \end{aligned}$$

from which we can calculate the power spectral density (power per unit frequency), PSD, of the signal

$$\text{PSD} \equiv |Y(n, k\Delta f)|^2 \ . \tag{A.24}$$

When one reduces a continuous-time signal to a discrete-time sequence and interpolates back to a continuous form, the fidelity of the result relies on the sampling frequency of the original signal. *Nyquist's theorem* introduces the criterion for the minimum sampling frequency required for perfect fidelity:

$$0 \leqslant f \leqslant f_s/2 \,, \tag{A.25}$$

where $f_s = 1/\Delta t$. If this condition is satisfied, then no information is lost in the sampling process. Moreover, Eq. (A.25) tells us that provided the original signal contains frequency components no higher than half the sampling rate, its Fourier transform will produce a spectrum containing all frequencies from zero to $f_s/2$.

Appendix B

Waikato Model

B.1 Differential equation for synaptic response

The total input flux $\Phi(t)$ is the temporal convolution of the synapse spike-rate $M(t)$ with the dendrite impulse response $H(t)$,

$$\Phi(t) = H(t) \otimes M(t) \equiv \int_0^t H(t-t')M(t')\,dt'$$

where $H(t)$ is the biexponential response function,

$$H(t) = \frac{\alpha\beta}{\beta-\alpha}\left(e^{-\alpha\,t} - e^{-\beta\,t}\right)$$

Differentiation under of the integral obeys the following theorem,

$$\frac{d}{dt}\left(\int_{a(t)}^{b(t)} f(t,t')\,dt'\right) = f(t,b(t))\frac{d}{dt}b(t) - f(t,a(t))\frac{d}{dt}a(t) + \int_{a(t)}^{b(t)} \frac{\partial}{\partial t}f(t,t')\;dt' \qquad \text{(B.1)}$$

Applying this theorem to (B.1),

$$\begin{aligned}
\frac{d}{dt}\Phi &= \frac{\partial}{\partial t}\int_0^t H(t-t')M(t')\,dt' \\
&= \frac{\alpha\,\beta}{\beta-\alpha}\left(\frac{\partial}{\partial t}\int_0^t \left(e^{-\alpha(t-t')} - e^{-\beta(t-t')}\right) M(t')\,dt'\right) \\
&= \frac{\alpha\,\beta}{\beta-\alpha}\int_0^t \left(-\alpha\,e^{-\alpha(t-t')} + \beta\,e^{-\beta(t-t')}\right) M(t')\,dt
\end{aligned}$$

Differentiating a second time,

$$\begin{aligned}
\frac{d^2}{dt^2}\Phi &= \frac{\alpha\,\beta}{\beta-\alpha}\left(\frac{\partial}{\partial t}\int_0^t \left(-\alpha\,e^{-\alpha(t-t')} + \beta\,e^{-\beta(t-t')}\right) M(t')\,dt\right) \\
&= \frac{\alpha\,\beta}{\beta-\alpha}\int_0^t \left(\alpha^2\,e^{-\alpha(t-t')} - \beta^2\,e^{-\beta(t-t')}\right) M(t')\,dt + \alpha\beta\,M(t) \qquad \text{(B.2)}
\end{aligned}$$

By adding and subtracting identical parts of (B.2) we obtain,

$$\frac{d^2}{dt^2}\Phi = \underbrace{\frac{\alpha\,\beta}{\beta-\alpha}\int_0^t \alpha^2\, e^{-\alpha(t-t')} - \alpha\beta\, e^{-\beta(t-t')} M(t')\, dt}_{-\alpha\frac{d}{dt}\Phi} +$$
$$\underbrace{\frac{\alpha\,\beta}{\beta-\alpha}\int_0^t \alpha\beta\, e^{-\beta(t-t')} - \alpha\beta\, e^{-\alpha(t-t')} M(t')\, dt'}_{-\alpha\,\beta\,\Phi} +$$
$$\underbrace{\frac{\alpha\,\beta}{\beta-\alpha}\int_0^t \alpha\,\beta\, e^{-\alpha(t-t')} - \beta^2\, e^{-\beta(t-t')} M(t')\, dt}_{-\beta\frac{d}{dt}\Phi} + \alpha\beta\, M(t)$$

Rearranging,

$$\frac{d^2}{dt^2}\Phi = -\alpha\frac{d}{dt}\Phi - \alpha\,\beta\,\Phi - \beta\frac{d}{dt}\Phi + \alpha\beta\, M(t)$$

$$\frac{d^2}{dt^2}\Phi + (\alpha+\beta)\frac{d}{dt}\Phi + \alpha\,\beta\,\Phi = \alpha\beta\, M(t)$$

which can be written in factorized form,

$$\left(\frac{d}{dt} + \alpha\right)\left(\frac{d}{dt} + +\beta\right)\Phi = \alpha\beta\, M(t) \tag{B.3}$$

B.2 Differential equation for soma response

As presented in (3.24), the soma resting potential is perturbed by input fluctuations from excitatory e and inhibitory i chemical synapses,

$$V_k(t) = \underbrace{V_k^{\text{rest}}}_{\text{soma resting potential}} + \underbrace{L_k(t) \otimes [E_k(t) + I_k(t)]}_{\text{input perturbation}} \tag{B.4}$$

$E_k(t)$ and $I_k(t)$ are the excitatory and inhibitory voltage inputs, and $L_k(t)$ is the decay exponential function for soma response,

$$L_k(t) = \frac{1}{\tau_k} e^{-t/\tau_k} \tag{B.5}$$

Expressing (B.4) in integral form,

$$V_k(t) = V_k^{\text{rest}} + \int_0^t L_k(t-t')[E_k(t') + I_k(t')]dt'$$

Applying theorem (B.1),

$$\begin{aligned}\frac{d}{dt}V_k(t) &= \frac{\partial}{\partial t}\int_0^t L_k(t-t')[E_k(t')+I_k(t')]\,dt' \\ &= \int_0^t \frac{1}{\tau_k}L_k(t-t')[E_k(t')+I_k(t')]\,dt' + L_k(0)[E_k(t)+I_k(t)] \\ &= -\frac{1}{\tau_k}\int_0^t L_k(t-t')[E_k(t')+I_k(t')]\,dt' + \frac{1}{\tau_k}[E_k(t)+I_k(t)]\end{aligned}$$

giving the soma voltage equation of motion

$$\tau_k\frac{d}{dt}V_k(t) = V_k^{\text{rest}} - V_k(t) + E_k(t) + I_k(t) \tag{B.6}$$

Appendix C

Derivation of the fluctuation spectrum for the HvP model

Applying the convolution theorem to the HvP equations (6.11–6.14), we transform to the frequency domain,

$$\widetilde{V}_e = L_{ee}\upsilon_{ee}\widetilde{\phi}_e + L_{ei}\upsilon_{ei}\widetilde{Q}_i + L_{es}\upsilon_{es}e^{-i\omega\tau/2}\widetilde{Q}_s \tag{C.1}$$

$$\widetilde{V}_i = L_{ie}\upsilon_{ie}\widetilde{\phi}_e + L_{ii}\upsilon_{ii}\widetilde{Q}_i + L_{is}\upsilon_{is}\widetilde{Q}_s e^{-i\omega\tau/2} \tag{C.2}$$

$$\widetilde{V}_r = L_{re}\upsilon_{re}\widetilde{\phi}_e e^{-i\omega\tau/2} + L_{rs}\upsilon_{rs}\widetilde{Q}_s \tag{C.3}$$

$$\widetilde{V}_s = L_{se}\upsilon_{se}\widetilde{\phi}_e e^{-i\omega\tau/2} + L_{sr}\upsilon_{sr}\widetilde{Q}_r + L_{sn}\upsilon_{sn}\phi_n \tag{C.4}$$

To derive the fluctuation function, the sigmoid functions in the time domain are linearised about steady state $(V_e^*, V_i^*, V_s^*, V_r^*)$,

$$Q(V_a) \approx Q(V_a^*) + \left.\frac{dQ}{dV_a}\right|_{V_a^*} (V_a - V_a^*) \tag{C.5}$$

Fourier transforming both sides of (C.5) gives,

$$\widetilde{Q}(V_a) \approx \sqrt{2\pi}\delta(\omega)Q(V_a^*) + Q'(V_a^*)(\widetilde{V}_a - \sqrt{2\pi}\delta(\omega)V_a^*) \tag{C.6}$$

We now drop the delta-functions at zero frequency since they have no impact on system dynamics,

$$\widetilde{Q}(V_a) \approx Q'(V_a^*)\,\widetilde{V}_a \qquad \text{or} \qquad \widetilde{V}_a \approx \frac{\widetilde{Q}(V_a)}{Q'(V_a^*)} \tag{C.7}$$

where $Q'(V_a^*)$ is the sigmoid slope at steady state.

For pairs of neuron types (a, b) located either within cortex or within thalamus, for $[i.e., (a,b) \in (e,e),(e,i),(i,e),(i,i),(r,s),(s,r)]$ the frequency response from neuron type b to neuron type a is given by,

$$\zeta_{ab}(\omega) = L_{ab}\upsilon_{ab}Q'(V_a^*) \tag{C.8}$$

For pairs of neuron types separated by a time delay [*i.e.*, $(a,b) \in (e,s),(r,e),(i,s),(s,e)$] the frequency response from neurons of type b contains a phase shift that is due to the propagation delay $\tau/2$ between cortex and thalamus and is given by

$$\zeta_{ab}(\omega) = L_{ab}\upsilon_{ab}Q'(V_a^*)(e^{-i\omega\tau/2}) \tag{C.9}$$

Substituting (C.7) in (C.1),

$$\widetilde{Q}_e = \zeta_{ee}\widetilde{\phi}_e + \zeta_{es}\widetilde{Q}_s + \zeta_{ei}\widetilde{Q}_i$$

where

$$\zeta_{ee} = L_{ee}\upsilon_{ee}Q'(V_e^*) \qquad \zeta_{es} = L_{es}\upsilon_{es}e^{-i\omega\tau/2}Q'(V_e^*) \qquad \zeta_{ei} = L_{es}\upsilon_{ei}Q'(V_e^*)$$

Applying the same method for the other neural populations, enables us to write simplified versions of Eqs. (C.1–C.4) as functions of firing rates:

$$\widetilde{D}\widetilde{\phi}_e = \zeta_{ee}\widetilde{\phi}_e + \zeta_{es}\widetilde{Q}_s + \zeta_{ei}\widetilde{Q}_i \tag{C.10}$$

$$\widetilde{Q}_i = \zeta_{ie}\widetilde{\phi}_e + \zeta_{is}\widetilde{Q}_s + \zeta_{ii}\widetilde{Q}_i \tag{C.11}$$

$$\widetilde{Q}_r = \zeta_{re}\widetilde{\phi}_e + \zeta_{rs}\widetilde{Q}_s \tag{C.12}$$

$$\widetilde{Q}_s = \zeta_{sn}\widetilde{\phi}_n + \zeta_{se}\widetilde{\phi}_e + \zeta_{sr}\widetilde{Q}_r \tag{C.13}$$

where $\widetilde{D}\widetilde{\phi}_e = \widetilde{Q}_e$ and $\widetilde{D}_e = (1 + \frac{i\omega}{\gamma})^2$. Substituting (C.12) in (C.13) and rearranging gives,

$$\widetilde{Q}_s = \frac{\zeta_{sn}\widetilde{\phi}_n + (\zeta_{se} + \zeta_{sre})\widetilde{\phi}_e}{1 - \zeta_{srs}} \tag{C.14}$$

Substituting (C.14) in (C.11) enables us to eliminate $\widetilde{Q}_s$. Solving (C.11) for $\widetilde{Q}_i$,

$$\widetilde{Q}_i = \frac{[\zeta_{ie}(1 - \zeta_{srs}) + (\zeta_{ise} + \zeta_{isre})]}{(1 - \zeta_{ii})(1 - \zeta_{srs})}\widetilde{\phi}_e + \frac{\zeta_{isn}}{(1 - \zeta_{ii})(1 - \zeta_{srs})}\widetilde{\phi}_e \tag{C.15}$$

Finally, substituting (C.15) in (C.10), we obtain

$$(\widetilde{D} - \zeta_{ee})\widetilde{\phi}_e = \frac{\zeta_{esn}\widetilde{\phi}_n + (\zeta_{ese} + \zeta_{esre})}{1 - \zeta_{srs}}\widetilde{\phi}_e + \frac{\zeta_{eie}(1 - \zeta_{eise} + \zeta_{eisre})}{(1 - \zeta_{ii})(1 - \zeta_{srs})}\widetilde{\phi}_e + \frac{\zeta_{eisn}}{(1 - \zeta_{ii})(1 - \zeta_{srs})}\widetilde{\phi}_n \tag{C.16}$$

which can be written as the transfer function $\widetilde{\phi}_e/\widetilde{\phi}_n$,

$$\frac{\widetilde{\phi}_e}{\widetilde{\phi}_n} = \frac{\zeta_{eisn} + (1 - \zeta_{ii})\zeta_{esn}}{[(\widetilde{D} - \zeta_{ee})(1 - \zeta_{srs}) - \zeta_{ese} - \zeta_{esre}](1 - \zeta_{ii}) - \zeta_{eie}(1 - \zeta_{srs}) - \zeta_{eise} - \zeta_{eisre}} \tag{C.17}$$

The dispersion relation corresponding to (C.17) is obtained by setting its denominator to zero,

$$[(\widetilde{D} - \zeta_{ee})(1 - \zeta_{srs}) - \zeta_{ese} - \zeta_{esre}](1 - \zeta_{ii}) - \zeta_{eie}(1 - \zeta_{srs}) - \zeta_{eise} - \zeta_{eisre} = 0 \qquad \text{(C.18)}$$

where the solution from (C.18) corresponds to thalamocortical resonance with damping rate $\mathrm{Im}(\omega)$ and angular frequency $\mathrm{Re}(\omega)$.

For representing the combined frequency response of different anatomical loops, the following definition is applied,

$$\zeta_{abc}(\omega) = \zeta_{ab}(\omega)\zeta_{bc}(\omega) \qquad \text{(C.19)}$$

the indexes are from right to left, applying (C.19) we have,

$$\zeta_{eisre}(\omega) = \zeta_{ei}(\omega)\zeta_{is}(\omega)\zeta_{sr}(\omega)\zeta_{re}(\omega) \qquad \zeta_{eie}(\omega) = \zeta_{ei}(\omega)\zeta_{ie}(\omega)$$

$$\zeta_{eise}(\omega) = \zeta_{ei}(\omega)\zeta_{is}(\omega)\zeta_{se}(\omega) \qquad \zeta_{eisn}(\omega) = \zeta_{ei}(\omega)\zeta_{is}(\omega)\zeta_{sn}(\omega)$$

$$\zeta_{srs}(\omega) = \zeta_{sr}(\omega)\zeta_{rs}(\omega) \qquad \zeta_{esn}(\omega) = \zeta_{es}(\omega)\zeta_{sn}(\omega)$$

Appendix D

Derivation of the fluctuation spectrum for the mHvP model

Full model equations for the mHvP for all neural populations are express as,

$$V_e = h(t) \otimes \left[\upsilon_{ee} \psi_{ee}(V_e)\, \phi_e(t) \right] + h(t) \otimes \left[\upsilon_{es} \psi_{es}(V_s)\, Q_s(t - \tau/2) \right] + h_{ei}(t) \otimes \left[\upsilon_{ei} \psi_{ei}(V_e) Q_i(t) \right] \tag{D.1}$$

$$V_i = h(t) \otimes \left[\upsilon_{ie} \psi_{ie}(V_i)\, \phi_e(t) \right] + h(t) \otimes \left[\upsilon_{is} \psi_{is}(V_i)\, Q_s(t - \tau/2) \right] + h_{ii}(t) \otimes \left[\upsilon_{ii} \psi_{ii}(V_i)\, Q_i(t) \right] \tag{D.2}$$

$$V_s = h(t) \otimes \upsilon_{sn} \phi_n + h(t) \otimes \left[\upsilon_{se} \psi_{se}(V_s)\, \phi_e(t - \tau/2) \right] + h_{sr}(t) \otimes \left[\upsilon_{sr} \psi_{sr}(V_s)\, Q_r(t) \right] \tag{D.3}$$

$$V_r = h(t) \otimes \left[\upsilon_{re} \psi_{re}(V_r)\, \phi_e(t - \tau/2) \right] + h(t) \otimes \left[\upsilon_{rs} \psi_{rs}(V_r)\, Q_s(t) \right] \tag{D.4}$$

where the weighting function ψ_{ab} is defined,

$$\psi_{ab}(V_a) = \frac{V_b^{\text{rev}} - V_a}{V_b^{\text{rev}} - V_a^{\text{rest}}},$$

and V_a^{rest} and V_a^{rev} represent the rest and reversal potential respectively. To derive dispersion relation, the modified model is simplified by linearising system variables,

$$\begin{aligned} V_a(t) &\approx V_a^* + \delta V_a(t) \qquad a = e, i, r, s \\ Q_a(t - \tau) &\approx Q_a^* + \delta Q_a(t - \tau) \\ \psi_{ab}(V_a) &\approx \frac{V_b^{\text{rev}} - V_a^*}{V_b^{\text{rev}} - V_a^{\text{ss}}} - \frac{\delta V_a(t)}{V_b^{\text{rev}} - V_a^{\text{ss}}} \end{aligned}$$

Substituting above definition in (D.1–D.4) and then applying convolution theorem, we transform to the frequency domain

$$\begin{aligned}\widetilde{V}_e(\omega) = L_{ee}\,\upsilon_{ee}\left(\frac{V_e^{\text{rev}}-V_e^*}{V_e^{\text{rev}}-V_e^{\text{ss}}}\right)\delta\widetilde{\phi}_e(\omega) + L_{es}\,\upsilon_{es}\left(\frac{V_s^{\text{rev}}-V_e^*}{V_s^{\text{rev}}-V_e^{\text{ss}}}\right)\delta\widetilde{Q}_s(\omega)\mathrm{e}^{-i\omega\tau} \\ -\left(L_{ee}\,\upsilon_{ee}\left(\frac{\phi_e^*}{V_e^{\text{rev}}-V_e^{\text{ss}}}\right) + L_{es}\upsilon_{es}\left(\frac{Q_s^*}{V_s^{\text{rev}}-V_e^{\text{ss}}}\right)\right) \\ + L_{ei}\,\upsilon_{ei}\left(\frac{V_i^{\text{rev}}-V_e^*}{V_i^{\text{rev}}-V_e^{\text{ss}}}\right)\delta\widetilde{Q}_i(\omega) - L_{ei}\,\upsilon_{ei}\left(\frac{Q_i^*}{V_i^{\text{rev}}-V_e^{\text{ss}}}\right)\end{aligned} \tag{D.5}$$

After applying definitions (C.8) and (C.9) in (D.5), we obtain cortical excitatory neuronal voltage in frequency domain,

$$\widetilde{V}_e(\omega)\,\mathrm{C}_e = \zeta_{ee}\left(\frac{V_e^{\text{rev}}-V_e^*}{V_e^{\text{rev}}-V_e^{\text{ss}}}\right)\delta\widetilde{\phi}_e(\omega) + \zeta_{es}\left(\frac{V_s^{\text{rev}}-V_e^*}{V_s^{\text{rev}}-V_e^{\text{ss}}}\right)\delta\widetilde{Q}_s(\omega) + \zeta_{ei}\left(\frac{V_i^{\text{rev}}-V_e^*}{V_i^{\text{rev}}-V_e^{\text{ss}}}\right)\delta\widetilde{Q}_i(\omega)$$

where

$$\mathrm{C}_e = 1 + L_{ee}\,\upsilon_{ee}\left(\frac{\phi_e^*}{V_e^{\text{rev}}-V_e^{\text{ss}}}\right) + L_{es}\upsilon_{es}\left(\frac{Q_s^*}{V_s^{\text{rev}}-V_e^{\text{ss}}}\right) + L_{ei}\,\upsilon_{ei}\left(\frac{Q_i^*}{V_i^{\text{rev}}-V_e^{\text{ss}}}\right)$$

Similarly, for cortical inhibitory neurons,

$$\widetilde{V}_i(\omega)\,\mathrm{C}_i = \zeta_{ie}\left(\frac{V_e^{\text{rev}}-V_i^*}{V_e^{\text{rev}}-V_i^{\text{ss}}}\right)\delta\widetilde{\phi}_e(\omega) + \zeta_{is}\left(\frac{V_s^{\text{rev}}-V_i^*}{V_s^{\text{rev}}-V_i^{\text{ss}}}\right)\delta\widetilde{Q}_s(\omega) + \zeta_{ii}\left(\frac{V_i^{\text{rev}}-V_i^*}{V_i^{\text{rev}}-V_i^{\text{ss}}}\right)\delta\widetilde{Q}_i(\omega)$$

where

$$\mathrm{C}_i = 1 + L_{ie}\,\upsilon_{ie}\left(\frac{\phi_e^*}{V_e^{\text{rev}}-V_i^{\text{ss}}}\right) + L_{is}\upsilon_{is}\left(\frac{Q_s^*}{V_s^{\text{rev}}-V_i^{\text{ss}}}\right) + L_{ii}\,\upsilon_{ii}\left(\frac{Q_i^*}{V_i^{\text{rev}}-V_i^{\text{ss}}}\right)$$

reticular neurons,

$$\widetilde{V}_r(\omega)\,\mathrm{C}_r = \zeta_{re}\left(\frac{V_e^{\text{rev}}-V_r^*}{V_e^{\text{rev}}-V_r^{\text{ss}}}\right)\delta\widetilde{\phi}_e(\omega) + \zeta_{rs}\left(\frac{V_s^{\text{rev}}-V_r^*}{V_s^{\text{rev}}-V_r^{\text{ss}}}\right)\delta\widetilde{Q}_s(\omega)$$

where

$$\mathrm{C}_r = 1 + L_{re}\,\upsilon_{re}\left(\frac{\phi_e^*}{V_e^{\text{rev}}-V_r^{\text{ss}}}\right) + L_{rs}\upsilon_{rs}\left(\frac{Q_s^*}{V_s^{\text{rev}}-V_r^{\text{ss}}}\right)$$

the relay neuronal voltages in frequency domain define by,

$$\widetilde{V}_s(\omega)\,\mathrm{C}_s = \zeta_{sn}\,\phi_n + \zeta_{se}\left(\frac{V_e^{\text{rev}}-V_s^*}{V_e^{\text{rev}}-V_s^{\text{ss}}}\right)\delta\widetilde{\phi}_e(\omega) + \zeta_{sr}\left(\frac{V_r^{\text{rev}}-V_s^*}{V_r^{\text{rev}}-V_s^{\text{ss}}}\right)\delta\widetilde{Q}_r(\omega)$$

where

$$\mathrm{C}_s = 1 + L_{se}\,\upsilon_{se}\left(\frac{\phi_e^*}{V_r^{\mathrm{rev}} - V_s^{\mathrm{ss}}}\right) + L_{sr}\upsilon_{sr}\left(\frac{Q_r^*}{V_r^{\mathrm{rev}} - V_s^{\mathrm{ss}}}\right) \tag{D.6}$$

Rearranging equations above according the definition of transfer function (see Appendix C more for details calculation), $\dfrac{\widetilde{\phi}_e}{\widetilde{\phi}_n}$

$$\frac{\widetilde{\phi}_e}{\widetilde{\phi}_n} = \frac{C_r\,\psi_{ei}^*\,\psi_{is}^*\,\zeta_{eisn} + (C_i - \zeta_{ii})\,C_r\psi_{es}^*\zeta_{esn}}{\mathrm{g}} \tag{D.7}$$

$$\text{where}\quad \mathrm{g} = \left[\left[f\,(\widetilde{D}\,C_e - \zeta_{ee}\,\psi_{ee}^*) - \left[\zeta_{ese}\,C_r\,\psi_{se}^* + \zeta_{esre}\,\psi_{sr}^*\,\psi_{re}^*\right]\psi_{es}^*\right](C_i - \zeta_{ii})\right]$$

$$- \psi_{ei}^*\left[F\,\zeta_{eie}\,\psi_{ie}^* + \psi_{is}^*\left[\zeta_{eise}\,C_r\psi_{se}^* + \zeta_{eisre}\,\psi_{sr}^*\,\psi_{re}^*\right]\right]$$

$$\text{and}\quad f = C_s\,C_r - \zeta_{srs}\,\psi_{rs}^*\,\psi_{sr}^*$$

To analyses the stability of the system, the denominator of (D.7) is zeroed, which giving the dispersion relation of the system.

$$\left[\left[f\,(\widetilde{D}\,C_e - \zeta_{ee}\,\psi_{ee}^*) - \left[\zeta_{ese}\,C_r\,\psi_{se}^* + \zeta_{esre}\,\psi_{sr}^*\,\psi_{re}^*\right]\psi_{es}^*\right](C_i - \zeta_{ii})\right] \tag{D.8}$$

$$- \psi_{ei}^*\left[F\,\zeta_{eie}\,\psi_{ie}^* + \psi_{is}^*\left[\zeta_{eise}\,C_r\psi_{se}^* + \zeta_{eisre}\,\psi_{sr}^*\,\psi_{re}^*\right]\right] = 0 \tag{D.9}$$

where the solution corresponds to thalamocortical resonance with damping rate $\mathrm{Im}(\omega)$ and angular frequency $\mathrm{Re}(\omega)$ in the mHvP model.

Appendix E

Source codes

This section includes selected Matlab source codes that generate dispersion curve results in the thesis.

```
for j=1:Nroots % cycle through each of the roots in turn...
ROOT  = flipud([Nroots*ones(Nroots,1)  range  domain]);
R = ROOT(j,:);
[  Nroots,   Qe,    Qi,   Ve,    Vi, lambda_e_A, lambda_e_N, lambda_i_a,
lambda_i_b, del_VeRest,   sc] = ...
deal(R(1), R(2),  R(3),  R(4), R(5),       R(6),       R(7),        R(8),
R(9),       R(10),  R(11));

% excitatory and inhibitory synaptic strengths
rho_e_A = lambda_e_A * H.ge;                % (AMPA)
rho_e_N = lambda_e_N * H.ge;                % (NMDA)
rho_i_a = lambda_i_a * H.gi; % (GABA_a)
rho_i_b = lambda_i_b * H.gi; % (GABA_b)

% define coefficient for Robinson wave equations in phi_ee, phi_ei
VL = H.v * H.Lambda;

% postsynaptic gains at steadystate
M_ek_A =  H.Nn_ek_A*Qsige(Ve) + sc*H.phi_ek_sc;  % (AMPA)
M_ek_N =  H.Nn_ek_N*Qsige(Ve) + sc*H.phi_ek_sc;  % (AMPA)
M_ik_a =  H.n_ik_a*Qsigi(Vi);  % (GABAa)
M_ik_b =  H.n_ik_b*Qsigi(Vi);  % (GABAb)

% derivatives of sigmoid functions
d_Qe = d_Qsige(Ve);
d_Qi = d_Qsigi(Vi);
```

```
if isempty(JAC)
%   if first call, recompute JAC
disp('--- Recomputing NUmeric Jacobian ---');
psi_ee_A = Psi_ee(Ve);
psi_ee_N = Psi_ee(Ve);
psi_ie_a = Psi_ie_a(Ve);
psi_ie_b = Psi_ie_b(Ve);



term1 = rho_e_A *H.d_psi_ee_A*M_ek_A;
term2 = rho_e_N*M_ek_N*(H.d_psi_ee_N*g_N(Ve,Mg,Theta);
+psi_ee_N*dg_N(Ve,Mg,Theta));
term3 = rho_i_a * H.d_psi_ie_a * M_ik_a;
term4 = rho_i_b * H.d_psi_ie_b * M_ik_b;

J11 = (-1 + term1   + term2 + term3 + term4 - D1*qwavenum.^2)/H.tau_e;
J13 = rho_e_A*psi_ee_A/H.tau_e;
J15 = rho_e_N*psi_ee_N*(g_N(Ve,Mg,Theta))/H.tau_e;
J17 = rho_i_a* psi_ie_a/H.tau_e;
J19 = rho_i_b* psi_ie_b/H.tau_e;

psi_ei_A = Psi_ei(Vi);
psi_ei_N = Psi_ei(Vi);
psi_ii_a = Psi_ii_a(Vi);
psi_ii_b = Psi_ii_b(Vi);

term5 = rho_e_A *H.d_psi_ei_A*M_ek_A;
term6 = rho_e_N*M_ek_N*(H.d_psi_ei_N*g_N(Vi,Mg,Theta);
+psi_ei_N*dg_N(Vi,Mg,Theta));
term7 = rho_i_a * H.d_psi_ii_a * M_ik_a;
term8 = rho_i_b * H.d_psi_ii_b * M_ik_b;

J22 = (-1+term5+term6 + term7+ term8 - D2*qwavenum.^2)/H.tau_i;
J23 = rho_e_A*psi_ei_A/H.tau_i;
J25 = rho_e_N*psi_ei_N*(g_N(Vi,Mg,Theta))/H.tau_i;
J27 = rho_i_a* psi_ii_a/H.tau_i;
J29 = rho_i_b* psi_ii_b/H.tau_i;
J34 = 1;
J41 = H.alpha_ek_A * H.beta_ek_A *H.n_ek_A * d_Qe;
```

```
J43 = -H.alpha_ek_A * H.beta_ek_A;
J44 = -(H.alpha_ek_A + H.beta_ek_A);
J4_11 = H.alpha_ek_A * H.beta_ek_A*H.N_ek_A ;
J56 = 1;
J61 = H.alpha_ek_N * H.beta_ek_N *H.n_ek_A * d_Qe;
J65 = -H.alpha_ek_N * H.beta_ek_N;
J66 = -(H.alpha_ek_N + H.beta_ek_N);
J6_11 = H.alpha_ek_N * H.beta_ek_N*H.N_ek_N ;
J78 = 1;
J82 = alpha_ik_a * H.beta_ik_a * H.n_ik_a*d_Qi;
J87 = -alpha_ik_a * H.beta_ik_a;
J88 = -(alpha_ik_a + H.beta_ik_a);
J9_10 = 1;
J10_2 = H.alpha_ik_b * H.beta_ik_b * H.n_ik_b*d_Qi;
J10_9 = -H.alpha_ik_b * H.beta_ik_b;
J10_10 = -(H.alpha_ik_b + H.beta_ik_b);
J11_12 = 1;

VL = H.v * H.Lambda;
J12_1 = VL^2 * d_Qe;
J12_11 = -VL^2-(H.v*qwavenum).^2;
J12_12 = -2*VL;

% the range of wave number

[F1 F2 F3 F4 F5 F6 F7 F8 F9 F10 F11 F12] =...
deal(NaN*ones(size(qwavenum)));

% the entry containing qwavenum will change
for i = 1: length(qwavenum);

Jac = [
J11(i) 0   J13   0  J15   0   J17   0  J19  0      0     0
0  J22(i)  J23   0  J25   0   J27   0  J29  0      0     0
0      0    0    1   0    0    0    0   0   0      0     0
J41    0   J43  J44  0    0    0    0   0   0   J4_11    0
0      0    0    0   0    1    0    0   0   0      0     0
J61    0    0    0  J65  J66   0    0   0   0   J6_11    0
```

```
0       0    0    0    0    0    1    0    0    0  ,    0    0
0     J82    0    0    0    0   J87  J88   0    0       0    0
0       0    0    0    0    0    0    0    0   J9_10   0    0
0    J10_2   0    0    0    0    0    0  J10_9 J10_10  0    0
0       0    0    0    0    0    0    0    0    0       0   J11_12
J12_1   0    0    0    0    0    0    0    0    0 J12_11(i)J12_12];

F = eig(Jac);

[tmp, I] = sort(real(F)); F = flipud(F(I));
end
end
```

References

[1] Adodra, S., Hales, T.G.: Potentiation, activation and blockade of $GABA_A$ receptors of clonal murine hypothalamic gt1-7 neurones by propofol. British Journal of Pharmacology **115**(6), 953–960 (1995)

[2] Allen, J.: Short-term spectral analysis, and modification by discrete Fourier transform. IEEE Transactions on Acoustics Speech and Signal Processing **25**(3), 235–238 (1977)

[3] Amabeoku, G.J., Farmer, C.C.: Gamma-aminobutyric acid and mefloquine-induced seizures in mice. Progress in Neuro-Psychopharmacology and Biological Psychiatry **29**(6), 917–921 (2005)

[4] Asl, F.M., Ulsoy, A.G.: Analysis of a system of linear delay differential equations. Journal of Dynamic Systems, Measurement, and Control **125**(2), 215–223 (2003)

[5] Austin, V.: Fundamentals of the nervous system and nervous tissue. Human Anatomy & Physiology, Sixth Edition. Pearson Education, Inc (2004)

[6] Bacsar, E., Bacsar-Eroglu, C., Karakacs, S., Schurmann, M.: Gamma, alpha, delta, and theta oscillations govern cognitive processes. International Journal of Psychophysiology **39**(2), 241–248 (2001)

[7] Bacsar, E., Dumermuth: EEG brain dynamics: relation between EEG and brain evoked potentials. Computer Programs in Biomedicine **14**(2), 227–228 (1982)

[8] Bai, D., Pennefather, P.S., MacDonald, J.F., Orser, B.A.: The general anaesthetic propofol slows deactivation and desensitization of $GABA_A$ receptors. The Journal of Neuroscience **19**(24), 10635–10646 (1999)

[9] Beierlein, M., Gibson, J.R., Connors, B.W.: A network of electrically coupled interneurons drives synchronized inhibition in neocortex. Nature Neuroscience **3**(9), 904–910 (2000)

[10] Bellman, R.E., Cooke, K.L.: Differential-difference Equations. Rand Corporation (1963)

[11] Bennett, M.V., Zukin, R.S.: Electrical coupling and neuronal synchronization in the mammalian brain. Neuron **41**(4), 495–511 (2004)

[12] Bergey, G., Britton, J., Cascino, G., Choi, H., Karceski, S., Kossoff, E., Meador, K., Murro, A., Park, Y., Ritzl, E., et al.: Implementation of an external responsive neurostimulator system (erns) in patients with intractable epilepsy undergoing intracranial seizure monitoring. Epilepsia **43**(suppl 7), 191 (2002)

[13] Bojak, I., Liley, D.: Modelling the effects of anaesthesia on the electroencephalogram. Physical Review E **71**(4), 041902 (2005)

[14] Bonta, I.L.: Schizophrenia, dissociative anaesthesia and near-death experience; three events meeting at the NMDA receptor. Medical hypotheses **62**(1), 23–28 (2004)

[15] Bronzino, J.D.: Principles of electroencephalography. The Biomedical Engineering Handbook **1** (1995)

[16] Buzsaki, G.: Rhythms of the Brain. Oxford University Press (2006)

[17] Ching, S., Cimenser, A., Purdon, P.L., Brown, E.N., Kopell, N.J.: Thalamocortical model for a propofol-induced α-rhythm associated with loss of consciousness. Proceedings of the National Academy of Sciences **107**(52), 22665–22670 (2010)

[18] Clements, J., Westbrook, G.: Activation kinetics reveal the number of glutamate and glycine binding sites on the N-methyl-D-aspartate receptor. Neuron **7**(4), 605–613 (1991)

[19] Daroff, R.B., Jankovic, J., Mazziotta, J.C., Pomeroy, S.L.: Bradley's Neurology in Clinical Practice. Elsevier Health Sciences (2015)

[20] Destexhe, A., Contreras, D., Steriade, M.: Cortically-induced coherence of a thalamic-generated oscillation. Neuroscience **92**(2), 427–443 (1999)

[21] Dilger, J.: The effects of general anaesthetics on ligand-gated ion channels. British Journal of Anaesthesia **89**(1), 41–51 (2002)

[22] Ermentrout, B., Terman, D.H.: Foundations of mathematical neuroscience. Citeseer (2010)

[23] Falbo, C.E.: Some Elementary Methods for Solving Functional Differential Equations. Sonoma State University (2003)

[24] Feshchenko, V.A., Veselis, R.A., Reinsel, R.A.: Propofol-induced alpha rhythm. Neuropsychobiology **50**(3), 257–266 (2004)

[25] Flohr, H., Glade, U., Motzko, D.: The neural correlate of consciousness and the mechanisms of general anaesthesia. Molecular Pharmacology of Anaesthesia pp. 12–24 (2000)

[26] Forman, S.A., Chin, V.A.: General anaesthetics and molecular mechanisms of unconsciousness. International Anaesthesiology Clinics **46**(3), 43 (2008)

[27] Franks N., L.W.: What is the molecular nature of general anaesthetic target sites? Trends in Pharmacological Sciences **8**(5), 169–174 (1987)

[28] Friedman, E.B., Sun, Y., Moore, J.T., Hung, H.T., Meng, Q.C., Perera, P., Joiner, W.J., Thomas, S.A., Eckenhoff, R.G., Sehgal, A., et al.: A conserved behavioral

state barrier impedes transitions between anaesthetic-induced unconsciousness and wakefulness: evidence for neural inertia. PloS one **5**(7), e11903 (2010)

[29] Fukuda, T., Kosaka, T., Singer, W., Galuske, R.A.: Gap junctions among dendrites of cortical gabaergic neurons establish a dense and widespread intercolumnar network. The Journal of Neuroscience **26**(13), 3434–3443 (2006)

[30] Gajda, Z., Gyengési, E., Hermesz, E., Ali, K.S., Szente, M.: Involvement of gap junctions in the manifestation and control of the duration of seizures in rats in vivo. Epilepsia **44**(12), 1596–1600 (2003)

[31] Gajda, Z., Szupera, Z., Blazsó, G., Szente, M.: Quinine, a blocker of neuronal cx36 channels, suppresses seizure activity in rat neocortex in vivo. Epilepsia **46**(10), 1581–1591 (2005)

[32] Gerstner, W.: A framework for spiking neuron models–the spike response model. Handbook of Biological Physics **4**, 469–516 (2001)

[33] Gottschalk, A.: Computational aspects of anesthetic action in simple neural models. Anaesthesiology **98**, 548–564 (2003)

[34] Guedel, A.E.: Inhalation anaesthesia: A fundamental guide. Anaesthesia and Analgesia **16**(2), 119–120 (1937)

[35] Gugino, L., Chabot, R., Prichep, L., John, E., Formanek, V., Aglio, L.: Quantitative eeg changes associated with loss and return of consciousness in healthy adult volunteers anaesthetized with propofol or sevoflurane. British Journal of Anaesthesia **87**(3), 421–428 (2001)

[36] Guzzella, L.: Analysis and synthesis of Single-input Single-output control systems. Hochschulverlag (2011)

[37] Hammond, C.: Cellular and Molecular Neurobiology. Academic Press (2001)

[38] Hewer, C.L.: The stages and signs of general anaesthesia. British Medical Journal **2**(3996), 274 (1937)

[39] Higham, D.J.: An algorithmic introduction to numerical simulation of stochastic differential equations. SIAM review **43**(3), 525–546 (2001)

[40] Hindriks, R., van Putten, M.J.: Meanfield modeling of propofol-induced changes in spontaneous EEG rhythms. NeuroImage **60**(4), 2323–2334 (2012)

[41] Hindriks, R., van Putten, M.J.: Thalamo-cortical mechanisms underlying changes in amplitude and frequency of human alpha oscillations. NeuroImage **70**, 150–163 (2013)

[42] Hodgkin, A.L., Huxley, A.F.: A quantitative description of membrane current and its application to conduction and excitation in nerve. The Journal of Physiology **117**(4), 500–544 (1952)

[43] Hutt, A.: The anesthetic propofol shifts the frequency of maximum spectral power in EEG during general anesthesia: analytical insights from a linear model. Frontiers in Computational Neuroscience **7** (2013)

[44] Hutt, A., Longtin, A.: Effects of the anesthetic agent propofol on neural populations. Cognitive Neurodynamics **4**(1), 37–59 (2010)

[45] Ivanov, A., Kazmerchuk, Y., Swishchuk, A.: Theory, stochastic stability and applications of stochastic delay differential equations: a survey of results. Differential Equations Dynam. Systems **11**(1-2), 55–115 (2003)

[46] Jacobson, G.M., Voss, L.J., Melin, S.M., Cursons, R., Sleigh, J.W.: The role of connexin36 gap junctions in modulating the hypnotic effects of isoflurane and propofol in mice. Anaesthesia **66**(5), 361–367 (2011)

[47] Jacobson, G.M., Voss, L.J., Melin, S.M., Mason, J.P., Cursons, R.T., Steyn-Ross, D.A., Steyn-Ross, M.L., Sleigh, J.W.: Connexin36 knockout mice display increased sensitivity to pentylenetetrazol-induced seizure-like behaviors. Brain Research **1360**, 198–204 (2010)

[48] Jahr, C.E., Stevens, C.: Glutamate activates multiple single channel conductances in hippocampal neurons. Nature Publishing Group (1987)

[49] Jahr, C.E., Stevens, C.F.: A quantitative description of NMDA receptor-channel kinetic behavior. The Journal of Neuroscience **10**(6), 1830–1837 (1990)

[50] Jahr, C.E., Stevens, C.F.: Voltage dependence of NMDA-activated macroscopic conductances predicted by single-channel kinetics. The Journal of Neuroscience **10**(9), 3178–3182 (1990)

[51] Jahromi, S.S., Wentlandt, K., Piran, S., Carlen, P.L.: Anticonvulsant actions of gap junctional blockers in an in vitro seizure model. Journal of Neurophysiology **88**(4), 1893–1902 (2002)

[52] Johnson, B., Sleigh, J., Kirk, I., Williams, M.: High-density EEG mapping during general anaesthesia with xenon and propofol: a pilot study. Anaesthesia and Intensive Care **31**(2), 155–163 (2003)

[53] Johnson, J., Ascher, P.: Glycine potentiates the NMDA response in cultured mouse brain neurons. Nature Publishing Group (1987)

[54] Juszczak, G.R., Swiergiel, A.H.: Properties of gap junction blockers and their behavioural, cognitive and electrophysiological effects: animal and human studies. Progress in Neuro-Psychopharmacology and Biological Psychiatry **33**(2), 181–198 (2009)

[55] Kerr, D., Ong, J., Johnston, G., Prager, R.: $GABA_B$-receptor-mediated actions of baclofen in rat isolated neocortical slice preparations: antagonism by phosphono-analogues of GABA. Brain Research **480**(1), 312–316 (1989)

[56] Kitamura, A., Marszalec, W., Yeh, J.Z., Narahashi, T.: Effects of halothane and propofol on excitatory and inhibitory synaptic transmission in rat cortical neurons. Journal of Pharmacology and Experimental Therapeutics **304**(1), 162–171 (2003)

[57] Koch, C.: Biophysics of Computation: Information Processing in Single Neurons. Oxford University Press (1998)

[58] Krasowski, M., Harrison, N.: General anaesthetic actions on ligand-gated ion channels. Cellular and Molecular Life Sciences CMLS **55**(10), 1278–1303 (1999)

[59] Kuizenga, K., Kalkman, C., Hennis, P.: Quantitative electroencephalographic analysis of the biphasic concentration-effect relationship of propofol in surgical patients during extradural analgesia. British Journal of Anaesthesia **80**(6), 725–732 (1998)

[60] Laser, H.: A critical analysis of the tissue slice method in manometric experiments: Effect of variations in O_2-and CO_2-tension. Biochemical Journal **36**(3-4), 319 (1942)

[61] Lewis, D.V., Jones, L.S., Mott, D.D.: Baclofen induces spontaneous, rhythmic sharp waves in the rat hippocampal slice. Experimental Neurology **106**(2), 181–186 (1989)

[62] Liley, D.T., Cadusch, P.J., Dafilis, M.P.: A spatially continuous mean field theory of electrocortical activity. Network: Computation in Neural Systems **13**(1), 67–113 (2002)

[63] Liley, D.T., Cadusch, P.J., Wright, J.J.: A continuum theory of electro-cortical activity. Neurocomputing **26**, 795–800 (1999)

[64] Lipton, P., Aitken, P., Dudek, F., Eskessen, K., Espanol, M., Ferchmin, P., Kelly, J., Kreisman, N., Landfield, P., Larkman, P., et al.: Making the best of brain slices; comparing preparative methods. Journal of Neuroscience Methods **59**(1), 151–156 (1995)

[65] Lodish, H.F., Berk, A., Zipursky, S.L., Matsudaira, P., Baltimore, D., Darnell, J., et al.: Molecular Cell Biology, vol. 4. Citeseer (2000)

[66] Maass, W.: Networks of spiking neurons: the third generation of neural network models. Neural Networks **10**(9), 1659–1671 (1997)

[67] Makram, H.: The blue brain project. Nature Reviews Neuroscience, (2006 February)

[68] Maranhão, M.V.M., Gomes, E.A., Carvalho, P.E.d.: Epilepsy and anesthesia. Revista brasileira de anestesiologia **61**(2), 242–254 (2011)

[69] Martella, G., De Persis, C., Bonsi, P., Natoli, S., Cuomo, D., Bernardi, G., Calabresi, P., Pisani, A.: Inhibition of persistent sodium current fraction and voltage-gated L-type calcium current by propofol in cortical neurons: Implications for its antiepileptic activity. Epilepsia **46**(5), 624–635 (2005)

[70] Martin, F.C., Handforth, A.: Carbenoxolone and mefloquine suppress tremor in the harmaline mouse model of essential tremor. Movement Disorders **21**(10), 1641–1649 (2006)

[71] Molaee-Ardekani, B., Senhadji, L., Shamsollahi, M.B., Vosoughi-Vahdat, B., Wodey, E.: Brain activity modelling in general anaesthesia: enhancing local mean-field models using a slow adaptive firing rate. Physical Review E **76**(4), 041911 (2007)

[72] Motalli, R., Louvel, J., Tancredi, V., Kurcewicz, I., Wan-Chow-Wah, D., Pumain, R., Avoli, M.: $GABA_B$ receptor activation promotes seizure activity in the juvenile rat hippocampus. Journal of Neurophysiology **82**(2), 638–647 (1999)

[73] Myshkis, A.: Linear Differential Equations with Retarded Argument. Nauka, Moscow (1972)

[74] Neligan, A.R.: The opium question: with special reference to Persia. J. Bale and Danielson, Limited (1927)

[75] Nowak, L., Bregestovski, P., Ascher, P., Herbet, A., Prochiantz, A.: Magnesium gates glutamate-activated channels in mouse central neurones. Nature Publishing Group (1984)

[76] Pais, I., Hormuzdi, S.G., Monyer, H., Traub, R.D., Wood, I.C., Buhl, E.H., Whittington, M.A., LeBeau, F.E.: Sharp wave-like activity in the hippocampus in vitro in mice lacking the gap junction protein connexin 36. Journal of Neurophysiology **89**(4), 2046–2054 (2003)

[77] Pereda, A.E.: Electrical synapses and their functional interactions with chemical synapses. Nature Reviews Neuroscience **15**(4), 250–263 (2014)

[78] Purves, D., Augustine, G., Fitzpatrick, D., Hall, W., LaMantia, A., McNamara, J., White, L.: Neuroscience, 2008. De Boeck, Sinauer, Sunderland, Mass

[79] Robinson, P., Rennie, C., Rowe, D.: Dynamics of large-scale brain activity in normal arousal states and epileptic seizures. Physical Review E **65**(4), 041924 (2002)

[80] Robinson, P., Rennie, C., Wright, J., Bourke, P.: Steady states and global dynamics of electrical activity in the cerebral cortex. Physical Review E **58**(3), 3557 (1998)

[81] Rudolph, U., Antkowiak, B.: Molecular and neuronal substrates for general anaesthetics. Nature Reviews Neuroscience **5**(9), 709–720 (2004)

[82] Sanjuan, D., Chiappa, K.H., Cole, A.J.: Propofol and the electroencephalogram. Clinical Neurophysiology **121**(7), 998–1006 (2010)

[83] Schwartz, R.S., Brown, E.N., Lydic, R., Schiff, N.D.: General anaesthesia, sleep, and coma. New England Journal of Medicine **363**(27), 2638–2650 (2010)

[84] Schwieler, L., Delbro, D., Engberg, G., Erhardt, S.: The anaesthetic agent propofol interacts with $GABA_B$-receptors: an electrophysiological study in rat. Life Sciences **72**(24), 2793–2801 (2003)

[85] Schwieler, L., Delbro, D., Engberg, G., Erhardt, S.: The anaesthetic agent propofol interacts with $GABA_B$-receptors: an electrophysiological study in rat. Life Sciences **72**(24), 2793–2801 (2003)

[86] Shampine, L.F., Thompson, S.: Solving DDEs in Matlab. Applied Numerical Mathematics **37**(4), 441–458 (2001)

[87] Shampine, L.: Solving ODEs and DDEs with residual control. Applied Numerical Mathematics **52**(1), 113–127 (2005)

[88] Steriade, M., Timofeev, I., Grenier, F.: Natural waking and sleep states: a view from inside neocortical neurons. Journal of Neurophysiology **85**(5), 1969–1985 (2001)

[89] Steyn-Ross, A., Steyn-Ross, M.: Modelling Phase Transitions in the Brain. Springer (2010)

[90] Steyn-Ross, D.A.: Modelling the anaestheto-dynamic phase transition of the cerebral cortex. Ph.D. thesis, University of Waikato (2002)

[91] Steyn-Ross, M.L., Steyn-Ross, D.A., Sleigh, J.W., Liley, D.: Theoretical electroencephalogram stationary spectrum for a white-noise-driven cortex: evidence for a general anaesthetic-induced phase transition. Physical Review E **60**(6), 7299 (1999)

[92] Steyn-Ross, M.L., Steyn-Ross, D.A., Sleigh, J.W.: Gap junctions modulate seizures in a mean-field model of general anaesthesia for the cortex. Cognitive Neurodynamics **6**(3), 215–225 (2012)

[93] Steyn-Ross, M.L., Steyn-Ross, D.A., Wilson, M.T., Sleigh, J.W.: Gap junctions mediate large-scale Turing structures in a mean-field cortex driven by subcortical noise. Physical Review E **76**(1), 011916 (2007)

[94] Sullivan, R.: The identity and work of the ancient Egyptian surgeon. Journal of the Royal Society of Medicine **89**(8), 467–473 (1996)

[95] Swartzwelder, H.S., Lewis, D., Anderson, W., Wilson, W.: Seizure-like events in brain slices: suppression by interictal activity. Brain Research **410**(2), 362–366 (1987)

[96] Teplan, M.: Fundamentals of electroencephalography measurement. Measurement Science Review **2**(2), 1–11 (2002)

[97] Traub, R.D., Jefferys, J.G., Whittington, M.A.: Fast oscillations in cortical circuits. MIT Press (1999)

[98] Velazquez, J.L.P., Carlen, P.L.: Gap junctions, synchrony and seizures. Trends in Neurosciences **23**(2), 68–74 (2000)

[99] Voss, L.J., Brock, M., Carlsson, C., Steyn-Ross, A., Steyn-Ross, M., Sleigh, J.W.: Investigating paradoxical hysteresis effects in the mouse neocortical slice model. European Journal of Pharmacology **675**(1), 26–31 (2012)

[100] Voss, L.J., Jacobson, G., Sleigh, J.W., Steyn-Ross, A., Steyn-Ross, M.: Excitatory effects of gap junction blockers on cerebral cortex seizure-like activity in rats and mice. Epilepsia **50**(8), 1971–1978 (2009)

[101] Voss, L.J., Sleigh, J.W.: Stability of brain neocortical slice seizure-like activity during low-magnesium exposure: Measurement and effect of artificial cerebrospinal fluid temperature. Journal of Neuroscience Methods **192**(2), 214–218 (2010)

[102] Wang, Y., Denisova, J.V., Kang, K.S., Fontes, J.D., Zhu, B.T., Belousov, A.B.: Neuronal gap junctions are required for NMDA Receptor–mediated excitotoxicity: Implications in ischemic stroke. Journal of Neurophysiology **104**(6), 3551–3556 (2010)

[103] Watson, C.J., Baghdoyan, H.A., Lydic, R.: A neurochemical perspective on states of consciousness. In: Suppressing the Mind, pp. 33–80, Springer (2010)

[104] Watts, A., Jefferys, J.: Effects of carbamazepine and baclofen on 4-aminopyridine-induced epileptic activity in rat hippocampal slices. British Journal of Pharmacology **108**(3), 819–823 (1993)

[105] Wentlandt, K., Samoilova, M., Carlen, P.L., El Beheiry, H.: General anaesthetics inhibit gap junction communication in cultured organotypic hippocampal slices. Anesthesia and Analgesia **102**(6), 1692–1698 (2006)

[106] Whittington, M., Jefferys, T., Traub, R.: Effects of intravenous anaesthetic agents on fast inhibitory oscillations in the rat hippocampus in vitro. British Journal of Pharmacology **118**(8), 1977–1986 (1996)

[107] Wright, E.M.: The linear difference-differential equation with constant coefficients. Proceedings of the Royal Society of Edinburgh. Section A. Mathematical and Physical Sciences **62**(04), 387–393 (1949)

[108] Yang, L., Ling, D.S.: Carbenoxolone modifies spontaneous inhibitory and excitatory synaptic transmission in rat somatosensory cortex. Neuroscience Letters **416**(3), 221–226 (2007)

[109] Yi, S., Nelson, P., Ulsoy, A.: Delay differential equations via the matrix Lambert-W function and bifurcation analysis: application to machine tool chatter. Mathematical Biosciences and Engineering **4**(2), 355 (2007)

[110] Zhang, S., Trussell, L.O.: Voltage clamp analysis of excitatory synaptic transmission in the avian nucleus magnocellularis. The Journal of Physiology **480**(Pt 1), 123 (1994)

[111] Zuleta-Alarcon, A., Castellon-Larios, K., Moran, K.R., Soghomonyan, S., Kumutala, L., Bergese, S.D.: Anesthesia-related perioperative seizures: pathophysiology, predisposing factors and practical recommendations. Austin Journal of Anesthesia and Analgesia **2**(4), 1026 (2014)